Recent Advances in Direct Air Capture by Adsorption

Xuancan Zhu[1], Wenwen Xie[2], Junye Wu[1], Yihe Miao[3], Chengjie Xiang[1], Chunping Chen[4], Bingyao Ge[1], Zhuozhen Gan[1], Fan Yang[1], Man Zhang[1], Tianshu Ge[1,*], Jia Li[3,5,6], Dermot O'Hare[4], Ruzhu Wang[1,*]

[1]Research Center of Solar Power & Refrigeration, School of Mechanical Engineering, Shanghai Jiao Tong University, 800 Dongchuan Road, Shanghai, 200240, China

[2]Institute of Technical Thermodynamics, Karlsruhe Institute of Technology, 76131, Germany

[3]China-UK Low Carbon College, Shanghai Jiao Tong University, No. 3 Yinlian Road, Shanghai 201306, China

[4]Chemistry Research Laboratory, Department of Chemistry, University of Oxford, 12 Mansfield Road, Oxford OX1 3TA, UK

[5]Jiangmen Laboratory for Carbon and Climate Science and Technology, No. 29 Jinzhou Road, Jiangmen, 529100, China

[6]The Hong Kong University of Science and Technology (Guangzhou), No.2 Huan Shi Road South, Nansha, Guangzhou, 511458, China

Corresponding authors:

E-mail: baby_wo@sjtu.edu.cn (T.S. Ge); rzwang@sjtu.edu.cn (R.Z. Wang)

Abstract

Significant progress has been made in direct air capture (DAC) in recent years. Evidence suggests that the large-scale deployment of DAC by adsorption is now technically feasible to achieve the ambitious goal of capturing 1% of the annual global CO_2 emissions. However, great efforts are still required to develop affordable DAC adsorbents such as amine-containing porous materials with large CO_2 capacities, fast kinetics, high selectivity, and long-term stability under ultra-low CO_2 concentration and humid conditions. It is also critically important to develop efficient DAC adsorptive processes and applications in aviation, agriculture, energy, and chemical industries. The synergy between DAC and carbon capture technologies for point sources can help to mitigate climate change effects in the long-term. Research and development in structured adsorbents that operate at low-temperature with excellent CO_2 capacities and kinetics, novel gas-solid contactors with low heat and mass transfer resistances, and energy-efficient regeneration methods using heat, vacuum, and steam purge are needed to commercialize adsorption-based DAC. This review provides an exhaustive description on materials development, adsorbent shaping, *in situ* characterization, adsorption mechanism simulation, process design, system integration, and techno-economic analysis of adsorption-based DAC over the past five years. This work benefits researchers concerned about global energy and environmental issues, and delivers perspective views for further deployment of negative-emission technologies.

1. Introduction

1.1. The urgency of developing DAC

1.1.1. CO_2 that needs to be captured. Fossil fuels are still the main energy source of the world. Emission from these sources leads to the total CO_2 emissions approaching 40 Gt yr^{-1}.[1] Although facing several limitations, integrated assessment models (IAMs),[2] the most effective tool to predict the CO_2 emission change in response to temperature rise target, suggested the CO_2 capture rate should reach 8–50 Gt yr^{-1} by 2100 to ensure the global average temperature rise within 2 °C.[3] Negative emission technologies (NETs) with a cumulative CO_2 capture of 400–800 Gt are required to achieve the more stringent 1.5 °C temperature rise target.[4] A recent study even claimed more negative CO_2 emissions than previously expected are required to compensate for the asymmetric climate-carbon cycle.[5] Most IAMs prefer bioenergy carbon capture and storage (BECCS) and afforestation as options to achieve negative emissions due to their perceived low costs and ability to generate energy.[6] However, the water and land-use marginal costs may be more expensive than estimated.[7,8] The lack of underlying data also makes the large-scale deployment of biological CO_2 removal highly uncertain.[9,10] In contrast, direct air capture (DAC) occupies much less land (*e.g.*, 0.003 ha per ton CO_2 captured per year) and requires 10–1000 times lower water utilization.[11] Thus, DAC can be a complementary technology to reduce the risk of negative emissions. Furthermore, deploying efficient DAC may delay the decommissioning fossil fuel-based power plants.[12]

While several previous IAMs included DAC,[13–16] Realmonte *et al.*[17] conducted the first inter-model comparison of different DAC technology options utilizing two IAM studies under several techno-economic assumptions. The results confirmed the potential of applying DAC to reduce the mitigation cost by more than 60%, and the large-scale deployment of DAC in the next half century with a fast DAC scale-up rate (*e.g.*, 1.5 Gt yr^{-1}) should be considered. In the meantime, they also warned that the failure to achieve this

scaling-up design of DAC as planned may cause a temperature overshoot of up to 0.8 °C. While preventive mitigation was previously recognized to be less expensive than deploying NETs in the business-as-usual scenario,[18] a recent modeling work by Bistline *et al.*[19] indicated that DAC is irreplaceable for achieving deep decarbonization in the electric power sector. Even under a high DAC deployment scenario, DAC accounts for less than 5% of the total electricity consumption and is much more cost-efficient than electrification and energy storage without NETs. Deep decarbonization in the industry and transport sectors also relies on the investment on a basket of NETs including DAC.[20] Chatterjee and Huang[21] hold the opposite view, suggesting that it is unrealistic to achieve deep CO_2 mitigation of 30 Gt yr^{-1} with the massive production of adsorbents and electricity and heat consumption required for DAC. Their analysis indicated that replacing the current energy sources with renewables is more efficient to reduce overall emissions. Furthermore, the at-scale deployment of NETs to reduce emissions has not yet been widely accepted by the public.[22] Nonetheless, there is still encouraging that technological advancements could significantly reduce the energy requirements of DAC, making it a promising long-term mitigation strategy.[23] In fact, recent studies advocated the near-term emergency deployment of DAC plants even under the current energy supply system to gain knowledge on lowering the operating costs.[24,25] They suggested large amounts of CO_2 can be removed by DAC, totaling 2.2–2.3, 13–20, and 17–27 Gt yr^{-1} in the years 2050, 2075, and 2100, respectively. It is highly encouraged carbon price trajectory is high initially with a moderate rise to avoid excessive carbon removal; but still retaining a substantial NET requirements (*e.g.*, 4 Gt yr^{-1} in 2050 and >10 Gt yr^{-1} in 2100).[26]

According to a recent International Energy Agency (IEA) report,[27] the global CO_2 capture rate should rise from 1.6 Gt yr^{-1} by 2030 to 7.6 Gt yr^{-1} by 2050. Most of the captured CO_2 is stored geologically and 5% is used for carbon-based fuel synthesis. This report suggested 2.4 Gt of CO_2 is removed directly from the

atmosphere through BECCS and DAC technologies, where 1.9 Gt of CO_2 is permanently stored, and the rest is used for synthetic fuels in applications such as aviation. The estimation that DAC captures several Gt yr^{-1} of CO_2 in 2050 fits well with optimized IAM scenarios considering constraints such as capacities, mitigation cost, as well as energy, water, and land use.[28] The Chinese Academy of Environmental Planning evaluated the target for CO_2 capture in China, concluding that the BECCS and DAC require annual reductions of 0.3–0.6 Gt and 0.2–0.3 Gt of CO_2, respectively, by 2060.[29] In addition, an IAM study suggested the necessity of applying NETs with a scaled-up CO_2 removal rate of 2.3–3.1 Mt yr^{-1} to achieve net-zero emissions by 2070 in Japan.[30] Depending on various quota principles, the European Union is responsible for removing 33–325 Gt of CO_2 by 2100 through NETs.[31] This huge quota cannot be realized without cross-border cooperation. For countries with limited biomass resources, such as the United Kingdom (7.1 Gt versus 11.9 Gt), it is necessary to deploy DAC to remove additional CO_2. IAM studies revealed that such a fast near-term deployment of NETs would benefit the long-term gross domestic product (GDP) and avoid temperature overshoot in most scenarios.[32] Particularly, the Gulf countries face the most severe welfare loss risk due to the "unburnable oil" to meet the temperature rise target; DAC is central in reducing 26% discounted GDP loss and allowing additional emission permits from international market exchange.[33]

1.1.2. Feasibility of large-scale DAC deployment. DAC is claimed to be already capable of achieving the goal of capturing 1% of annual global CO_2 emissions.[34] DAC coupled with hydrocarbon synthesis is also appealing as net-zero emission energy systems.[35] It is vital to comprehensively explore the net effects of this newly developed thermodynamic energy system on the atmosphere. Life cycle assessment (LCA) is an effective multi-step method to evaluate the feasibility of large-scale DAC deployment by considering the thermodynamic system efficiencies and environmental impact of the technology.[34,36–50]

While DAC has been previously considered as an energy-consuming process to capture CO_2 directly from

air at ultra-low CO_2 concentrations (~400 ppm), a recent LCA analysis conducted by van der Giesen *et al*.[36] illustrated that under specific conditions, a humidity-swing-based DAC (HS-DAC) could be largely passive, and its parasitic load (33–46 kJ mol^{-1}) was less than twice that of monoethanolamine-based post-combustion capture (MEA-PCC) (60–72 kJ mol^{-1}). Considering environmental impacts as a function of net greenhouse gas mitigation, powering distributed HS-DAC with photovoltaics increased nine environmental impacts by 18% compared to the value of 31% for MEA-PCC. Madhu *et al*.[47] adopted a fully transparent LCA to quantify the comparative life-cycle impacts of DAC technologies and found that the gigaton-scale deployment of DAC is not limited by input requirements such as land, water, chemical material, and energy. The temperature swing adsorption DAC (TSA-DAC) outperforms the high-temperature aqueous solution by a factor of 1.3–10 in all studied environmental impact categories and exhibits a higher net carbon removal ratio of 86%. Creutzig *et al*.[38] compared the performance of BECCS and direct air carbon capture and storage (DACCS), showing that the DACCS displayed a higher sequestration efficiency of 75–100% over the entire life cycle than that of BECCS (50–90% or less). Such a difference was mainly ascribed to the low land requirement of the DACCS (two orders of magnitude less than that of the BECCS). They also argued that although the current CO_2 removal costs of the DACCS are higher than those of BECCS, the modularity and granularity help the DACCS foster technological learning to less than 100 \$ t_{CO2}^{-1}.

Considering that the results of LCA highly depend on the original data adopted, the following metrics should be carefully evaluated for adsorption-based DAC: (1) the raw materials used to fabricate adsorbent materials, (2) the types of energy used to power the operation, (3) whether renewable energy was adopted as the power source, and (4) the raw material and equipment installation for such renewable energy. After comprehensively comparing a set of NETs using LCA, Terlouw *et al*.[50] pointed out that avoided emissions due to the substitution of certain processes can be easily misinterpreted as negative emissions. It is recommended to interpret available LCA results more carefully and transparently to fully understand the environmental impacts and trade-offs between NETs before large-scale deployment. Note that because

DAC technology is still in its early stages, the corresponding data are limited and lack transparency.[47,48,50] Using estimated and public data from practical operation systems is inevitable, even for much more recent studies. Consequently, controversial voices that speak of social cost and climate and health impacts appear. For instance, Jacobson[39] holds a negative attitude towards DAC and other carbon capture, utilization, and storage technologies. His analysis of a DAC plant using aqueous KOH sorbent driven by natural gas[51] concluded that only 10.5% and 20–31% of the removed CO_2 directly from the air can be achieved over 20 and 100 years, respectively. DAC plants increase air pollution and total social costs relative to no capture. However, according to the LCA analysis of commercial adsorption-based DAC plants located in Hinwil and Hellisheidi,[34] both systems can achieve negative emissions with capture efficiencies of 85.4 and 93.1%, respectively. The climatic benefits of DAC largely depend on the energy supply, adsorbent material, and plant construction. Other environmental impacts will increase by up to 0.057% when using wind power and 0.30% for the global electricity mix for 2050. Clearly, the obtained LCA results vary with the different capture technologies, system regeneration energy sources, and other criteria such as climate and environmental effect, air pollution, and social cost adopted. Overall, the LCA analysis shows the potential for deploying DAC as a climate-mitigation strategy.

1.1.3. DAC facility operation. DAC technology was originally developed for air pre-purification in air separation units[52] and for trace CO_2 removal in confined spaces.[53] The technology is now a research hotspot due to the threat of global climate change. The severe climate change problems and huge carbon emission actuality stress the indispensableness of DACs as effective NETs (**Fig. 1**).[54–56] Compared with conventional CO_2 capture technologies that separate CO_2 from existing large point source emissions, DAC systems capture CO_2 from any point or distributed sources. The DAC process can avoid the degradation of adsorbent caused by direct exposure to high concentrations of flue gas pollutants, such as SO_x, NO_x, and heavy metal

ions. Through the combination of DAC and BECCS, the demands for land can be reduced to achieve affordable negative emissions targets.

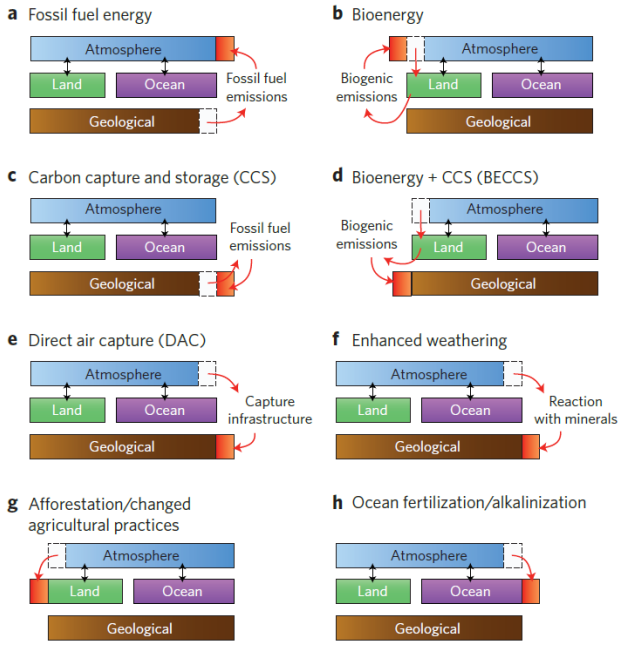

Fig. 1 Working principles of different NETs (Reproduced from ref. 55 with permission from Springer Nature, copyright 2016).

Early commercial DAC systems extracted CO_2 through causticization or alternative causticization by using alkali/alkaline earth metal hydroxide absorbents.[57,58] However, high energy consumption during the thermal regeneration process above 800 °C, high water loss, and the use of pure oxygen have limited the widespread applications of this absorption process. At present, only Carbon Engineering operates absorption-based DAC pilot plants.[51] Oak Ridge National Laboratory recently proposed a multistage absorption-based DAC cycle based on amino acids and organic salts, achieving regeneration at much lower temperatures.[59–62] However, this technology needs further pilot-scale study. In contrast, adsorption-based processes selectively separate CO_2 from the air and then are regenerated at 80–120 °C. In spite of the common understanding about the high minimum work required,[63] the actual energy consumption of pilot-scale DACs is currently only two to three times higher than that of capturing CO_2 from flue gas.

The components of a DAC facility that require electricity mainly include air blowers, switch valves, vacuum pumps, and control systems. Heat is also needed for optional steam production during thermal regeneration and heating sorbents and gas-solid contactors.[64] Using electricity from a coal-fired power plant to operate DACs may not be prudent because the plant produces extra CO_2.[65] A better way is to use renewable energy sources (*e.g.*, wind, photovoltaic, solar-thermal, geothermal, and vapor condensation heat), low-temperature waste heat from power plants and industries, or low-carbon fuels.[66–69] For instance, Carbon Engineering estimated that their absorption-based DAC plant requires either 8.81 GJ of natural gas or 5.25 GJ of gas and 366 kWh of electricity to capture and convert one ton of CO_2 from air to a compressed liquid at 15 MPa.[51] Another pilot-scale DAC built by Climeworks in Iceland is powered by geothermal energy, in which the geothermal fluid flows into a double-flash plant to co-generate electricity and steam at 120 °C.[70] Modularized DAC facilities could also be established in cities and driven by industrial waste heat. Coupling high temperature heat pump using green electricity further cuts down the energy consumption of DAC.

DAC technologies inevitably require the movement of a large amount of air for sufficient contact with adsorbents. A forced draft, usually electronically driven, is required to overcome the pressure drop in gas-solid contactors. The direct use of renewable energy can be explored to provide airflow and save electricity. For example, a solar updraft tower with large thermal reservoirs in the base was applied to provide continuous airflow in a DAC system.[71] Recent progress in dual-function materials, which are active for both CO_2 capture and utilization, offers a new perspective on system design.[72–74] DAC and reduction take place in sequence so that regeneration can be avoided. In practice, the sorbent particle size, packing surface area, and height/diameter ratios of contactors, among others, should be assessed. Also, periodic weather changes are sometimes important.

1.1.4. Policy roadmap. As BECCS, DACCS, and afforestation/reforestation (AR) are the three commonly featured NETs in low-carbon-emission scenarios induced by IAMs, Grant *et al.*[75] conducted an expert survey on the feasibility of the three technologies, accounting for only non-technical and societal/governance constraints. A comparison of the feasible carbon-emission-reduction potential between the results of their expert survey and the IAMs concludes AR is the largest NET before 2050; however, the long-term potential of AR is low, owing to the land availability, sink saturation, and institutional challenges. The DACCS shows the greatest long-term potential and the largest cumulative potential among the three NETs, although the DACCS has limited potential before 2050 owing to its high cost and low technological readiness. In addition, public opinion is essential for the deployment of DAC.[76–80] As most people are unfamiliar, DAC should be described and promoted in a cautious manner to avoid excessive concerns about its risks.[76,78]

The high capital cost is considered to be an obstacle for the development of DAC.[54,75,80–82] Therefore, generalized models for the cost analysis of DAC are necessary to determine the important parameters impacting the cost.[54] Azarabadi and Lancker proposed a techno-economic model of a net-present value equation to evaluate the maximum affordable budget (MAB) of a sorbent for any DAC system by using widely understood parameters.[81] The model inputs are three material-based parameters (C_0: initial CO_2 capture capacity of the sorbent, t_{cycle}: duration of one loading/unloading cycle, and f_t or f_{cycle}: exponential rate of degradation), two system-based parameters ($n_{O\&M}$: operating and maintenance (O&M) cost per unit time per unit mass of sorbent and V_{BoP}: capital cost per unit mass of sorbent), and two market-based inputs (P: the unit mass price of CO_2 and r: discount rate). The MAB and sorbent lifetime (t_{life}) are two important model outputs. As the P and r of CO_2 are two exogenous parameters, the effects of the three material-based parameters on the feasibility of DAC systems were discussed. The MAB estimation of existing DAC

sorbents selected in previous studies indicates that the high capacity, short cycle durations, and high resistance to degradation of each sorbent are the three dominant factors for realizing the economic feasibility of DAC systems. This is also the information for policymakers to provide research funding for achieving a trade-off between the cost and excellent performance of DAC sorbents. As the focus of current research is mainly on new DAC sorbents, the study of the kinetics and stability of DAC sorbents is highly recommended by Azarabadi and Lancker; this is reviewed and discussed, based on existing work, in the following sections.

Although the CO_2 price is an exogenous parameter for determining the final cost of DAC, it plays an important role in determining the feasibility of DAC deployment. **Table 1** lists the estimated CO_2 prices by the IEA among different countries over different periods for net–zero-emission (NZE) scenarios.[27] According to the results reported by Azarabadi and Lancker,[81] if a CO_2 price of 75 \$ t^{-1} is assumed, DAC will become commercially feasible after 2030 in most advanced economies. In addition, a low discount rate would be necessary to realize the feasibility of DAC in the early stage. In the study conducted by Azarabadi and Lancker, the discount rate was fixed at 5%; however, policymakers should provide stronger financial support, such as green loans for DAC, to lower the discount rate and promote the development of DAC. Herein, we propose that a discount rate of 1–2% is reasonable for future studies.

Table 1 CO_2 prices for electricity, industry, and energy production in NZE scenarios (Reproduced from ref. 27 with permission from International Energy Agency, copyright 2021).

USD (2019) per tonne of CO_2	2025	2030	2040	2050
Advanced economies	75	130	205	250
Selected emerging market and developing economies*	45	90	160	200
Other emerging market and developing economies	3	15	35	55

*Includes China, Russia, Brazil, and South Africa.

The importance of DAC in achieving net-zero emissions is becoming indisputable; however, a market to

advance DAC remains elusive; this can be ascribed to the current high cost and limited market demands of the primary product of DAC, that is, CO_2. These challenges require effective policies to promote DAC development from several perspectives, as discussed earlier. Recently, Meckling and Biber suggested a policy formula, "financial incentives + deployment or performance mandate," based on electric vehicles and renewables. Mandating DAC mainly includes upstream regulation (regulation of the extraction of fossil fuels from the ground) and downstream regulation (regulation of the sale of fossil fuels for consumption by end-users). In particular, California's Low Carbon Fuel Standard (LCFS) is a successful example of downstream regulation. Downstream regulation allows players from outside the oil and gas industry to drive the DAC business, and policymakers can use "financial incentives + deployment or performance mandates" to level-up fuel standards step-by-step from low-carbon to carbon-neutral and, finally, to carbon-negative scenarios, as shown in **Fig. 2**, before gradually increasing the public demand for climatic actions. In addition, Meckling and Biber reported a series of lessons learnt from failure of the current carbon capture and storage (CCS) policies. First, deploying CCS on power plants or industrial emission sources requires very high initial investments and long time-frames, especially for the construction of an entirely new source. Therefore, financial support from the government can only permit very limited projects. Subsequently, entrants to the CCS industry are rare, and the benefits of repeated experimentation and failure begin to diminish. Second, CCS is geographically restricted to locations where point-emission sources are located because of the cost limitations of CO_2 transportation. In addition, the pathway to net-zero emissions through electrification and 100% renewable electricity will strongly promote the development of DAC.[82,83]

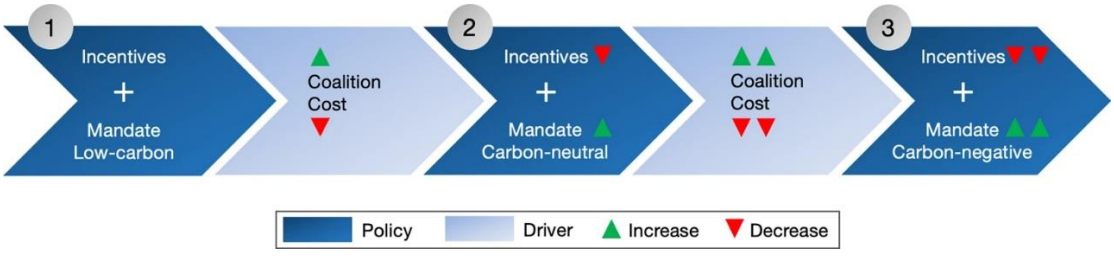

Fig. 2 Policy sequence for climate leaders to develop DAC technology. Climate leaders, in particular those

with an existing LCFS, could start market development for DAC through an "incentive + mandate" policy mix. Over time, they could intensify the stringency of the mandates, while reducing incentives as cost declines and political support broadens (Reproduced from ref. 84 with permission from Springer Nature, copyright 2021).

The European Union (EU), United Kingdom (UK), and United States (US) have pledged to achieve net-zero emissions before 2050. Germany, as the dominant economy in the EU, is committed to realizing net-zero emissions before 2045. In particular, China, as the largest developing country, promised to reach its maximum carbon emissions before 2030 and become carbon-neutral by 2060. Undoubtedly, these political pledges are accelerating NET-promotion policies and investments, especially for DAC. The EU has delivered innovation funding of EUR 15 million, through the "Horizon Europe Work Programme" for 2021-2022, to establish the technological feasibility of DACCS.[85] Recently, the UK committed to delivering £100 million innovation funding for DACCS.[86] During the net-zero transition, DACCS is envisaged to be at a commercial scale in the UK by 2030, owing to the efforts in demonstration and piloting during the 2020s, with the support from the UK government.[86] A consensus study conducted by the US National Academies of Sciences, Engineering, and Medicine in 2018 highlighted the absence of an economic driver that restricts the rapid testing and deployment of DAC.[87] This report suggested staggering funding from policymakers, as depicted in **Fig. 3**, to construct a pipeline of DAC technology from basic and applied research through the deployment of DAC systems. The funding over 15 years should focus on research and development that transitions to demonstration and deployment projects.

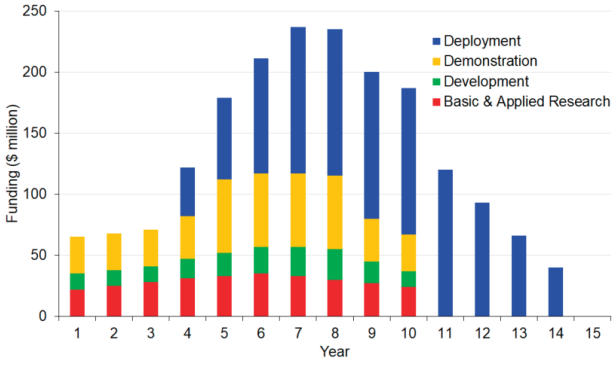

Fig. 3 Recommended annual U.S. federal funding allocations for basic and applied research, demonstration, development, and deployment of DAC technology (Reproduced from ref. 87 with permission from National Academies Press, copyright 2019).

"The Long-Term Strategy of the United States: Pathways to Net-Zero Greenhouse Gas Emissions by 2050," published in 2021 by the U.S. Department of State, also emphasized that the difficulties of determining the cost of DAC and the adverse impact of DAC at a large scale would hinder the future development of DAC.[88] In November 2021, the U.S. Department of Energy's (DOE's) third Energy Earthshots, "Carbon Negative Shot," became the U.S. government's first major effort in NET and set a new goal to remove gigatons of CO_2 from the air and durably store it for less than 100 \$ t^{-1} of CO_2-equivalent (CO_{2e}). In 2021, the DOE announced two special funding schemes to incentivize the development of DAC, each worth \$12 and \$14.5 million. As China has not reached its peak in terms of carbon emissions, three government research institutions in China reported that DAC would achieve demonstration scale by 2035 in China and that the period leading up to 2035 is crucial for lab- and pilot-scale development work.[29] According to a special report on China from the IEA, DAC would significantly contribute to emission reduction from 2040, and most DAC plants would be located in the western provinces, which are the areas with the most suitable solar and wind resources and with high potential CO_2 storage capacity.[89] To the best of our knowledge, the Science and Technology Commission of the Shanghai Municipality first announced a local technology innovation fund of *ca.* RMB 1.5 million, aiming at developing DAC technology in 2021.[90] We appraise that DAC would attract considerable research interests during the 2020s and achieve deployment at demonstration and pilot scales in many countries during the 2030s.

1.2. Overview of adsorption-based DAC technologies

Several reviews have been published about DAC.[91–96] In early 2016, Sanz-Pérez *et al*.[91] provided a historical overview of DAC, describing the use of basic solvents, the supported amine and ammonium materials, and metal-organic frameworks (MOFs) in DAC, as well as techno-economic analyses on DAC. Later, Shi *et al*.[95] categorized the major types of DAC sorbents as physisorbents (activated carbon, zeolites, MOFs, and novel materials), amine-modified sorbents, and moisture swing sorbents. Notably, the concept of DAC is now being widely recognized as a necessary NET to achieve a stringent 1.5 °C temperature target. Hundreds of papers sharing new ideas about materials and processes for DAC have been published during the past five years (**Fig. 4**). Among them, amine-functionalized porous materials are the most widely studied DAC adsorbents due to their high tolerance to moisture, low energy requirement for regeneration, amine groups having strong affinity towards CO_2.[97,98] Reliable shaping methods such as pelleting, hollow fibering, granulating, extruding, 3D printing, and electrostatic spinning have been tested to fabricate structured DAC adsorbents with reduced mass transfer resistance.[99] Understanding the influence of water on CO_2 adsorption under ultradilute conditions is now clearer thanks to the development of *in situ* characterization techniques and material simulation tools.[100] The thermal, hydrothermal, and chemical stabilities of DAC adsorbents upon exposure to high temperatures, oxygen, dry CO_2, and steam are largely improved.[101] Adsorption-based DAC technologies have been applied in many areas such as Power-to-X, CO_2 control in confined spaces, agricultural greenhouse, mineralization, and microalgae cultivation.[102–105] Providing a comprehensive review of recent advances in adsorption-based DAC from molecular to process scale is timely, considering that the technology is an irreplaceable solution to avoid catastrophic climate change.

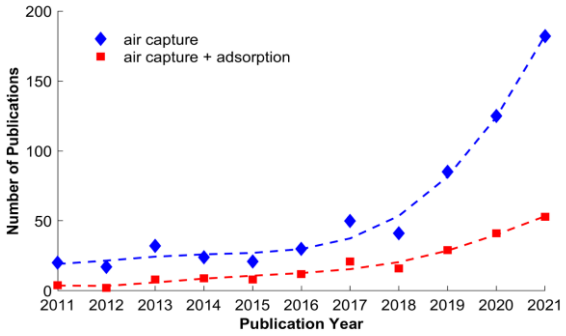

Fig. 4 Number of publications during 2011–2021 on Web of Science database with the keywords of (a) air capture, and (b) air capture and adsorption.

1.2.1. Amine-functionalized adsorbents. Amine-functionalized porous materials have great potential for commercial-scale DAC applications because of their low cost, high amine density, suitable heat of adsorption, ease of preparation, and relatively large CO_2 adsorption capacity under ultradilute conditions. Branched polyethyleneimine (PEI) with a low degree of polymerization and rich primary amines is commonly used for preparing polyamine-impregnated adsorbents because small amine molecules lead to significant amine leakage and high-molecular-weight PEI impedes the diffusion of CO_2 through porous substrates. Previous work has also verified the feasibility of other polyamines such as polyallylamine (PAA), tetraethylenepentamine (TEPA), and poly(propylene guanidine) (PPG) for DAC. The supported polyamine leads to low amine efficiencies, mainly because of the disordered stacking of amines blocking the active sites and slowing down the diffusion rate of CO_2. In addition, the stability of aminopolymer-impregnated adsorbents under thermal regeneration and oxygen-containing conditions is a concern owing to the weak interaction between amines and supports. Therefore, researchers are simultaneously developing amine-grafted adsorbents that graft small amines onto supports through covalent chemical bonds. From 2017 to 2022, the research activities mainly included the following five aspects: (1) synergetic enhancement between amines and supports, (2) oxidative degradation avoidance, (3) H_2O and CO_2 cooperative adsorption, (4) mechanistic studies, and (5) novel amine-functionalized adsorbents.

While amine loading is considered as the main factor determining the CO_2 adsorption capacity of amine-functionalized porous materials under ultradilute conditions, the morphology of amine molecules in the support and the change of gas-solid interaction change between the texture and surface microstructure of the support can also significantly affect the overall CO_2 capture efficiency. Most recently, a better understanding of the synergetic enhancement between amines and supports have been ellucidated.[106–125] Extensive studies have been conducted to increase the hybrid capacity to chemisorb CO_2 and the adsorption efficiency through high amine grafting density. It is now clear that the hybrid properties can be correlated with solvent polarity, more specifically, with the interaction between the inorganic matrix surface and the solvent during grafting. Methods for multiple and multilayer amine grafting have been proposed, and the clumping and agglomeration of the support under wet grafting conditions due to interparticle polymerization of amines have been solved. The CO_2 uptake and thermal/oxidative stabilities of linear and branched aminosilanes were evaluated. The use of supercritical CO_2 grafting further enhanced amine grafting efficiency. Studies have also suggested that chemisorbed CO_2 species formed on supported and hindered amines are weakly bound, leading to reduced energy costs associated with regeneration if such materials are deployed in a practical separation process.

Prototypical PEI degrades oxidatively at elevated temperatures. In particular, primary and tertiary amines appeared to be stable against oxidation, whereas secondary amines were degraded via imine and amide formation. Recently, several breakthroughs have been achieved in proving the oxidative stability of supported PEI or finding alternative amine polymers.[101,126–130] The chemical kinetics of the oxidation of PEI have also been well illustrated to quantitatively estimate the material lifetime.[131]

Considering that water vapor is a ubiquitous component of air, understanding its impact on CO_2 adsorption is critical. In the presence of amine-containing adsorbents, water is an excellent promoter of CO_2 adsorption;

it increases the rate of CO_2 capture and is even necessary for long-term stability. Recent work has discussed the effect of humidity on CO_2 uptake and adsorption kinetics.[100,132–135] Novel mechanistic co-adsorption isotherm models have been introduced accordingly.[136] The effect of water on the regeneration heat has also been discussed.[137]

Although porous aminopolymers are widely recognized as the most promising DAC adsorbents, the existence of chemisorbed CO_2 species on the aminopolymer surface is still under debate and requires new experimental proof of assignment. Recent work combining *in situ* spectroscopy and theoretical approaches have provided a molecular-level understanding of chemisorbed CO_2 species in amine-functionalized adsorbents.[138–140] In particular, the hydrated bicarbonate formation by chemisorption of CO_2, which has not been detected by solid-state nuclear magnetic resonance (NMR), CP/MAS ^{13}C-NMR, has been experimentally identified.[141] The deactivation mechanism by CO_2 and O_2 has also been elaborated.[142,143]

Several novel amine-functionalized adsorbents have recently been developed, exhibiting promising CO_2 capture ability from air sources. The M_2(dobpdc) series (M = Mg, Mn, Fe, Co, Ni, Zn; dobpdc^{4-} = 4,4-dioxido-3,3-biphenyldicarboxylate), expanded analogs of the MOF-74 structure type, have high-density open metal sites that are postmodified by diamines. Such functionalization enables exceptional CO_2 capacities under dilute and ultradilute conditions, with adjustable adsorption and desorption characteristics. Recent work overcomes two challenges of diamine-tethered MOFs to achieve stable uptake under humid conditions and low regeneration temperatures for energy savings.[144–153] The enhancement mechanism of diamine functionalization on gas adsorption was illustrated. The working capacities and low-pressure adsorption amounts were found to correlate with the number of alkyl substituents and the alkyl chain length. In addition, a new cooperative mechanism for CO_2 adsorption was observed in alcoholamine- and alkoxyalkylamine-functionalized Mg_2(dobpdc), a key to achieving cooperative CO_2 adsorption.

Quaternary ammonium-based anion exchange resin can effectively adsorb CO_2 from dry air and release it when wet. Such moisture-swing adsorbents offer a new approach for regenerating CO_2 sorbents because water-handling cost is low. Recent work revealed the working mechanism of moisture swing adsorbents as free energy change of the chemical reaction.[154–163] The influence of pore size, cation spacing, and surface hydrophobicity of the adsorbent on the CO_2 capture efficiency was elucidated. Potential supports for moisture-driven sorbents have also been extended to covalent organic frameworks (COFs), zeolites, silica, graphene oxides, functionalized carbon black, and MOFs.

Although the presence of water enhances the CO_2 adsorption capacities and avoids CO_2 deactivation of amine-functionalized adsorbents, it leads to several drawbacks, such as amine leaching, increased regeneration energy, and structural degradation. Recently, several novel amine-based adsorbents with hydrophobic character have been synthesized, either through hydrophobic supports or hydrophobic organic moieties.[164–166]

1.2.2. Cyclic processes. Rapid scaling-up design of efficient adsorption-based DAC processes has been witnessed in recent years, such as temperature concentration swing adsorption (TCSA) using an inert gas purge or a CO_2 purge,[167,168] temperature vacuum swing adsorption (TVSA),[169–176] steam-assisted TCSA (S-TCSA),[177–179] and steam-assisted temperature vacuum swing adsorption (S-TVSA).[177,180] By applying the hybrid desorption process combined with vacuum, heating, and steam purge, steam can be supplied to S-TVSA at low temperatures using solar energy or waste heat. In addition, the sweeping effect of the steam purge provides a larger driving force for desorption at lower CO_2 partial pressures than that in TVSA. A techno-economic assessment was conducted to assess the feasibility of large-scale deployment of an adsorption-based DAC.[54,181–184]

Novel adsorbent shaping technologies and gas-solid contactors with enhanced heat and mass transfer are also critical to meet the cost requirements of the DAC process for commercialization. Naturally-powdered DAC adsorbents can be shaped through pelleting, granulating, extruding, hollow fiber forming, 3D printing, coating on monoliths, and electrostatic spinning.[99,106,135,185–191] It has been proven that hydrophobic polymer coatings improve the hydrolytic stability and gas sorption performance of adsorbents under humid conditions. Remarkable progress has been made in the development of monolithic adsorbents via 3D printing, which allows 80–90 wt.% adsorbent loading and makes materials easily tuned to fit any column. On this basis, the adsorption of CO_2 under ultradilute conditions relevant to DAC using packed bed breakthrough systems was comprehensively investigated to examine the effects of flow rate, temperature, and CO_2 concentration on the observed breakthrough profiles, isotherm shape, mass transfer resistance, and adsorption/desorption kinetics.[133,192–197] Overall, the system performance (i.e., rate of CO_2 extraction, CO_2 capture fraction, and breakthrough curve types) for different feed concentrations of CO_2 was identified. A thermodynamic tool was introduced to determine the energy requirements for CO_2 capture using amine-functionalized adsorbents.[198] Several other novel gas-solid contactors such as rotating columns, moving beds, and radial flow contactors have also been proposed for DAC.[199,200]

1.2.3. Industrial applications. DAC facilities are found worldwide.[61,201–204] Existing DAC companies include Carbon Engineering (Canada), Climeworks (Switzerland), Global Thermostat (USA), Infinitree (USA), Antecy (Netherlands), Skytree (Netherlands), Carbon Collect (Ireland), and Hydrocell (Finland). A detailed technical and economic analysis of existing DAC devices has been reported in the latest literature.[205] Among all commercial DAC devices, Global Thermostat reported the lowest operating energy requirements (150–260 $kWh_{el}\ t^{-1}$ and 1170–1410 $kWh_{th}\ t^{-1}$). The cost of CO_2 capture using a solvent absorption DAC demonstration unit based on high-temperature regeneration is estimated to be 94–232

$ t^{-1}[151] and is expected to drop below 60 $ t^{-1} by 2040. Because the heat of desorption of the adsorbents is lower than the heat of the CO_2 absorption process, the use of solid adsorbents to capture CO_2 will further reduce the cost. Depending on the application, the lowest cost of adsorption-based DAC ranges from 29 to 91 $ t^{-1}.[81]

Because a DAC facility can provide on-site CO_2 generation anywhere, its application is advantageous in addition to its environmental benefits. Recently, the potential application of adsorption-based DAC in indoor air removal,[111,189,191,206,207] greenhouse,[174,208] biomass production,[209–213] fuel production (CH_4,[66,68,73,214–220] methanol,[69,221–224] aviation fuel,[71,225–230] hydrocarbon[231]), chemicals (Fischer-Tropsch process,[232,233] carbon nanotubes,[234] dimethyl carbonate,[235] syngas[236,237]), mineralization,[238–242] storage,[243,244] enhanced oil recovery (EOR),[245] and cogeneration in power plants or chemical industries[67,246–248] has been reported.

1.3. Content summary

This review is organized as follows. In the introduction section (Section 1), the urgency of the development of DAC, including the exact amount of CO_2 we need to capture, the feasibility of large-scale DAC deployment, DAC facility operation, and policy roadmap, are illustrated mainly from the results of IAM predictions, LCAs, and policy studies. Following the introduction, recent advances in DAC adsorbents, processes, and systems are briefly summarized to provide an overview of adsorption-based DAC technologies. The concepts are elaborated in subsequent sections.

In particular, we focus on amine-functionalized porous materials as the most effective DAC adsorbents, such as silicas, activated carbons, zeolites, MOFs, aluminum oxide, cellulose, resin, and layered double hydroxides (LDHs) through amine impregnation, surface silylation, *in situ* polymerization, and other

synthetic strategies. In Section 2, amine types, supports, and additives, and the synergetic enhancement between amines and supports are discussed. The design of DAC adsorbents with suitable morphologies, strong affinities for polyamines, good thermal stabilities, and hydrothermal stabilities are also illustrated. Section 3 discusses recent breakthroughs in proving the oxidative stability of supported PEI and finding alternative amine polymers, such as using dendritic structures that consist of only primary and tertiary amines, epoxidation of primary and secondary amines, and addition of additives. In Section 4, recent advances in the effect of humidity on CO_2 uptake and kinetics and co-adsorption isotherm modeling are discussed. Section 5 reviews recent work on understanding the chemisorbed CO_2 species of amine-functionalized adsorbents through experimental identification methods and theoretical approaches. Section 6 reviews the recent breakthroughs in three novel amine-functionalized adsorbents for potential application in DAC: diamine-tethered MOFs, moisture swing adsorbents, and hydrophobic amine-containing adsorbents.

In Section 7, shaping methods for naturally-powdered DAC adsorbents are reviewed, emphasizing material selection and optimization, geometric structuring, and industrial scale-up. Subsequently, the adsorption of CO_2 under ultradilute conditions relevant to DAC using packed bed breakthrough systems is reviewed. The system performance is determined for different feed concentrations of CO_2. Several other novel gas-solid contactors, such as rotating columns, moving beds, and radial flow contactors, have also been described for DAC. The operating efficiency and energy consumption of the adsorption-desorption processes for DAC are evaluated using techno-economic analysis. Finally, the potential application of adsorption-based DAC in indoor air removal, greenhouses, biomass production, and fuel production is presented.

In the last section, major challenges and perspectives in adsorbents, shaping methods, adsorber reactors, and separation systems for DAC are summarized. DAC fundamental studies and pilot-scale separation development are also explained.

2. Synergetic enhancement between amines and supports

Supported amines exhibit higher CO_2 capacity than that of the support or amine alone, indicating there is a synergistic enhancement between amines and supports. A plausible explanation is that the supports provide sufficient spaces for the amine dispersion, and thus increase the available CO_2 adsorption sites. The amine property, support structure, and additive utilization affect the interaction strength and change the adsorption capacity, kinetics, and amine efficiency. A deep understanding of their roles in the synergetic enhancement is instructive for optimizing the material design.

2.1. Effect of amines

2.1.1. Aminopolymer-impregnated adsorbents. Aminopolymer-impregnated adsorbents rely on physical impregnation into the available pore window of a mesoporous solid support by stirring the support with the desired amine in the organic dispersant. They typically have large capacities because of their high amine contents. The prominent advantages of easy preparation and relatively desirable performance make aminopolymer-impregnated materials more widely investigated than other adsorbents. However, shortcomings, such as lack of stability due to the leaching of amines over adsorption/desorption cycles and limited transport of CO_2 to active support sites due to hindered diffusion, pose challenges associated with applications of these materials.

The selection of the amine type is a key factor affecting the performance of amine-impregnated adsorbents. The properties of the synthesized supported amines can differ according to the characterization of the

amines themselves. In most cases, larger aminopolymers have been adopted for impregnation, whereas the use of shorter amine moieties has also been reported. The molecular formulas of aminopolymers and small amines used for DAC are shown in **Fig. 5**. Among the various amines, PEI has been the most investigated because of its high amine content, stability, convenient customization, and availability. Several researchers have utilized PEI-modified adsorbents.[95,249,250] They exhibited good performance, but there is much room for improvement. In recent years, an increasing number of studies have been conducted on the development of other aminopolymers for adsorbent synthesis. Similar to PEI, polypropyleneimine (PPI) is a type of aminopolymer that can form linear, branched, or dendritic shapes and contains three methyl groups on the monomer. PPI showed enhanced oxidation resistance compared to PEI. However, a relatively complex monomer synthesis and time-consuming polymerization limit its development. Pang *et al.*[126,128] compared PPI- and PEI-modified sorbents in DAC. Regardless of the amine loading or aminopolymer architecture, PPI-based sorbents were found to be more efficient for CO_2 capture than PEI-based sorbents. The effect of acid initiators on branched PPI synthesis and CO_2 sorption performance was investigated.[114] Sorbents with 30 wt.% polymers synthesized using HBr and $HClO_4$ exhibited higher CO_2 capacities than those prepared with HCl or CH_3SO_3H. The extended aging (1.5–2 years) on linear PPI (LPPI) has been tested.[129] Aged LPPI-based sorbents preserved their ability with modestly decreased CO_2 uptake lower than 20% compared to the fresh polymers, indicating their long-term use ability.

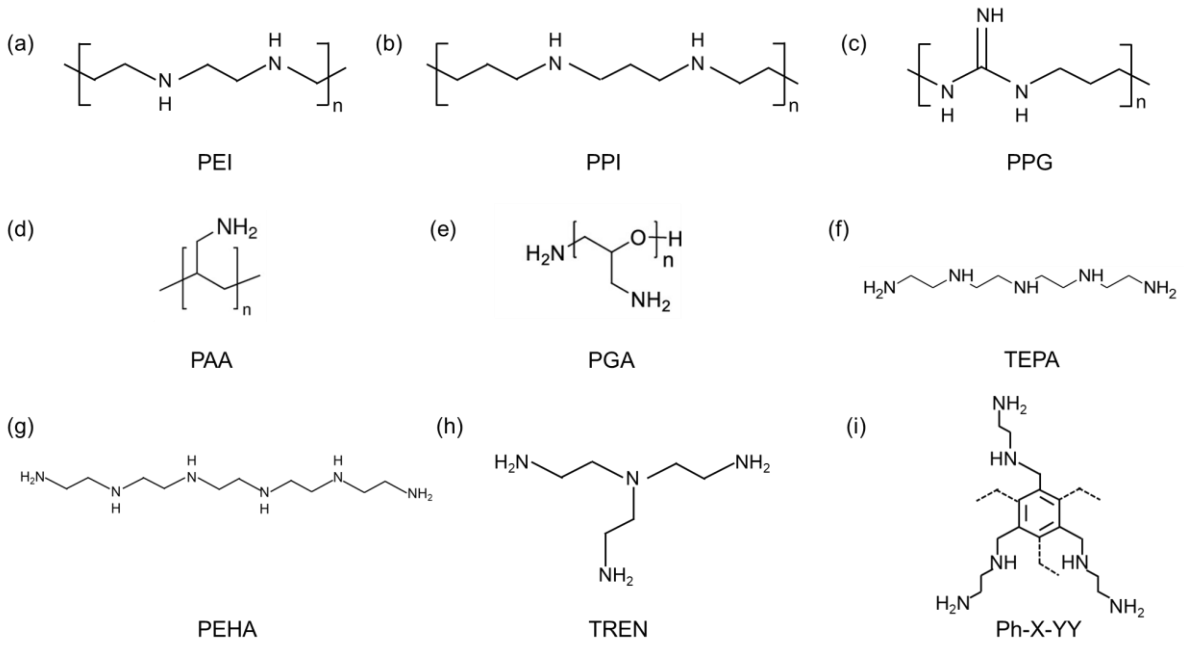

Fig. 5 Molecular formula of the main types of amines used for DAC.

A PPG-based oligomer/polymer was also synthesized by poly-condensation of 1,3-diamino propane and guanidine hydrochloride impregnated into SBA-15.[251] Such sorbents exhibited lower pseudo-equilibrium capacities but faster kinetics than PEI based sorbents under 400 ppm CO_2. PAA is another type of aminopolymer which consists of dense primary amines. It also shows enhanced oxidative and thermal resistance,[252] which makes it a potential material for CO_2 capture. Studies have been performed to impregnate PAA into mesocellular siliceous foams (MCFs) and fumed silica for DAC.[253,254] PAA was further reacted with short fluoroalkyl chains and cross-linked with C_{60}.[255] The incorporation of fluoroalkyl chains generates free volume elements that act as intramolecular diffusion pathways, resulting increased trace CO_2 capture efficiencies. Poly(glycidyl amine) (PGA) is a polymer that contains both ethylene oxide and amine groups in each repeat unit. PGA consists of only primary amines, so it has the potential to achieve better CO_2 capture than PEI. Sujan *et al.*[115] synthesized PGA-impregnated SBA-15 to capture CO_2 from flue gas and air. The PGA-modified adsorbents showed approximately 0.6 mmol g^{-1} capacity in simulated air and less oxidative degradation than that modified with PEI on a relative basis. PGA has been

demonstrated as a candidate polymer for amine/oxide hybrid CO_2 sorbents.

The development of smaller amines for aminopolymer-impregnated adsorbent synthesis also facilitates research on DAC. Several studies have proved that TEPA-impregnated sorbents show a high capacity for DAC, although they suffer from obvious cyclic stability problems.[127,256,257] Pentaethylenehexamine (PEHA) contains one more amine group than TEPA, and has been verified to exhibit promising capacities and stabilities for DAC.[127] Tris (2-amino ethyl) (TREN) is a small amine with a high density of primary amines; thus, it has great potential for excellent uptake. Darunte *et al*.[258] use TREN to impregnate MIL-101(Cr), and the results showed higher capacity than that of PEI, although a significant loss of amines was observed. In a recent study by Kumar *et al*.,[113] alkyl-aryl amine-rich small molecules (Ph-X-YY) were prepared by one-step nucleophilic substitution of tri- (X = 3) and hexa-bromine-substituted (X = 6) aromatic cores with two different aliphatic diamines, ethylenediamine (YY = ED) and propylenediamine (YY = PD). The Ph-X-YY impregnated solid sorbents showed capacities of 1.6–1.9 mmol g^{-1} in 400 ppm CO_2, along with good thermal stability. Overall, smaller amines result in decreased diffusion resistance and high amine loading. Lower regeneration temperature is required to alleviate their thermal volatility problems.[112]

One significant advantage of aminopolymers is their structural tunability; that is, their molecular weight and chain type can be regulated by varying their synthesis conditions. Aminopolymers with larger molecular weights have lower volatility; thus, their thermal stability is enhanced. However, larger aminopolymers can have a negative effect on CO_2 diffusion because of their higher viscosity and tendency to cause pore blockage, which deteriorates the adsorption capacity and kinetics. In contrast, shorter chains may exhibit an advantage of higher capacity, but cyclic stability can lead to a shorter service life. To achieve a compromise between the two extremes, for instance, the molecular weight of PEI is typically controlled at 400–25000 g mol^{-1}.[259] By regulating the chain shape of the aminopolymer, the primary, secondary, and

tertiary amine contents can be altered. Linear PEI mostly consists of secondary amines, whereas branched PEI contains more primary amines at the ends of its backbones. Tertiary amines are formed at the branched points of the chain, typically in dendrimer chains. Primary and secondary amines are typically preferred owing to their ability to capture CO_2 under both dry and humid conditions. Some studies have pointed out that primary amines have faster kinetics, higher oxidative resistance, and less regeneration energy requirement.[260,261] This is possibly because the primary amine preferentially bonded to CO_2 through the formation of intermolecular ammonium carbamates, whereas CO_2 was predominantly stabilized as carbamic acid when interacting with secondary amines.[261] Tertiary amines react with CO_2 to form ammonium bicarbonates on solid-supported amines, but the slow reaction rates make them be poor CO_2 sorbents.[262,263] To increase the amine efficiency of the supported amines, both the molecular weight and amine-type ratio should be properly controlled.

Another issue affecting the performance of supported amines is the amine distribution inside the pores. The amine distribution pattern is closely related to the accessibility of amines to CO_2, which plays a key role in determining amine efficiency. Xu *et al*.[264] pointed out that at low temperatures, PEI exists in the channels of silica-like nanosized particles. In this case, only the CO_2 affinity sites on the surfaces of the particles can readily react with CO_2. At high temperatures, PEI has a diverging distribution, allowing internal adsorption sites to be accessible to CO_2. According to Holewinski *et al*.,[265] PEI firstly forms a thin conformal coating on the pore walls, and additional polymer aggregates into plugs that grow along the pore axis. The PEI plugs increased the CO_2 diffusion barriers, and reduced the performance. Rother *et al*.[266] holds the view that the physical properties of the CO_2-adsorbing polymers are altered by their interactions with supports, which in turn impacts their capture properties (**Fig. 6**a–c). After dispersing aminopolymer films in nanoporous silica and carbon, strong densification is only found for polymers imbibed in mesoporous

carbon. These distinct amine distribution patterns result in different adsorption performances of carbon and silica (**Fig. 6**d–e).

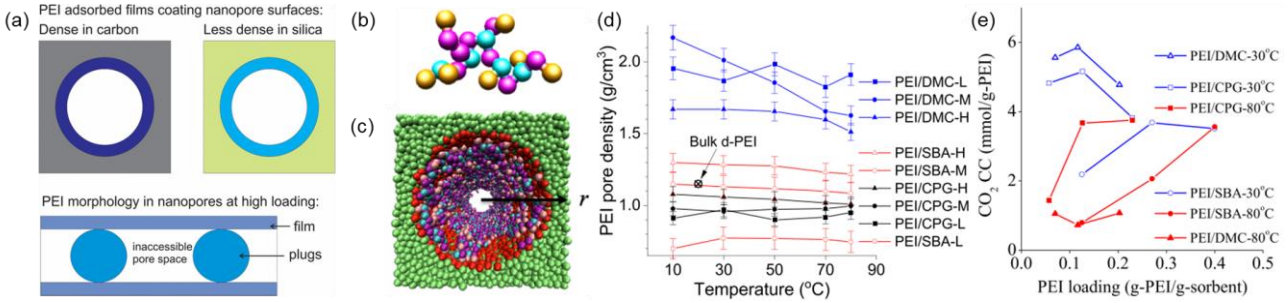

Fig. 6 Interactions of PEI with nanoporous silica and carbon. (a) Amine distribution in the pores of the supports. (b) Bead spring model of the branched PEI; the gold, magenta, and cyan beads represent primary, secondary, and tertiary amines, respectively. (c) Cylindrical pore impregnated with PEI that shows attractive beads and green repulsive support beads. (d) Mean pore densities of PEI inside nanopores of the three substrates for different filling degrees and temperatures. (e) CO_2 capture capacity (CC) of PEI/controlled pore glass (CPG), PEI/SBA, and PEI/carbon (C) (Reproduced from ref. 266 with permission from American Chemical Society, copyright 2021).

When amine was impregnated into the support, the amine loading amount had a significant influence on the adsorbent performance. Theoretically, a higher amine loading gives more amine groups in the support, resulting in more adsorption sites. However, it has been proven that excess amine can lead to greater diffusion resistance and limit CO_2 adsorption, which decreases amine efficiency. Therefore, there is an optimal loading that is determined by the pore structure of supports. The theoretical maximum amine loading can be estimated through multiplying amine density by the cumulative pore volume, assuming that all amines are filled inside the pores of the support.[267] However, the actual optimal loading is typically not equal to the maximum loading, possibly because the amines cannot completely enter the pores and deposit on the surface as bulk polymers. Most studies reported that the optimal amine loading is between 30 and 70 wt.%. As shown in **Fig. 7**a, Cogswell *et al.*[268] stated that the optimal amine loading is determined in the loading regime before pore blocking occurs. They suggested developing a new sort of support structure that allows decoupling the amine loading from increasing resistance. For instance, a 3-dimensional silica

mesoporous framework was loaded with large or small amine-containing molecules.[269] The obtained adsorbents demonstrated fast sorption kinetics while maintaining high amine efficiencies (**Fig. 7**b and c), which indicates that using a support with interconnected but distinctly sized pore channels can overcome the trade-off between amine loading and diffusion resistance. They later verified this strategy again by synthesizing a hierarchical supramolecular porous material with tailorable porosity (**Fig. 7**d and e).[270]

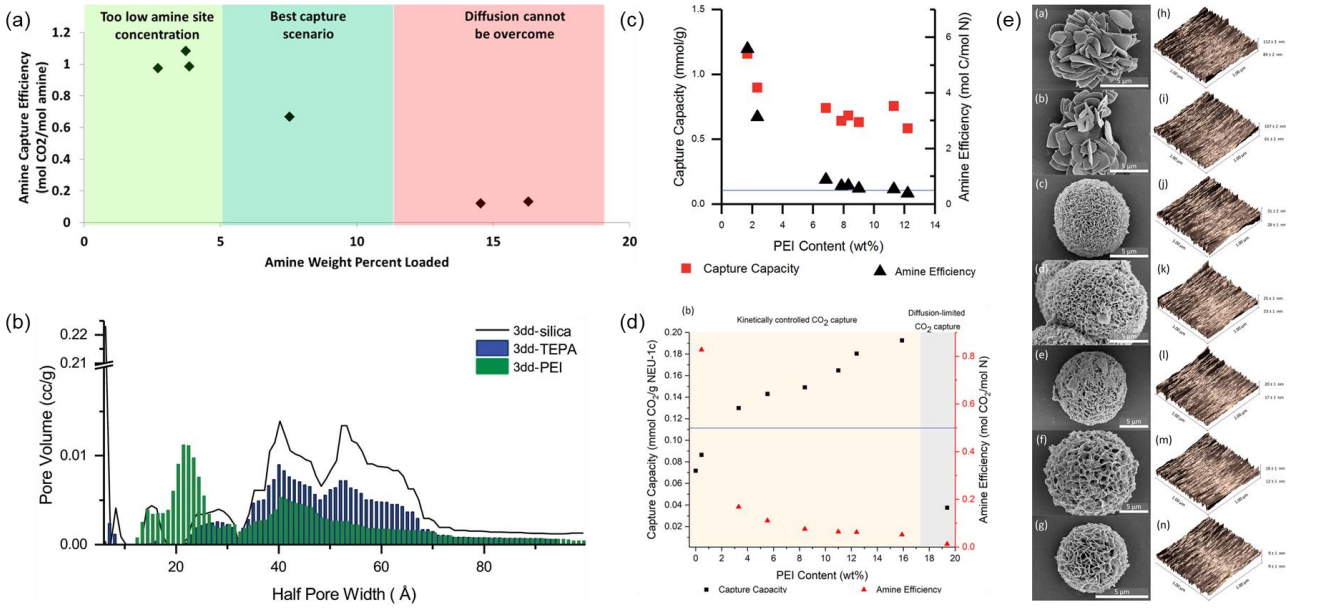

Fig. 7 Strategy decoupling the amine loading from increasing diffusion resistance. (a) Amine efficiency of PEI-impregnated MCM-36 versus amine weight percentage loaded (Reproduced from ref. 268 with permission from American Chemical Society, copyright 2015). (b) Density functional theory pore size distribution analysis of 3dd-silica, 3dd-TEPA, and 3dd-PEI.[269] (c) and (d) Capture capacity and amine efficiency of 3dd-PEI and NEU-1c adsorbent; the blue line marked the maximum theoretical amine efficiency of 0.5. (e) Scanning electron microscopy images and atomic-force micrographs of $Zn(BPDI)(Py)_2$ and NEU-1 (Reproduced from ref. 270 with permission from American Chemical Society, copyright 2020).

2.1.2. Amine-grafted adsorbents. The effective amine efficiency (CO_2/N atomic mole ratio) of physically impregnated polyamines is much lower than the theoretical maximum of 0.5, which is mainly due to the disordered stacking of amines that blocks the active site and slows down the CO_2 diffusion. In addition, the weak interaction between amines and supports leads to the stability problem of polyamine-based adsorbents during thermal regeneration under humid and oxygen-containing conditions.[101] Alternatively, researchers

are developing amine-grafted adsorbents via covalent chemical bonds, either by silylation reactions between aminosilanes and hydroxyl groups or, in rare cases, by cross-coupling reactions.[95]

So far, various aminosilanes including aminomethyl- (C1),[271] 2-aminoethyl- (C2),[271] 3-aminopropyl- (APS),[116,121,122,271–286] 4-aminobutyl- (C4),[271] 5-aminoamyl- (C5),[271] N-methylaminopropyl- (MAPS),[272] N-butylaminopropyl- (NBAPS),[287,288] 3-amino-3-methylbutyl- (AMBS),[123] *tert*-butylaminopropyl- (TBAPS),[123] N-cyclohexylaminopropyl- (CHAPS),[123] N-phenylaminopropyl- (PHAPS),[287] N,N-dimethylaminopropyl- (DMAPS),[272] 3-(2-aminoethylamino)propyl- (DI),[274,286,289–291] 3-(2-aminopropylamino)propylsilane (L-propyl),[274] N,N'-bis(3-trimethoxysilpropyl)urea (UREA),[273] 3-[2-(2-aminoethylamino)ethylamino]propyl- (TRI),[110,116,124,125,286,292–294] 3-(2-aminoethylamino)methylsilane (CH_2DETA),[295] bis(2-aminoethyl)amine (B-ethyl),[274,295] bis(2-aminopropyl)amine (B-propyl),[274] and TREN,[117,258,274] have been tested for their ability to capture CO_2 from ultradilute concentrations of gas mixtures. In general, primary amines have higher amine efficiencies than secondary and tertiary amines due to the entropy effect,[272,287] which has led to the widespread use of APS for capturing CO_2 under ultradilute conditions. The propyl linker of APS was found to be sufficiently flexible to trap CO_2 molecules through two adjacent amines, whereas longer linkers provided no additional benefit.[271] However, the low N content of APS-grafted adsorbents (usually less than 5 mmol g^{-1}) limits their overall CO_2 adsorption capacity.

Aminosilanes containing multiple amine groups on the linker have been extensively studied to achieve high amine loadings. For example, the monolayer grafted TRI on SBA-15 and pore-expanded MCM-41 (PE-MCM-41) reached an amine loading of 6.0[118] and 6.2 mmol g^{-1}.[296] Supported triamine with moderate-to-high loadings has both acceptable CO_2 capacities and fast kinetics under DAC conditions, and enhanced performance in the present of moisture.[286] In comparison, the performance of diamine is insufficient,

probably due to the unavailable secondary amine moieties that are either sterically hindered by chemisorbed CO_2 species or hydrogen-bonded with surface silanols (**Fig. 8**a and b). Recently, an array of branched and linear aminosilanes linked by either ethyl or propyl spacers was explored (**Fig. 8**c).[274] Branched silane-grafted adsorbents (B-ethyl, B-propyl) containing two primary amines showed amine efficiencies similar to those of APS, which were higher than those of linear silane (DI and L-propyl). However, linear silane can be densely grafted with silane loadings higher than 1.7 mmol Si/g under anhydrous conditions, whereas the loading of branched silane cannot exceed 1.3 mmol Si/g (**Fig. 8**d and e). All grafted adsorbents exhibited good thermal stability, and the adjacent amines connected by a propyl spacer achieved higher oxidative stability.

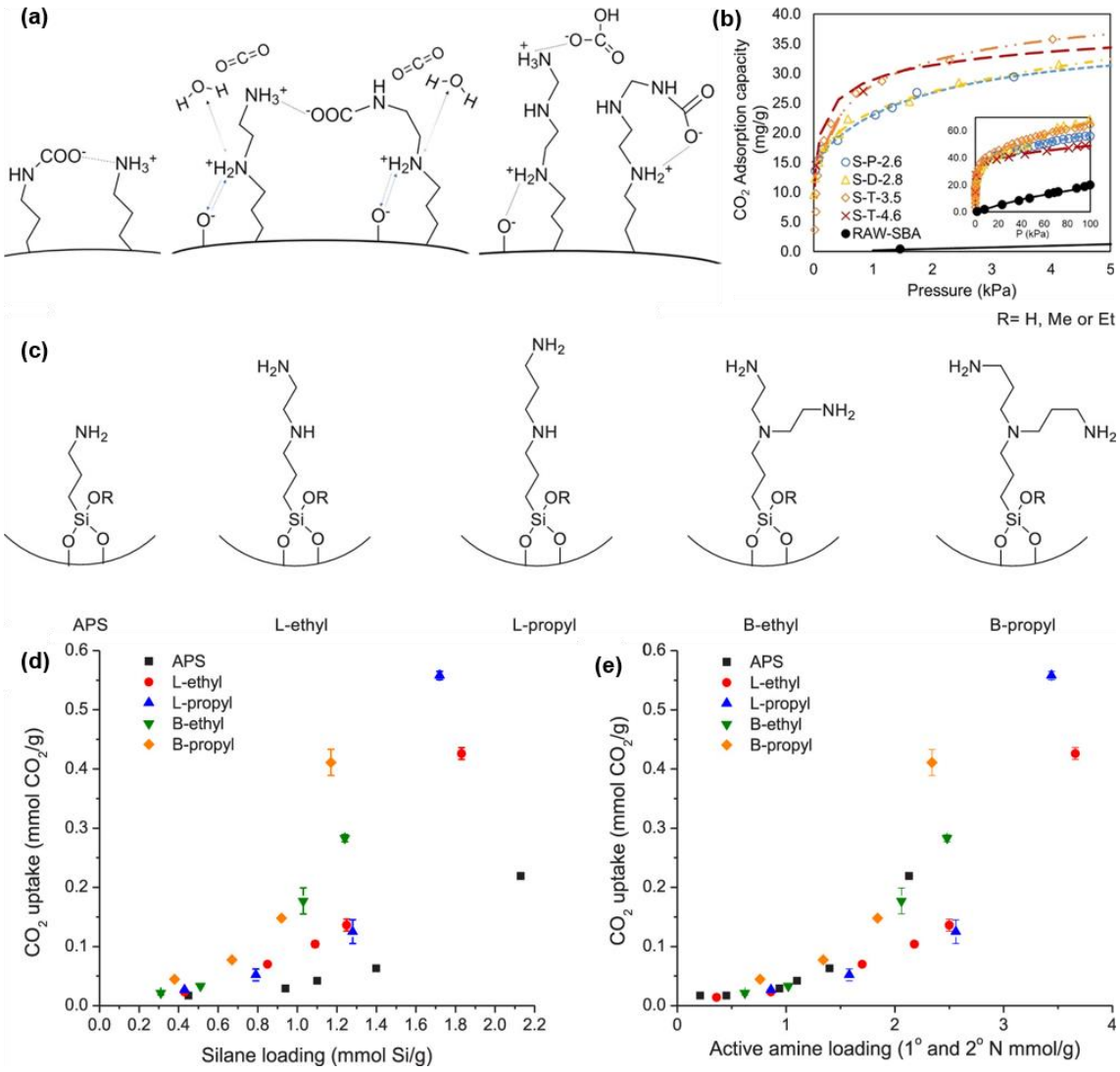

Fig. 8 (a) Possibly formed species from the adsorbed CO_2 in the presence of water of supported APS, DI, and TRI. (b) CO_2 adsorption isotherms of RAW–SBA (raw SBA-15), S-P-2.6 (supported APS at an amine loading of 2.6 mmol g^{-1}), S-D-2.8 (supported DI at an amine loading of 2.78 mmol g^{-1}), S-T-3.5 (supported TRI at an amine loading of 3.52 mmol g^{-1}), and S-T-4.6 (supported TRI at an amine loading of 4.66 mmol g^{-1}) at 25 °C (Reproduced from ref. 286 with permission from American Chemical Society, copyright 2021). (c) Structures of various aminosilanes containing multiple amine groups, and CO_2 uptake as a function of (d) silane loadings and (e) active amine loading at 25 °C and 400 ppm of CO_2 (Reproduced from ref. [274] with permission from American Chemical Society, copyright 2020).

Multilayer amine grafting in the presence of water is another approach to increase amine loading by breaking the availability limitation of the surface hydroxyl groups of supports. This process involves the hydration of porous supports by adding water to the toluene solution, followed by the surface polymerization of aminosilanes under heating. Belmabkhout *et al.*[292] previously reported an impressive CO_2 capacity of 0.98 mmol g^{-1} of wet-grafted TRI on PE-MCM-41 with an enhanced amine loading of 7.9 mmol g^{-1} at 400 ppm and 25 °C. The material was hydrothermally stable during steam purge regeneration tests.[273,292] Since then, the concept of wet grafting has been widely applied to other mesoporous supports such as SBA-15,[119,124,280,294,297] Al_2O_3,[279] KIT-6,[298] and hierarchical bimodal mesoporous silica (HBS).[294] An unexpected finding is that the wet grafted silica gel, which is commercially available and once believed to be poor in adsorbing CO_2 from air,[289] can equally achieve promising capacities of 0.773 and 1.098 mmol g^{-1} under dry and wet conditions, respectively (**Fig. 9**).[125] Such high amine loadings cannot be explained by the expected silylation reaction happening between the hydrolyzed alkoxy of amine molecules and the surface hydroxyl of porous supports to produce monolayer grafting. In fact, surface water enhances the hydrolysis of unreacted alkoxy groups and provides additional hydroxyl groups for the multilayer coating of aminosilanes through Si-O-Si bridges. The presence of water also significantly shortens the grafting time (*e.g.*, less than 30 min), probably because of the formation of highly reactive silanol groups from aminosilane alkoxy groups.[297] While wet grafting undoubtedly increases the CO_2 capacity, the interparticle polymerization of amines may lead to the agglomeration of supports.

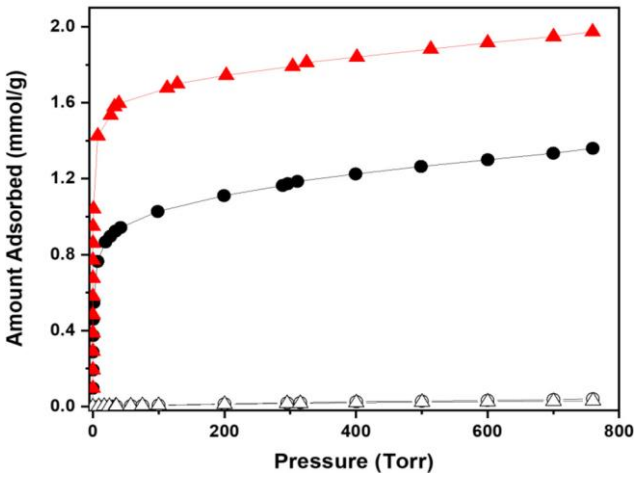

Fig. 9 CO_2 (filled symbols) and N_2 (open symbols) adsorption isotherms for dry-grafted silica gel (●) and wet-grafted silica gel (▲) at 25 °C (Reproduced from ref. 125 with permission from American Chemical Society, copyright 2020).

Ammonium carbamates are preferentially formed as chemisorbed CO_2 species on supported primary and secondary amines; they require two amines to bind one CO_2 molecule. Ammonium bicarbonates with CO_2 binding on a single nitrogen atom can avoid such cross-linking behavior that may otherwise increase the CO_2 diffusional limitation. Forming bicarbonates also reduces the energy for regeneration, as they are less thermally stable than carbamate species. Spectroscopic studies have identified the existence of bicarbonate in all types of amines.[141] Compared with primary and secondary amines, tertiary amines that exclusively form bicarbonates may achieve higher amine efficiencies. Unfortunately, the use of supported tertiary amine is not practical due to its poor kinetics, even in the presence of moisture.[263] Recently, three sterically-hindered primary (AMBS) and secondary (CHAPS and TBAPS) were tested for DAC (**Fig. 10**).[123] They are prone to form weakly bounded bicarbonates under wet conditions while maintaining a fast CO_2 adsorption rate. Furthermore, AMBS with a hindered primary amine remained stable after an accelerated oxidation experiment. However, the overall CO_2 capacities of supported hindered amines were much lower than those in aqueous solution,[299] and this discrepancy may be better understood by further exploring the effect of solvation and hydrogen bonding on chemisorbed CO_2.

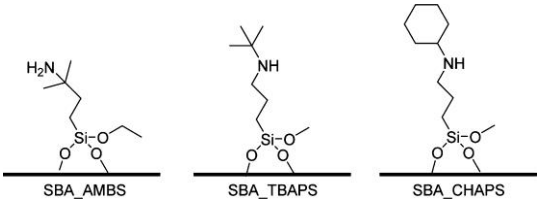

Fig. 10 Structures of hindered aminosilanes, AMBS, TBAPS, and CHAPS (Reproduced from ref. 123 with permission from American Chemical Society, copyright 2018).

To date, toluene is the most commonly used solvent for aminosilane grafting. Recent work has shown that solvent properties greatly affect the surface configuration of organic-inorganic hybrids. A typical example is alkylamine-tethered MIL-101(Cr), which does not exhibit impressively high CO_2 capacities despite its structural advantages of an ultraporous framework and extraordinary stability under harsh conditions. By simply changing the grafting solvent from dichloromethane to cyclohexane, the TREN-modified MIL-101(Cr) achieved more than twice the CO_2 uptake and remarkable CO_2/N_2 selectivity.[117] The improvement was ascribed to the use of a less polar solvent that weakens its attraction towards amine molecules, allowing more efficient loading (**Fig. 11**a). A later study explored three nonpolar, two dipolar-aprotic, and three polar-protic solvents for amine grafting, confirming the high correlation between the solvent polarity and hybrid properties.[284] More specifically, the CO_2 capacities and efficiency of grafted amines depend on the interactions between the support matrix and solvents (**Fig. 11**b). Cyclohexane is superior to other nonpolar solvents (hexane and toluene), being the most promising solvent for grafting, with a high N loading of 5.21% and a stable surface configuration of C/N = 4.34. These findings suggest the possibility of solvent-driven surface design for amine-grafted adsorbents.

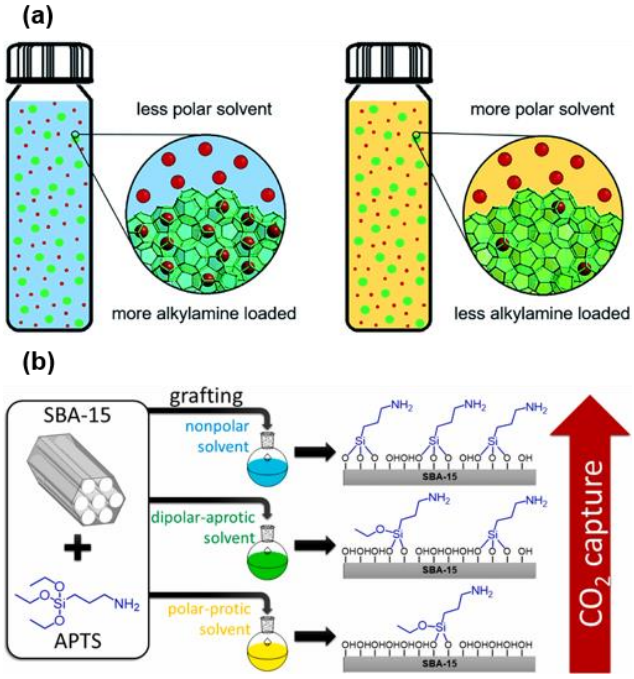

Fig. 11 (a) Interface between an alkylamine solution and MIL-101(Cr).[117] (b) Possible linkage configurations for amine grafting using non-polar, dipolar-aprotic, and polar-protic solvents, and their CO_2 capacity abilities (Reproduced from ref. 284 with permission from Elsevier, copyright 2021).

Adopting the conventional grafting process in organic solvents in industrial-scale material synthesis may lead to significant solvent wastage and oligomerization side reactions. Supercritical CO_2 ($scCO_2$) can be a sustainable alternative, allowing fast transfer and surface functionalization of amine precursors.[300–302] The $scCO_2$ approach typically occurs at 40–60 °C and at 12.5–20.0 MPa with reaction times of 2–3 h, in which the CO_2 fluid is recovered after the reaction by reducing the pressure. Because the $scCO_2$ solvent could react with primary and secondary amines to form carbamates, the addition of alcohols facilitates the solubilization of the aminoalkylcarbamate salts. In a recent work, a DI-grafted SBA-15 was prepared by $scCO_2$ in 10% ethanol or ethanol at 50 °C and 12.5 MPa, and exhibited amine efficiencies up to 0.4 at 25 °C.[291] The CO_2 diffusion of the functionalized DI was not hindered until the amine loading reached 3 mmol N g^{-1}. In contrast, the amine efficiency of the reference sample from the traditional process using toluene was less than 0.1, which was attributed to the mesopore filling of SBA-15 with vertical polymeric depositions.

2.2. Effects of supports

2.2.1. Aminopolymer-impregnated adsorbents. To overcome the weakness of aminopolymer-impregnated materials, there are other paths of improvement. Various types of supports create great opportunities to develop desirable adsorbents. Several requirements are summarized to achieve aminopolymer-impregnated adsorbents with better performance: a) the support should have a larger pore volume to retain higher amine loading; b) the amine should be well dispersed in the support; c) a stronger bond between the support and the amine should be formed to strengthen the thermal stability; d) the support should not degrade in a moist atmosphere, so as to be applied in humid air and steam stripping regeneration; and e) the production cost of the support can be affordable to facilitate scale-up. Owing to the synergistic effect between the amine and support, the texture characteristics and surface microstructure of the support were strongly related to the amine morphology. When the interaction between the support and amine is altered, the capture performance can vary. As such, many studies have developed customized supports to illustrate this synergistic effect. A variety of porous materials have been used as supports for amine impregnation, including siliceous materials, carbonaceous materials, alumina, aluminosilicates, organic polymers, MOFs, and LDHs. The DAC adsorption properties of amine-impregnated materials mentioned in this section are summarized in **Table 2**.

Table 2 Adsorption properties of amine-impregnated supports for DAC.

Supports	Amine	Loading	Capacity (mmol g^{-1})	Adsorption condition	Desorption condition	Stability	Ref.
SBA-15	PEI	50 wt.%	1.55	30 °C, 400 ppm, dry	110 °C, He	N/A	265
SBA-15	PEI	75 wt.%	1.12	25 °C, 400 ppm, dry	110 °C, N_2 purge	5.5% loss after 10 cycles	112
SBA-15	PPI	45 wt.%	1.35	35 °C, 400 ppm, dry	70 °C, N_2 purge	Stable after 4 cycles	126
SBA-15	PPI	50 wt.%	1.0	35 °C, 400 ppm, dry	110 °C, He purge	Nearly no loss after 20 cycles	129
SBA-15	PPI	14 mmol N g_{SiO2}^{-1}	1.25	25 °C, 400 ppm, dry	110 °C, N_2 purge	Nearly no loss after 50 cycles	128
SBA-15	PGA	15–45 wt.%	0.6	25 °C, 400 ppm, dry	110 °C, N_2 purge	10.9% loss after 20 cycles	115
SBA-15	PPG	50 wt.%	0.6	30 °C, 400 ppm, dry	120 °C, He purge	54.5% loss after 5 cycles	251
SBA-15	Ph-3-ED	60 wt.%	1.4	25 °C, 400 ppm, 30% RH	110 °C, He purge	Stable after 25 cycles	113
SBA-15	PEI	30 wt.%	0.19	25 °C, 400 ppm, dry	110 °C, Ar purge	41.2% loss after 4 cycles	303
Al-SBA-15	PEI	34 wt.%	0.29	25 °C, 400 ppm, dry	110 °C, Ar purge	N/A	303
Ti-SBA-15	PEI	32 wt.%	0.64	25 °C, 400 ppm, dry	110 °C, Ar purge	6% loss after 4 cycles	303
Ce-SBA-15	PEI	33 wt.%	0.68	25 °C, 400 ppm, dry	110 °C, Ar purge	N/A	303
Zr-SBA-15	PEI	35 wt.%	0.85	25 °C, 400 ppm, dry	110 °C, Ar purge	Stable after 4 cycles	303
Zr-SBA-15	PEI	50 wt.%	1.05	30 °C, 400 ppm, dry	110 °C, N_2 purge	N/A	304
EtSNTs	PEI	33 wt.%	1.0	25 °C, 400 ppm, dry	100 °C, N_2 purge	Stable after 8 cycles	305
SBA-15	TEPA	50 wt.%	2.3	25 °C, 400 ppm, dry	110 °C, N_2 purge	2.8% loss after 10 cycles	112
MCF pellets	PEI	68 wt.%	1.94	46 °C, 420 ppm, dry	81 °C, N_2 purge	N/A	135
MCF pellets	PEI	68 wt.%	2.52	46 °C, 420 ppm, 2 vol.% H_2O	81 °C, N_2 purge	N/A	135
Hierarchical silica	PEI	2.62 g g_{SiO2}^{-1}	2.6	30 °C, 400 ppm, dry	110 °C, He purge	Stable after 5 cycles	108
Hierarchical silica	PEI	2.62 g g_{SiO2}^{-1}	3.36	30 °C, 400 ppm, 19% RH	110 °C, He purge	18.15% loss after 5 cycles	108
AHTSA	PEI	10 wt.%	1.64	25 °C, 400 ppm	130 °C, N_2 purge	Stable after 15 cycles	282
Fumed silica	PO-PEHA	50 wt.%	2.25	25 °C, 1000 ppm, 50% RH	50 °C, 400 ppm CO_2 purge	Stable after 5 cycles	127

Fumed silica	PO-TEPA	50 wt.%	2.0	25 °C, 1000 ppm, 50% RH	50 °C, 400 ppm CO_2 purge	Stable after 45 cycles	127
Fumed silica	HBPG	50 wt.%	0.80	25 °C, 420 ppm, 35% RH	100 °C, N_2 purge	N/A	306
Mesoporous carbon	PEI	60 wt.%	2.25	25 °C, 400 ppm, dry	110 °C, N_2 purge	Stable after 10 cycles	307
Carbon nanotube	PEI	10 wt.%	1.07	25 °C, 3500 ppm, dry	80 °C, vacuum	N/A	308
γ-Alumina	PEI	48 wt.%	1.74	25 °C, 400 ppm, dry	110 °C, steam stripping	Stable after 3 cycles	309
γ-Alumina	PEI	7.95 g N g_{Al2O3}^{-1}	1.96	30 °C, 400 ppm, dry	110 °C, steam stripping	N/A	310
Alumina monolith	PEI	0.44 g g_{Al2O3}^{-1}	0.9	30 °C, 400 ppm, dry	110 °C, steam stripping	14% loss after 5 cycles	311
Halloysite nanotube	PEI	40 wt.%	1.25	25 °C, 400 ppm, dry	80 °C, vacuum	3.28% loss after 50 cycles	312
Zeolite Y	TEPA	10 wt.%	1.12	25 °C, 5000 ppm	100 °C, N_2 purge	Stable after 5 cycles	256
NPEI-SIPs	PEI	49 wt.%	1.7	50 °C, 400 ppm, dry	120 °C, N_2 purge	7.8% loss after 20 cycles	106
Resin HP2MGL	PEI	50 wt.%	2.13	25 °C, 5000 ppm, dry	100 °C, N_2 purge	Stable after 5 cycles	313
Resin HP2MGL	PEI	50 wt.%	3.04	25 °C, 5000 ppm, 40% RH	100 °C, N_2 purge	Stable after 5 cycles	313
Resin HP20	PEI	50 wt.%	2.26	25 °C, 400 ppm, dry	100 °C, N_2 purge	Almost no loss after 5 cycles	314
Resin MR10	PEI	50 wt.%	2.64	25 °C, 1000 ppm, dry	70 °C, N_2 purge	10.6% loss after 3 cycles	111
Resin MR10	PEI	50 wt.%	2.92	25 °C, 1000 ppm, 50% RH	70 °C, N_2 purge	N/A	111
Resin KBS	PEI	20 wt.%	1.59	20 °C, 4000 ppm, 1.56 vol.% H_2O	50 °C, N_2 purge	N/A	315
MIL-101(Cr)	PEI	60 wt.%	1.04	25 °C, 400 ppm, dry	110 °C, He purge	4.6% loss after 3 cycles	258
MIL-101(Cr)	PEI	50 wt.%	1.17	–20 °C, 400 ppm, dry	60 °C, He purge	Stable after 15 cycles	316
MIL-101(Cr)	TREN	45 wt.%	2.76	25 °C, 400 ppm, dry	110 °C, He purge	15.1% loss after 3 cycles	258
MIL-101(Cr)	TEPA	30 wt.%	0.72	–20 °C, 400 ppm, dry	25 °C, He purge	30% loss after 15 cycles	316
PEI-$Mg_{0.55}$Al-O	PEI	67 wt.%	1.66	25 °C, 400 ppm, dry	120 °C, N_2 purge	N/A	107

PEI-$Mg_{0.55}Al$-O	PEI	67 wt.%	2.27	25 °C, 400 ppm, humid	120 °C, N_2 purge	2.7% loss after 20 cycles	107
TEPA-$Mg_{0.55}Al$-O	TEPA	67 wt.%	3.0	25 °C, 400 ppm, dry	120 °C, N_2 purge	Maintain ~90% after 80 cycles	317

Among them, siliceous materials have been the most studied owing to their tunable pore structure, high availability, and desirable amine-containing capability. Conventional silicas, such as the SBA, MCM, and KIT series, have been found to have outstanding textural structures and high solvent thermal stabilities.[318–323] SBA-15 has highly ordered hexagonal pores with narrow pore size distribution within 4–30 nm, thicker pore wall and larger pore volumes. These characterizations provide an excellent support for amine functionalization. Recent studies utilized SBA-15 as a support to investigate amine effects, adsorption heats, oxidative stability, and adsorption temperature, demonstrating its applicability and compatibility under various conditions.[113,115,126,128,129,251,323,324]

Modifying the synthetic process enhances the adsorption properties. For instance, Jones *et al.*[303] incorporated a series of metal atoms (Al, Zr, Ti, and Ce) into SBA-15. By creating more acid/base sites on the silica surface, the metal atoms result in improved uptake, kinetics, and thermal stability. Such an enhancement is also closely related to the textural and morphological nature of the SBA-15.[304] Kleitz *et al.*[325] impregnated amines and phosphines on the surface of metalated SBA-15 to generate air-stable solid-supported Lewis acid-base pairs. The synergistic effect between Zr atoms and the amine/phosphine Lewis bases was reported to enhance the CO_2 adsorption. Liu *et al.*[305] added 1,2-bis(trimethoxysilyl)ethane and KCl to the SBA-15 synthesis solvent and synthesized ethane-bridged SBA-15 (EtSBA-15) and ethane-bridged organosilica nanotubes (EtSNTs). Compared with SBA-15, the ethane-bridged samples had larger specific surface areas and pore diameters. In particular, for the EtSNTs with both tubular channels and intervoid spaces, PEI is highly dispersed in the pores, and thus, a higher capacity and fast equilibrium time under ultradilute conditions were achieved.

Silica with a three-dimensional pore channel is considered to exhibit enhanced kinetics.[326,327] MCF is an interconnected cellular nanostructured silica with larger pore volumes than SBA-15.[328–330] It comprises

uniform spherical cells with a narrow size distribution, which could have potential as a good CO_2 adsorbent. A recent study verified its DAC capability in the temperature range of 33 to 81 °C.[135] In 420 ppm CO_2, the highest capacity of PEI-impregnated MCF was 1.94 mmol g^{-1} and 2.52 mmol g^{-1} under dry and humid conditions, respectively. The uptake at 81 °C is negligible, indicating a relatively low regeneration temperature. Kwon *et al.*[108] recently prepared a hierarchical silica support with bimodal meso/macroporosities, which has a pore size distribution of 70–700 nm. The maximum sorption capacity of PEI-impregnated silica was 2.6 mmol g^{-1} at 400 ppm CO_2, and increased to 3.4 mmol g^{-1} in the presence of water. This is partially due to the large pore volume from the macropores.

Despite their appreciable properties, the above siliceous supports face the problems of relatively complex synthesis and higher affordability, which limits their large-scale application. To this end, cost-effective supports have raised the interest of the community. Aerogels are nanoporous materials with three-dimensional networks consisting of nanoparticles and nanopores, leading to unique properties such as low density, high specific surface area, pore volume, and porosity. Aerogels have been produced on an industrial scale with lower capital cost.[331] Many studies have reported the application of amino aerogels for carbon capture, including post-combustion conditions[332,333] and ultradilute concentrations.[334–336] Kong *et al.*[281–283,285,337,338] carried out a series of studies on amine-modified aerogels. A recent study proposed a simple, cost-effective, and environmental-friendly route for the synthesis of an amine hybrid titania/silsesquioxane composite aerogel (AHTSA).[282] The effects of amine loading and CO_2 concentration on the pore structure and CO_2 adsorption performance of the AHTSA were investigated. It reported that AHTSA has a capacity of 1.64 mmol g^{-1} at dry 400 ppm CO_2, short adsorption halftime, and high amine efficiency, revealing potential applications in DAC (**Fig. 12**a–c). The fumed silica has large surface areas and pore sizes between 5–50 nm. It is readily available and inexpensive. Recent studies utilized fumed silica to support epoxide-

modified polyamines and amine-containing hyperbranched polyglycerols (HBPGs), demonstrating desirable capacities to capture CO_2 from air (**Fig. 12**d–e).[127,306]

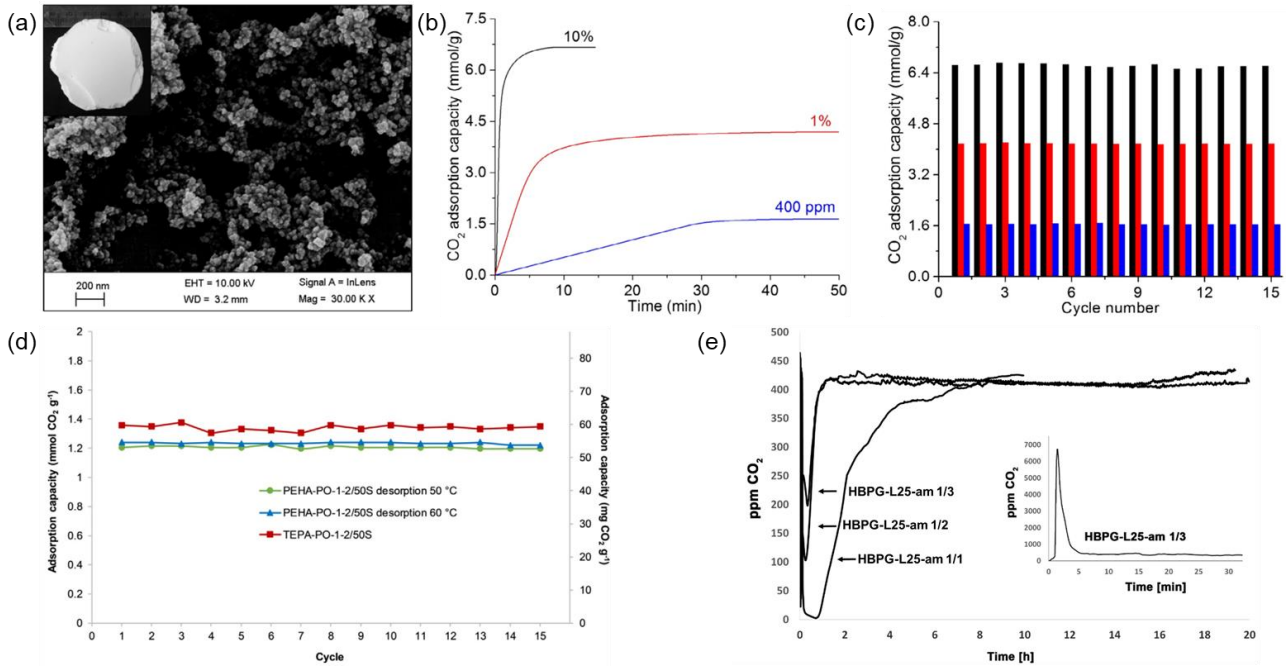

Fig. 12 (a) Scanning electron microscopy and digital photo of AHTSA. (b) CO_2 adsorption uptake of AHTSA versus adsorption time under different CO_2 concentrations. (c) Cyclic adsorption capacity of AHTSA in dry air (blue), 1% (red), and 10% (black) CO_2 stream (Reproduced from ref. 282 with permission from Elsevier, copyright 2016). (d) Cyclic adsorption capacity of PEHA-PO-fumed silica and TEPA-PO-fumed silica from 400 ppm CO_2 in air (Reproduced from ref. 127 with permission from John Wiley and Sons, copyright 2019). (e) Adsorption breakthrough curves of HBPG/fumed silica adsorbents (25 °C, 35% relative humidity) and typical desorption curve of HBPG-L25-am 1/3 sample at 100 °C; 1/3, 1/2, 1/1 means that the adsorbent contains 1 weight part of polymer HBPG-L25-am and 1, 2, and 3 weight parts of fumed silica, respectively (Reproduced from ref. 306 with permission from Elsevier, copyright 2018).

Carbonaceous materials are considered to have potential for carbon capture. In addition to their desirable properties, sub-categories such as activated carbon and biochar can be synthesized from biomass, which brings benefits such as cost reduction and environmental protection.[339,340] There have been systematic reviews about the carbonaceous materials for CO_2 capture. However, their applications in terms of DAC are limited. One example is Wang *et al*.[307] utilized a type of mesoporous carbon for PEI impregnation. The kinetics diffusion of this mesoporous carbon with high pore volume was enhanced by employing a diffusion additive and the capacities are 3.34 mmol g^{-1} for 5000 ppm and 2.25 mmol g^{-1} for 400 ppm.

In another study, carbon nanotubes were utilized to support PEI, and reaches a CO_2 uptake of 1.068 mmol g^{-1} under the CO_2 pressure of 0.0035 bar.[308] Other studies focusing on carbon-based materials for DAC include the use of biochar[341] and activated carbons,[342] though they are not used as amine supports. Considering their excellent channel structure, high tunability, and wide range of sources, there is a large possibility for them to be applied in DAC.

Alumina is a popular support owing to its unique stability in steam flow. Considering the industrial utilization of CO_2 adsorbents, practical regeneration methods should be developed, including temperature-vacuum swing, CO_2 flow stripping, and steam flow stripping. The latter is more favorable for avoiding excess energy consumption and amine degradation under the premise that the support is resistant to steam stripping. Alumina-supported amines are particularly suitable for ultradilute CO_2 capture and have high stability in vapor atmosphere.[309] A series of subsequent studies have analyzed the viability of their practical applications.[252,310,311,343,344] These amine-modified alumina materials exhibited capacities of 0.8–1.3 mmol g^{-1} for DAC, and the capital cost calculation proved that the use of alumina is economic.[311]

Aluminosilicate materials, such as zeolites and clays, have attracted attention for CO_2 capture because of their potential for surface modification and outstanding hydrothermal stability. They are mostly microporous materials comprising stable and highly porous networks. They can be derived from waste materials or natural resources; therefore, the production cost is greatly reduced.[345] Recently, amine-loaded zeolites and clays have been reported to be capable of capturing CO_2 from the ambient air. Thakkar *et al.*[256] developed zeolites ZSM-5, zeolite Y, and SAPO-34 from kaolin clay for carbon capture from air. Zeolites exhibited a bimodal pore network consisting of micropores and mesopores. The zeolite Y with 10 wt.% TEPA loading exhibited a capacity of 1.12 mmol g^{-1} in 5000 ppm CO_2. The higher capacity over other zeolites was due to the larger mesopore volume of zeolite Y. Cai *et al.*[312] synthesized halloysite nanotubes

impregnated with PEI. The optimal capacity reaches 1.25 mmol g^{-1} in air, and the adsorbent exhibited a mild regeneration at 80 ℃ as well as high cyclic stability.

Organic polymers, including organic hybrid nanoparticle materials and resins, have been explored as support materials for amine-based CO_2 adsorbents. They afford a high degree of chemical tunability, as well as potential capacity, owing to their large surface area and pore volume. Rim *et al.*[106] reported novel solvent-impregnated polymers (SIPs) loaded with liquid-like nanoparticle organic hybrid materials (NOHMs) for DAC (**Fig. 13**a). The CO_2 capture kinetics of NOHM-SIPs show a remarkable 50-fold increase compared to that of neat NOHMs functionalized with PEI (NOHM-I-PEI) because of the large increase in the NOHMs-CO_2 interfacial surface area provided by the SIP design (**Fig. 13**b and c). The effects of amine loading and temperature on the adsorption properties were investigated (**Fig. 13**d–g). The high capacity of 1.7 mmol g^{-1} and the high thermal stability suggest that it can effectively capture CO_2 from air.

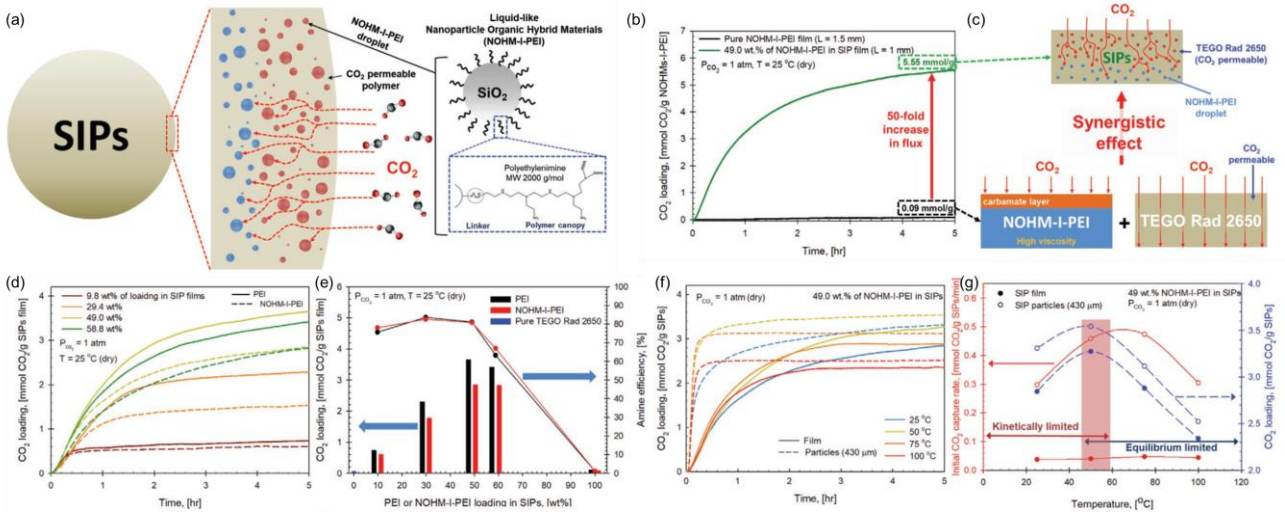

Fig. 13 (a) Interior structure of the SIPs. (b) CO_2 uptake of NOHMs loaded SIPs and neat PEI-functionalized NOHMs. (c) Schematic illustration of the synergistic effect between PEI-functionalized NOHMs and the CO_2 permeable polymers. (d-e) Effects of PEI-functionalized NOHMs and PEI loading on the adsorption kinetics, capacity, and amine efficiency. (f-g) Effects of temperature on adsorption kinetics, initial capture rate, and capacity (Reproduced from ref. 106 with permission from John Wiley and Sons, copyright 2021).

The first study on PEI-impregnated resin to capture CO_2 from air was reported by Chen *et al.*[314] In this study, commercialized resin HP20 was loaded with PEI in a range of 30–55 wt.%. The highest capacity was 2.26 mmol g^{-1}, but the kinetics seemed to be relatively slow. Wang *et al.*[111] prepared PEI-impregnated resin PEI-MR10 for indoor CO_2 capture. It was found that PEI loading narrowed the pore size distribution but increased the average pore size of PEI-MR10. Under variable indoor conditions, the adsorbed amounts of CO_2 maintained high values from 2.05 to 3.09 mmol g^{-1}. It also showed faster adsorption rate and mild regeneration at approximately 70 °C. Si *et al.*[315] fabricated a PEI-impregnated porous polymer resin and found increased CO_2 adsorption capacity with the assistance of H_2O in humid 4000 ppm CO_2 gas stream. Owing to their particularly high mesopore volume, amine-loaded resins typically exhibit a higher capacity. The typical drawbacks are kinetic limitations and stability problems, which should be primarily solved to facilitate their applications.

MOFs are a class of crystalline porous materials constructed from inorganic ions or clusters joined by multitopic organic ligands. They are attractive adsorbents owing to their high degree of control over the pore size, shape, and surface chemistry through synthesis modification. Recent years have witnessed the rapid development of MOFs, and thus far, amine-modified MOFs have been investigated for DAC.[346,347] In a study by Darunte *et al.*,[258] MIL-101(Cr) was impregnated with PEI or TREN and used to capture CO_2 from the air. MIL-101(Cr)-TREN showed high CO_2 capacities for high loading of TREN, but a significant loss of amines was observed in multicycle TSA experiments. In contrast, MIL-101(Cr)-PEI-800 showed a capacity of 1–1.3 mmol g^{-1} and stable cyclic performance. Rim *et al.*[316] impregnated TEPA or PEI on MIL-101(Cr) and measured the adsorption behavior in both the presence and absence of humidity in the temperature range of –25 to 25 °C (**Fig. 14**a). The effects of amine loading and adsorption temperature on the adsorption/desorption behaviors were investigated (**Fig. 14**b–e). The adsorbents show promising

working capacities of 0.72 mmol g^{-1} at an ultralow regeneration temperature (*e.g.*, sorption at –20 °C and desorption at 25 °C), which can be further enhanced under humid conditions (**Fig. 14**f).

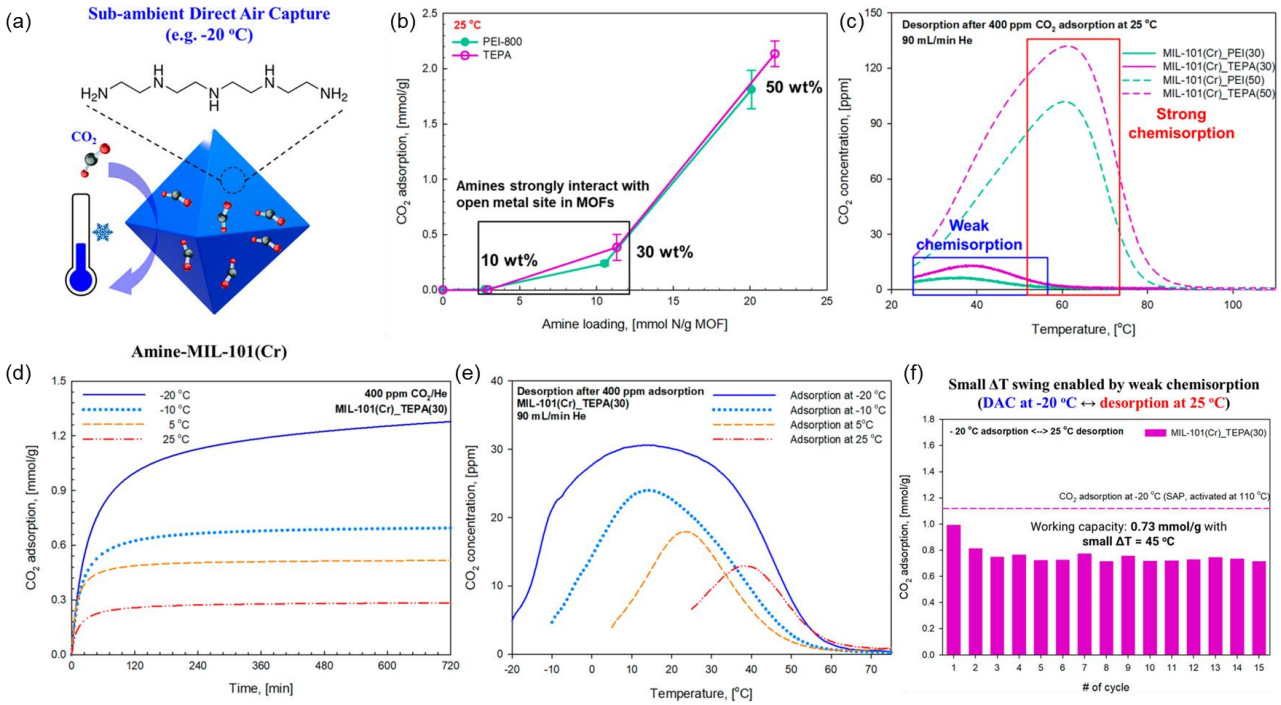

Fig. 14 (a) Scheme of the TEPA-impregnated MIL-101(Cr). (b) Effect of amine loading on the adsorption capacity at 25 °C. (c) Effect of temperature on the adsorption behavior of amine-impregnated MIL-101(Cr). (d) Adsorption kinetics under different temperatures. (e) Desorption behavior after adsorption at different temperatures. (f) Working capacity of TEPA-MIL-101(Cr) over small temperature swing cycles (Reproduced from ref. 316 with permission from American Chemical Society, copyright 2022).

LDHs are two-dimensional layered materials comprising brucite-like layers separated by charge-compensating anions and interlayered water with a general formula of $[M_{1-x}^{2+}M_x^{3+}(OH)_2]^{x+}(A^{n-})_{x/n}{\cdot}yH_2O$ (M^{2+} and M^{3+} are divalent and trivalent cations, respectively; x is the ratio of divalent and trivalent metal cations; A^{n-} is the interlayer anion). By the aqueous miscible organic solvent treatment (AMOST), the stacked bulk LDHs can be exfoliated into small plates with large specific surface areas and tunable metal cations.[348] Further, they forms mixed metal oxides (MMOs) with abundant surface defects after undergoing thermal treatment at mild condition (400–600 °C).[349] These unique characterizations make them rather attractive for synthesizing customized adsorbents for CO_2 capture. Recently, attempts to impregnate amines into MMOs have successfully demonstrated the viability of adopting LDHs as DAC adsorbents. Zhu *et*

al.[107] synthesized an aminopolymer-impregnated adsorbent by loading 67 wt.% branched PEI onto $Mg_{0.55}Al$–O MMOs, which exhibited large CO_2 uptakes (2.27 mmol g^{-1}), fast kinetics (1.1 mmol g^{-1} h^{-1}), and high stability over 20 cycles at 25 °C under 0.4 mbar CO_2 (**Fig. 15**a and b). The ultrahigh thermal stability of the amine-impregnated oxide was achieved that was ascribed to the strong electrostatic interactions between the MMO layers and amines (**Fig. 15**c–e).

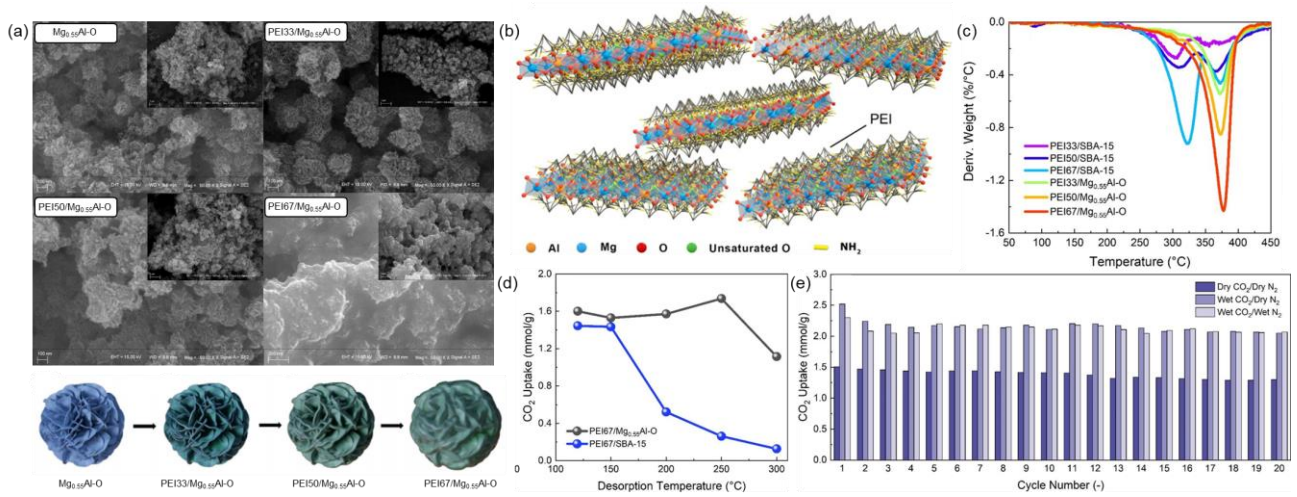

Fig. 15 (a) Scanning electron microscopy of MMOs impregnated by 0, 33, 50, 67 wt.% of PEI. (b) Schematic diagram of the PEI/MMO structure. (c) Thermal-induced weight change rate of the PEI/MMO and PEI/SBA-15 that characterizes the thermal stability of adsorbents. (d) CO_2 uptake of PEI/MMO and PEI/SBA-15 in 2 h at 400 ppm CO_2 and 25°C after desorption at different temperatures. (e) Working capacity of PEI67/$Mg_{0.55}Al$–O over 20 cycles under dry and wet conditions (adsorption: 400 ppm CO_2, 25°C; desorption: N_2 purge, 120°C).[107]

Later, Zhao *et al.*[317] loaded TEPA onto MMOs for DAC. The optimal $Mg_{0.55}Al$–O–TEPA67% demonstrates another high CO_2 uptake of 3.0 mmol g^{-1} and excellent regenerability, maintaining ~90% of the initial adsorption amount after 80 adsorption/desorption cycles. Through density functional theory (DFT) calculations, the stronger bonding between the $Mg_{0.55}Al$–O support and the amine was revealed to be caused by the abundance of oxygen defects on the MMOs, which was confirmed by the X-ray photoelectron spectroscopy (XPS) and electron spin resonance analysis. These studies demonstrate the prominent advantages of MMO-based amino solids in terms of capacity, kinetics, and stability compared to common

silica-based materials. Furthermore, LDHs synthesized from inexpensive raw material via scalable approach can facilitate industrial carbon capture applications.[350]

2.2.2. Amine-grafted adsorbents. The efficient assembly of amine-grafted adsorbents relies on supports with a high specific surface area, adjustable pore structure, and rich surface hydroxyl groups. Most amine-grafted CO_2 adsorbents use ordered mesoporous silica as supports, such as MCM-41,[120,296] pore-expanded MCM-41,[120,273,276,292] MCM-48,[351] SBA-15,[118,119,121,123,124,141,263,271,274,275,280,284,286,291,299] KIT-6,[297,298] and MCF.[272] Understanding the effect of the pore structure of siliceous supports on amine grafting and CO_2 adsorptive performance is essential. It is well known that the large pore size and pore volume of pore-expanded MCM-41 enhance the CO_2 capacities and kinetics of grafted amines under ultradilute conditions.[120,292] Recently, the same trend was also observed for SBA-15, especially under wet grafting conditions, in which small pores cause significant pore blockage and poor amine accessibility.[119] Anyanwu *et al.*[124] reported that the clumping and agglomeration of TRI molecules on wet-grafted SBA-15 was ascribed to interparticle amine polymerization. After expanding the pore size of SBA-15 from 8 to 12.3 nm by adding mesitylene during the synthesis, agglomeration was not observed. As a result, wet-grafted pore-expanded SBA-15 achieved higher CO_2 capacities than that of wet-grafted conventional SBA-15 even at similar amine loadings. Unfortunately, wet-grafted pore-expended SBA-15 showed breakthrough CO_2 capacities of less than 0.15 mmol g^{-1} for DAC under high gas hourly space velocities, indicating significant diffusion resistance.

Compared with 2-dimensional structured silicas with long straight channels, 3-dimensional materials, which consist of interconnected mesopores, potentially allow better surface amine functionalization and boost CO_2 diffusion during adsorption. Pioneering works conducted by Chaffee and co-workers showed aminosilane grafted on hexagonal mesoporous silica (HMS) with a “wormhole structure” achieved high

amine efficiencies (*e.g.*, 0.69) for post-combustion CO_2 capture.[352,353] Recently, functionalized HMS materials with different textural properties were tested for adsorption of atmospheric CO_2.[110] Using dodecylamine with a chain length of C12 as a structure-directing agent and subsequently removing it by calcination created optimal pore structure of HMS for amine grafting without hindering the CO_2 diffusion at a loading of 5.4 mmol g^{-1}. Overall, the small pore size (2.5–2.9 nm) of HMS materials limits multilayer amine grafting to achieve higher loadings. In another work, an HBS containing two interconnected cylindrical pores around 9.1 and 33.8 nm was identified as effective support, allowing deep aminosilane accessibility to pore channels and excellent amine dispersion (**Fig. 16**).[294] Wet-grafted HBS retains significant mesopores at high amine loadings and is less kinetically limited compared to wet grafted SBA-15. Under a dry air feed with a GHSV of 3000 h^{-1}, the novel adsorbent achieved high breakthrough CO_2 capacities of up to 1.04 mmol g^{-1}.

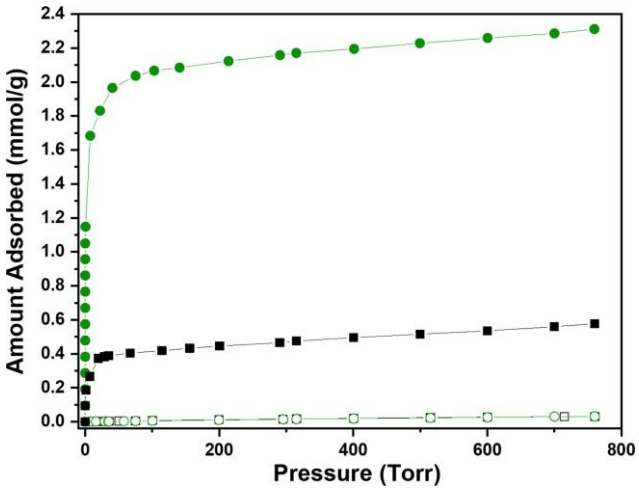

Fig. 16 CO_2 (filled symbols) and N_2 (open symbols) adsorption isotherms for wet-grafted HBS (●) and SBA-15 (■) at 25 °C (Reproduced from ref. 294 with permission from Elsevier, copyright 2022).

Ordered mesoporous silica is formed by polymerizing silica precursors around organic templates as structure-directing agents, which are subsequently removed to create the desired porosity. Air calcination at high temperatures is commonly used for template removal, but a long heating time may cause dehydroxylation, which reduces the silanol density for amine grafting. Although several alternative

template removal methods working under mild conditions have been proposed, such as solvent extraction[354] and glow discharge,[355] they are costly, time-consuming, or unable to remove most of the organic temples. Recently, ionic liquids (IL) were successfully applied for removing the P123 template from as-synthesized SBA-15 at a temperature of 120 °C (**Fig. 17**).[121] The IL-treated SBA-15 maintained a silanol number of more than 5.1 OH nm^{-2}, much higher than that of 3.0 OH nm^{-2} in calcined SBA-15. Furthermore, both the organic template and the IL can be recovered/reused from the process, showing great feasibility for commercial applications. After grafting amine, the IL-treated SBA-15 showed 51% more amine loading and nearly triple CO_2 capacities for DAC compared to the conventionally treated one. The underlying mechanism of the IL treatment is the breakage of hydrogen bonding between the surface silanol groups and the EO moiety in the P123 template, similar to the well-known cellulose dissolution by ILs. Hopefully, the combination of proper pore design, template removal method, and wet grafting would further enhance the CO_2 adsorption of ordered mesoporous silica under ultradilute conditions.

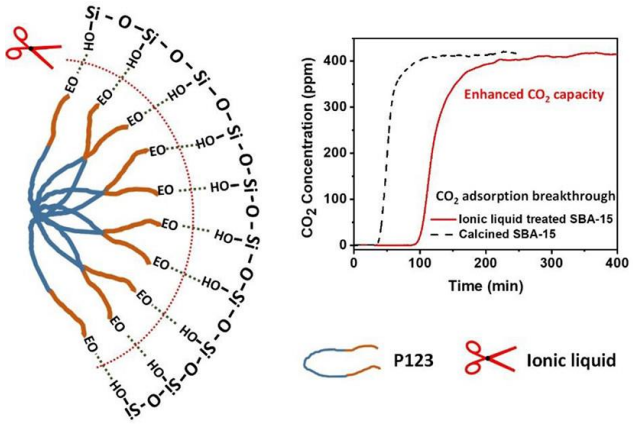

Fig. 17 Concept of template removal by IL treatment for amine grafting (Reproduced from ref. 121 with permission from American Chemical Society, copyright 2020).

Currently, the mass production of ordered mesoporous silicas is still inefficient and costly, prompting the search for alternative supports for amine grafting. Naturally available nanofibrillated cellulose (NFC) consisting of rich hydroxyl groups in a cellulose backbone is one potential choice.[277,290,356] It was reported

that the CO_2 working capacity of DI-grafted NFC reached a stable value of 0.695 mmol g^{-1} in 20 DAC cycles,[290] and decreased by 5% after 100 DAC cycles under wet conditions.[356] Mesoporous γ-alumina is another feasible host for amine grafting, exhibiting superior hydrothermal stability than silica and thus enables the maintenance of porosity and structure during long-term steam purging. After wet-grafting APS at a loading of 2.92 mmol g^{-1}, γ-alumina achieved a high capacity of 0.79 mmol g^{-1} at 25 °C with 400 ppm CO_2.[279] Basic alumina potentially participates in the CO_2 adsorption. However, under ultradilute conditions and high amine loadings, amine-grafted alumina showed a similar CO_2 adsorption mechanism to silica-supported materials, which was confirmed by *in situ* Fourier-transform infrared (FTIR) spectroscopy.[122]

Considering that each metal cation in the LDH-derived nanosheets is coordinated by six edge-sharing hydroxyl groups,[357] exfoliated LDHs offer great potential for high-density amine grafting. Preliminary studies have reported several examples of LDH silylation.[358,359] While the addition of water greatly increases the amine loading on the support,[119,120,125,360] the formation of cross-linked siloxane networks by wet grafting blocks the mesopores of the supports and affects the adsorption kinetics. Recently, monolayer primary amine- and triamine-grafted, organic solvent-treated LDHs have been reported to efficiently and rapidly capture CO_2 from ambient air (**Fig. 18**).[116] The size and thickness of the LDH nanosheets and their stacking morphology mainly determine the maximum amine loading. For example, bulk-phase Mg_2Al-LDH prepared by the urea hydrothermal method could barely graft amines, while acetone-washed $Mg_{0.55}Al$-LDH ($Mg_{0.55}Al$-a) with extremely fine (20 nm) and thin (2.5 nm) nanosheets and flower-like morphology had an amine loading of 6.399 mmol g^{-1}. Consequently, TRI-$Mg_{0.55}Al$-a reached a CO_2 adsorption capacity of 1.05 mmol g^{-1} at 25 °C and 400 ppm CO_2, which is 30% higher than that of TRI-modified SBA-15. APS-grafted $Mg_{0.55}Al$-a containing only the primary amine had an even higher amine efficiency of 0.212. Monolayer amine grafting significantly reduced the pore blockage of amine and preserved the high specific

surface area (162 m^2 g^{-1}) and pore volume (0.553 cm^3 g^{-1}) of the support. These ideal CO_2 diffusion channels could ensure rapid adsorption kinetics, in which over 70% CO_2 uptake was achieved within 30 min. Furthermore, the strong chemical bond between amines and LDHs resulted in almost no performance degradation over 50 adsorption/desorption cycles.

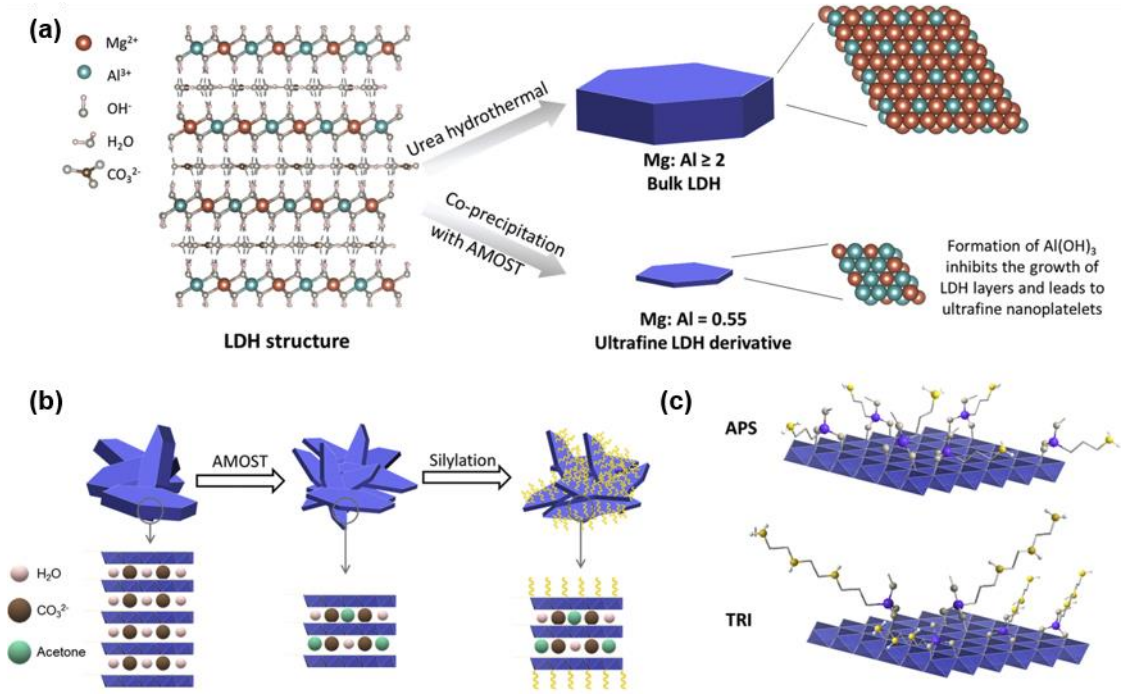

Fig. 18 (a) Fabrication process of amine-monolayer-grafted bulk and ultrafine MgAl-LDHs, (b) Silylation of AMOST-treated LDHs, and structure of grafted amines (Reproduced from ref. 116 with permission from Elsevier, copyright 2021).

Kong *et al.*[281–283,285,338,361,362] prepared a series of amine hybrid aerogels through one-pot sol-gel process, followed by supercritical drying for low-concentration CO_2 capture. Spherical amine hybrid aerogels were also developed by a ball drop method (**Fig. 19**).[283] Benefiting from the unique properties of aerogels with high surface areas and large inter-connected mesopores, significant porosity remained after *in situ* polymerization at high amine loadings (*e.g.*, 7.64 mmol g^{-1}).[281,361,362] As a result, amine hybrid silica aerogels exhibited surprisingly high capacities up to 5.55 mmol g^{-1} at 25 °C and humid 1% CO_2 flow stream.[338] Replacing the silica source (TEOS) with transition metal-based precursor (tetra-n-butyl titanate) during sol-gel synthesis formed hybrid titania/silsesquioxane aerogel with equally high CO_2 capacities

(1.64 mmol g^{-1} @ 400 ppm CO_2).[282] Cellulose aerogels were not as effective as silica aerogels for CO_2 capture, probably because of the low quantity of surface hydroxyl group and fibrous structure in cellulose aerogels that restrict amine loading (1.56 mmol g^{-1}).[285] While amine hybrid aerogels are attractive for DAC, a further in-depth study is still required to understand the polymerization process of aminosilanes inside the porous network of these aerogel-based adsorbents during the sol-gel process, as well as its effect on the CO_2 adsorption kinetics and stability under ultradilute conditions. The application of alternative chemicals and drying methods is also necessary to solve the cost and environmental issues.

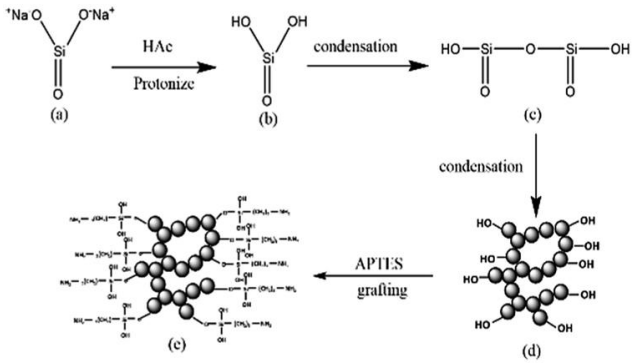

Fig. 19 Synthesis process of spherical amine silica aerogels.[283]

2.3. Effect of additives

The incorporation of additives in the amine-functionalization process has been widely investigated to improve the carbon capture efficiency of amino solids. These additives are typically CO_2-neutral molecules or polymers. The possible reasons for the improvement could be that they increase the amine sites accessibility, reduce the CO_2 diffusion resistance, and change the amine speciation. Furthermore, the additives may lead to hydrogen bond formation between amines and additives. These influences jointly cause changes in the adsorption capacity, rate, heat, and stability. The investigation of the additive type, amine/addition ratio, and application condition could assist in revealing the influence mechanism of additives to provide a guide for improved adsorbent design and applications.

Several studies have explored the role of additives in carbon capture, and most of them were performed under post-combustion conditions.[363–368] Accordingly, the main types of effective additives are surfactants (poly(ethylene glycol) (PEG),[299,369–372] glycerol, cetyltrimethylammonium bromide (CTAB), cetyltrimethylammonium chloride (CTAC), Pluronic P123, and sorbitan monooleate (Span80), silanes,[373,374] sulfur-containing compounds, antioxidants,[375] ionic liquids,[376] and potassium carbonate.[377] PEG has been investigated most frequently and proved positive effects on adsorption properties, possibly because of its rich hydroxyl groups that can facilitate better amine dispersion and attract more water molecules. Wang *et al.*[378] previously suggested surfactants are beneficial to the adsorption performance improvement owing to the deeper diffusion of CO_2 into the PEI films. Later, they investigated the effects of additives on the DAC performance of amino solids.[313] A commercially available polymethacrylate-based resin HP2MGL was impregnated with PEI with CTAB, Span80, and PEG were used as additives. The surfactants improve the amine efficiency by breaking the bulk amine films and their adsorption product. CTAB was observed to be the most effective promotor by increasing 9.6% CO_2 capacity. In another study, a mesoporous carbon was impregnated with PEI with Span80 as the additive.[307] Similarly, the adsorption capacity of additive-containing adsorbents was increased up to 30.5% under 5000 ppm CO_2 compared to that of additive-free adsorbents.

Sakwa-Novak *et al.*[344] provided a deeper insight into the efficacy of additives incorporation on the adsorption performance of PEI-impregnated oxides upon exposure to 400 ppm CO_2. Three additives (CTAB, PEG200, PEG1000) were compared and PEG was observed to perform best by increasing the amine efficiency to 0.16 from 0.10. Qi *et al.*[257] investigated the role of the brush-like additive, CTAC, in enhancing amine efficiency. CTAC was used as a template to synthesize micro-mesoporous silica nanoparticles (MMSN) that were later impregnated with TEPA. The MMSN-30/TEPA-50 with an appropriate amount of

CTAC exhibited higher CO_2 adsorption capacity (3.68 mmol g^{-1} under simulated dry air conditions) than that of adsorbents with no or less additives. FTIR confirmed that the adsorption production was converted from carbamate to carbamic acid, which explains the increase in amine efficiency.

In addition to the enhanced capacity and kinetics, the additives were found to be effective in improving oxidation resistance. While such an enhancement was commonly ascribed to hydrogen bond formation between the additive and the amines,[379,380] a recent study by Vu *et al*.[375] proposed a different idea. They selected sulfur-containing compounds and traditional antioxidants as additives to study the oxidative degradation of TEPA- and PEI-impregnated MCFs. Results showed that traditional antioxidants catalyzed oxidative degradation. In contrast, sulfur-containing additives, which are effective in free radical scavenging and peroxide decomposition, decrease the oxidation rate.

There is still lack of research on the additive functions under DAC conditions. In fact, the influence of additives becomes more obvious under ultradilute conditions because of eliminated physical adsorption. PEG has been mostly applied for promotion because of its effect on hydrogen bond formation, kinetic enhancement, and production conversion, while other materials act in different ways. It has been shown that all of these enhancements are more likely to be kinetic rather than thermodynamic; however, a more fundamental description of what gives rise to these phenomena still must be elucidated. Comprehensive characterizations and systematic theory also need to be explored. More types of additives and a wider range of application scenarios should be examined to achieve general promotion strategy.

3. Avoidance of oxidative degradation

3.1. Pathway of oxidative degradation

Oxidative stability is a dominant factor that determines the lifetime of amine-functionalized adsorbents.

The oxidative degradation of amine-loaded adsorbents principally results in the chemical instability of loading amines,[101] producing new characteristic bonds including carbonyl (C=O),[252,274,381–384] aliphatic C=C,[381] heterocyclic C=N,[274,381–383] aromatic C=C[381] owing to the formation of acid, amide, imide, and/or urea linkages.[252,274,381–385] ^{13}C cross-polarization magic-angle spinning (CP-MAS) solid state NMR,[252,380–385] XPS,[381] diffuse reflectance infrared Fourier transform (DRIFT) spectroscopy,[252,380,382–384,386,387] and FT-Raman[252] are usually employed to examine the effect of oxidative treatments on solid adsorbents. However, the exact pathway of this oxidation process remains unclear. Furthermore, some specific species, such as amides and imines, cannot simply be identified through IR spectra because of their similar vibration locations. Sayari *et al*. proposed a solvent extraction method to remove the species generated by the oxidative degradation of amine-grafted[388] and amine-impregnated[389] mesoporous silicas. Based on 1D and 2D NMR analyses, two chemical structures produced from air-deactivated trimethoxy[3-(methylamino)propyl]silane (sMono)-grafted PE-MCM-41 and four chemical compounds of air-deactivated TRI-grafted PE-MCM-41 were determined (**Fig. 20**a and b). Air-deactivated species containing –HC=O and –HC=N– units were also identified in linear PEI (M_w ~ 2500) and branched PEI (M_n ~ 600)-impregnated mesoporous SBA-15 silica (**Fig. 20**c).

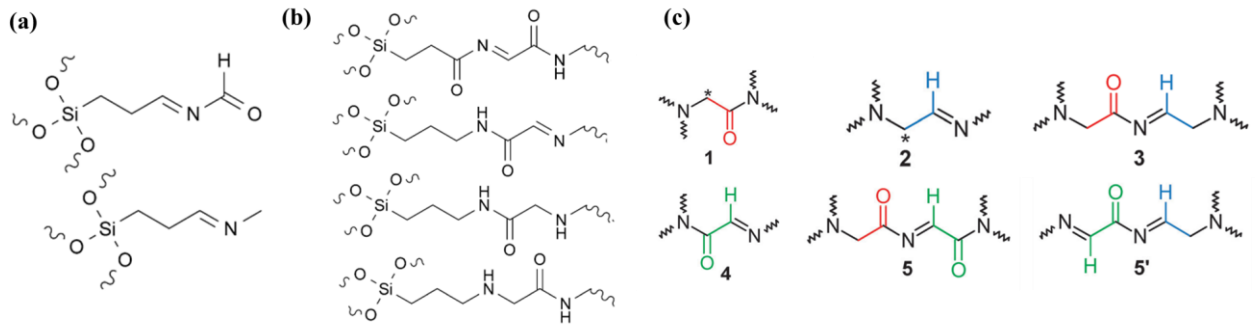

Fig. 20 Possible structures of –HC=O and –HC=N– units identified for air-deactivated (a) sMono, (b) TRI (right) (Reproduced from ref. 388 with permission from John Wiley and Sons, copyright 2013), and (c) PEI (linear and branched).[389] All six fragments were detected in deactivated branched PEI, but only the first three were identified in linear PEI.

On the other hand, oxidation kinetics are strongly associated with transient changes in the adsorbents. Therefore, the quantitative estimation of sorbent lifetime requires an insightful investigation of oxidative degradation rates. Jones *et al.*[131] recently proposed an experimental framework to identify the oxidative kinetics of PEI-impregnated γ-Al_2O_3 in simulated ambient air. The oxidative extent of oxidation over time was expressed in terms of the oxidation reaction heat from DSC testing. The variations in the molar ratios of C/N and H/(C+N) in PEI during oxidative degradation provided two important pieces of information (**Fig. 21**). First, the species lost during oxidation are not simply caused by cleavage or evaporation of low molecular weight polymer fractions, which agrees with the formation of hydroxylamine and ammonia. Second, the H species were lost at a highly disproportionate rate relative to the repeat units of PEI. This is consistent with the supposition of the formation of non-volatile oxidation products, such as amides and imines, which contain double bonds.

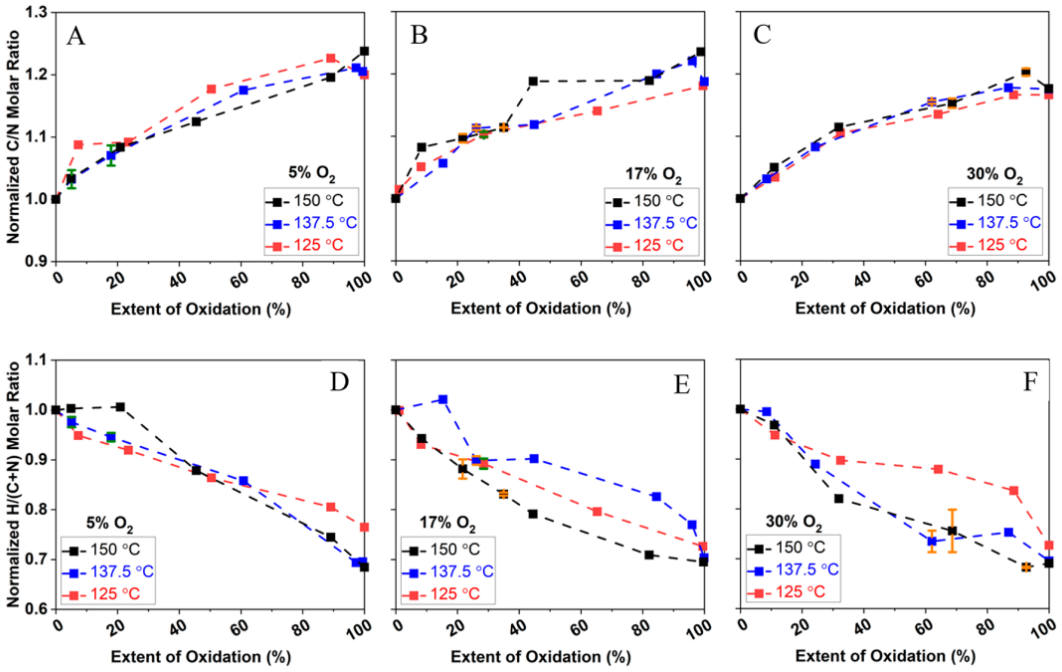

Fig. 21 (a–c) C/N and (d–f) H/(C+N) molar ratios of the oxidized sorbents normalized with the ratios of a fresh PEI sorbent over the extent of PEI oxidation. Green error bars indicate the sample-to-sample reproducibility and orange error bars show the run-to-run reproducibility of a chosen number of elemental analysis (Reproduced from ref. 131 with permission from American Chemical Society, copyright 2021).

The effective oxidation rate of the suite of oxidative reactions is represented by equation (1), which means that the parameters extracted from the equation are not specific to a given reaction and are effective in nature. It is interesting to note that there is a perfect overlap in the activation energy among the O_2 concentrations of 5%, 17%, and 30% at the extent of oxidation below 20%. This phenomenon suggests that at the early stages of oxidation, there is a similar set of oxidative reactions occurring in the adsorbents under these different O_2 concentrations. The region of reaction rate keeps increasing until the extent of oxidation arrives at 50%, then the reactor order gradually decayed to zero. The rate of the reaction is likely to be controlled by the limited number of active reaction sites remaining on PEI.

$$r_{\text{eff}} = k_{0,\text{eff}} \exp\left(\frac{\Delta H_{\text{rxn,eff}}}{RT}\right)[O_2]^x \quad (1)$$

3.2. Alternative amine polymers

Accelerated oxidative treatment by exposing sorbent samples to an oxygen atmosphere is usually deployed to simulate the oxidative processes in actual applications for amine-loaded adsorbents.[115,126,128,129,131,252,274,381–385,390] The variation in CO_2 capacity or amine efficiency before and after accelerated oxidative treatment is used to determine the oxidative stability of the samples. This variation commonly results from the O_2-induced deactivation.[126]

Several early studies proved that monoamine-grafted adsorbents showed better oxidative resistance than diamine- and triamine-grafted adsorbents, where primary amines are better than secondary amines.[381,383,391] However, the elusive interactions of these findings have not been discussed and provided. Jones and coworkers investigated the effect of the alkyl linker length of grafted primary amines on oxidative stability.[385] Compared to supported methyl, supported ethyl and propyl exhibited more favorable oxidative resistance. They proposed a mechanism of amine interactions with the surface and adjacent amines, which

can occur based on the alkyl linker length (**Fig. 22)**. It was assumed that methyl and ethyl linker materials will only interact with adjacent amines, whereas amines with propyl linkers are able to interact with surface silanols as well as neighboring amines. The stability tests also proved that aminomethyl-functionalized adsorbents suffered from severe degradation at high operating temperatures (135 °C) compared to their ethyl and propyl counterparts.

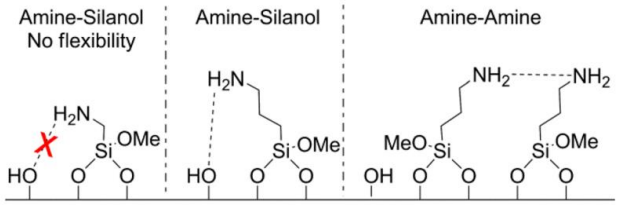

Fig. 22 Proposed amine interactions with the surface and neighboring amines that can occur based on alkyl chain length. Amines with short alkyl chains have no ability (methyl) or very limited ability (ethyl) to interact with the silanols on the surface (Reproduced from ref. 385 with permission from American Chemical Society, copyright 2014).

Another study investigated the effect of alkyl spacer length as well as branched (B-ethyl, B-propyl) and linear (L-ethyl, L-propyl) structures on the oxidative stability of amine-grafted adsorbents under DAC conditions **(Table 3)**.[274] All grafted adsorbents showed favorable thermal stability following the stability trend of APS > L-propyl > B-propyl > B-ethyl > L-ethyl. The oxidation resistance of these grafted adsorbents showed the same decreasing trend as the thermal stability, but the value varied significantly. In addition, after oxidation, the molar ratios of C/N of the four samples changed slightly; however, the variation in the molar ratios of C/(H+N) of the four samples was significant and showed the same decreasing trend as the oxidative stability.

Table 3 Summary of accelerated oxidative degradation data under the DAC condition on amine-grafted SBA-15.

Amine Loading	Oxidative treatment condition	Adsorption condition	Desorption condition	CO_2 capacity loss (%)	Ref.
APS	110 °C in simulated air (21% O_2/79% N_2) for 12 h	25 °C in 400 ppm CO_2/He for 3 h	110 °C in He for 3 h	1	274
L-ethyl	110 °C in simulated air (21% O_2/79% N_2) for 12 h	25 °C in 400 ppm CO_2/He for 3 h	110 °C in He for 3 h	45	274
L-propyl	110 °C in simulated air (21% O_2/79% N_2) for 12 h	25 °C in 400 ppm CO_2/He for 3 h	110 °C in He for 3 h	5	274
B-ethyl	110 °C in simulated air (21% O_2/79% N_2) for 12 h	25 °C in 400 ppm CO_2/He for 3 h	110 °C in He for 3 h	28	274
B-propyl	110 °C in simulated air (21% O_2/79% N_2) for 12 h	25 °C in 400 ppm CO_2/He for 3 h	110 °C in He for 3 h	11	274

The L-propyl-grafted SBA-15 showed strong resistance to oxidation even though L-propyl contains secondary amines, which indicates that the propyl spacer between the secondary amine and the neighboring primary amine may enhance oxidative resistance. This hypothesis was later supported by the analysis of the αC−H bond dissociation energy near the primary amine, which increased as the alkyl chain length increased. The oxidative stability of B-ethyl was better than that of L-ethyl owing to the absence of secondary amines. The formation of oxidized species on both branched and linear amino silanes was explored by *in situ* IR spectroscopy (**Fig. 23**). The stretching peak of the carbonyl group (1633 or 1670 cm^{-1}, C=O) was observed for the L-ethyl-grafted adsorbent, and the N−H (1600 cm^{-1}) bond was possibly derived from amide or imine (1633 or 1670 cm^{-1}, C=N) species owing to the formation of a possibly oxidized species of -NH-C=O.

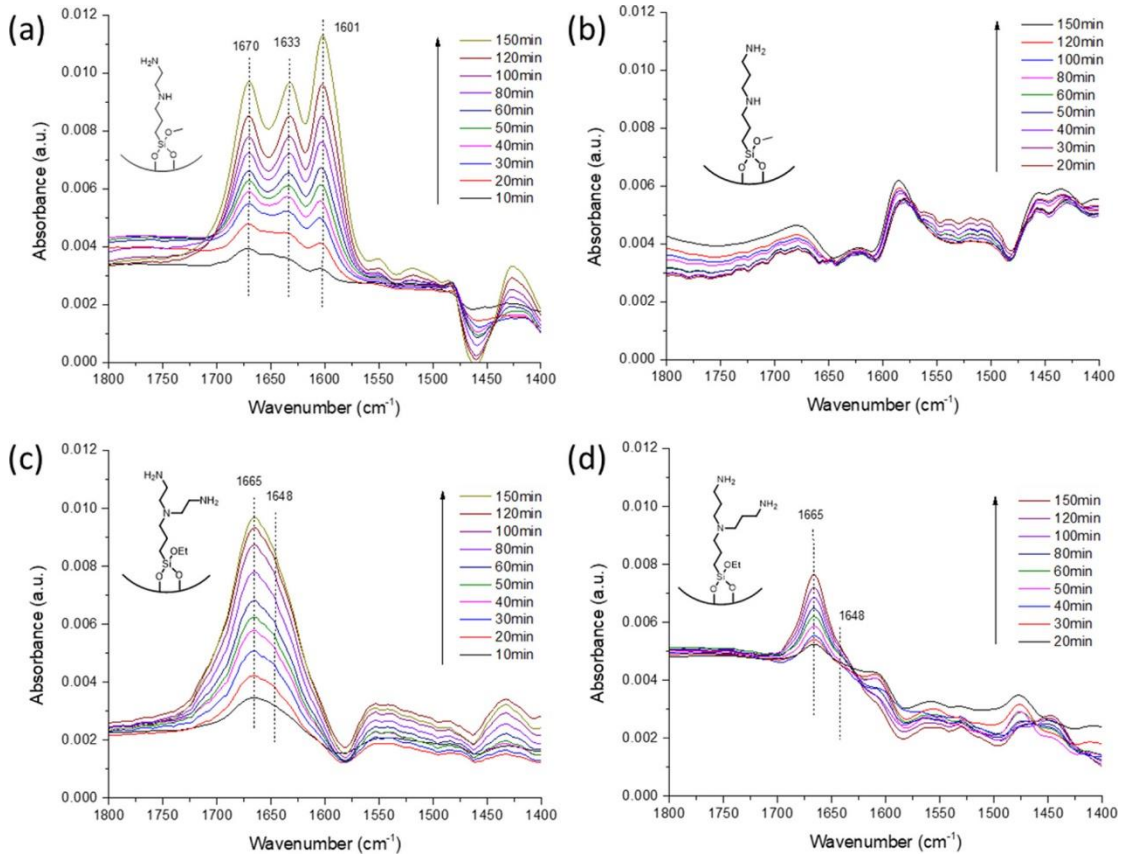

Fig. 23 *In situ* IR spectra for CO_2 adsorbents of (a) L-ethyl, (b) L-propyl, (c) B-ethyl, and (d) B-propyl, respectively during the oxidation under simulated air atmosphere (21% O_2/N_2) at 110 °C for 150 min (Reproduced from ref. 274 with permission from American Chemical Society, copyright 2020).

Hallenbeck *et al.*[392] examined the stability of Lewatit VP OC 1065, a commercialized primary amine-functionalized ion-exchange resin, by exposing the resin to a simulated flue gas stream containing 12% CO_2, 4% O_2, and 84% N_2. The cyclic capacities were stable after 17 continuous adsorption-desorption cycles via a thermal swing between 50 and 127 °C. However, the capacity of treated resin was reduced 79% compared to fresh adsorbents after 7 days of continuous exposure at 120 °C in air. Later, Yu *et al.*[393] claimed that although Lewatit VP OC 1065 is thermally and hydrothermally stable at high temperatures (*e.g.*, 100–150 °C), the oxidative degradation can occur at moderate temperatures (above 70 °C) for adsorbents treated by air as well as flue gas with 12% O_2. Nevertheless, a comprehensive investigation of the oxidative stability of Lewatit VP OC 1065 under DAC conditions is lacking.

PEI is considered as one of the most promising commercially supported amines for both fuel gas capture and DAC. The oxidative stability of PEI-functionalized adsorbents has attracted much research interest.[126,128,252,382,384,389,390,394] Oxidative degradation depends on the operating temperature in addition to the oxygen partial pressure. For example, 55 wt.% PEI/SBA-15, as the first PEI-modified adsorbent being reported focusing on the oxidative stability according to our best knowledge, lost 22% and 70% of CO_2 uptake after accelerated oxidative treatment under carbon-free air flow at 90 °C and 100 °C, respectively.[384] The combination of material loss by amine evaporation and oxidative reactions caused the loss of CO_2 capacity. Yuan *et al.*[390] recently proved that PEI-modified silica was oxidatively stable under air exposure at mild temperatures, but the oxidative degradation would indeed occur at more harsh temperatures (above 90 °C). PEI/SiO_2 would be significantly degraded under O_2-containing flue gas at above 105 °C, due to the oxidation of the available amine sites. Linear PEI (Mn ~ 2500)/SBA-15 shows better oxidative resistance than branched PEI (Mn ~ 600)/SBA-15, though fresh linear PEI/SBA-15 exhibits lower CO_2 uptake.[389]

Compared to supported PEI, PAA-impregnated mesoporous γ-alumina containing only primary amines

showed significantly improved oxidative resistance but lower initial CO_2 capacity (**Fig. 24**a and b).[252] Supported PGA was reported for CO_2 capture from flue gas and air.[115] Exposure to simulated air (21% O_2/N_2) for 24 h at 110 °C reduces 50% of CO_2 capacity using PGA-50 impregnated SBA-15 for capturing CO_2 from simulated flue gas. In comparison, 50% branched PEI-modified SBA-15 lost 90% of its CO_2 capacity for capturing CO_2 from simulated air (400 ppm CO_2 in He) after the same oxidative treatment. Oxidized PGA/SBA-15 showed a prominent peak at 1660 cm^{-1} as PEI/SBA-15 (**Fig. 24**c). Compared to more oxidatively stable PAA, it is likely that the presence of oxygen in the backbone of PGA accelerates or enables the oxidation reaction to occur.

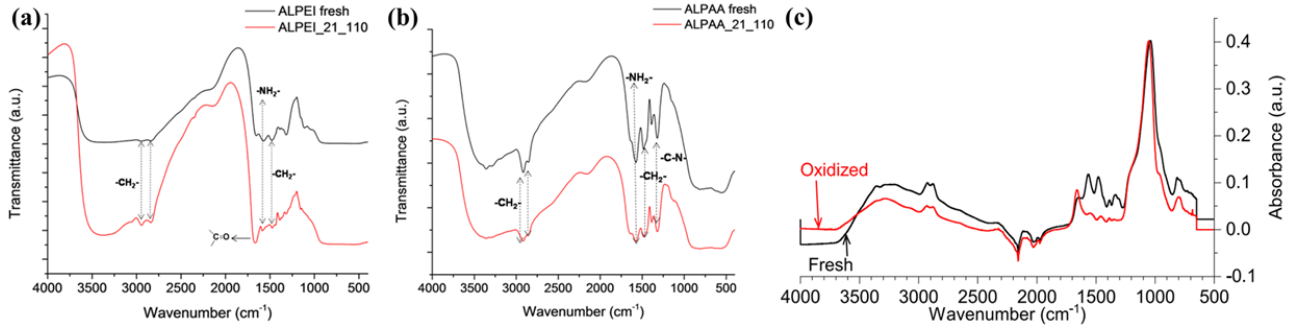

Fig. 24 FTIR spectra of fresh (a) PEI-impregnated γ-alumina and oxidized sorbent (ALPEI_21_110) treated with 21% oxygen at 110 °C for 20 h as well as (b) PAA-impregnated γ-alumina (ALPAA fresh & ALPEI_21_110) (Reproduced from ref. 252 with permission from American Chemical Society, copyright 2013). (c) IR spectra of fresh and oxidized PGA-impregnated SBA-15 (Reproduced from ref. 115 with permission from American Chemical Society, copyright 2019).

The oxidative stability of branched PEI-impregnated silica was also investigated under the DAC condition.[382] After 24 hours of pure O_2 flow treatment at 90 °C, a mild reduction of organic content can be observed (**Fig. 25**). A further decrease occurred at 110 °C, due to the evaporation, leaching, and/or cracking of aminopolymer. An increase in the organic content of oxidized samples treated from 110 to 130 °C is likely due to oxygen addition to the aminopolymers or fragments by forming amide or other oxygen-containing species above 110 °C. The CO_2 uptake of PEI/SBA-15 decreased by 29% after the oxidation at 90 °C, but the loss of organic content was only 15%.

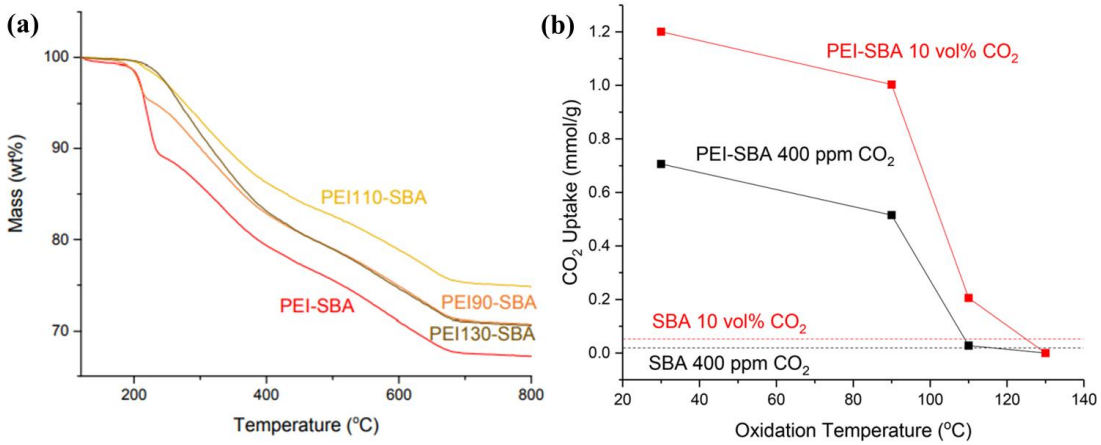

Fig. 25 (a) Thermogravimetric analysis to assess the organic content of PEI-impregnated SBA-15 (PEI-SBA) after oxidative treatment at the specified temperatures. (b) Variation in CO_2 uptake of the PEI-SBA series as a variation of oxidation treatment temperature for both 10 vol.% and 400 ppm of CO_2 in He, compared to the bare SBA-15 support (Reproduced from ref. 382 with permission from American Chemical Society, copyright 2019).

Given this disparity, it is assumed that the lost or degraded aminopolymer was the most effective species for adsorbing 400 ppm of CO_2. To conclude, a dramatic decrease in CO_2 uptake of PEI/SBA-15 occurred when the treatment temperature increased from 90 to 110 °C and is ascribed not only to the aminopolymer evaporation, leaching, and/or cracking, but also the oxidative reaction of the amine species into amides and heterocycles, which has been proven by the results of the ^{13}C solid state NMR. PEI-SBA oxidized at 130 °C showing the same uptake as the bare SBA-15, suggesting that it has been completely oxidized and cannot chemisorb CO_2. It is interesting to note that PEI-impregnated SBA-15 exhibited different variations between flue gas capture and DAC after the same oxidative treatments, which requires further investigation. Jones *et al.*[114,126,128,129] systematically explored the relationship between the length of the alkyl spacer separating the functional amine groups of polymers and amine oxidative degradation. They found PEI with an ethyl spacer is more susceptible to oxidation than PPI with a propyl spacer, despite small linear molecules of PPI, tripropylenetetramine (TPTA), containing secondary amines (**Fig. 26**a). The small molecules of PPI, TPTA, and N^1,N^1,N^3,N^3-tetrakis(3-aminopropyl)propane-1,3-diamine (PI-den) impregnated SBA-15 showed a more efficient CO_2 capacity than the corresponding triethylenetetramine (TETA)- and

N^1,N^1,N^3,N^3-tetrakis(2-aminoethyl)propane-1,3-diamine (EI-den) modified adsorbents (**Fig. 26**b), which might be ascribed to the increased basicity as well as the decreased extent of nearest-neighbor interactions with the increased length of the alkyl spacer.

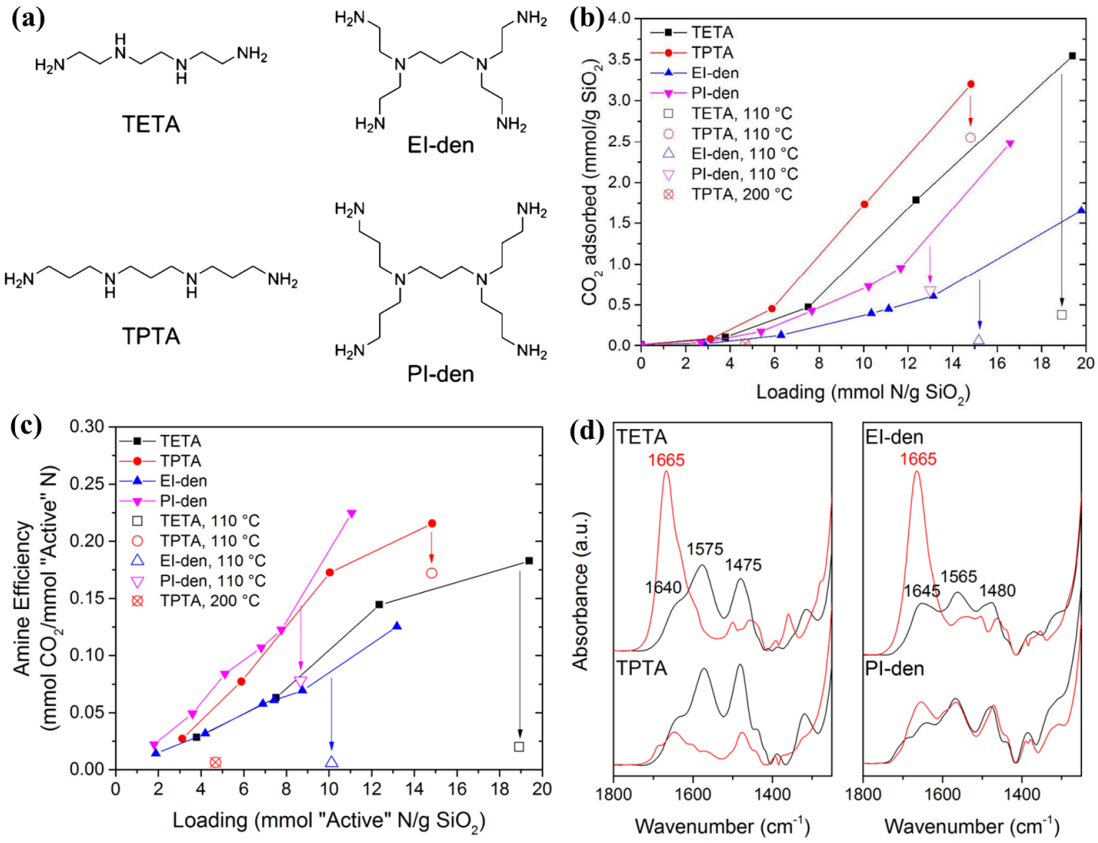

Fig. 26 (a) Structure of linear and dendritic PEI, referring to TETA) and EI-den, and PPI, referring to TPTA and PI-den. (b) CO_2 capacity and (c) amine efficiencies of aminopolymers impregnated in SBA-15 at 400 ppm of CO_2/N_2 and 35 °C over a range of amine loadings. Amine efficiencies were normalized to the number of amines that are active for CO_2 capture under dry conditions (1° and 2° only). Open symbols indicate samples exposed to oxidative treatment at the listed temperature. (d) FTIR spectra for samples with fresh aminopolymers (black) and aminopolymers oxidatively treated at 110 °C for 24 h (red). Spectra were acquired under vacuum and normalized to the Si−O−Si framework bending mode at 460 cm^{-1} (Reproduced from ref. 126 with permission from American Chemical Society, copyright 2017).

In addition, there is no significant branching dependence in the adsorption capability of small-molecule modified adsorbents. After accelerated oxygen treatment at 110 °C for 24 h, the CO_2 capacity and amine efficiency of oxidized TETA and EI-den modified adsorbents containing secondary amines showed a significant server loss (**Fig. 26**c). Although TPTA also contains secondary amines, the CO_2 capacity and

amine efficiency of oxidized TPTA loaded SBA-15 only decreased around 20%. Furthermore, oxidized PI-den impregnated adsorbent showed around 50% loss in CO_2 capacity and amine efficiency, exhibiting higher oxidative resistance than EI-den with over a 90% loss. Therefore, it can be concluded that polyamines with propylene linkers are more resistant to oxidative degradation than those with ethylene linkers. After oxidative treatment, an intense peak at 1665 cm^{-1}, which is attributed to the stretching mode of the C=O or C=N groups, can be observed in the FTIR spectra of the SBA-15-supported samples with TETA and EI-den (**Fig. 26**d). Combining additional results from ^{1}H and ^{13}C NMR spectra and electrospray ionization mass spectrometry, the authors concluded that the observed deactivation of TPTA was likely to be a thermal rearrangement reaction assisted by oxygen, contributing to intramolecular cyclization and/or alkylamine chain transfer reactions.

The same group also elaborately investigated oxidatively stable linear PPI-containing adsorbents with different molecular weights.[128] The adsorbent modified with linear PPI with a molecular weight of 1000 g mol^{-1} showed the best performance with 0.16 mmol CO_2 $mmol^{-1}$ N of amine efficiency and 1.25 mmol g^{-1} of CO_2 capacity (**Fig. 27**a). After exposure to a flow of simulated air at 110 °C for 24 h, linear PPI modified samples with high molecular weights retained most of the CO_2 capture capability and over 83% amine efficiency (**Fig. 27**a and b). FTIR spectra showed that the major bonds in linear PPI-impregnated SBA-15 samples (N-H stretching at 3240 cm^{-1} and CH_2 stretching at 2940, 2873, and 2815 cm^{-1}) basically remained the same after the accelerated oxidative treatment (**Fig. 27**c). However, a significant band at 1670 cm^{-1}, referring to C=N or C=O groups, was observed for PEI/SBA-15. The significant reduction in the intensity of the N-H and CH_2 stretches of PEI/SBA-15 suggests more severe oxidative degradation than that of PPI/SBA-15. The oxidative resistance of the extended aging (~2 years) of linear PPI confined in SBA-15 was also studied, and aged adsorbents also exhibited desirable stability after 24-hour exposure at 110 °C

under 21 % O_2/He flow.[129]

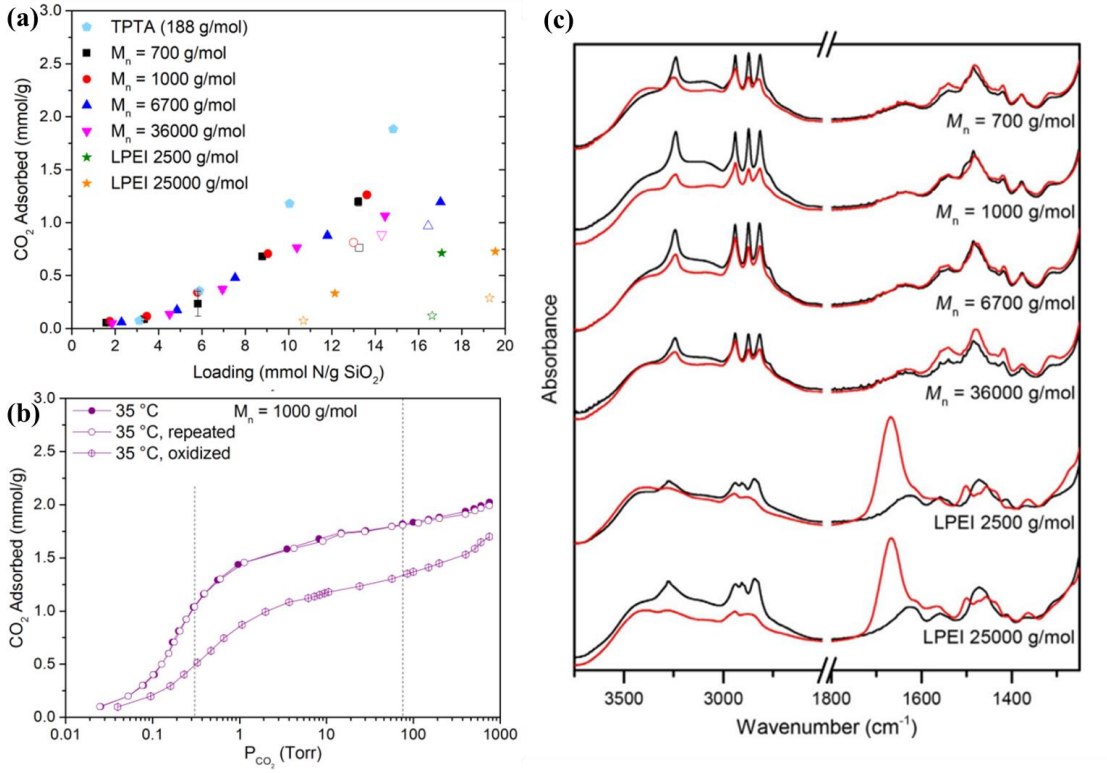

Fig. 27 (a) CO_2 capacities of linear PPI and PEI-impregnated in SBA-15 (adsorption in 400 ppm CO_2/N_2 at 35 °C, 18 h) over a range of amine loading. Open symbols indicate samples exposed to oxidative treatment (21% O_2/N_2 at 110 °C, 24 h) prior to CO_2 adsorption. Error bars indicate the standard deviation of three separate adsorption experiments on three different powder samples. (b) CO_2 adsorption isotherms for the 50 wt.% linear PPI (1000 g mol^{-1})/SBA-15 sample, where open symbols indicate a repeated isotherm measurement after acquiring all other isotherms to ensure no degradation or loss of aminopolymer had occurred due to thermal treatment under vacuum, and samples with cross indicate the isotherm obtained for a sample that had first been exposed to the oxidative treatment. (c) FTIR spectra of linear PPI and PEI-impregnated in SBA-15 before (black) and after exposure to oxidative treatment (21% O_2/N_2 at 110 °C, 24 h) (red). Spectra were acquired under a flow of UHP N_2 and normalized to the Si-O-Si framework bending mode at 460 cm^{-1} (Reproduced from ref. 128 with permission from John Wiley and Sons, copyright 2018).

Branched PPI is another promising alternative to commonly used branched PEI.[114] As shown in **Fig. 28**, PPI made with $HClO_4$ and HBr initiators showed higher CO_2 capacity, amine efficiency, and oxidative resistance (~80%) after exposure to air at 110 °C for 12 h. In comparison, branched PEI only retained 40% of CO_2 capacity. The performances of these aminopolymer-impregnated adsorbents after oxidative treatments for DAC are listed in **Table 4** in detail.

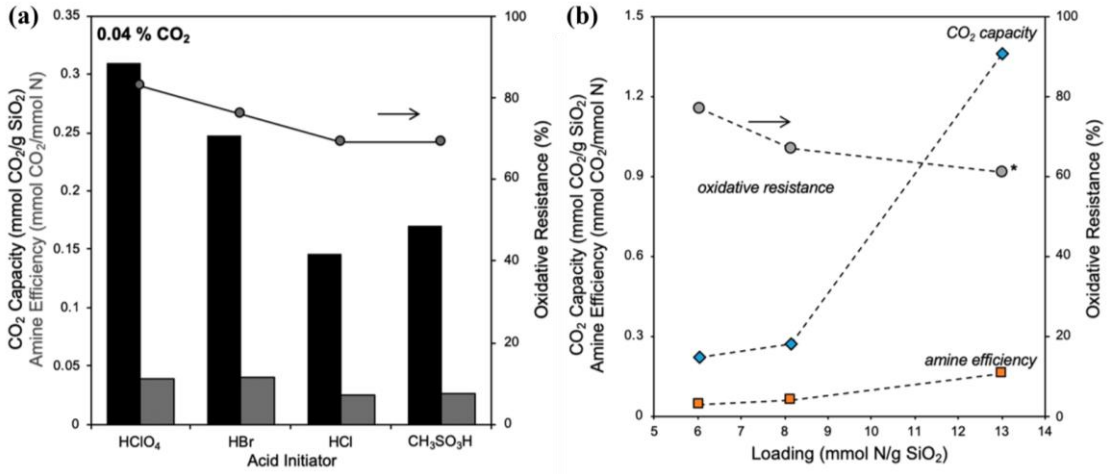

Fig. 28 (a) CO_2 capacity (mmol CO_2 g^{-1} SiO_2; black) and amine efficiency (mmol CO_2 $mmol^{-1}$ N; gray) measured under 0.04% CO_2 streams at 35 °C for polymers made with various acid initiators. All sorbents were approximately 30 % weight polymer in SBA-15. (b) CO_2 capacity, amine efficiency, and oxidative resistance measured under 0.04% CO_2 streams at 35 °C for polymers made with hydrobromic acid at various loadings in SBA-15. Oxidative resistances are shown by data points under 0.04% CO_2 conditions and are calculated as the ratio of uptake capacities before and after 12 h oxidation in air at 110 °C (or for 24 h in the case of the sorbent with the highest polymer loading) (Reproduced from ref. 114 with permission from American Chemical Society, copyright 2019).

Table 4 Summary of accelerated oxidative degradation data under the DAC condition on amine-impregnated SBA-15.

Amine Loading	Oxidative treatment condition	Adsorption condition	Desorption condition	CO_2 capacity loss (%)	Ref.
~30% branched PEI (Mw ~800)	90/110 °C in air for 24 h	35 °C in 400 ppm CO_2/He for 6 h	110 °C in pure N_2 for 2 h	29 (90 °C) >95 (110 °C)	382
40% TETA	110 °C in air for 24 h	35 °C in 400 ppm CO_2/N_2 for 3 h	70 °C in pure N_2 for 2 h	~90	126
40% TPTA	110 °C in air for 24 h	35 °C in 400 ppm CO_2/N_2 for 3 h	70 °C in pure N_2 for 2 h	~20	126
45% EI-den	110 °C in air for 24 h	35 °C in 400 ppm CO_2/N_2 for 3 h	70 °C in pure N_2 for 2 h	~90	126
45% PI-den	110 °C in air for 24 h	35 °C in 400 ppm CO_2/N_2 for 3 h	70 °C in pure N_2 for 2 h	~50	126
50% Linear PEI (2500 g mol^{-1})	110 °C in air for 24 h	35 °C in 400 ppm CO_2/N_2 for 18 h	110 °C in pure N_2 for 2 h	>80	128
50% Linear PEI (25000 g mol^{-1})	110 °C in air for 24 h	35 °C in 400 ppm CO_2/N_2 for 18 h	110 °C in pure N_2 for 2 h	60-75	128
50% Linear PPI (700 g mol^{-1})	110 °C in air for 24 h	35 °C in 400 ppm CO_2/N_2 for 18 h	110 °C in pure N_2 for 2 h	~35	128
50% Linear PPI (1000 g mol^{-1})	110 °C in air for 24 h	35 °C in 400 ppm CO_2/N_2 for 18 h	110 °C in pure N_2 for 2 h	~35	128
50% Linear PPI (6700 g mol^{-1})	110 °C in air for 24 h	35 °C in 400 ppm CO_2/N_2 for 18 h	110 °C in pure N_2 for 2 h	<17	128
50% Linear PPI (36000 g mol^{-1})	110 °C in air for 24 h	35 °C in 400 ppm CO_2/N_2 for 18 h	110 °C in pure N_2 for 2 h	<17	128
40% Branched PEI	110 °C in air for 12 h	35 °C in 400 ppm CO_2/N_2 for 12 h	110 °C in pure N_2 for 3 h	60	114
30% Branched PPI made with $HClO_4$	110 °C in air for 12 h	35 °C in 400 ppm CO_2/N_2 for 12 h	110 °C in pure N_2 for 3 h	17	114
30% Branched PPI made with HBr	110 °C in air for 12 h	35 °C in 400 ppm CO_2/N_2 for 12 h	110 °C in pure N_2 for 3 h	24	114
30% Branched PPI made with HCl	110 °C in air for 12 h	35 °C in 400 ppm CO_2/N_2 for 12 h	110 °C in pure N_2 for 3 h	31	114
30% Branched PPI made with CH_3SO_3H	110 °C in air for 12 h	35 °C in 400 ppm CO_2/N_2 for 12 h	110 °C in pure N_2 for 3 h	31	114
50% Branched PEI (Mw ~800）	110 °C in air for 24 h	35 °C in 400 ppm CO_2/N_2 for 18 h	110 °C in pure N_2 for 2 h	90	115

Although TEPA is also a popular and inexpensive amine for amine-impregnated adsorbents, it suffers from unfavorable thermal stability and chemical stability compared with PEI and other polymer amines.[101,380] The effects of oxidation duration time, treatment temperature, oxygen concentration, and TEPA loading on silica adsorbents were comprehensively studied by Yogo *et al*.[395] It is interesting to note that after oxidative treatment at a moderately high temperature of 80 °C for 18 h, the oxidative resistance of samples increased when the TEPA loading increased from 30% to 60%. Under these treatment conditions, the oxidation rate depended on the rate of O_2 diffusion to the amine molecules. The O_2 diffusion rate decreased with increasing amine loading owing to the agglomeration of amine molecules in the pores of the mesoporous silica (**Fig. 29**). However, when the TEPA loading increased to 70%, the surface of the silica was almost completely covered by TEPA molecules. Therefore, O_2 reacts more easily with amines, causing a decrease in oxidative resistance.

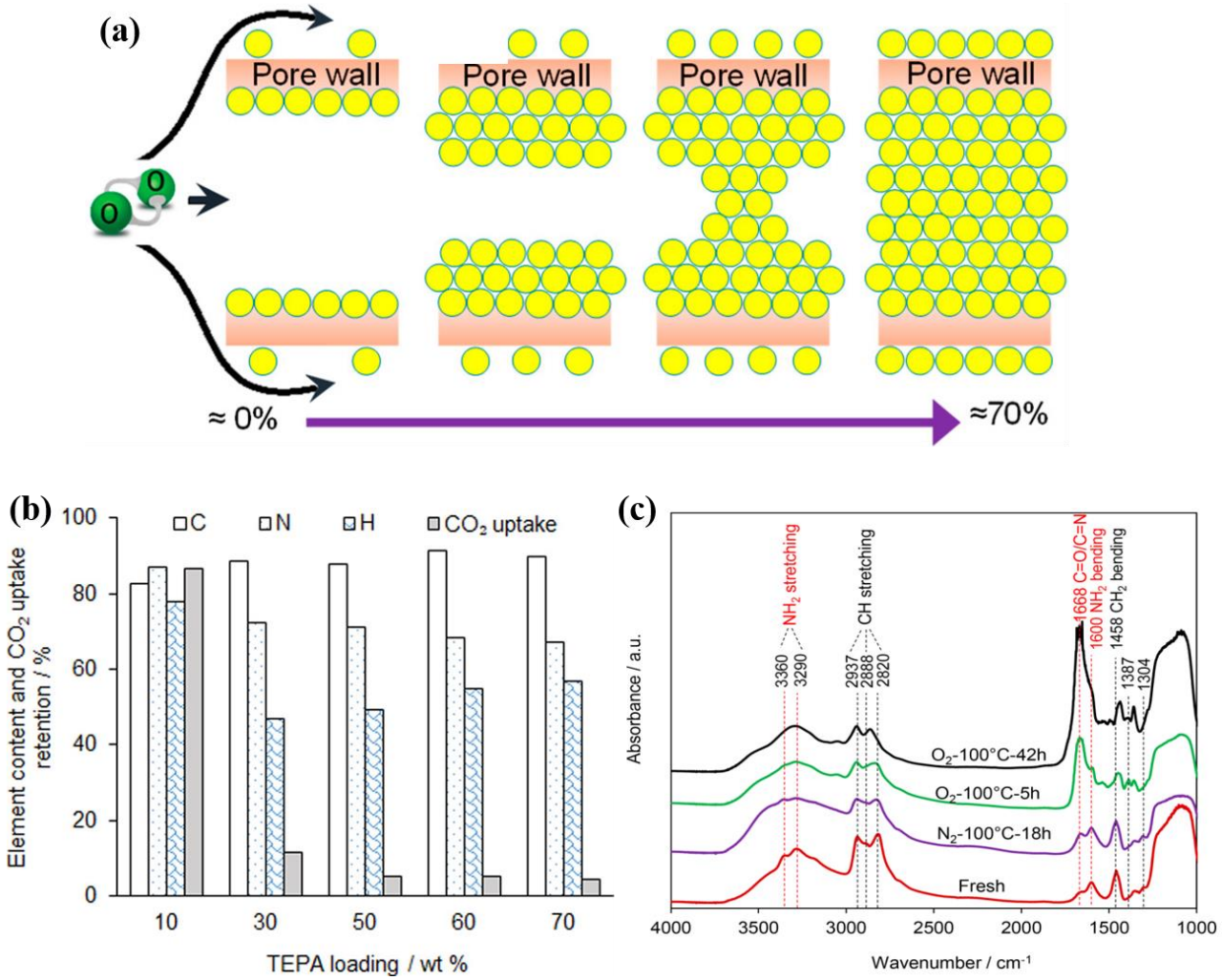

Fig. 29 (a) Agglomeration of amine molecules in the pores and on the surface of silica with amine loadings in the range of 10–70 wt.%. (b) Elemental content and CO_2 uptake retention of sorbents after degradation in pure O_2 at 100 °C over 18 h. (c) FTIR spectra of TEPA70/MF before and after exposure to O_2/N_2 at 100 °C for different durations (Reproduced from ref. 395 with permission from American Chemical Society, copyright 2019).

When the oxidation temperature is lower than 100 °C, the slow rate of O_2 diffusion to amine molecules leads to favorable oxidative stability of different TEPA loading adsorbents. According to the elemental analysis, the change in functional groups rather than the evaporation of amine mainly caused the observed reduction in the CO_2 capacity after the oxidation treatment. In addition, the results of gas chromatography revealed that 1-(2-aminoethyl)-4-[[(2-aminoethyl)amino]ethyl]piperazine showed higher oxidative stability than the other three main components of TEPA (1,4,7,10,13-pentaazatride cane, 4-(2-aminoethyl)-N-(2-aminoethyl)-N-[2-[(2-aminoethyl)amino]ethyl]-1,2-ethanediamine, and 1-[2-[[2-[(2-

aminoethyl)amino]ethyl]amino]ethyl]-piperazine). However, the effects of oxygen on TEPA-functionalized adsorbents in DAC systems have been rarely reported.

3.3. Alternative supports

Porous cross-linked poly(vinyl alcohol) (PVA) was reported to support PEI for CO_2 capture (15% CO_2/air) by the Chuang group with enhanced degradation resistance compared to PEI/SiO_2.[396] After oxidative treatment by exposing PEI/SiO_2 or PEI/PVA to 15% CO_2/air at 130 °C, PEI/PVA exhibited higher oxidative degradation resistance than that of PEI/SiO_2, owing to the formation of hydrogen bonds between hydroxyl (−OH) groups of PVA and secondary amines (−NH) of PEI. The decreased intensity of −NH_2/−NH at 3297 cm^{-1} in the IR absorption spectra compared to that of −NH_2 at 3365 cm^{-1} on PEI/SiO_2 strongly supports this conclusion **(Fig. 30)**. However, hydrogen bonding is likely to facilitate polymer chain entanglement between PEI and PVA, thus limiting the amine efficiency and CO_2 capacity of PEI/PVA. In addition, most studies on the oxidative performance of amine-modified adsorbents for DAC are mainly based on the silica support SBA-15. Therefore, the effect of alternative supports on the oxidative stability of amine-modified adsorbents for DAC is a promising research topic.

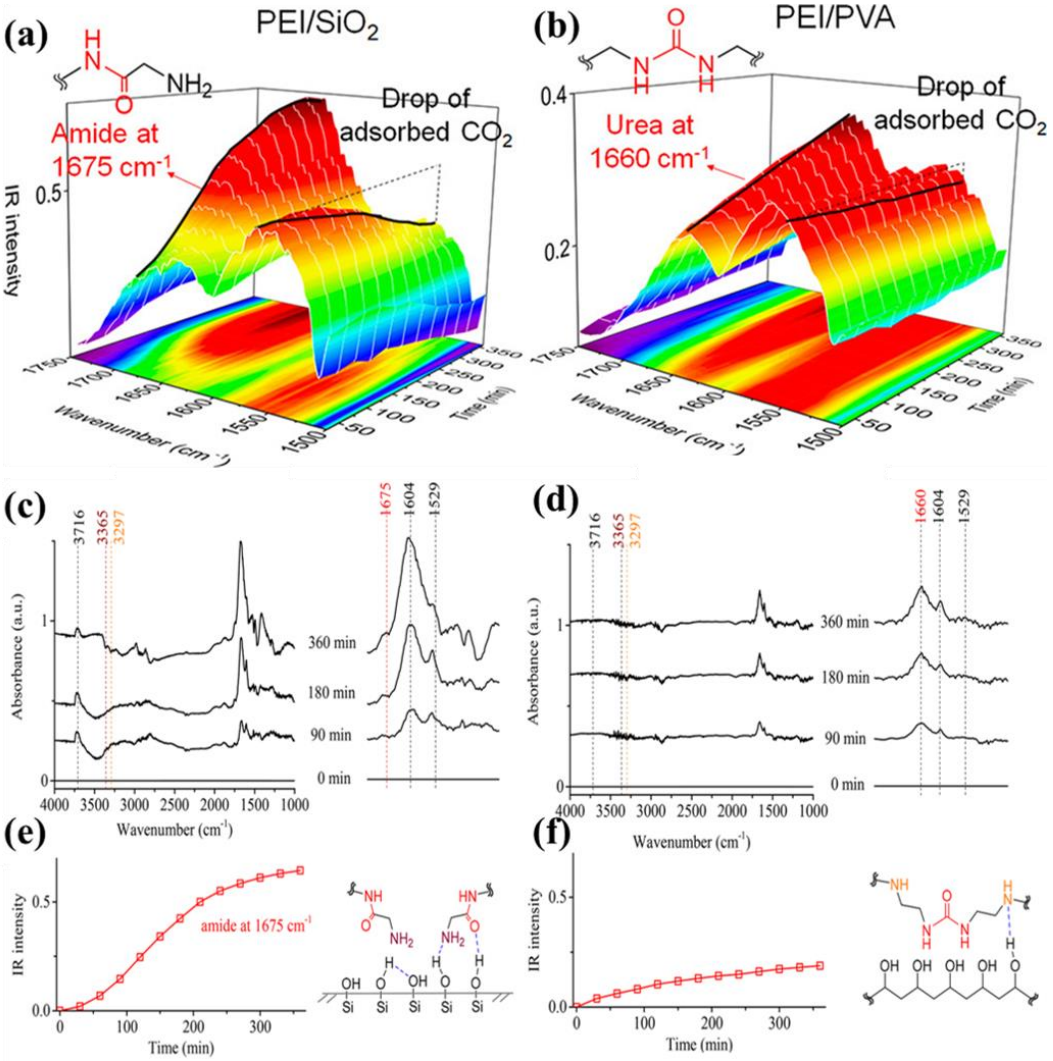

Fig. 30 (a) 3D color map of the IR spectra of adsorbed CO_2 on (a) PEI/SiO_2 and (b) PEI/PVA obtained only from the adsorption process of 12-cycle adsorption/degradation. Degraded species obtained following degradation at 130 °C and cooling to 40 °C on (c) PEI/SiO_2 and (d) PEI/PVA. IR spectral intensities of the degraded species on (e) PEI/SiO_2 at 1675 cm^{-1} (amide) and (f) PEI/PVA at 1660 cm^{-1} (urea) (Reproduced from ref. 396 with permission from American Chemical Society, copyright 2017).

3.4. Epoxidation of primary and secondary amines

To resolve the stability puzzle of PEI-modified adsorbents and further improve their oxidative resistance, Choi *et al.*[387] first utilized 1,2-epoxybutane (EB) to suppress the oxidative degradation and urea formation of PEI (**Fig. 31**a). Liquid-phase ^{13}C NMR analysis proved that functionalization with EB selectively converted primary amines to secondary amines as well as tertiary amines (**Fig. 31**b). After the oxidative

treatment conducted in synthetic air (20% O_2/N_2) for 24 h, the PEI/SiO_2 with EB showed enhanced oxidative stability. FTIR spectra suggest that no new infrared peak of the C=O species appears on PEI/SiO_2 with EB after oxidative aging (**Fig. 31**c).

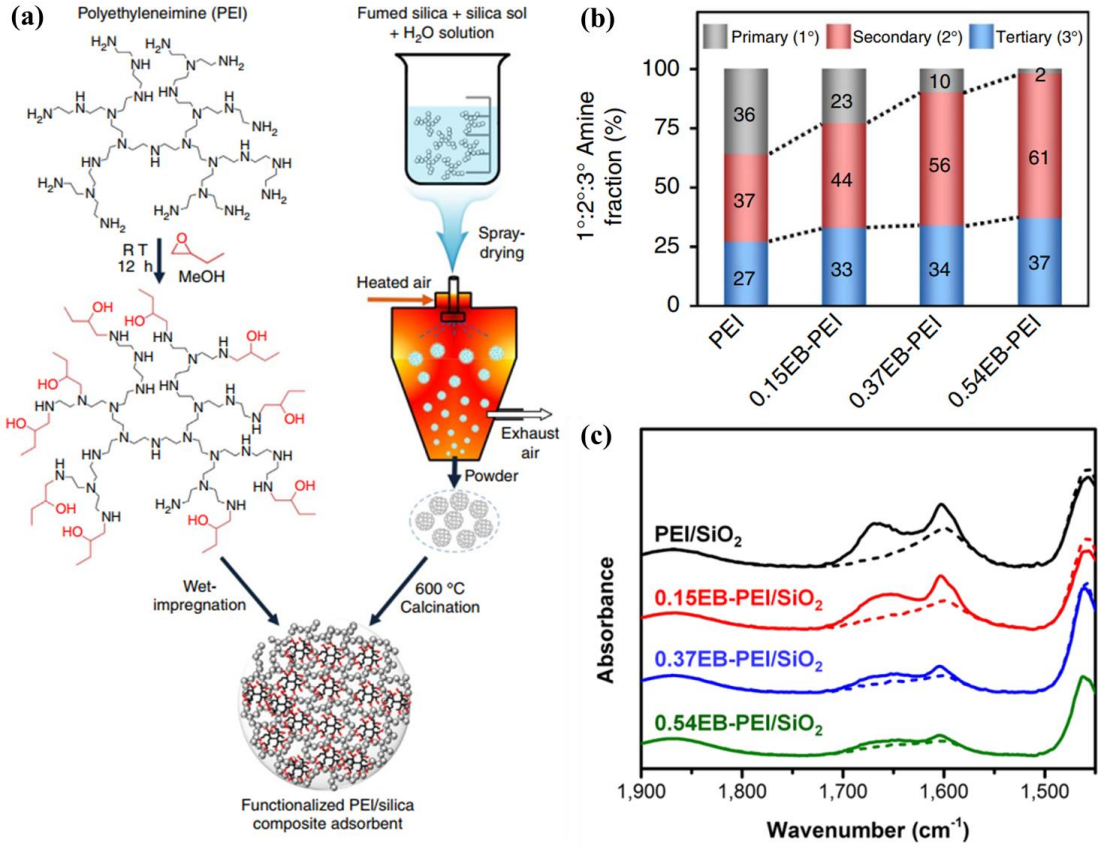

Fig. 31 (a) Schematic of the scalable synthesis of the CO_2 adsorbent. (b) Amine state distributions of PEI and functionalized PEIs analyzed by ^{13}C NMR. PEI was functionalized with EB, which generated tethered 2-hydroxybutyl groups. (c) FTIR spectra of the adsorbents that were measured after pre-treatment in synthetic air (20% O_2 in N_2) at 120 °C over 24 h in an *in situ* IR cell. Dashed lines indicate the spectra of the fresh samples, while solid lines indicate those of the pre-treated samples (Reproduced from ref. 387 with permission from Springer Nature, copyright 2016).

The enhanced stability of PEI/SiO_2 with EB might be attributed to the increased ratio of secondary amines at the expense of primary amines or the formation of hydrogen bonds between the generated hydroxyl (−OH) groups (**Fig. 32**a).[397] Furthermore, polymeric amines usually contain ppm-level metal impurities, such as Fe and Cu, which possibly catalyze amine oxidation.[397] Adding a small amount of chelators (<2 wt.%) into silica support before the impregnation of PEI avoid the negative influence of metal impurities. After 30-

days oxidative aging under 3% O_2, 15% CO_2, 10% H_2O in a N_2 balance at 110 °C, EB-PEI/SiO_2 with Na_3PO_4 (trisodiumphosphate, TSP) still retained 91.5% of the initial capture capacity because of the lower polarity (**Fig. 32**a and b).[397]

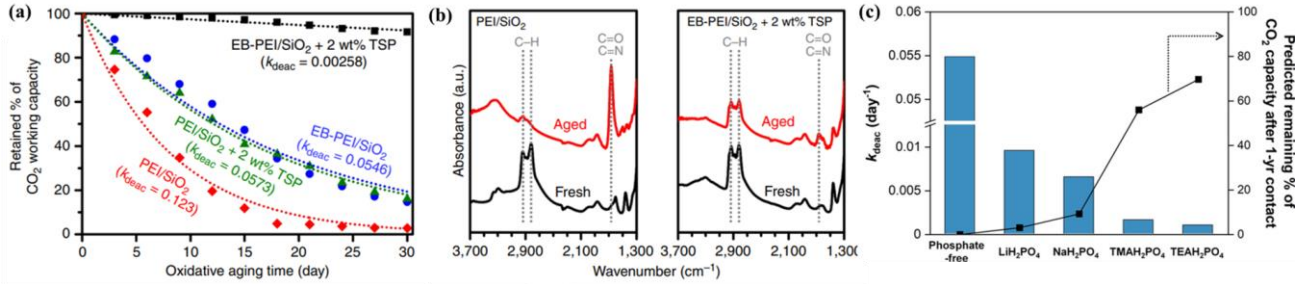

Fig. 32 (a) Retained CO_2 working capacity (%) of PEI/SiO_2 and EB-PEI/SiO_2 prepared with and without 2 wt.% TSP after aging under 3% O_2, 15% CO_2, 10% H_2O, and 72% N_2 at 110 °C. The trend lines were obtained by fitting the first-order deactivation model. (b) FTIR spectra of PEI/SiO_2 without TSP and EB-PEI/SiO_2 with 2 wt.% TSP, before and after 30 d of aging (Reproduced from ref. 397 with permission from Springer Nature, copyright 2018). (c) First-order deactivation rate constants (indicated with bars) and predicted remaining CO_2 adsorption capacity (in %) after 1 yr contact with flue gas at 110 °C (indicated in solid lines) (Reproduced from ref. 398 with permission from American Chemical Society, copyright 2021).

Choi's groups further investigated the amine-stabilization effects of monocationic phosphate salts containing cations of different charge densities, such as Li^+, Na^+, tetramethylammonium (TMA^+), and tetraethylammonium (TEA^+).[398] According to the long-term oxidative stability test (**Fig. 32**c), the adsorbent with organophilic $TEAH_2PO_4$ showed the highest stability with a very minor decrease in CO_2 capacity (<3.5%) even after 1 month of aging in O_2-containing flue gas (15% CO_2, 3% O_2, and 10% H_2O in N_2 balance) at 110 °C. Organophilic phosphates are believed to be better dispersed and loosely associated with the ion pair within organic amine polymers, which is beneficial for binding with metal impurities (Fe and Cu).

Although supported TEPA and PEHA usually exhibit high CO_2 capture capacity and low manufacturing cost, they always encounter vitalization and leaching problems owing to their low molecular weight, and therefore suffer from stability problems. Goeppert *et al.*[127] proposed the modification of low molecular weight amines, such as TEPA and PEHA, by the epoxide of propylene oxide (PO). The reaction between

the modified low molecular weight amines and PO during the synthesis process is shown in **Fig. 33**a, and the intramolecular addition of OH groups can be observed. After 20-hour treatment in air, the PO-modified TEPA- and PEHA-based silicas exhibited excellent oxidative resistance compared to adsorbents without PO modification.

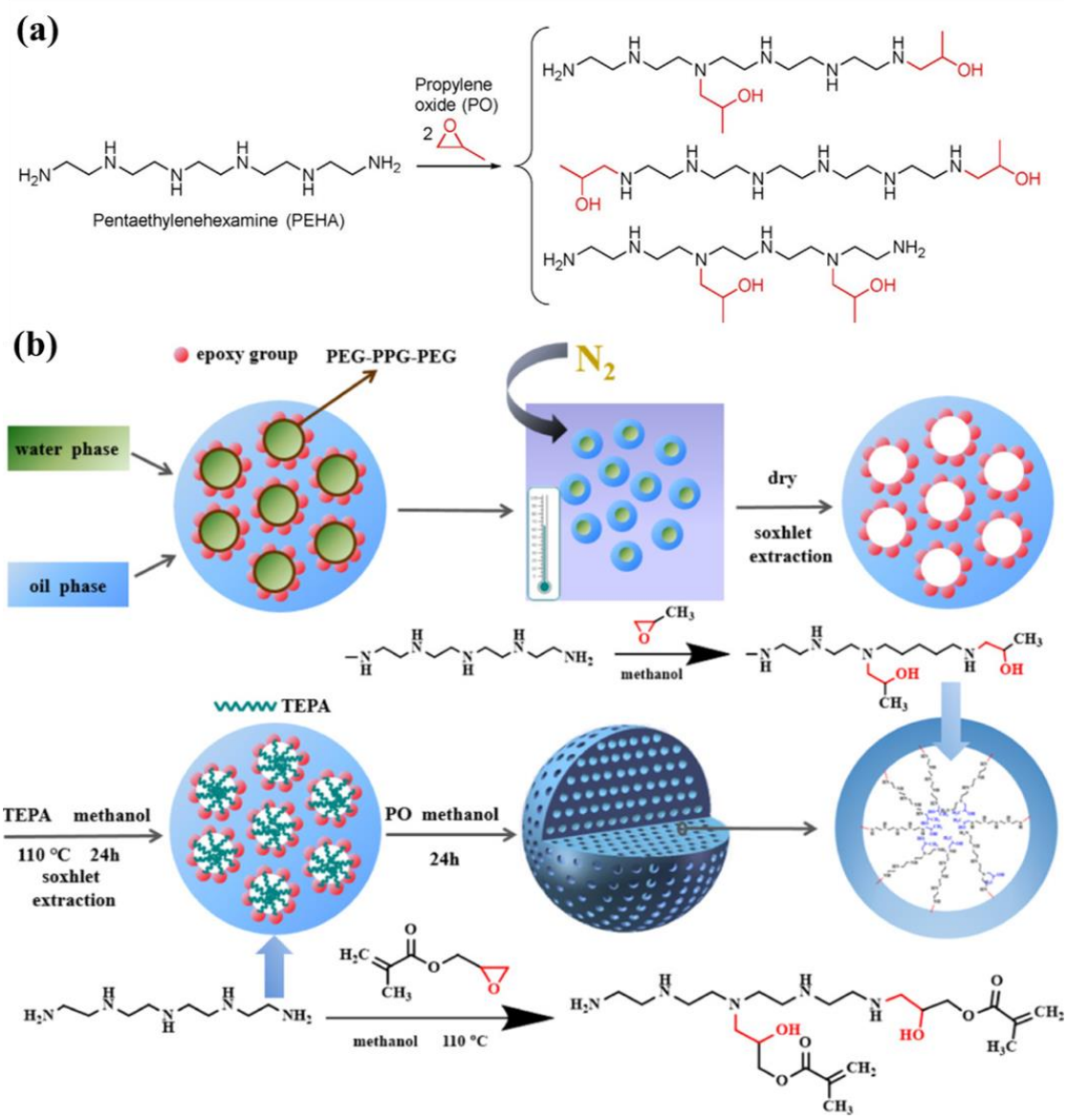

Fig. 33 (a) Examples of reaction products of PEHA with two molar equivalents of PO (Reproduced from ref. 127 with permission from John Wiley and Sons, copyright 2019). (b) Schematic of the preparation process of PG−TEPA−PO (Reproduced from ref. 165 with permission from American Chemical Society, copyright 2020).

In addition, Guo *et al.*[165] reported epoxide functionalization of grafted TEPA on the framework of an

acrylate copolymer (PG-TEPA-PO) with improved oxidative degradation resistance (**Fig. 33**b). It was observed that epoxide functionalization could decrease the ratio of primary amines, which contributed to the improved anti-oxidation performance, although it was inevitable to sacrifice the adsorption capacity to some degree.

Epoxidation was proven to improve the oxidative stability by sacrificing some CO_2 uptakes for capturing pure CO_2 or flue gas. However, the effect of epoxidation on the performance of adsorbents for DAC remains unknown. Thus, achieving a balance between decreased CO_2 uptake and enhanced oxidative stress via epoxide introduction for DAC will be an interesting research topic.

3.5. Additive incorporation

Chuang *et al.*[379,380,386,396] also attempted to improve the performance of supported TEPA (TEPA/SiO_2), especially in terms of oxidative stability, by modifying TEPA with PEG. Comprehensive spectroscopic investigations were carried out to identify the mechanism of the enhanced oxidative resistance by PEG during the 12-hour treatment under air flow at 100 °C. They proposed that the hydrogen bonds, which were formed by the OH groups from PEG interacting with the NH_2/NH of TEPA, are beneficial for the dispersion of TEPA on SiO_2 and block O_2 from accessing TEPA for oxidation.

To the best of our knowledge, most recent studies have focused on the effect of additives on improving the oxidative resistance of adsorbents under high CO_2 concentration conditions, and there are few reports on DAC conditions. Given that the performance of amine-functionalized adsorbents after oxidation under fuel gas and DAC conditions is varied,[114,129] the effect of additives on the oxidative stability of adsorbents to capture CO_2 at ultralow concentrations requires further comprehensive investigation.

4. Cooperative adsorption of H_2O and CO_2

Porous solid sorbents not only capture CO_2 selectively but also adsorb significant amounts of H_2O from the air. Because ambient air contains more H_2O than CO_2, the co-adsorption of H_2O and CO_2 is non-negligible. H_2O may promote or inhibit the CO_2 capture ability depending on the type of adsorbent and may even affect the long-term stability of the adsorbents. The co-adsorption of H_2O also leads to an increase in energy consumption for regeneration.[132,399] Consequently, understanding the effect of H_2O on CO_2 adsorption and exploring the co-adsorption mechanism of H_2O and CO_2 is critical for the screening of adsorption materials, design of adsorption cycles, and optimization of the DAC system.

Over the past several years, much research has been conducted on the effects of H_2O co-adsorption on amine-functionalized sorbents. Previous studies have indicated that H_2O affects the adsorption of CO_2, but the presence of CO_2 does not significantly affect the adsorption of H_2O.[108,277,399] While several studies on the development of new adsorbent materials have explored their adsorption properties in the presence of H_2O, little is known about the detailed mechanism of the interaction between H_2O and CO_2.

In an early study, Gebald *et al.*[277] explored the single and binary CO_2/H_2O adsorption of amine-functionalized NFC under DAC conditions, modeled the adsorption isotherm, and calculated the corresponding adsorption heats. However, the total mass loss in the TGA caused by the desorption of H_2O or CO_2 was indistinguishable. To determine the influence of H_2O and CO_2, Smal *et al.*[400] proposed a method based on a coupled TG-FTIR analysis system to characterize the adsorption capacity of adsorbents for H_2O and CO_2. Such a simple method can be used for preliminary comparison and screening of laboratory-scale adsorbents (10–20 mg).

In terms of adsorbent materials, Madden *et al.*[401] evaluated the CO_2 capture capacity of ten physical sorbents, including four hybrid ultramicroporous materials, five MOFs, and an ultramicroporous MOF. They found

that the presence of H_2O inhibited the adsorption performance of the physical sorbents, which could be alleviated by controlling the pore size and pore chemistry. In contrast, the presence of H_2O leads to the enhanced CO_2 adsorption performance of amine-functionalized adsorbents.[108,113,185] In addition, Kwon *et al.*[108] investigated the effect of H_2O on the CO_2 adsorption of aminopolymer-impregnated hierarchical silica adsorbent and found that the CO_2 adsorption capacity increased with increasing adsorption temperature under dry conditions and decreased with increasing adsorption temperature under wet conditions. They explained that the presence of H_2O alleviated the kinetic constraints of the aminopolymer sediments. Sujian *et al.*[185] reported that the presence of H_2O increased the pseudoequilibrium CO_2 capacity of a PEI-CA-SiO_2 fiber adsorbent from 0.59 mmol g_{fiber}^{-1} under dry conditions to 1.6 mmol g_{fiber}^{-1} under humid conditions at 35 °C. The CO_2 breakthrough and equilibrium capacities remained largely unchanged after multiple humid breakthrough cycles. They demonstrated that the presence of H_2O leads to the release of additional free amine groups, resulting in the formation of more carbamate ions and bicarbonates. Kumar *et al.*[113] measured the adsorption properties of 60 wt.% alkyl-aryl polyamine impregnated SBA-15 under dry and 30% relative humidity conditions and found that the equilibrium CO_2 capacity increased from 1.6 mmol g_{SiO2}^{-1} to 2.9 mmol g_{SiO2}^{-1}, which was equivalent to an 81% increase.

The various effects of moisture on the adsorption performance of amine-functionalized materials under different temperature conditions and moisture levels may suggest a change in the binding force of CO_2 to the amine sites or the generation of new species.[135] Recent work discussed the methods to investigate the effect of H_2O on CO_2 adsorption, including thermogravimetric analysis, dynamic column-breakthrough technique, and static multicomponent equilibrium adsorption.[100] The effect of H_2O on CO_2 adsorption of various materials, such as physical adsorbents, amine-functionalized adsorbents, and reactive adsorbents, were comprehensively summarized. On this basis, Bitan Ray *et al.*[402] reviewed the materials and innovative

strategies for capturing CO_2 under humid conditions and concluded that the stability and CO_2 adsorption capacity of materials could be improved by adjusting their overall properties, such as hydrophobicity, porosity, and amine modifications.

Qualitative analysis of the influence of H_2O is not sufficient for the optimization of the DAC process and reduces energy consumption. As mentioned earlier, most studies have shown that H_2O can increase the equilibrium adsorption capacity of amine-functionalized sorbents to CO_2. However, mathematical descriptions of the enhanced CO_2 and H_2O co-adsorption are poorly understood, leading to inaccurate modeling. In the past five years, quantitative studies have been conducted on the co-adsorption of H_2O and CO_2 from molecular models,[403] adsorption equilibrium,[136,177,277,404,405] and adsorption kinetics.[134,406] Buijs *et al.*[403] studied the molecular modeling of Lewatit R VP OC 1065 and concluded that carbamic acid is mainly formed by amine or amine-H_2O catalytic reactions in the presence of CO_2 and H_2O. Wurzbacher *et al.*[405] used a temperature-dependent Toth model to describe the CO_2 adsorption isotherm under dry conditions and combined it with an enhancement factor to express the effect of humidity. Nevertheless, this enhancement factor was obtained through four measurements of bilinear interpolation; therefore, this model cannot accurately describe the co-adsorption of H_2O and CO_2. Similarly, Stampi-bombelli *et al.*[177] described the adsorption equilibrium on NFC by proposing empirical adjustments to the pure Toth model and introducing two parameters describing the adsorption equilibrium based on Wurzbacher's model. In contrast to most of the previous studies being empirical models, Young *et al.*[136,404] recently developed two novel approaches to modeling the co-adsorption of CO_2 and H_2O onto chemical adsorbents: the mechanistic co-adsorption model and weighted-average dual-site Toth (WADST) co-adsorption model, and accurately predicted the co-adsorption performance on the Lewatit R VP OC 1065 (**Fig. 34**). The former considers the variation in amine efficiency, change in adsorption heat, and effect of amine site blocking by adsorbed H_2O

molecules, while the latter is a more general empirical model.

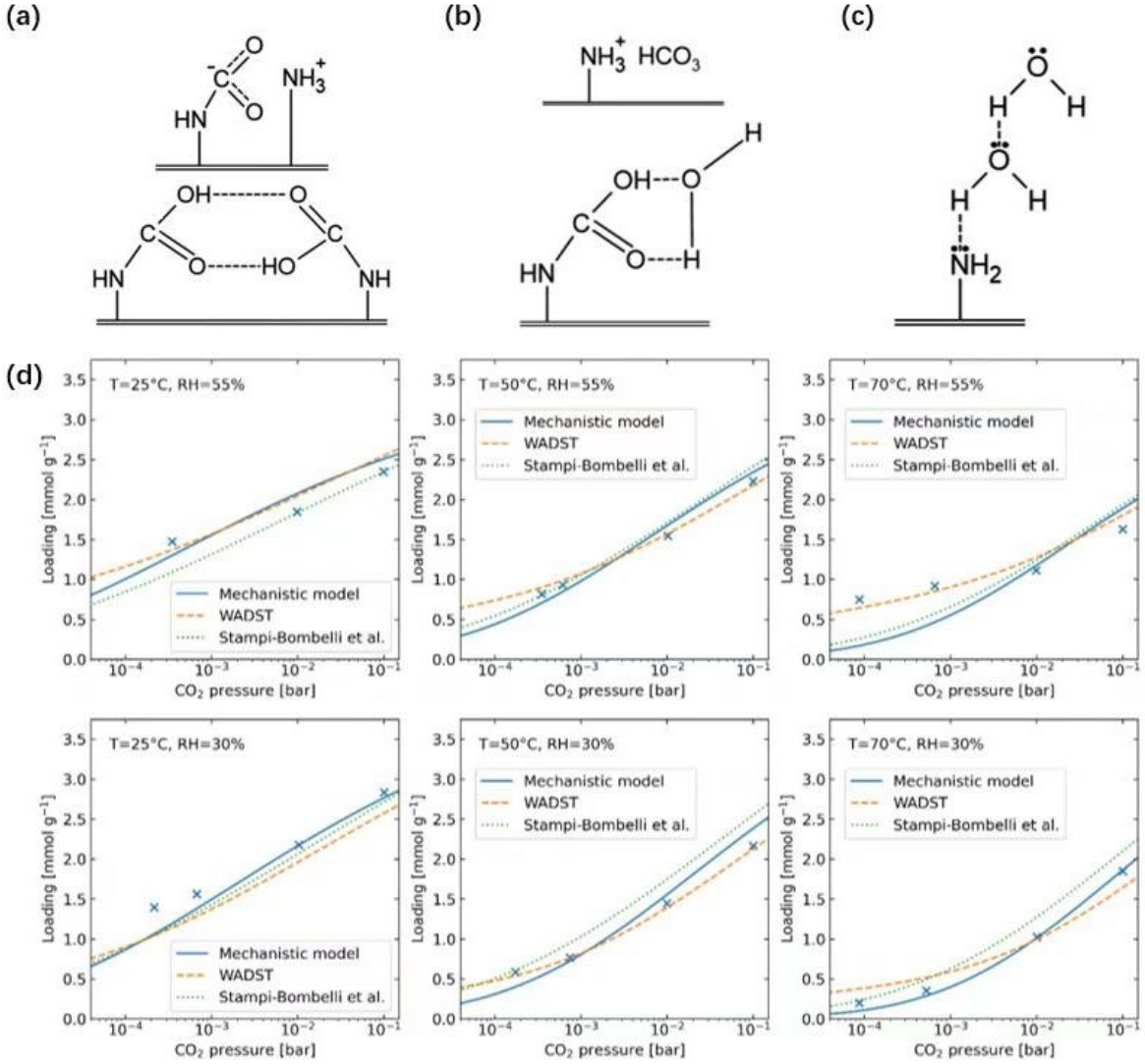

Fig. 34 (a–c) Three governing mechanisms: (a) species that adsorb CO_2 as on amine-functionalized sorbents in the absence of water, including ammonium carbamate and paired carbamic acid; (b) additional species that adsorb CO_2 as on amine-functionalized sorbents in the presence of water, including ammonium bicarbonate and water-stabilized carbamic acid; (c) hydrogen bonding between water and the supported amine groups. (d) Experimental co-adsorption CO_2 isotherms (markers), at various temperatures (T) and relative humidities (RH), fitted to an empirical literature co-adsorption model.[136]

Amine-functionalized solid adsorbents require additional energy consumption during regeneration to desorb H_2O and separate it from CO_2 via condensation. Therefore, the DAC system design requires a detailed understanding of both the co-adsorption equilibrium and the kinetics of CO_2 and H_2O to determine the parameters driving the process under the given conditions. Although these data can be acquired by

packed-bed reactors, TGA, and volumetric adsorption systems, Ng *et al.*[134] suggested that measurements of the co-adsorption kinetics of CO_2 and H_2O are influenced by external heat and mass transfer effects. Therefore, they developed a closed-loop experimental setup to investigate the co-adsorption kinetics of amine-functionalized NFC under DAC conditions without external heat and mass transfer interference using a gas-mixing tank and a differential sorbent bed placed outside it. Later, Elfving *et al.*[406] proposed a kinetic model for CO_2 adsorption from air by amine-functionalized resins under dry and humid conditions, which is based on a different CO_2 adsorption mechanism than that of other amine-functionalized adsorbents. Their work filled the gaps between mechanistic theory and kinetic data of the co-adsorption of CO_2 and H_2O on amine-functionalized sorbents.

Studies have also been conducted on the effect of co-adsorption on energy consumption and economic analysis of the entire DAC process. The pioneering DAC process modeling work conducted by Sinha *et al.*[178] considered contactors coated by two amine-based adsorbents and were operated using steam as the stripping agent. However, they did not consider the co-adsorption of H_2O and CO_2, which led to inaccurate models and economic analyses. Subsequent researchers considered co-adsorption in the design of the DAC process, demonstrated the feasibility of steam purging for solid amine adsorbents, and quantitatively determined the effect of co-adsorption of H_2O and CO_2 on the working capacity and energy demand.[133,180] These studies confirmed that co-adsorbed H_2O would increase the working capacity of CO_2 and reduce the energy demand for desorption. Wijesiri *et al.*[137] further demonstrated that the steam-assisted process resulted in superior CO_2 adsorption/desorption kinetics. Compared to the average desorption rate of 0.23 mmol g^{-1} h^{-1} of conventional DAC process under the same conditions, the fastest average desorption rate of the steam-assisted process could reach 3.75 mmol g^{-1} h^{-1}.

Despite the first attempt to predict the co-adsorption performance of Lewatit R VP OC 1065 for DAC using

mechanistic models,[136] the universal applicability of accurate co-adsorption models to other types of amine-functionalized adsorbents has not yet been verified. Material development in the area of DAC is very fast; therefore, it is urgent to screen the co-adsorption properties of H_2O and CO_2 on new amine-functionalized materials with more efficient experimental and simulation tools.

5. Mechanism study

Although solid amines have been widely recognized as promising DAC adsorbents with significant CO_2 capture capacity and selectivity, their CO_2 adsorption mechanisms remain unclear. Recent studies have provided new evidence for the unexplained existence of adsorbed CO_2 species on amines. FTIR spectroscopy is a leading tool for elucidating the pathway of CO_2 adsorption by evaluating the intensity variations of the amine and product. Zhai *et al.*[139] conducted a series of *in situ* FTIR studies on TEPA/SiO_2, concluding that ammonium carbamate preferentially forms on primary amines through the proton migration of zwitterions, followed by carbamic acid formation on the secondary amines (**Fig. 35**). The former adsorbed species exhibited higher bond energy and tended to constitute a hydrogen-bonded network. High CO_2 concentrations are required to overcome such diffusion barriers for further access of CO_2 to the amine sites. They also suggested that CO_2 from air (400 ppm) could compete with H_2O (0.5%) for adsorption on amines. However, results from DFT calculations suspect the existence of zwitterions on solid amines.[407] Proton transfer/exchange is more likely accomplished through a six-membered mechanism assisted by a Brønsted base.

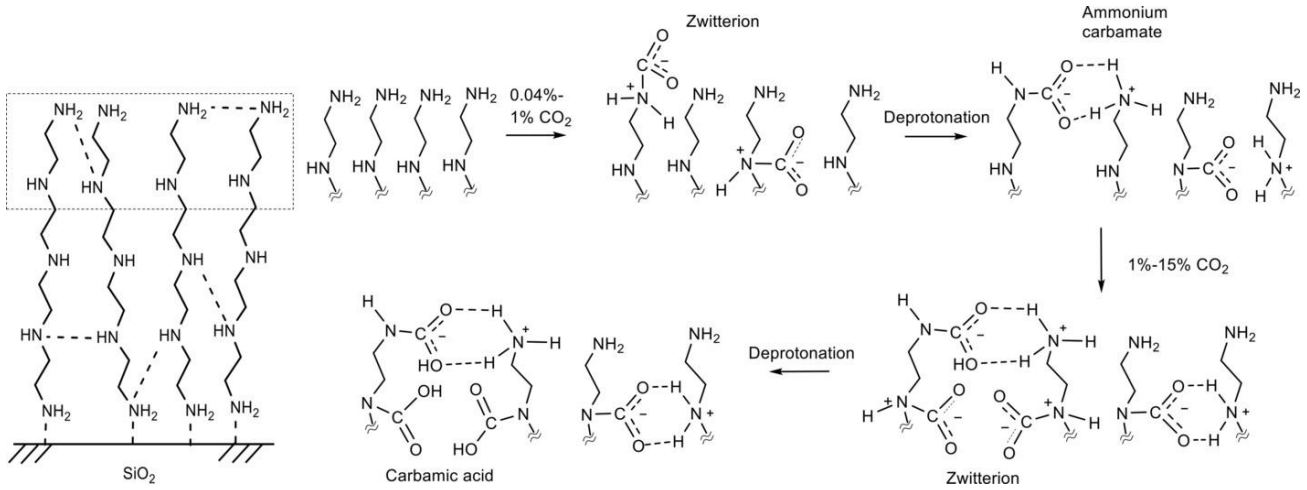

Fig. 35 CO_2 adsorption pathway on supported TEPA (Reproduced from ref. 139 with permission from John Wiley and Sons, copyright 2017).

Several groups have reported the detection of ammonium bicarbonate on solid amines upon reaction with CO_2 in the presence of H_2O; however, they commonly assign inconsistent infrared bands to the bicarbonate. This leads to some doubt regarding the existence of bicarbonate.[408–410] Solid-state NMR is a powerful alternative for species identification. Many researchers have observed ^{13}C resonances at around 160–161 and 164–165 ppm upon CO_2 adsorption, indicating the formation of carbamic acid and carbamate, respectively.[149,411–413] These species were identified on grafted primary amines via ^{15}N NMR at 88 ppm.[414] In fact, ^{29}Si NMR had also been applied to accurately determine the amine loadings.[118,279] Unfortunately, NMR is challenging for bicarbonate identification, partly because the bicarbonate resonance is sensitive to the environment[415] and is sometimes even shielded by other product resonances.[416] Interestingly, when shifting the ^{13}C NMR sequence from the routine CPMAS to MAS Bloch decay, a bicarbonate resonance at 163 ppm was clearly observed on both DMAPS-and APS-grafted mesoporous silica (**Fig. 36**).[141] Further experiments proved that the bicarbonate signal on CPMAS could only be detected at very low temperatures after arresting its dynamic motion due to the surrounding water. These findings demonstrated the possibility of inadvertently missing CO_2 chemisorption products using the most frequently employed experiments.

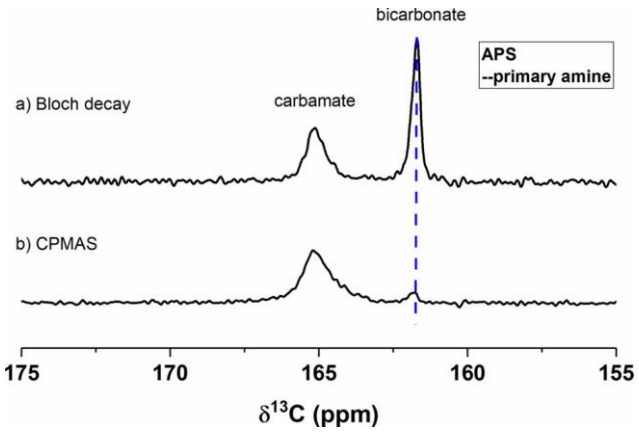

Fig. 36 *In situ* ^{13}C NMR spectra suggesting "missing" bicarbonate groups (Reproduced from ref. 141 with permission from American Chemical Society, copyright 2018).

The nature of the surface carbonaceous species also depends on the amine type. *In situ* FTIR spectroscopy with the aid of isotope labeling suggested that both monomeric and dimeric carbamic acids appeared on the secondary amine, while only monocarbamic acid formed on the primary amine (**Fig. 37**).[417] These carbamic acids were stabilized by different surface groups due to steric hindrance by additional alkyl chains. $^{13}CO_2$ experiments also revealed two carbamate species on primary amines, and only one was detected on secondary amines. Additionally, bicarbonate can be formed on all three types of amines but it is difficult to observe on primary and secondary amines. Afonso *et al.*[138] provided molecular-level understanding of all possible CO_2 adsorbed species on aminosilica surfaces by combining NMR experimental evidence and DFT modeling. Their theoretical calculations support the formation of bicarbonate under wet conditions, although carbamic acid with a Gibbs energy 12 kJ mol^{-1} higher was favored in some samples. The presence of surface-bonded carbamate and ditethered carbamic acid, postulated from spectroscopic observations, was thermodynamically unfavorable. Overall, ammonium carbamate and carbamic acid with various conformations were the predominant CO_2 species under the DAC conditions. The same group also extended the discussion on moisture-induced CO_2 chemisorption, suggesting that the energetically stable CO_2 adsorbed species on the primary and tertiary were different.[140]

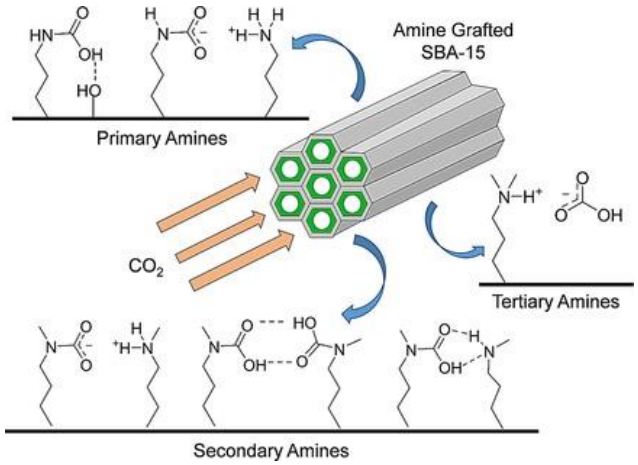

Fig. 37 Formation of CO_2-adsorbing species on primary, secondary, and tertiary amines (Reproduced from ref. 417 with permission from American Chemical Society, copyright 2018).

Buijs *et al.*[142,143,403,418] conducted a series of molecular modeling studies to elucidate the preferred CO_2 adsorption mode and deactivation mechanism on a commercial adsorbent, Lewatit R VP OC 1065, with benzyl amine groups. They suggested that carbamic acid predominantly forms in the presence of CO_2 and H_2O through amine or amine-H_2O catalytic reactions (**Fig. 38**a and b).[403] This conclusion was supported by CO_2 adsorption isotherms, which could be described well by the dual-site Langmuir model. One detrimental effect on the application of Lewatit R VP OC 1065 is the deactivation caused by either the presence of O_2 at 80 °C or CO_2 at 120 °C.[393] A three-step process was then proposed to explain the CO_2-induced deactivation (**Fig. 38**c).[142] At high CO_2 partial pressures and temperatures, carbamic acid was formed through a self-catalyzed reaction. Carbamic acid then decomposed to an isocyanate intermediate with an activation barrier of 144.4 kJ mol^{-1}. Finally, the highly reactive isocyanate transformed into an irreversible urea species after coupling with another amine group. Oxidative degradation of Lewatit R VP OC 1065 initiated with the formation of α-amino-benzyl hydroperoxides, followed by its decomposition to the corresponding amide and half-aminal (**Fig. 38**d).[143] The half-aminal was further predominantly solvolyzed to an aldehyde. The thermal decomposition of hydroperoxides caused a loss of CO_2 capacity because the yield sites could not capture CO_2. Recently, Buijs also demonstrated the decisive role of the

structure of solid amines in the CO_2 capture mechanism, indicating that carbonic acid might also be the main form of linear PEI.[418]

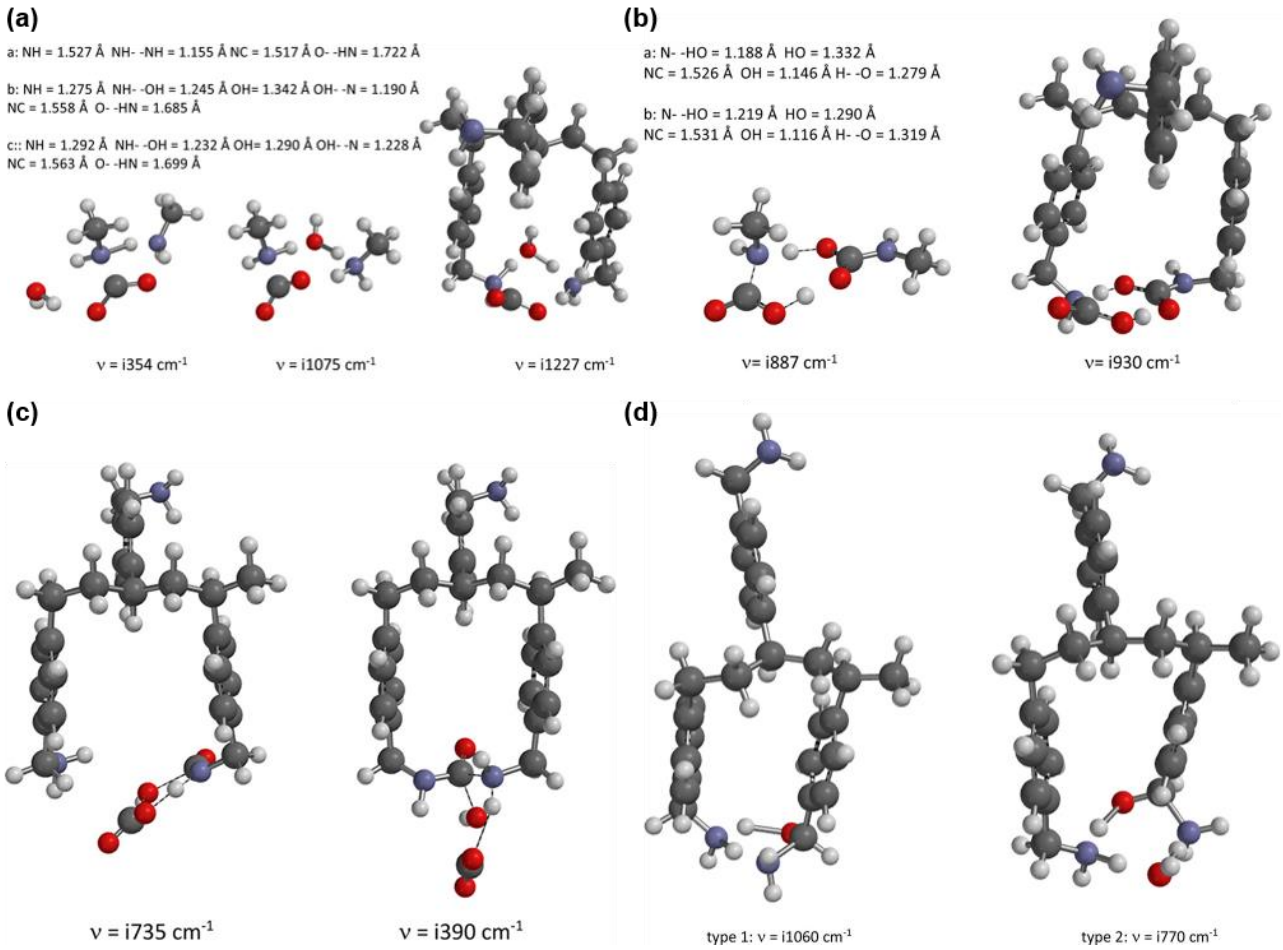

Fig. 38 Formation of carbamic acid in the presence of CO_2 and H_2O through (a) amine-H_2O catalytic reactions and (b) amine catalytic reactions (Reproduced from ref. 403 with permission from American Chemical Society, copyright 2017). (c) Formation of an isocyanate intermediate (Reproduced from ref. 142 with permission from American Chemical Society, copyright 2019). (d) Aminolysis of the half-aminals (Reproduced from ref. 143 with permission from American Chemical Society, copyright 2019).

Despite the straightforward involvement of species such as carbamic acid, ammonium carbamate, and/or bicarbonate, the CO_2 interaction mechanisms with amines under ultradilute conditions are still not fully understood. Specifically, it needs further investigation on the role of hydrogen bonding as a CO_2 binder to reduce energy barriers and enhance the stability of products, the effect of densities and types of surface amines on CO_2 adsorbed species and capacity, the inconsistency of real amine efficiency to the theoretical value, the difference in CO_2 capacity enhancement upon exposure to H_2O, and the formation pathway of

CO_2 adsorbed species on amines under complicated structures and orientations. Recent advances have illustrated that integrating *in situ* spectroscopy and theoretical calculations is an effective approach to unravel the nature of adsorbed CO_2.

6. Novel amine-functionalized adsorbents

6.1. Diamine-tethered metal-organic frameworks

M_2(dobpdc) (M = Mg, Mn, Fe, Co, Zn; dobpdc^{4-} = 4,4-dioxido-3,3-biphenyldicarboxylate), a new family of isostructural MOF with large pore size and high density of open metal sites, has received significant attractive for amine functionalization. The amine-tethered M_2(dobpdc) demonstrated superior CO_2 capture performance to that of other solid sorbents under DAC conditions.[419] In particular, it showed high CO_2 selectivity even under humid conditions and received significant attention after the mmen−Mg_2(dobpdc) (mmen = N,N′-dimethylethylenediamine, containing two secondary amines) displayed an exceptional CO_2 capacity (2.0 mmol g^{-1} @ 0.39 mbar, 25 °C).[420] In a later work, en−Mg_2(dobpdc) (en = ethylenediamine, containing two primary amines) was found to exhibit an even higher capacity (2.83 mmol g^{-1} @ 0.39 mbar, 25 °C).[421]

Unlike conventional Langmuir-type adsorption, amine-tethered M_2(dobpdc) behaved as 'phase-change' adsorbents, with unusual step-shaped CO_2 adsorption isotherms which shift markedly with temperature and pressure. Because of a cooperative insertion mechanism,[422] which can be represented as CO_2 inserts into each metal-amine bond to form ion-paired ammonium carbamate chains that propagate vertically with the pore wall of the frameworks, large working capacities are achieved under small temperature swings. Moreover, their adsorption step position can be tuned by varying the amine,[421–424] metal molecule,[422] and organic linker.[424,425] Recent work on diamine-tethered MOFs mainly focused on the adjustment of material

properties and enhancement of the cooperative mechanism, especially in humid conditions. Such novel adsorbents have also been tested in fixed bed-based CO_2 separation systems coupled with heat recovery, and their scale-up utilization can be costly than a state-of-the-art MEA capture system.[426]

6.1.1 Enhancement of cooperative adsorption. For a comprehensive synthetic strategy to adjust CO_2 capture capabilities, cumulative datasets are required. Hong *et al.*[427] provided a systematic and comprehensive investigation of three tethered amine primary diamines (en = ethylenediamine, men = 1-methylethylenediamine, and den = 1,1-dimethylethylenediamine). The step pressure was affected by the temperature and showed a decreasing trend with increasing bulkiness of the side groups, which was also observed in later work[149].

Long *et al.*[146] studied nine diamines (1°/2°-, 1°/3°-, and 2°/2°-alkylethylenediamines, 1°, 2°, 3° present primary, secondary, and tertiary amines, respectively) and found that small change of the diamine structure can shift the step pressure for cooperative CO_2 adsorption by over four orders of magnitude at a given temperature. They concluded that steric bulk on the metal-bound amine leads to lower step pressures by destabilizing the diamine-bound phase, while substituents added to the terminal amine cause higher step pressures due to weaker ion-pairing interactions within the ammonium carbamate chains. The 1°/2°-alkylethylenediamines appended variants of Mg_2(dobpdc) were more appropriate for CO_2 capture from dilute gas (40 mbar), giving improved thermal stabilities, lower step pressures, and minimal hysteresis upon CO_2 desorption. In addition to mmen–Mg_2(dobpdc), e-2-e–Mg_2(dobpdc) (e = ethyl, 2 = the number of carbons on the alkyl bridge connecting the amines) was also investigated for DAC recently.[146] Unfortunately, a greater temperature range is required to utilize the full adsorption capacity owing to its two-stage isothermal adsorption line. Two-step CO_2 adsorption/desorption profiles are formed as the substituents on the terminal amine grow (**Fig. 39**a–c), which occurs because diamines bearing large alkyl groups impede

the stabilization of adjacent ammonium carbamate chains in Mg_2(dobpdc).[428]

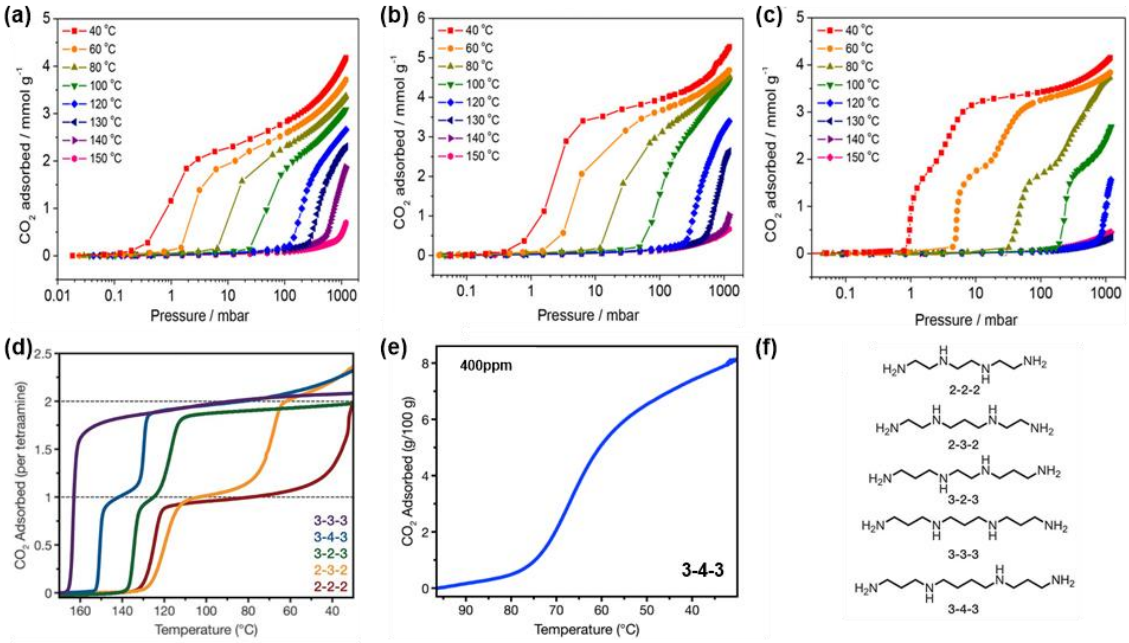

Fig. 39 CO_2 adsorption isotherms of diamine-functionalized Mg_2(dobpdc) by (a) nmen (N-methyl ethylenediamine), (b) een (N-ethyl ethylenediamine), and (c) ipen (N-isopropyl ethylenediamine) in the range of 40–150 °C (Reproduced from ref. 428 with permission from John Wiley and Sons, copyright 2018). CO_2 uptake by tetraamine-Mg_2(dobpdc): (d) pure CO_2 adsorbed isobars at 1 bar. Dashed lines indicate the theoretical adsorption of one or two CO_2 molecules per tetraamine. (e) Thermogravimetric adsorption isobar for (3-4-3)-Mg_2(dobpdc) under 400 ppm CO_2 at a temperature ramp rate of 0.1 °C/min. (f) Tetraamines and their abbreviations (Reproduced from ref. 144 with permission from American Association for the Advancement of Science, copyright 2020).

In practical applications, the working capacity of CO_2 adsorbents and low-pressure adsorption amounts affected by step pressure are more important than the absolute CO_2 adsorption amount. The working capacity of eight diamine−Mg_2(dobpdc) was measured using the TSA protocol from the difference between the adsorption amounts at T_{ads} (adsorption temperature) and T_{des} (desorption temperature).[428] It was found that the working capacity at T_{ads} = 40 °C is correlated with the number of alkyl substituents and alkyl chain length. The thermodynamics of CO_2 adsorption by chiral-diamine-appended Mg_2(dobpdc) has also been studied, and it is affected by enantioselective interactions between the ammonium carbamate chains and the chiral channels of the framework.[147]

Alcoholamine- and alkoxyalkylamine-functionalized variants of Mg_2(dobpdc) are new framework

materials capable of cooperative CO_2 chemisorption, and they are cheaper than diamine-appended MOFs.[150] Similar to diamine–Mg_2(dobpdc) materials, their substituents affect the step temperatures and pressures. For alcoholamine–Mg_2(dobpdc), longer amine alkyl chains generally led to an increase in the adsorption threshold temperature or a decrease in the adsorption threshold pressure.

A family of robust tetraamine-functionalized frameworks that retain cooperativity was also reported by Long *et al.*[144] for CO_2 capture, inspired by the idea that tetraamines could bridge nearest-neighbor metals across the pore with chain lengths of the order of two N-alkylethylenediamines. The frameworks (except (3-3-3)−Mg_2(dobpdc)) exhibited two-step adsorption profiles, with each step corresponding to half of the theoretical capacity of two CO_2 molecules per tetraamine (**Fig. 39**d). (3-4-3)–Mg_2(dobpdc) displays a high CO_2 capacity of approximately 2.0 mmol g^{-1} at 0.40 mbar and 25 °C (**Fig. 39**e), indicating these tetraamine−Mg_2(dobpdc) are also suitable for DAC. Because the size of the alkyl group on the secondary amine increases and affords enhanced stability,[152] these materials can overcome the limitation of diamine volatilization upon regeneration in practical capture processes and enable CO_2 desorption with inexpensive steam. Overall, changing tethered-amines is an important route for designing suitable appended MOFs for CO_2 capture in various applications with different stepped pressures.

Metal molecules and organic parts are one of non-negligible factors in amine-functionalized MOFs. The step pressure of mmen-M_2(dobpdc) shifts following the order of metal-amine bond strength Mg < Mn < Fe < Zn < Co when cooperative adsorption occurs, while mmen-Ni_2(dobpdc) only shows normal Langmuir-type adsorption.[422] This trend can also be observed in other alkylethylenediamine-appended variants, indirectly proving the formation of ammonium carbamate chains.[149] For alcoholamine-M_2(dobpdc) (M = Mg, Mn, Co, Zn, and Ni), only the variants of M^{2+} = Mg exhibit step-like CO_2 adsorption characteristics. Changing the M^{2+} type to tailor the CO_2 capture performance is limited considering the cost and range of

metals which can be used in the synthesis.[150] Mg-based diamine-appended MOFs have obvious advantages in CO_2 adsorption because of the low cost of metal precursor salts, high adsorption capacities, and low step pressures.

The organic components can alert the CO_2 adsorption properties of the functionalized MOFs by changing the pore characteristics. In fact, en−Mg_2(dobdc) [Mg-MOF-74, dobdc = 2,5-dioxido-1,4-benzenedicarboxylate] was previously used to capture CO_2 from simulated ambient air (~1.5 mmol g^{-1} @ 0.40 mbar, 25 °C).[425] The Mg_2(dobdc) channel is too narrow (~11 Å wide) to accommodate the larger amine appended. A later study applied a smaller diamine molecule (N_2H_4) and achieved a record for DAC (3.89 mmol g^{-1} @ 0.40 mbar, 25 °C).[424] However, N_2H_4 is highly toxic that is not possible to be applied for DAC. In comparation, M_2(dobpdc) with a wider channel of 18.4 Å is more suitable for amine tethering.[420] While bulky secondary amine appended Mg_2(dobpdc) exhibit unpromising multi-stepped adsorption, a recent study confirmed the isoreticularly expanded framework Mg_2(dotpdc) (dotpdc^{4-} = 4,4″-dioxido-[1,1′:4′,1″-terphenyl]-3,3″-dicarboxylate) and Mg_2(pc-dobpdc) (pc-dobpdc^{4-} = 3,3′-dioxidobiphenyl-4,4′-dicarboxylate) can achieve a single CO_2 adsorption/desorption step in all cases (**Fig. 40**a–c).[152] Such a change is due to minimize the steric interactions between ammonium carbamate chains induced by the asymmetrical hexagonal pores of Mg_2(dobpdc). The isobar of dmen−Mg_2(dobpdc) features approximately half of the theoretical adsorption capacity at 30 °C. By extending the organic linker, the dmen−Mg_2(pc-dobpdc) can avoid the half-capacity trap (**Fig. 40**d).[429]

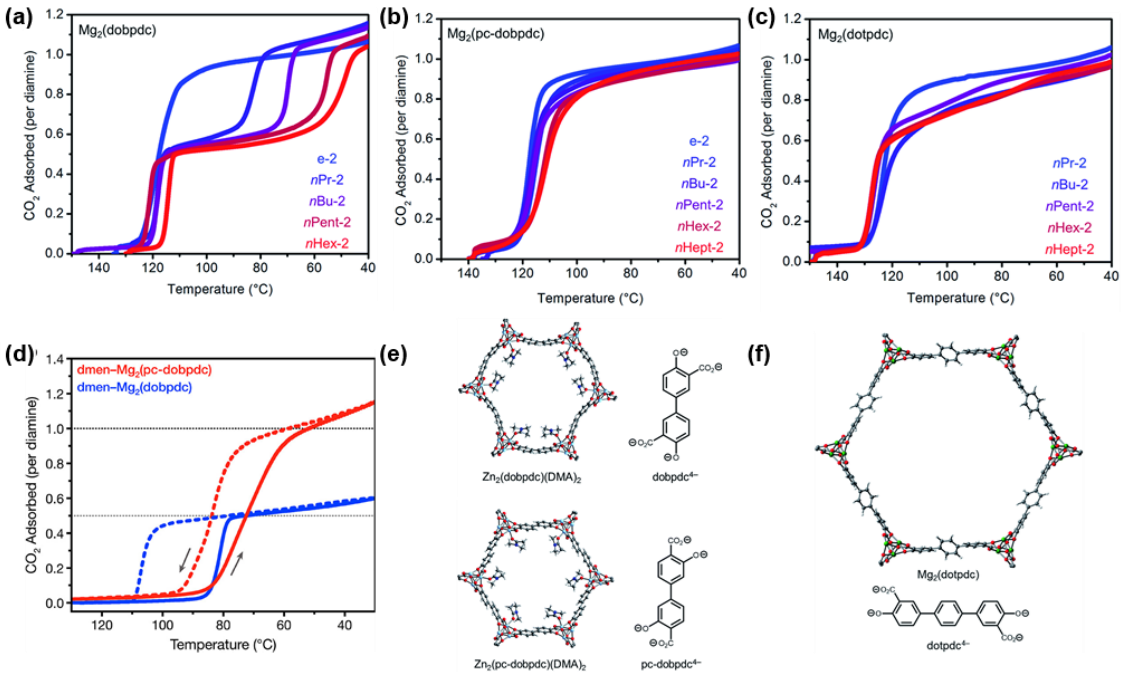

Fig. 40 CO_2 adsorption isobars obtained for (a) Mg_2(dobpdc) and (b) Mg_2(pc-dobpdc) (c) Mg_2(dotpdc) functionalized by a series of primary- and secondary-alkylethylenediamine-appended variants under pure CO_2. (d) Adsorption and desorption data for Mg_2(dobpdc) and Mg_2(pc-dobpdc) functionalized by dmen, indicated with solid and dashed lines, respectively. Gray and black dashed lines indicate half- and full-capacity (4.0 mmol g^{-1}), respectively. Arrows point in the direction of temperature change. (e) Single-crystal X-ray diffraction structures of Zn_2(dobpdc)$(DMA)_2$ (DMA = N,N-dimethylacetamide) (top) and Zn_2(pc-dobpdc)$(DMA)_2$ (bottom) collected at 100 K (note: The structure of the magnesium-based materials is similar). (f) Model of the hexagonal pore of Mg_2(dotpdc) (right). The structures of the ligands are included for comparison. Light blue, green, gray, red, dark blue, and white spheres correspond to Zn, Mg, C, O, N, and H, respectively[152] (Reproduced from ref. 429 with permission from American Chemical Society, copyright 2021).

The synthesis method also significantly affects the properties of amine-tethered MOFs. The general method involves activating MOF by heating to remove coordinated solvent molecules and to generate open metal sites.[430] The MOF with coordinatively unsaturated metal sites is then soaked in non-coordinating solvents, such as dry toluene, together with desirable amines.[431] Functionalization by diamines in the open metal sites can be conducted using different methods, such as stirring or static for a long time and subsequent drying. Recently, Hong *et al.*[427] demonstrated that combining sonication and microwave irradiation is a more efficient method that facilitates the diffusion of diamine into the pores, compared with methods of stirring for 18 h, refluxing for 3 h, sonicating for 3 h, or irradiating in a microwave reactor at 90 °C for 3 h.

They also developed a simple and facile method to stabilize and reinforce amine-tethered MOF adsorbents under wet conditions by placing MOFs and polydimethylsiloxane (PDMS) in a sealed tube followed by heating 235 °C for 6 h.[153] The PDMS-coated epn−Mg_2(dobpdc) (epn = 1-ethylpropane-1,3-diamine) material presented unprecedented and desirable performances to capture CO_2 from indoor (~2.3 mmol g^{-1} @ 1 mbar, up to 98% RH).[186] In addition, MOF spheres with a diameter of 2–3 mm prepared by a hydrophobic polymer binder PVDF (poly(vinylidene fluoride)) and functionalized by epn follow the same CO_2 insertion mechanism, showing one-month stability at 25 °C at 60% RH.[432]

A deeper understanding of the unprecedented cooperative adsorption mechanism of mmen-M_2(dobpdc) was first reported by McDonald *et al.*[422] in 2015. The mechanism of diamine-M_2(dobpdc) such as the dmen-M_2(dobpdc) series[433] and mmen-M_2(dobpdc) series[434] were investigated using more advanced experimental and simulation tools such as van der Waals (vdW)-corrected density functional theory calculations (DFT−D3), single-crystal X-ray diffraction experiments, and quantum chemical methods. The preferred reaction pathway was divided into two steps, where the first step was the rate-determining step. For the cooperative adsorption mechanism of most diamine-appended M_2(dobpdc), each metal atom of M_2(dobpdc) forms an M-N bond with one amine of the diamine, and the other amine is free as a Lewis base. The CO_2 molecule attaches to the free amine and inserts into metal-amine bonds with the help of an adjacent diamine nucleophilic attack to form M−O bonds and C−N bonds, forming the chains of ion-paired ammonium carbamate along the framework channels (**Fig. 41**a). Such reaction path indicates that one diamine takes up to one CO_2 molecule, and the insertion behavior results in the sudden rise in CO_2 capacity by changing the pressure and temperature.

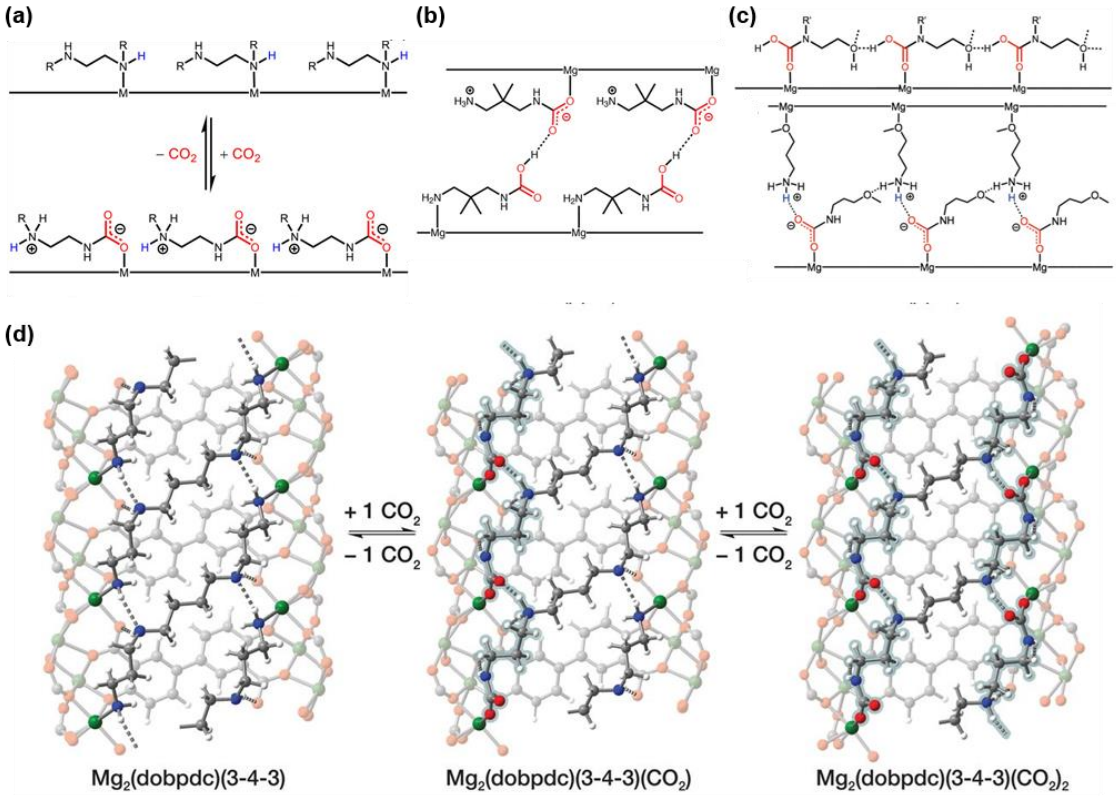

Fig. 41 (a) General structure of alkylethylenediamine-appended variants of M_2(dobpdc) (Reproduced from ref. 149 with permission from American Chemical Society, copyright 2017). (b) Lewis structure with a 1:1 ratio of ammonium carbamate and carbamic acid for the proposed mixed-chemisorption on dmpn−Mg_2(dobpdc) (Reproduced from ref. 145 with permission from American Chemical Society, copyright 2018). (c) Structural model of the CO_2 adsorption mechanism for Mg_2(dobpdc) functionalized by e-2-OH (top) and 3-methoxypropylamine (bottom) (Reproduced from ref. 150 with permission from John Wiley and Sons, copyright 2020). (d) Predicted adsorption mechanism obtained from structural relaxations based on vdW-corrected DFT. Green, dark blue, red, gray, and white spheres represent Mg, N, O, C, and H, respectively (Reproduced from ref. 144 with permission from American Association for the Advancement of Science, copyright 2020).

Recently, Milner *et al.*[149] conducted ^{13}C nuclear NMR and X-ray diffraction and suggested that the CO_2 absorption mechanism of dmpn−Mg_2(dobpdc) was more complicated as expected. The formation of carbamate acid pairs in the first experimental verification could compete with ammonium carbamate to form chains. Subsequently, Forse *et al.*[145] proposed a new mixed chemisorption mechanism of dmpn−Mg_2(dobpdc) according to the NMR and DFT results (**Fig. 41**b). In the presence of CO_2, dmpn−Mg_2(dobpdc) displayed a structure of ammonium carbamate and carbamate acid in a molar ratio of 1:1. The ammonium carbamate and carbamate acid chains propagate along the c-axis. Hydrogen bonds

exist not only on the ammonium carbamate chain but also between the hydrogen in carbamate acid and the unbound oxygen atoms in the adjacent carbamate.

In addition, two new cooperative CO_2 chemisorption mechanisms were found for alcoholamine- and alkoxyalkylamine-functionalized Mg_2(dobpdc) according to the NMR data (**Fig. 41**c).[150] The main feature of the new mechanisms is the insertion of CO_2 molecules into covalent bonds formed by O in the amine and metal in the frameworks.

In situ IR and solid-state NMR spectroscopies verified a two-step adsorption mechanism in tetramine−Mg_2(dobpdc), which is different from adsorption due to steric conflicts between neighboring ammonium carbamate chains (**Fig. 41**d).[144] The initial chemical adsorption of CO_2 was assumed to occur at one amine tethered on Mg atoms, generating ammonium carbamate running along a vertex of the hexagonal channel. The other unreacted binding amine forms a second group of ammonium carbamate chains. Such a unique structure, in which one tetramine is bridged by two metal sites, greatly enhances the stability under steam regeneration conditions.

The kinetic analysis of diamine−Mg_2(dobpdc) is necessary for practical applications. Martell *et al.*[435] systematically investigated the CO_2 adsorption kinetics of diamine–Mg_2(dobpdc) variants under different operating conditions. Most of them exhibited faster adsorption kinetics and shorter induction periods at lower temperatures, contrary to Arrhenius behavior. An unusual induction period, starting from the entry of CO_2 into the furnace to the maximum uptake rate, appeared because of the unique cooperative CO_2 chemisorption mechanisms in diamine−Mg_2(dobpdc). Hughes *et al.*[426] established for the first time a mathematical kinetic model of dmpn−Mg_2(dobpdc) by considering a modified weighted dual-site Langmuir isotherm model and a dual-site Sips isotherm model without the presence of water. They confirmed that dmpn−Mg_2(dobpdc) exhibits better adsorption kinetics at low temperatures. More studies on adsorption

kinetics of various appended amines are still needed.

6.1.2. Effects of water. A series of studies have shown that amine-functionalized MOFs can improve water stability compared to bare MOFs.[422,423] Besides, an early study found that MOF functionalized with alkylamines, especially mmen–Mg_2(dobpdc) frameworks, can also maintain a significant CO_2 capacity and minimal H_2O adsorption under simulated coal flue gas condition.[419] Recently, Darunte *et al.*[187] found mmen−Mg_2(dobpdc) showed higher stability and lower water adsorption at relative humidity up to 40% than mmen-Mn_2(dobpdc). However, the adsorbents exhibited varying degrees of loss in specific surface areas with preserved crystallinity. Siegelman *et al.*[146] showed that although the step pressure of the 1°/3° diamine−Mg_2(dobpdc) is relatively high, it adsorbed less water compared with the frame functionalized with 2°/2° and 1°/2°.

However, both studies only involved one-component adsorption. In the practical applications, it is necessary to investigate the effects of water under multicomponent conditions. Notably, recent studies on amine−Mg_2(dobpdc) frameworks have shown that H_2O enhances the carbamate insertion mechanism as promoter.[144,148,149,152] Milner *et al.*[149] performed multicomponent measurements of CO_2 adsorption by bubbling the incident gas stream through water to study the ability of dmpn−Mg_2(dobpdc) in the presence of water. The adsorbent maintained a high diamine loading of 97% after 1000 adsorption cycles. The cyclic stability of the 1°/2° alkylethylenediamine-appended MOF variants under wet conditions was also studied (**Fig. 42**). It is found that the water co-adsorption was minimal at temperatures above 60 °C, indicating that the water co-adsorption could be minimized in the humid flows at higher temperatures.[148,152] Adding large alkyl groups in the pores of MOF is another potential strategy to minimize water co-adsorption.[152]

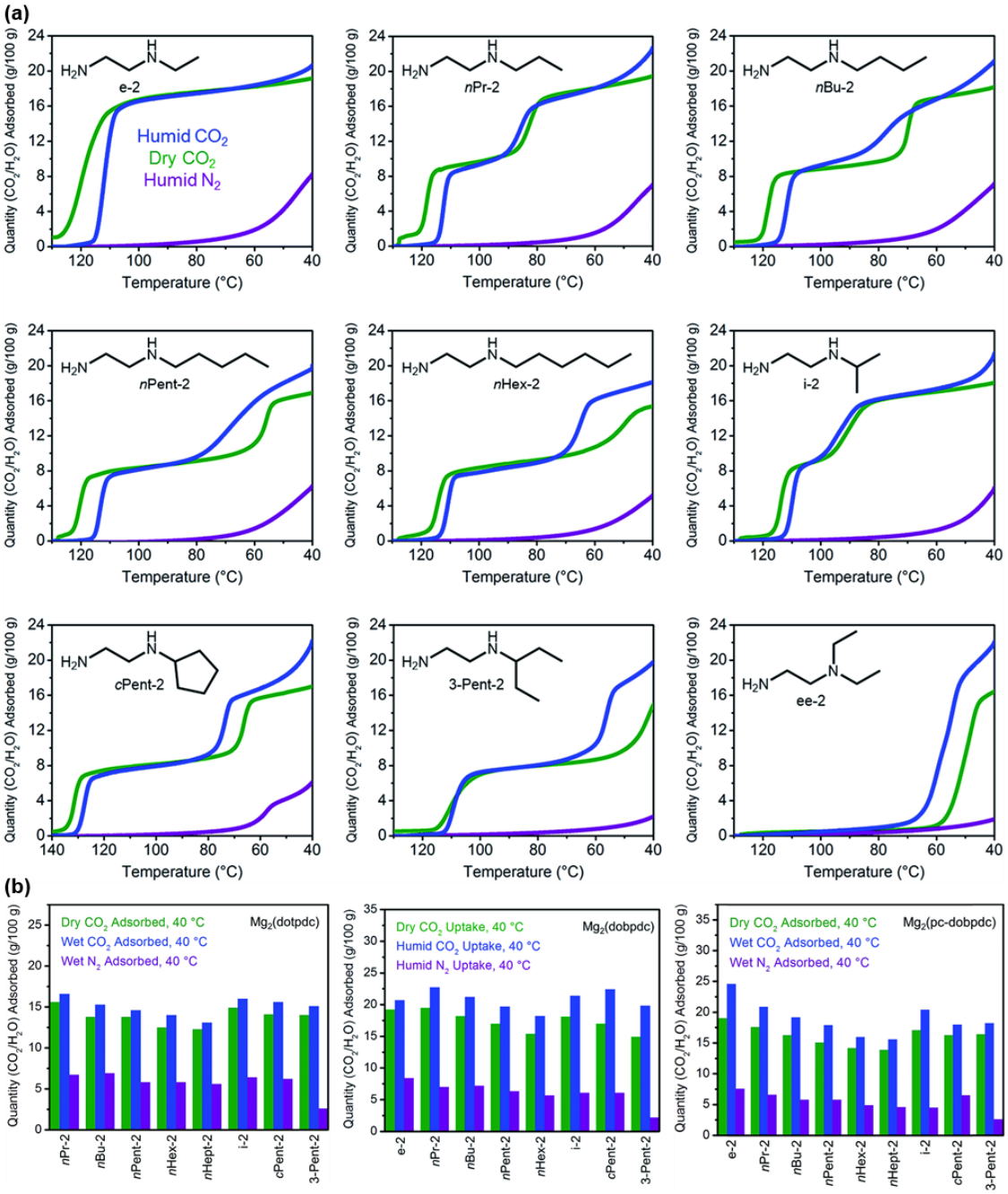

Fig. 42 (a) Adsorption isobars for a series of alkylethylenediamine-appended variants of Mg_2(dobpdc). (b) Summary of the adsorption capacities at 40 °C for amine-functionalized Mg_2(dobpdc), Mg_2(dotpdc), and Mg_2(pc-dobpdc). Dry CO_2 (green), humid CO_2 (blue), and humid N_2 (purple).[152]

However, TGA testing can just be used to identify the adsorbed amounts without the adsorbed species. Forse *et al.*[145] investigated the effects of water on CO_2 chemisorption using magic-angle spinning (MAS) NMR experiments and concluded that the major chemisorption products of dmpn−Mg_2(dobpdc) are at least two different ammonium carbamate conformations under wet conditions. This result is different from those

obtained under dry conditions, supporting that ammonium carbamate formation is more favorable in the presence of water.[414,436] A vdW-corrected DFT study by Lee *et al.*[151] indicated that CO_2 insertion to form an O-bound carbamate in mmen–M_2(dobpdc) is much more favorable than binding H_2O at the open metal site of the corresponding bare M_2(dobpdc) frameworks. This finding is consistent with experimental observations that these materials can selectively adsorb CO_2 under humid conditions. Later, Siegelman et al.[148] characterized the effect of water on the behavior of 2-ampd–Mg_2(dobpdc) (2-ampd = cyclic diamine 2-(aminomethyl)piperidine) and predicted its structure and energetics. The DFT-calculated binding energy of CO_2 in the co-adsorbed structure was larger than that of H_2O, indicating that H_2O desorbs before CO_2 (**Fig. 43**).

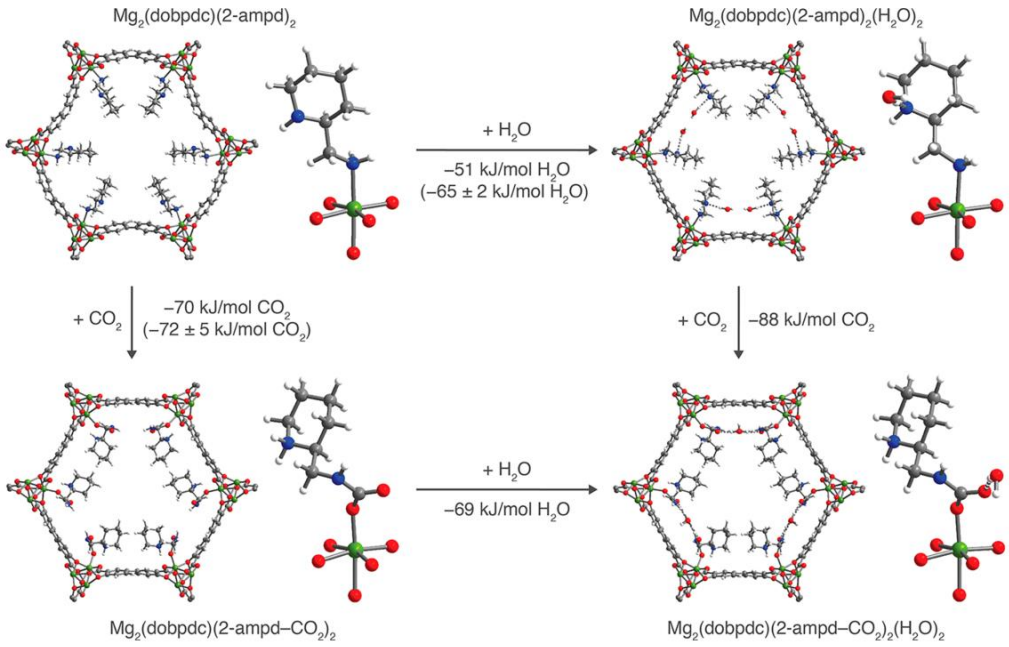

Fig. 43 vdW-corrected DFT-calculated structures and energetics. Evacuated L-2-ampd–R-Mg_2(dobpdc) (top left), water adsorption (top right), the framework following CO_2 insertion (bottom left), and co-adsorption of CO_2 and H_2O (bottom right) are shown, including experimental differential binding enthalpies (ΔH_{ads}) in parentheses. Green, dark blue, gray, red, and white spheres represent Mg, N, C, O, and H atoms, respectively (Reproduced from ref. 148 with permission from American Chemical Society, copyright 2019).

6.2. Moisture swing adsorbents

Quaternary ammonium-based ion exchange resins (IER) can effectively adsorb CO_2 from dry air and

release it in wet condition.[437] Such moisture-swing adsorbents offer an innovative approach to regenerate CO_2 adsorbents because the energy source from water is inexpensive. Simply wetting the resin with liquid water[438] or water vapour[439] provides free energy for CO_2 release and increases the equilibrium partial pressure by up to two orders of magnitude. The heat of adsorption of the IER (32 kJ mol^{-1}[438]) is much lower than that of a Ca-based process (179 kJ mol^{-1}[440]) and amine solution (80 kJ mol^{-1}[267]). In addition to IER, other functional porous materials such as modified carbon black,[441] order colloidal crystals,[442] and high internal phase emulsion polymers[443] have been designed for reversible CO_2 capture from air by moisture swinging. Recent studies have extended the family of moisture swing adsorbents by using inexpensive biomass materials such as quaternized cellulose, starch, and chitosan/PVA aerogels.[444] Some of them exhibit 10-fold faster kinetics than commercialized materials owing to the accessibility and connectivity of micro- and mesopores. These adsorbent powders can be embedded in porous electrospun scaffolds, allowing for effective exposure to air and enhanced heat removal.[190]

The working mechanism of moisture-swing adsorbents is of particular interest because it cannot be simply ascribed to the competitive binding of CO_2 and water vapor. Previous DFT calculations show that during CO_2 adsorption, hydrated water leads to the proton transfer of adsorbents with the anion CO_3^{2-}.[445] Molecular dynamic modeling further demonstrates that the free energy of CO_3^{2-} hydrolysis to HCO_3^- and OH^- is negative when water is accessible to the nanostructured resins.[446] The formation of OH^- promotes spontaneous CO_2 binding from dry air. The transformed HCO_3^- decreases the hydrophilicity of materials, leading to a unique self-cooling effect.[156]

The hypothesis that the equilibrium between HCO_3^- and CO_3^{2-} depends on the number of water molecules in the nanopores was later verified by calculating ion hydration energy through quantum mechanics simulations (**Fig. 44**a).[154] The environmental factors of adsorbents greatly affect the CO_2 capture efficiency.

For instance, high CO_2 capacities can potentially be achieved by selecting supporting materials such as zeolite, water-stable MOFs, and COFs with small pore sizes, SiO_2 with short cation distances, and carbon black with hydrophobic properties (**Fig. 44**b). The counterintuitive phenomenon of ion hydration in confined spaces is ubiquitous and applicable to other weak bases. A recent work suggested that strong bases such as guanidine also follow this moisture swing principle.[159]

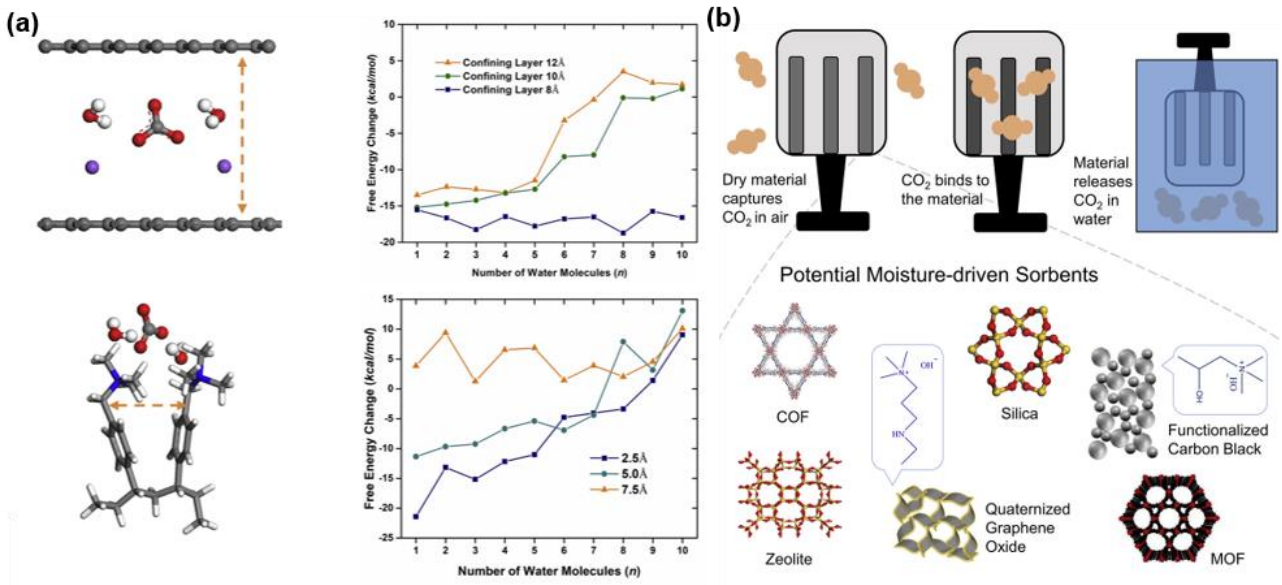

Fig. 44 (a) Quantum mechanics calculations of the ion hydration energy as a function of the number of water and (b) potential moisture swing adsorbents (Reproduced from ref. 154 with permission from Elsevier, copyright 2020).

Amine-functionalized air capture materials face kinetics problems as the amine molecules preferentially fill micro/mesopores and lead to 1–2 orders of magnitude loss of surface area.[314,326] The quaternary ammonium adsorbents based on commercial moisture swing resins generally have CO_2 capacities above 0.8 mmol g^{-1}, but require adsorption halftimes as high as 100 min.[447,448] The small overall activation free energies of the hydrolysis of CO_3^{2-} (< 46 kJ mol^{-1})[160] indicate the chemical reaction should not constrain the adsorption kinetics of moisture swing adsorbents. On the other hand, compared to the gas film diffusion limitation, the adsorption kinetics under ultradilute CO_2 are more likely controlled by diffusion inside the adsorbent particle.[449] Therefore, optimizing the porosity and size of the support materials can potentially

enhance the overall kinetics.

While applying macroporous materials[163] or cellulose fiber[162] as supports promotes the adsorption kinetics to some extent, Wang *et al*.[157] recently reported ultrafast kinetics with an adsorption halftime of 2.9 min by grafting quaternary ammonium onto mesoporous resins (**Fig. 45**). Superb CO_2 adsorption kinetics were achieved because of the uniform cylindrical mesopore structures of the supports, which were created by employing proper swelling agents to overcome steric hindrance. The mesopores also changed the local humidity properties, thus altering the binding energy of the surface amines to CO_2. A relatively low cyclic capacity (i.e., 0.26 mmol g^{-1}) may be the main limitation of such adsorbents, which is expected to be improved by introducing hydrophobic groups, such as fluorine-containing monomers,[155] onto the mesoporous matrix.

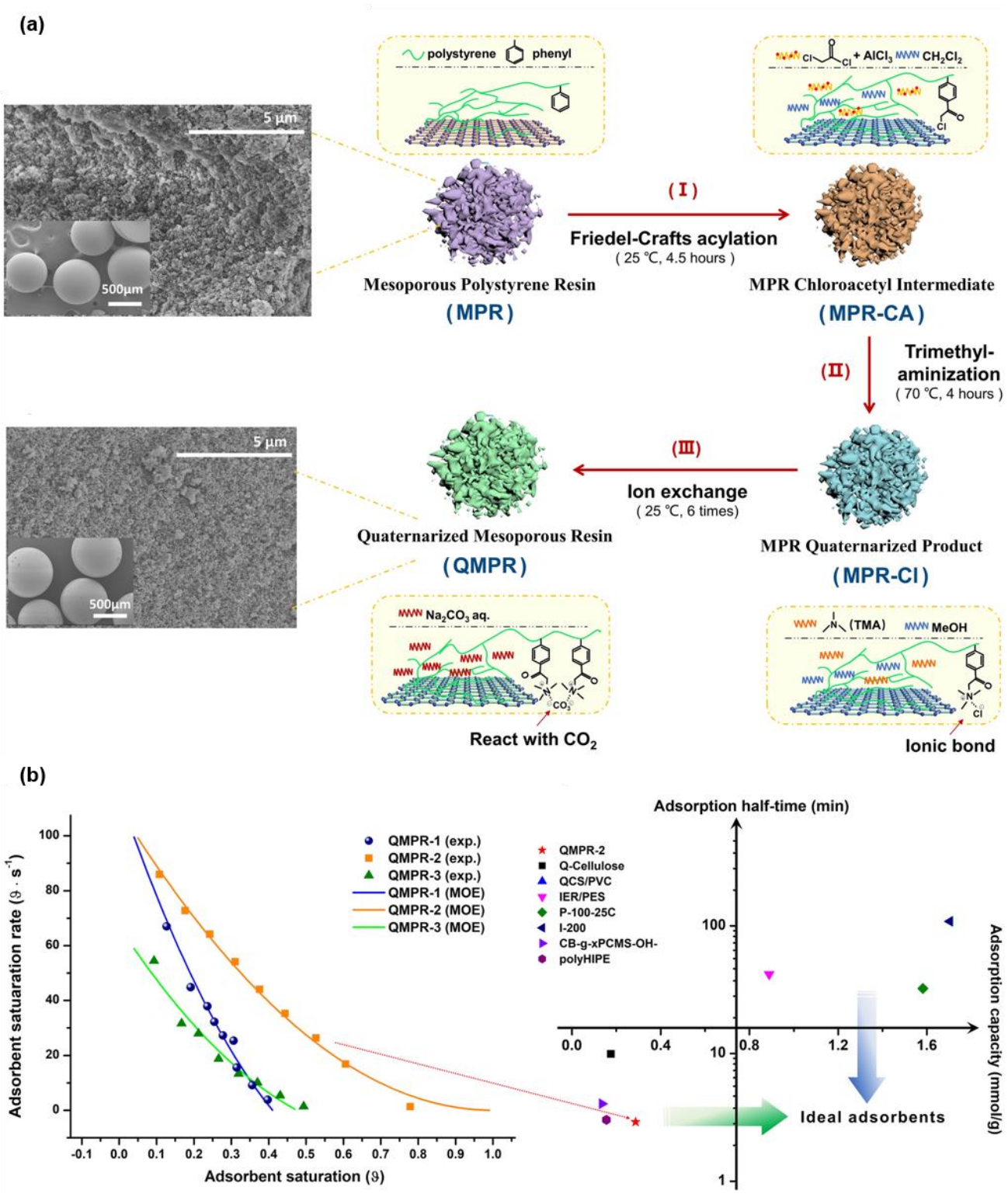

Fig. 45 (a) Fabrication of quaternary ammonium-functionalized mesoporous resins and (b) CO_2 adsorption kinetics at 20 °C and 21% RH and the comparison among moisture swing adsorbents for DAC (Reproduced from ref. 157 with permission from Springer Nature, copyright 2020).

At present, CO_3^{2-} is the main active group in the moisture swing for DAC owing to its large difference in hydration energies and swing sizes compared to other anions such as fluoride and acetate.[163] A recent work

reported a new moisture swing adsorbent that loads movable PO_4^{3-} ions onto the IER, exhibiting 80% higher working capacity and much faster kinetics than CO_3^{2-} based absorbents during moisture swing.[161] Similar to the CO_3^{2-}/HCO_3^- transformation, PO_4^{3-} is hydrolyzed into OH^- and HPO_4^{2-}/H_2PO^{4-} in a dry environment. CO_2 is adsorbed on the produced OH^-, and is released by increasing humidity. In fact, the hydrolysis of other weak acid ions, such as S^{2-}, SO_3^{2-}, HPO_4^{2-}, and SO_4^{2-}, is also possible by changing the surrounding humidity and is thus potentially applied to moisture swing adsorbents.[450] Other efforts have been devoted to investigating the effects of positively charged amine groups in addition to quaternary ammonium.[158] Surprisingly, the overall capture performance of amine-based resins, particularly their adsorption capacities, depends more on the chemical functional groups than on the physical properties. The underlying mechanism can be illustrated by the difference in hydrolysis free energy. In dry environments, resins with stronger amine groups (*e.g.*, quaternary amines) tend to produce more OH^- groups for CO_2 adsorption than those with weak amines (*e.g.*, tertiary amines).

One disadvantage of moisture-swing adsorbents is the low partial pressure of released CO_2, requiring additional concentration for subsequent conversion or storage. Greenhouse enrichment might be a potential application, since the optimal CO_2 concentrations for plants and algae are only 1–2 orders of magnitude higher than those in air. While there is little public information, moisture swing adsorption-based DAC companies, such as Infinitree and Skytree, focus on niche markets for supplying greenhouse CO_2 to urban agriculture. Other disadvantages include contamination by impurity anions, water consumption, and weather restrictions,[95] and the requirements for the design of novel adsorbent materials with more robust structures and higher hydration efficiencies, as well as coupling of heat and water recovery systems.

6.3. Hydrophobic amine-containing adsorbents

While hydration helps amine-containing adsorbents achieve better CO_2 adsorption, additional energy is required to release the adsorbed water. The presence of H_2O also leads to leaching or segregation of the amine in the impregnated amine sorbent owing to the water solubility of the amine. Hydrophobic modification can reduce the adverse effects of water vapor. Recently developed hydrophobic amine-containing adsorbents can be roughly divided into two categories: hydrophobic coating encapsulation and hydrophobic functional group grafting. Hydrophobic encapsulation of the adsorbents, such as using Pickering emulsions to encapsulate liquid amines in microspheres,[451] or a clay-based superhydrophobic material as a protective coating[166] achieved promising CO_2 adsorption capacities and long-term stability under ultradilute conditions, but the separation performance depends on humidity conditions.

A more attractive approach is the introduction of hydrophobic functional groups into amine-containing adsorbents, such as long-chain alkyl groups,[164] aryl groups,[452] oxysilane-based,[166,333] and fluorine-based.[155] Rather *et al.*[164] extended the 1, 4-conjugated addition reaction between branched PEI and dipentaerythritol pentaacrylate, in which residual acrylate groups were modified with small molecules from propylamine to octadecylamine. The length of the alkyl chain in the amines imparted a different degree of hydrophobicity to the CO_2 adsorbent. Furthermore, superhydrophobic cotton based on amine amplification was designed, and the effect of water wettability on the CO_2 capture performance was systematically evaluated.

The combined effect of amine amplification and hydrophobicity resulted in excellent CO_2 capture performance at ambient temperature and pressure. However, it should be noted that although long-chain alkyl groups can increase hydrophobicity, they also increase steric hindrance for CO_2 diffusion. Inagaki *et al.*[452] introduced hydrophobic aryl groups as amine ligands to inhibit the hydration of neutral carbamates and found that ortho-, meta-, and para-xylylenediamines (OXDA, MXDA, and PXDA) only adsorb CO_2 in air without hydration. Notably, MXDA·CO_2 can exist in the form of anhydrous carbamate, even in water.

This is because MXDA·CO_2 self-assembles into a structure similar to a reverse lipid bilayer, as opposed to a normal lipid bilayer, the hydrophobic aryl groups of self-assembled MXDA·CO_2 face the water and protect the intermediate carbamate from hydration. Hou *et al.*[155] synthesized fluorinated diblock copolymerization, which enhanced CO_2 adsorption by promoting the dissociation of H_2O owing to increased hydrophobicity, with a CO_2 adsorption capacity of 2.07 mmol g^{-1} at 21 °C/40%RH. It should be noted that crosslinking can increase the density of amines to synthesize a support-free CO_2 adsorbent through the ring-opening reaction of epoxides and amine groups.[165,453] Hamdy *et al.*[453] developed PEI-based adsorbents crosslinked by epoxy resin. Because epoxy resin was only used as "hardening agent," the dosage was much smaller than PEI, only a minority of amine reacted, and the majority of unreacted amines were used for CO_2 adsorption. Through the hydrophobic functionalization modification of the poly (amine) chain, the adsorption capacity of CO_2 was greatly improved, especially at low temperatures.

Although various hydrophobic modification methods have proven to be effective, we need to maintain the principle of using as few non-adsorbents as possible while maintaining CO_2 adsorption capacity. In addition to hydrophobic modifications, hydrophobic solvents are viable options. Mobley *et al.*[454] developed a mixture of hydrophobic 2-fluorophenethylamine and octafluoropentanol as a non-aqueous solvent. The energy required to release captured CO_2 can potentially be reduced by 40–50% compared to the conventional CO_2 capture processes.

7. Scaling-up design for adsorption-based direct air capture

7.1. Adsorbent shaping technologies

Most DAC adsorbents are synthesized in the form of powders. In actual applications, the gas-solid contact efficiency is an important factor. In particular, under ultralow CO_2 concentrations, a much larger amount of

feed gas is blown into the contactor than that in post-combustion capture. To this end, powdery adsorbents are transformed into so-called “structured adsorbents” with a specific geometric structure and shape when using shaping technologies. The use of structured adsorbents in the contactor can reduce the gas pressure drop and increase the thermal and mass transfer properties, thus enhancing the capture performance and reducing energy consumption.

Through pelletization and granulation, the powdered adsorbent can be transformed into a structured adsorbent in the form of millimeter-sized cylinders, cuboids, or spheres. Pelletization and granulation are conventional shaping technologies with advantages of simplicity and convenience. These are suitable for a wide range of powdered materials. However, because the pellets and granules are still packed into the beds, the improvement in the gas-solid contact is limited. Therefore, they are regarded as “incomplete” shaping technologies. The typical process of pelletization is extrusion (to form lumpy adsorbents), whereas granulation is typically performed through the agglomeration and packaging of powder adsorbents (to form beaded adsorbents).

In a typical palletization process, the powder materials first undergo pre-treatments such as carbonation or mixing with a binder.[328,455,456] They are subsequently compressed in a millimeter-sized mold, followed by optional drying and calcination. The binder composition, carbonation temperature, and compressive force affect the mechanical integrity and adsorption properties of the pelleted adsorbent. The capability for CO_2 capture from air using pellet-shaped adsorbents was recently illustrated by Tomas *et al.*[342] and Wijesiri *et al.*[135] In the former study, activated carbon was extruded into pellets with a diameter of 2 mm and a length of 4–5 mm. Such a pelleted adsorbent exhibited a CO_2 capacity of 0.5 mmol g^{-1} in TSA cycles with an adsorption condition of 5000 ppm CO_2 at 20 °C. In the latter one, carbonated MCF powder in pure CO_2 was made into 4 mm diameter cylindrical pellets using a TDP-6T single-punch tablet press. Each pellet was

cut into quadrants with an approximate mean Sauter diameter of 1.8 mm. Under fixed bed testing, the MCF pellets showed a capacity of 1.94 and 2.52 mmol g^{-1} under dry and humid conditions, respectively, in 420 ppm CO_2/N_2.

Granulation results in less negative structural effects on the structured adsorbents because of the avoidance of the extrusion step, and it enables the functional tunability of the wrapping layers outside the powder to obtain enhanced hydrophobicity, mechanical strength, and thermal conductivity.[457–459] For instance, Choe *et al*.[460] synthesized Mg_2(dobpdc)/Al beads by using a spray dry method after mixing MOF powders with alumina sol, followed by amine functionalization and alkyl chain silane coating. The resulted beads exhibited significant CO_2 capacity as well as high hydrophobicity (**Fig. 46**a). Luzzi *et al*.[457] embedded zeolite 13X in a highly porous chitosan aerogel (**Fig.46**b). Remarkable CO_2 capture performance was achieved after the 13X powder was shaped into beads. In terms of DAC, Park *et al*.[432] fabricated Mg_2(dobpdc)/poly (vinylidene fluoride) (PVDF) composite beads via a phase inversion method, followed by post-functionalization with 1-ethylpropane-1,3-diamine (epn) (**Fig. 46**c). The DMF solution of Mg_2(dobpdc) and PVDF was dropped into a nonsolvent solution to form beads during solvent exchange. As the MOFs were encapsulated by hydrophobic PVDF, their water durability was significantly enhanced while maintaining good CO_2 capture capability from indoor air. Guo *et al*.[461] prepared a kilogram scale MOF/polyacrylates composite to circumvent the defects of NbOFFIVE-1-Ni (**Fig. 46**d and e). Polyacrylate beads was prepared by copolymerization of acrylate monomers and grafted with amine, after which the NbOFFIVE-1-Ni crystals were *in situ* grown within the macropores of the beads.

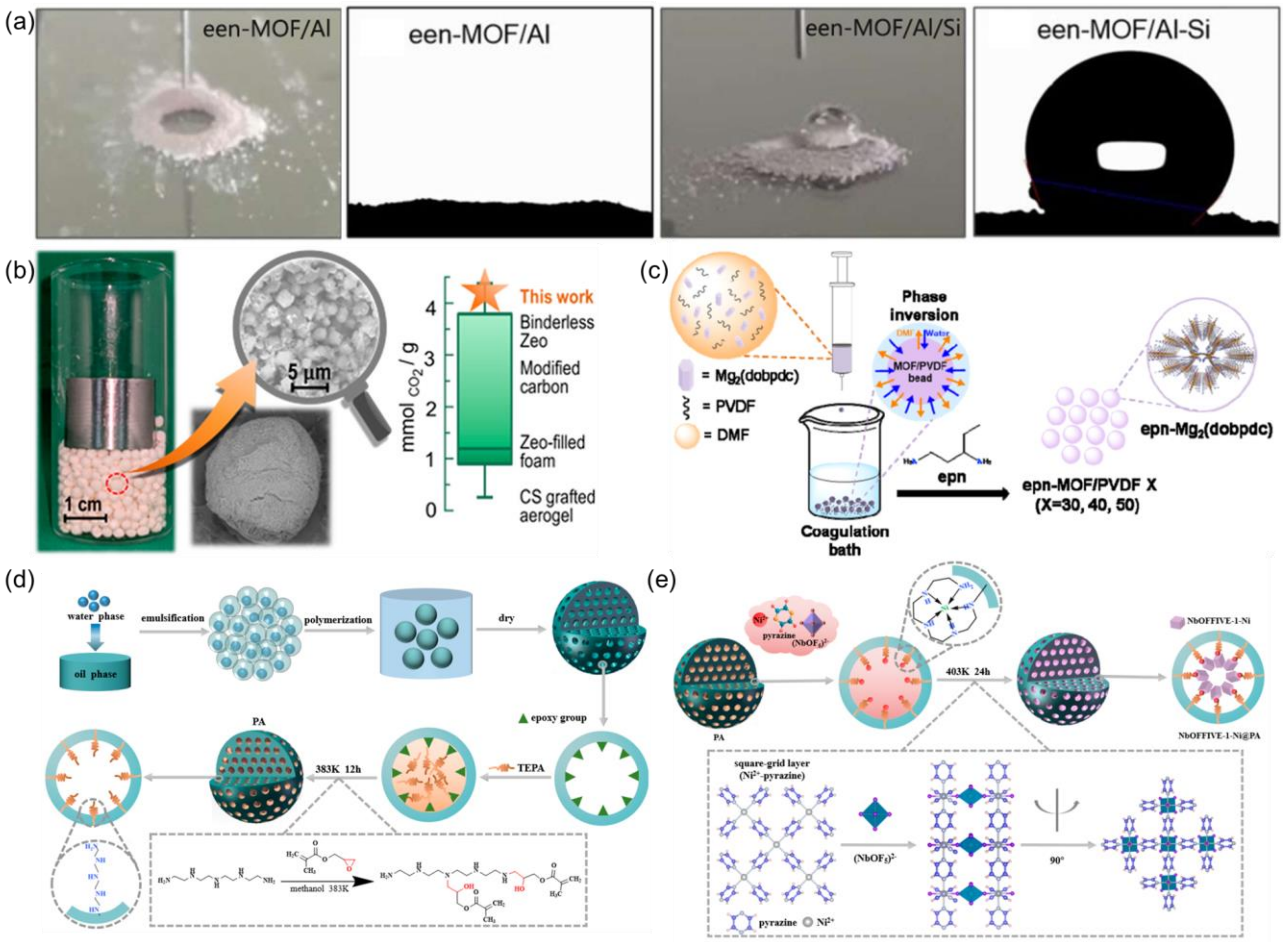

Fig. 46 (a) Photograph and contact angle of een–MOF/Al and een–MOF/Al–Si after adding water dropwise (Reproduced from ref. 460 with permission from Springer Nature, copyright 2021). (b) Granulation of zeolite 13X beads using a chitosan aerogel as the binder (Reproduced from ref. 457 with permission from American Chemical Society, copyright 2021). (c) Granulation of Mg_2(dobpdc) in the PVDF and DMF solution via phase inversion method (Reproduced from ref. 432 with permission from American Chemical Society, copyright 2021). (d) Synthesis scheme of polyacrylate beads, (e) NbOFFIVE-1-Ni crystals *in situ* growth inside the pores of polyacrylate beads (Reproduced from ref. 461 with permission from American Chemical Society, copyright 2021).

Pelletization and granulation only provide pellet- and granule-shaped materials, respectively. Improved techniques are required to construct more complex structures to fully realize the advantages of shaping. Coating is another conventional, direct, and facile method for manufacturing structured adsorbents. Typically, a coating solution containing adsorbents or adsorbent precursors is doped onto a substrate through dip coating, spray coating, or spin coating. The obtained adsorbents could be in the form of a membrane, honeycomb, or foam, according to the shape of the substrate. Binders are typically utilized to

enhance the combination of the adsorbent and the substrate; however, binders may reduce the adsorption capacity in some cases.

Recently, several attempts have been made to fabricate coated adsorbents to capture CO_2 from the air. Membrane-shaped adsorbents can be attached to the sheet surface as a passive control of indoor air CO_2. Krishnamurthy *et al.*[189] incorporated silica-supported aminopolymers into polyacrylic-based latex and coated the pigment on a flat alumina (**Fig. 47**a–c). Pigments were effective in controlling the indoor CO_2 concentration, with only a ~20% decrease in the adsorption efficiency compared to that of the powder-based adsorbent.

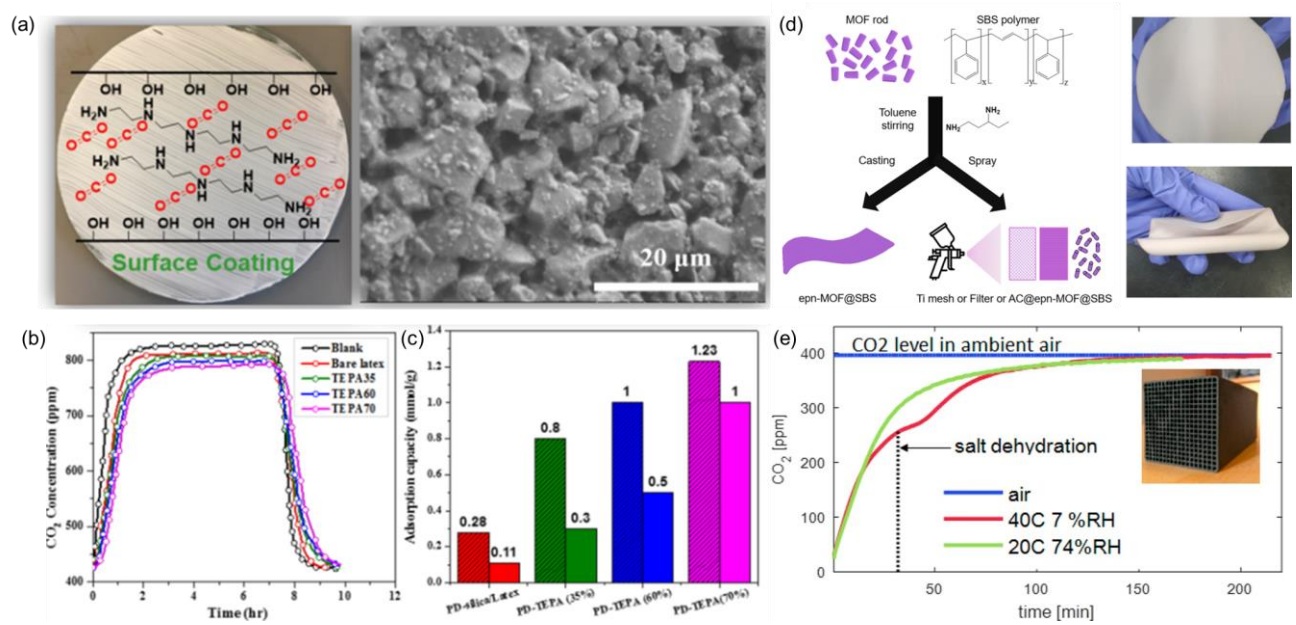

Fig. 47 (a) Amine-based latex coated on the alumina sheet and its surface morphology. (b) Chamber tests of the coated latex at 800 ppm and 15% RH. (c) Corresponding calculated CO_2 uptake for paints (solid) and powder sorbents (shaded) (Reproduced from ref. 189 with permission from American Chemical Society, copyright 2019). (d) epn-functionalized Mg_2(dobpdc) made into self-standing membranes or films on the substrates with SBS as the binder (Reproduced from ref. 462 with permission from Elsevier, copyright 2022). (e) Hydrated K_2CO_3 coated on the activated carbon honeycomb (Reproduced from ref. 463 with permission from American Chemical Society, copyright 2018).

Self-standing membranes could also be fabricated to separate CO_2 from the indoor air using the coating method. Shiue *et al.*[464] blended PVA and PAA solutions and coated this material onto the surface of a reverse osmosis membrane via a spin coater. The obtained separation layer was modified by the hydroxyl and amine

functional groups. The osmosis exhibited a larger gas permeability toward CO_2 than N_2 at 25 °C. When the pressure was 0.75 cm Hg, 1 wt.% PVA + 7 wt.% PAA had the greatest CO_2/N_2 gas selectivity ratio of 10.7. In another example, the coating solution was made into self-standing membranes as well as films coated on solid substrates. Chae *et al.*[462] mixed epn-functionalized Mg_2(dobpdc) with a polystyrene-block-polybutadiene-block-polystyrene (SBS) hydrophobic polymer and fabricated a membrane-shaped composite (**Fig. 47**d). The epn-Mg80@SBS exhibited a CO_2 capacity of 2.8 mmol g^{-1} at 1000 ppm. The composites were also coated onto the surface of a Ti mesh, air filter, and granular activated carbon via a simple spraying coating method, confirming the feasibility of producing structured adsorbents with the composite. In the study of Mosqueda *et al.*,[463] an adsorbent coated activated carbon honeycomb is made (**Fig. 47**e). The commercial honeycomb monolith (2.9×2.9×3.0 cm) was immersed in the K_2CO_3 solution, and was then shaken to remove the excess liquid and calcinated in the N_2 atmosphere. The resulted structured adsorbent showed a high capture capacity of 0.249 mmol g^{-1}, whereas the salt loading was only 0.0558 g_{K2CO3} $g_{adsorbent}^{-1}$. The salt content was kept low because of the physical deterioration of the carrier at higher loadings.

The development of coating methods is unfortunately hampered owing to the shortcoming of weak bonding between the coating films and the substrate, which may cause wear and peeling problems during long-term operation. Therefore, strategies to form stronger combinations have been proposed. By covalently anchoring adsorbents to the substrate through *in situ* growth, uniform adsorbent films and well-ordered crystal orientations connected by rigid bonding could be achieved. The growth conditions vary for different types of adsorbents, and so this method is relatively less versatile and more time-and energy-consuming. However, the superior tunability and retention of the original adsorbent properties make it attractive for the synthesis of high-performance materials.

The growth method was initially used to synthesize zeolites on substrates.[465] Recently, increasing numbers of MOFs, including Mg_2(dobpdc), MOF-74, and UTSA-16 coated on different substrates were explored for CO_2 capture.[187, 466–468] In one case, Mg_2(dobpdc) films were synthesized on a cordierite monolith surface wash-coated with α-alumina with MgO nanoparticles as the metal precursor and demonstrated good crystallite density and favorable orientation.[187] In another study, the layer-by-layer technique was found to be suitable for MOF-74 film growth, while *in situ* dip coating resulted in high UTSA-16 weight gain on the cordierite.[468] Lawson *et al.*[467] utilized 3D-printing to impregnated kaolin-based monolith with the precursor Co, and facilitated the UTSA-16 growth via a solvothermal method. The UTSA-16 loaded monolith not only retained high mechanical integrity, but also exhibited similar adsorption properties to its powder analogue (**Fig. 48**a).

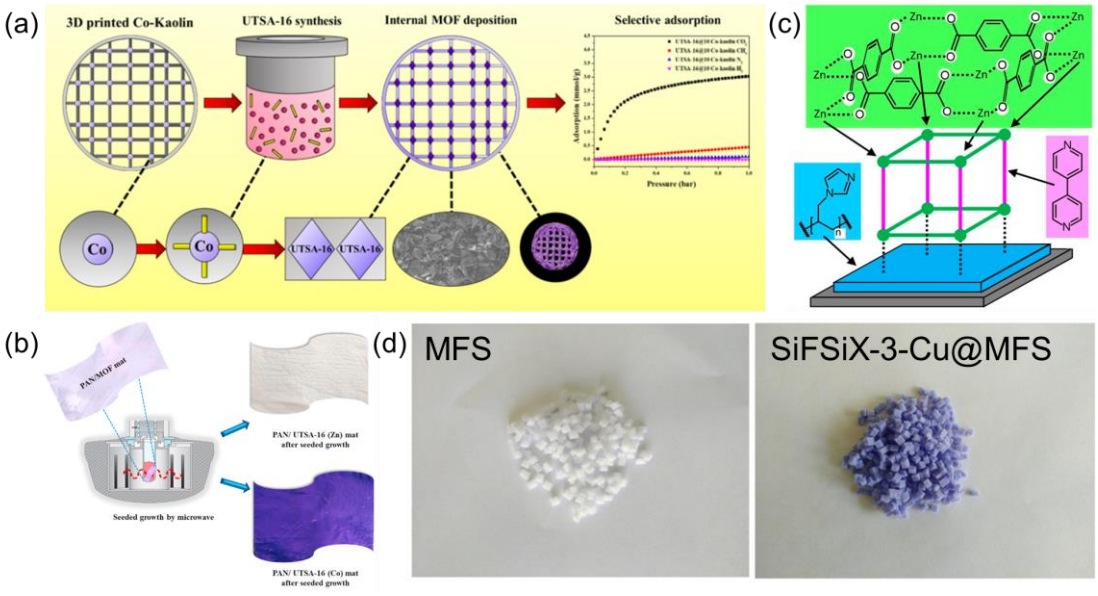

Fig. 48 (a) UTSA-16 growth on the kaolin monolith (Reproduced from ref. 467 with permission from American Chemical Society, copyright 2018). (b) UTSA-16 growth on the electrospun fiber mats.[466] (c) Epitaxial growth of the MOF-508a on QCM discs (Reproduced from ref. 469 with permission from American Chemical Society, copyright 2018). (d) MFS without and with SIFSIX-3-Cu growth (Reproduced from ref. 470 with permission from Elsevier, copyright 2020).

The growth of UTSA-16 on electrospun fiber mats was also explored and tested for CO_2 concentration capture.[466] The MOF powders were dispersed within polyacrylonitrile fiber networks and processed to

produce MOF crystalline layers under microwave irradiation for the seeded growth of MOFs (**Fig. 48**b). Wilson *et al.*[469] used plasmonic deposition to achieve epitaxial growth of MOF-508a on quartz crystal microbalance (QCM) discs or polytetrafluorethylene membranes (**Fig. 48**c). In this study, structurally well-defined pulsed plasma deposited poly(1-allylimidazole) layers provided surface imidazole linker groups for the directed layer-by-layer growth of MOF-508a at 25 °C. The results showed that MOF-508a exhibited a high affinity towards CO_2 with a maximum capacity of 2.75 μg cm_{disc}^{-2} under a CO_2 partial pressure of 0.4 mbar. Activated carbon-supported HKUST-1 and melamine formaldehyde sponge (MFS) monolith-supported SIFSIX-3-Cu were synthesized by Zhen *et al.*[470,471] (**Fig. 48**d). Metal ions were introduced into the pores of the supports, followed by addition of organic ligands. It was shown that the *in situ* growth of SIFSIX-3-Cu in the MFS avoided crystal stacking, presenting a multi-level pore structure. With an MOFs loading ratio of 5 g g^{-1} MFS, the monolith composite showed CO_2 uptake of 1.02 mmol g^{-1} with a CO_2 concentration of 5000 ppm at 20℃.

The flexibility of the growth method enables the attachment of the adsorbents to various substrates. Nevertheless, only limited types of materials have been synthesized by *in situ* growth. The synthesis strategies must be optimized to shorten the growth time and increase the adsorbent loading. The relationship between the substrate surface properties and adsorption properties of the attached MOFs requires further exploration.

Monolith extrusion has been extensively used in molding various inorganic and organic materials. Similar to pelletization and granulation, this method mixes the adsorbents, binder, and pore additives to prepare pastes. The pastes are then added to a mold and extruded to form a specific shape. Extrudates generally exhibit rigid mechanical structures and high adsorbent loadings. However, the structural design of extrudates cannot be altered flexibly, and objects with discontinuous structures cannot be fabricated owing

to the mold shape limitation.

Extruded zeolite, activated carbon, alumina, and MOFs monoliths have been fabricated for CO_2 capture.[472] Recently, zeolite and conductive carbon were extruded together to prepare hybrid monoliths for electric swing adsorption (**Fig. 49**a and b).[473,474] It has been reported that extrusion has additional positive effects, including an increase in the heat capacity of the material, a decrease in the water heat of adsorption, and an increase in the CO_2 isosteric heat of adsorption.[474] Hong *et al.*[475] compared MIL-101(Cr) and zeolite 13X monoliths at an adsorbent loading of 75 wt.% (**Fig. 49**c). Bentonite clay and Licowax C micropowder PM were used as the binder and pore former, respectively. In another experiment, the adsorption properties of extruded alumina monoliths were compared with those of powdered adsorbents for DAC.[311] The monolith demonstrated a volumetric capacity of 350 mol m^{-3} and an equilibration time of 350 min.

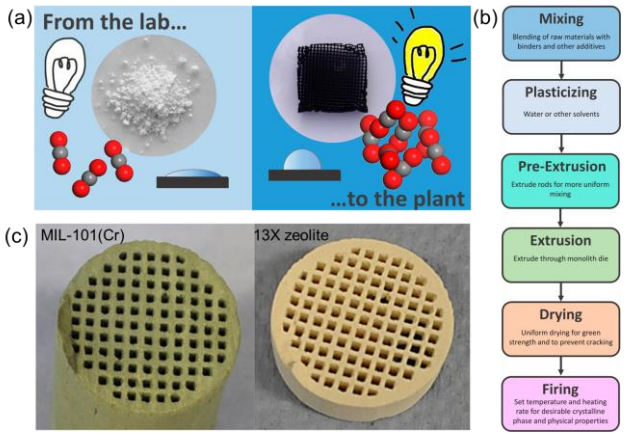

Fig. 49 (a) Zeolite/electrically conductive carbon monolith produced from powders by extrusion. (b) Conventional process of preparation of extruded ceramic honeycomb monoliths (Reproduced from ref. 474 with permission from American Chemical Society, copyright 2017). (c) Extruded MIL-101(Cr) and zeolite 13X honeycomb monolith (Reproduced from ref. 475 with permission from Elsevier, copyright 2020).

The extrusion method faces manufacturing difficulties, such as paste composition adjustment for different materials and adsorbent enlargement. There are very few researches on extrudates that capture CO_2 from air. Nevertheless, it remains a feasible method for producing high-performance structured adsorbents. Further research should be performed to verify other types of materials like amino solids for effective CO_2

adsorption.

The sol-gel method also produces structured adsorbents with high adsorbent content. Sol-gel enables uniform mixing of active compounds as precursors in the liquid phase. After undergoing hydrolysis and condensation reactions, the colloidal solution polymerizes to form a solid gel with a specific structure. Typically, beads, membranes, and cylindrical adsorbents are fabricated. The sol-gel process is highly adjustable because of the abundant precursor materials and flexible synthesis methods. Various adsorbents have been proven the capability for DAC application.

Wörmeyer *et al.*[335,476] investigated amine-functionalized aerogels as cylinders and microspheres, either by pouring the precursor solution into a cylindrical mold or using the emulsion method. Kong *et al.*[281] developed an amine hybrid resorcinol–formaldehyde/silica composite aerogel through a solvothermal-assisted sol-gel process, reaching a CO_2 adsorption capacity of 1.85 mmol g^{-1} in humid air. Later, an amine hybrid titania/silsesquioxane composite gel with a short adsorption half-life and high amine efficiency was prepared using a one-pot sol-gel process followed by supercritical drying.[282] Song *et al.*[444] synthesized quaternized chitosan (QCS)/PVA hybrid aerogels using a sol-gel method with glutaraldehyde as the cross-linking agent (**Fig. 50**). The hydrogel was soaked in a NaOH solution to replace chlorine ions with hydroxide ions. Rim *et al.*[106] developed solvent impregnated polymers loaded with NOHMs for DAC. Firstly, SIPs were fabricated using an encapsulation technique. Then, NOHM-I-PEI were incorporated into the SIPs and ultraviolet-cured to produce gas-permeable solid sorbents with uniform NOHMs loading.

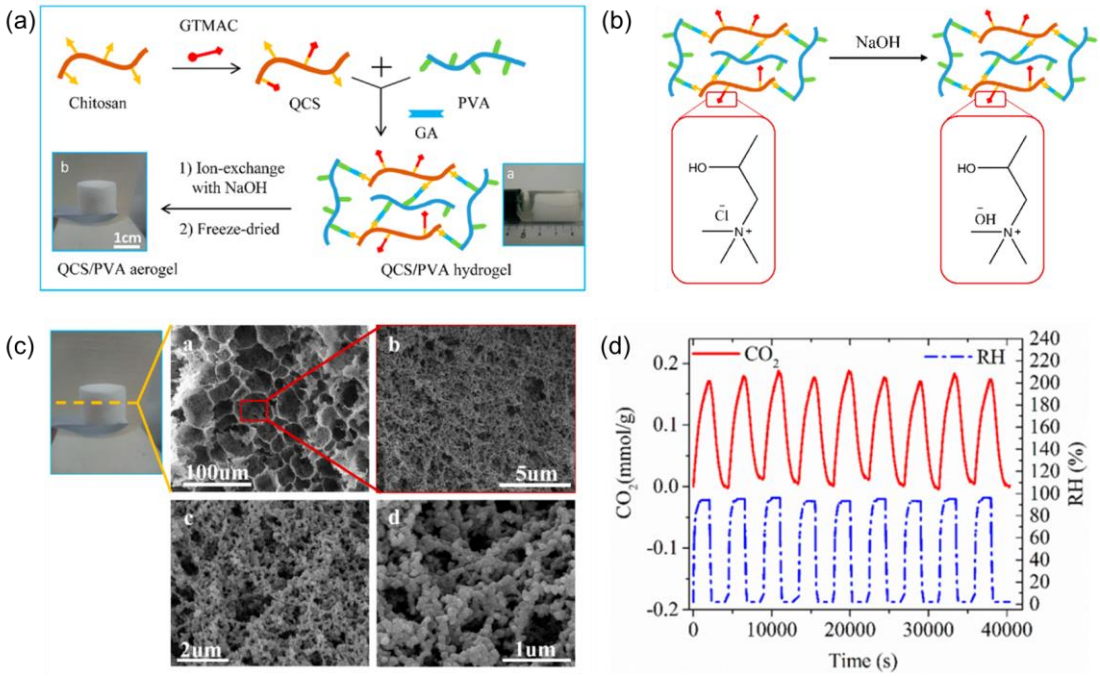

Fig. 50 (a) Quaternized chitosan is cross-linked with PVA, ion-exchanged with NaOH, and freeze-dried to form the aerogel. (b) Ion-exchange process of QCS/PVA hydrogel with the NaOH solution. (c) Microscopic morphology of QCS/PVA aerogel. (d) Adsorption cycles of QCS/PVA aerogel at 20 °C (Reproduced from ref. 444 with permission from American Chemical Society, copyright 2018).

Through adequate regulation, an adsorbent shaped by sol-gel methods can achieve high adsorption performance and is further beneficial from heteroatom doping.[477] One of the main obstacles in facilitating the broader application of the sol-gel method is the size enlargement. As the shape of the adsorbents is mainly determined by the container, complex structures, such as honeycombs and foams, are more difficult to manufacture.

Owing to the advantages of high flexibility, adjustable size, and low production cost, fiber adsorbents fabricated through dry-wet spinning or electrospinning are favorable for manufacturing unique gas-solid contacts that allow adequate mass transfer, low pressure drop, and advanced thermal modulation. Nevertheless, current research on fiber adsorbents has been conducted mostly at the laboratory level. Koros *et al.*[478] first synthesized a hollow polymer fiber embedded with adsorbent zeolite 13X particles in the fiber walls using the dry-jet wet-quench spinning method. Since then, a series of studies on hollow fibers have

been reported.[185,365,479–493] The system takes advantage of the hollow fiber morphology by passing cooling water through the bores during adsorption to maximize the capacity and steam through the bores during desorption to desorb CO_2. For instance, Sujan *et al.*[185] recently applied a polymer/silica fiber adsorbent for DAC. Monolithic fiber sorbents composed of cellulose acetate and SiO_2 were synthesized via the dry wet-spinning technique, followed by functionalization with PEI in a post-spinning infusion step (**Fig. 51**a). The amine-loaded monolithic fibers effectively extracted CO_2 from ambient air (~380 ppm) and produced high-purity (>97%) CO_2 under both dry and humid conditions. Lee *et al.*[494] investigated the synthesis of Mg-based MOF nanocrystals within a polymeric fiber loaded with stable metal-oxide precursors. The scalable amine-appended Mg_2(dobpdc) fiber captured CO_2 with a capacity of 1.99 mmol g^{-1} under DAC conditions. (**Fig. 51**b and c)

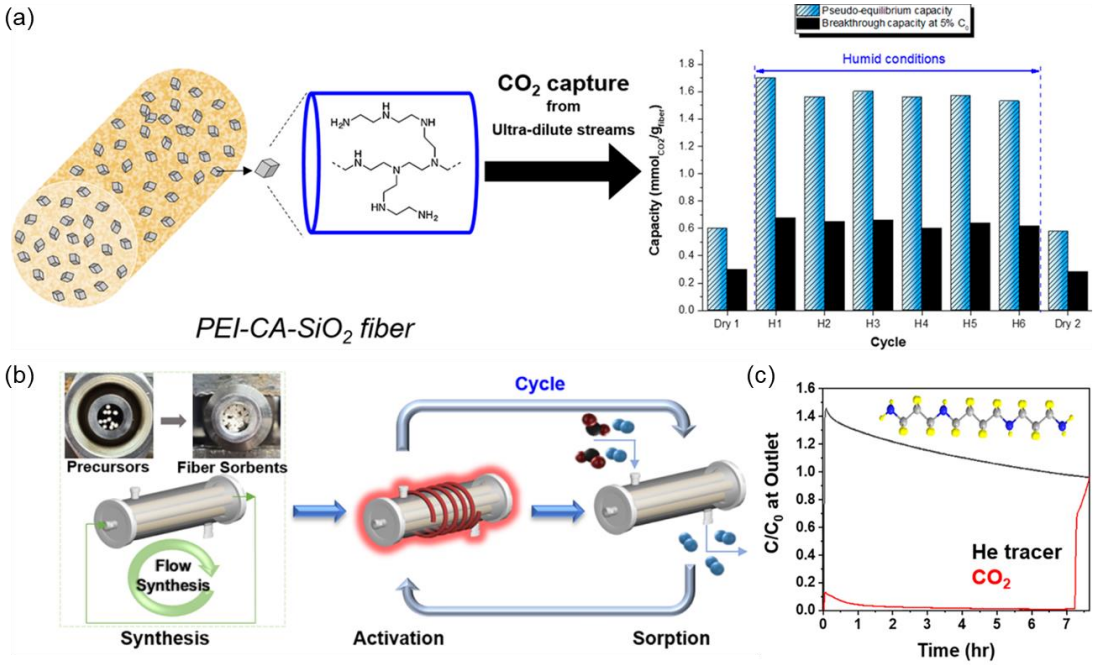

Fig. 51 (a) PEI-loaded polymer/silica fiber sorbents (Reproduced from ref. 185 with permission from American Chemical Society, copyright 2019). (b) Workflow diagram of a modular device that contains the fiber sorbents. (c) Breakthrough curve of tetraamine-Mg_2(dobpdc)/PEI fiber sorbent module with 11 fibers under dry 400 ppm CO_2 condition (Reproduced from ref. 494 with permission from American Chemical Society, copyright 2021).

Another route for generating nanofibers is electrospinning. In early 2010, Ostermann *et al.*[495] successfully

prepared hierarchical porous nanofibers by electrospinning MOF nanoparticles using suitable carrier polymers. Subsequent studies have expanded the material range applied in electrospun fibers and explored the synthesis factors affecting the fiber textural properties, providing new concepts for further development.[496–499] Recently, Armstrong *et al*.[190] developed IER-containing porous electrospun fibers using the solvothermal polymer additive removal technique. Different particle scaffolds, including commercially available industrial films, dense electrospun fibers, and porous electrospun fibers, were compared for their ability to capture CO_2 from ambient air. The porous fiber had 90% IER availability, whereas the dense fiber had 50% particle accessibility. The sorption halftime for both electrospun fiber sample was 10 ± 3 min, and IER embedded in porous electrospun fibers showed the highest cycle capacity with an uptake rate of 1.4 mol g^{-1} h^{-1}. Compared to conventional techniques, spinning exhibits greater potential for application on a large scale, although rational design, materials, and cost assessment are still required to drive further development.

The additive manufacturing technique, 3D printing, is a rapid shaping technique based on numerical model files and manufactures structured adsorbents through layer-by-layer accumulation. The technique takes advantage of the ease control of the material structure and active site distribution by model file modification and paste composition regulation. These excellent metrics have facilitated the wide application of 3D printing in determining the crucial printing parameters and their optimization strategies for CO_2 adsorption.[99] However, a limited number of experiments on 3D-printed adsorbents for DAC have been performed.[74,188,500–502] The latest study reported an integrated DAC and oxidative dehydrogenation of propane system that achieved a combination of carbon capture and utilization in a single bed (**Fig. 52**).[74] Dual-functional material adsorbent/catalyst monoliths comprising CaO and M@ZSM-5 heterogeneous catalysts were manufactured using 3D printing. Varying the metal dopant in the catalysts can flexibly

control the chemical properties of the structured DFM, so as to simultaneously achieve the effective carbon capture and conversion.

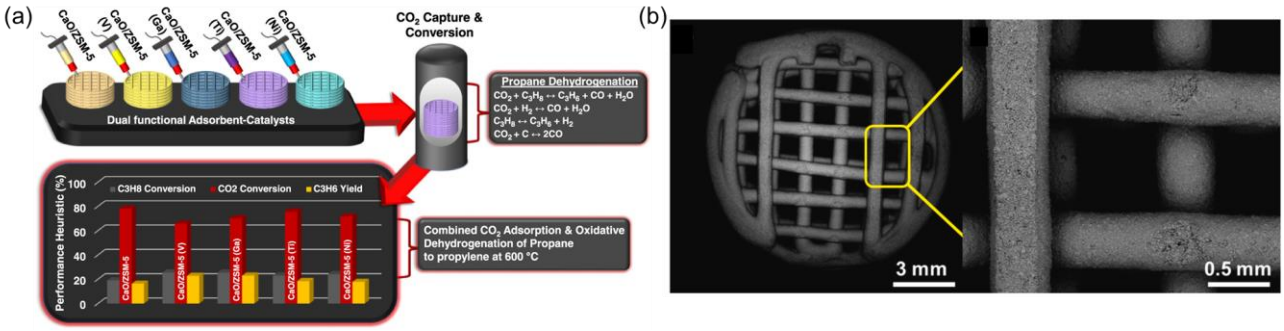

Fig. 52 (a) Dual-functional adsorbent/catalyst monoliths and their conversion performance and (b) Microscopic morphology of the 3D-printed monolith (Reproduced from ref. 74 with permission from Elsevier, copyright 2022).

7.2. Gas-solid contactors

To meet the cost requirements for commercialization, the design of an efficient DAC process is critical; this can be achieved by designing gas–solid contactors with high heat and mass transfer efficiencies.[405] In addition, a DAC adsorber should have a high volumetric adsorption rate and a low pressure drop to minimize equipment and operational costs. The adsorber is divided into three types of configurations (**Fig. 53**).[503] The fixed-bed type is widely applied because of its simple reactor configuration, in which air is passed through the sorbents directly. However, the pressure drop is quite large in some cases, particularly when the sorbents are powdered. Therefore, the size of the adsorbents should be enlarged and the flow rates should not be too high to reduce the pressure drop. In addition, the heat transfer inside the adsorption bed is poor.[503] It is better to design the configuration of an axially-fixed-bed into a “pancake-shaped” flat-bed to reduce the pressure drop.[199] Radial flow beds have also been scaled up recently.[199,504]

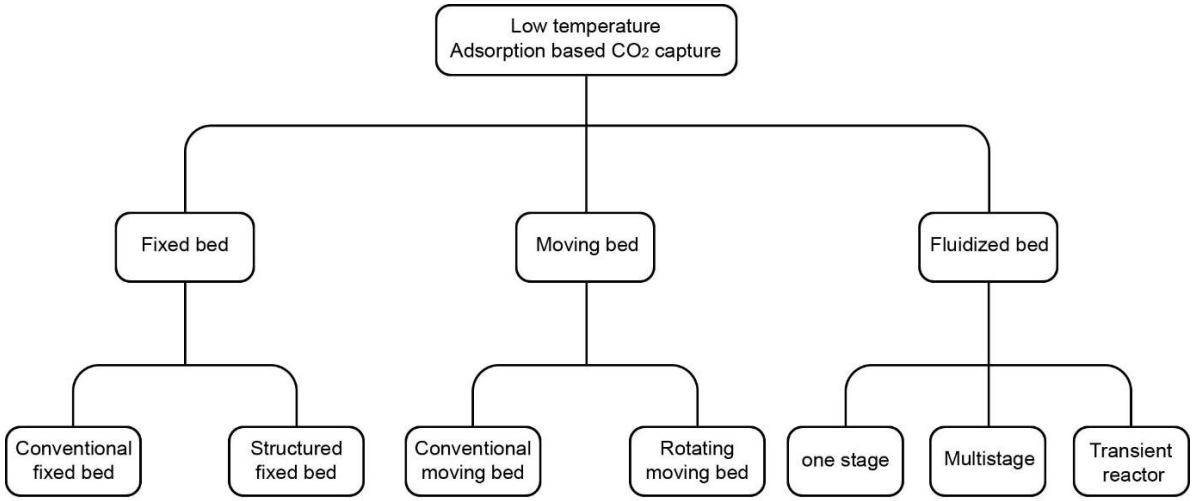

Fig. 53 Reactor configurations used in the adsorption-based CO_2 capture (Reproduced from ref. 503 with permission from American Chemical Society, copyright 2021).

The distribution of the feed gas is complicated for both flat-bed axially fixed-bed and radial flow beds. To overcome these problems, monoliths, another type of solid contactor, has been developed. Typically, a sorbent is mixed with a binder and extruded into a designed structure. Recently, 3D printing has been rapidly developed for the fabrication of monolithic sorbents. Compared to packed beds, the pressure drop is much lower, the mass transfer rate is improved, and the attrition of adsorbents is weakened. However, the loading of the adsorbent is reduced per unit volume.[505]

The concept of a moving belt adsorber has been proposed. This type of bed shows a lower pressure drop, but the movement of large particles is difficult. Drechsler *et al*.[200] proposed a novel moving bed and the bed was divided into several zones, which is helpful in realizing a high degree of thermal integration. In addition, the rotary bed is another type of moving bed that has achieved large-scale application.[51] The rotary bed configuration was divided into adsorption and desorption sections. The device was operated continuously without switching. The TSA can be used to regenerate the rotary bed. However, leaks and gas flow distribution are challenges that must be addressed.

The fluidized bed was also proposed for CO_2 capture; the adsorbents were suspended in the feed gas,

resulting in a good heat transfer rate. However, this method can cause serious abrasion of the adsorbent. Some previously investigated gas–solid contactors used for DAC are summarized in **Table 5**.

Table 5 Comparative study of gas-solid contactors used for DAC.

Bed (height, diameter)	Adsorbent (weight)	Adsorption conditions	Desorption conditions	Ref
Packed bed (5.5 cm, 0.4 cm)	Mg_2(dobpdc) (0.06 g)	400 ppm CO_2/He, 23, 49, 70 °C 1000 ppm CO_2/He 5660 ppm CO_2/He 10020 ppm CO_2/He	115 °C in He for 4 h	193
Fixed-bed (4.8 cm, 0.9 cm)	Aminoresin (0.5 g g^{-1})	400 ppm CO_2/N_2, 25 °C	Heating Heating, inert gas purging Heating, vacuum Heating, inert gas purging, vacuum Heating, vacuum, closed	192
Fixed-bed (1 cm, 8 cm)	APDES-NFC	400 ppm CO_2/Air/50%RH	Heating, vacuum Heating, steam purging, vacuum	177
Packed bed (1 cm, 10 cm)	Lewatits VP OC 1065	400 ppm CO_2/N_2/30% 50%RH, 25, 50, 70 °C	Heating, vacuum	136
Fixed-bed (60 cm, 1.3 cm)	Lewatits VP OC 1065 (53.6 g)	400 ppm CO_2/N_2 20°C 5000 ppm CO_2/N_2 20°C	Heating, steam purging, vacuum	133
Fixed-bed (1.7 cm, 0.45 cm)	Amine-functionalized resin (0.5 g)	200–4000 ppm CO_2/N_2, 25–50 °C, H_2O 0.16 to 1.86 vol.%	Heating, vacuum, N_2 purging	406
Fixed-bed (2.4 cm, 40 cm)	Lewatits VP OC 1065	410 ppm CO_2/N_2, 20 °C, 50% RH	Heating, vacuum, CO_2/N_2 purging	506
Fixed-bed (12 cm, 1 cm)	PEI_80b (3.45 g)	420 ppm CO_2/ N_2	Heating, steam purging, vacuum	137
Rectangular reactor (7.2 cm, 7.2 cm, 50 cm)	APDES-NFC-FD (85.9 g)	400–490 ppm CO_2/N_2, 58.3% RH	Heating, vacuum	405
Radial flow reactor (40 cm, 15.4 cm)	Lewatits VP OC 1065 (1700 g)	429–464 ppm CO_2/N_2, 19–22 °C 40–65% RH	120 °C in N_2 for 16 h	199
Radial flow reactor (50 cm, 1.6 cm)	Lewatits VP OC 1065 (1–3 g)	400 ppm CO_2/ N_2, 25 °C	80 °C in N_2	504
Moving belt adsorber (2900 cm, 0.5 cm)	Lewatits VP OC 1065	400 ppm CO_2/N_2	Heating	200

In such a configuration, the inlet gas typically consists of CO_2, N_2, O_2, and water. The relative humidity of the gas was regulated using either an evaporator filled with water (in a heated water bath) or a water-filled

syringe driven by a syringe pump. Darunte *et al.*[193] studied stepped CO_2 adsorption isotherms in packed beds to determine the CO_2 uptake at different flow rates and concentrations using mmen-Mg_2(dobpdc). A sharp breakthrough curve can improve bed utilization. With partial pressures of 0.4 and 1 mbar, the profiles show a rapid initial shock followed by a long wave (**Fig. 54**). This breakthrough has resulted in poor utilization and a lower CO_2 extraction rate (0.11/0.44 mmol g^{-1} h^{-1}). For 5.67 and 10.02 mbar CO_2, a sharp breakthrough curve could be observed and results in an increased CO_2 capture fraction and rate (3.34/5.86 mmol g^{-1} h^{-1}). At lower flow rates, the breakthrough profile exhibited two shockwaves with a lower CO_2 extraction rate. At higher flow rates, the breakthrough profile broadens with a higher CO_2 extraction rate. These results indicate that increasing the CO_2 concentration improves the CO_2 extraction rate. Moreover, it was proven that the Avrami model could be used to describe the CO_2 adsorption kinetics at a CO_2 concentration of 400 ppm. The Michaelis−Menten expression has been shown to be more suitable at higher CO_2 concentrations.

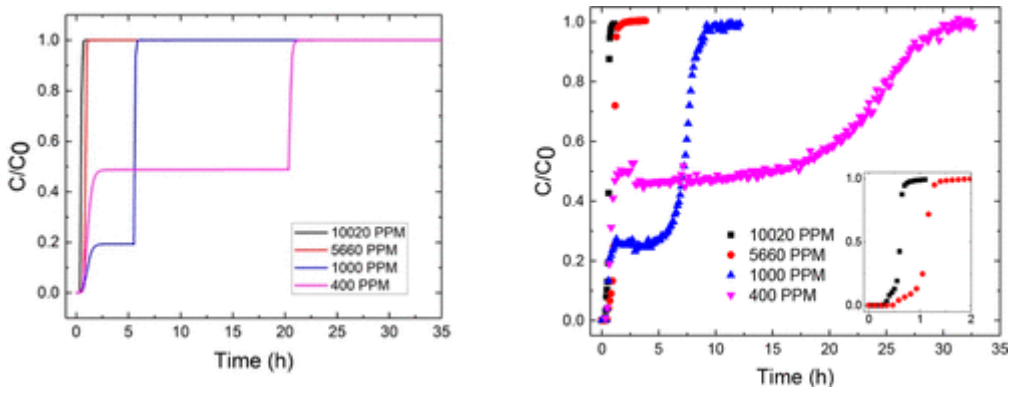

Fig. 54 Breakthrough curves of mmen−Mg_2(dobpdc) at 23 °C and a flow rate of 17.2 NmL min^{-1}. The left one is simulative results and right one is experimental results (Reproduced from ref. 193 with permission from American Chemical Society, copyright 2019).

The desorption capacities after each step of the regeneration process described above is shown in **Fig. 55**. The authors attributed the difference between 1000 and 40 mL min^{-1} to the different calculation methods. The desorption capacity at 60 °C could reach 85–86% of the total desorption capacity. Moreover, it could

extend beyond 90% when coupled with purge flow at 60 °C in a vacuum environment. The working capacity at 60 °C is 0.47 $mmol_{CO2}$ $g_{sorbent}^{-1}$, which shows a minimum regeneration specific energy requirement (SER) of 4.2 MJ kg^{-1} CO_2. Using a mild vacuum of 500 mbar instead of 25 mbar decreased the regeneration SER dramatically, from 26 MJ kg^{-1} CO_2 to 7.5 MJ kg^{-1} CO_2. This indicates that changing the temperature in a vacuum atmosphere coupled with air or inert gas purge flow has more advantages in terms of productivity, and a mild vacuum could be adopted to reduce energy consumption.

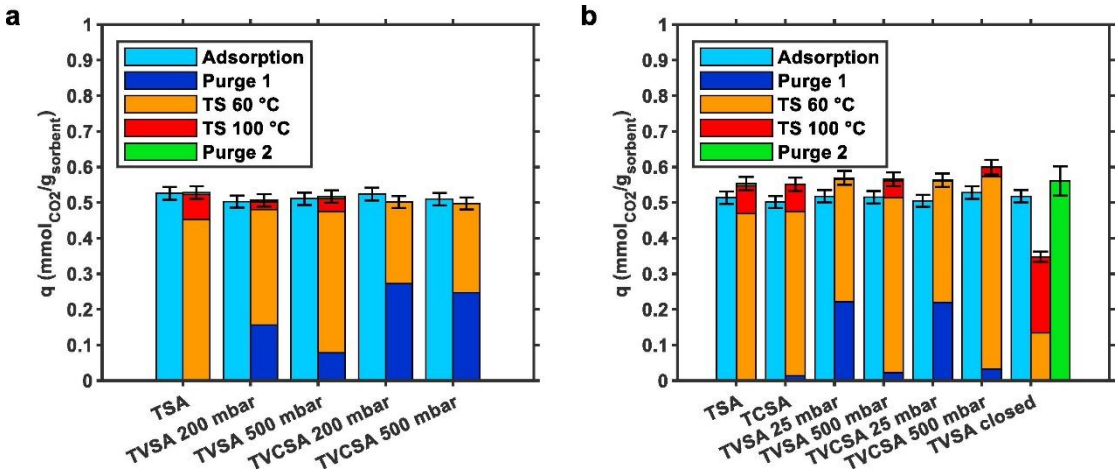

Fig. 55 CO_2 adsorption and desorption capacities using total flow rates of a) 1000 mL min^{-1} and b) 40 mL min^{-1} in the desorption phase. Error bars indicate the uncertainty (Reproduced from ref. 192 with permission from Elsevier, copyright 2021).

Furthermore, it has been reported that an inert gas purge can be replaced by a steam purge.[177] After desorption, the outlet gas contained only CO_2 and steam. The steam was condensed, and the final product was high-purity CO_2. Desorption kinetics can be optimized with the assistance of steam. The desorption rate is 3.75 mmol g^{-1} h^{-1} at 12 kPa abs/100 °C, while the rate is only 0.23 mmol g^{-1} h^{-1} without the purge of steam under the same working conditions.[137]

The electrical versus thermal energy consumption for different evacuation pressures and steam flow rates provides a clear illustration of how to achieve target productivity with relatively low energy consumption (**Fig. 56**).[177] It was found that the productivity could not reach 2.45×10^{-5} kg h^{-1} at high p_L (100 mbar). In

addition, it could not reach such productivity without steam purge (gray triangular markers). Therefore, a decreased evacuation pressure or increased steam purge is necessary to increase CO_2 production. These calculations are based on the energy at the entrance of the adsorption bed. Bos et. al.[133] analyzed the energy consumption from different perspectives. The sensible heat of the sorbent, water, CO_2, reaction heat, latent heat of water, and compression energy were included in the total energy consumption. Interestingly, the author found that steam purge is helpful in improving the CO_2 working capacity. However, the energy consumption for desorption remains almost unchanged owing to the latent heat of the water. The difference in results may be because one is calculated from the perspective of supply, and the other is calculated from the perspective of demand. If low-quality waste heat or renewable energy are available, steam-purged desorption is a promising option.

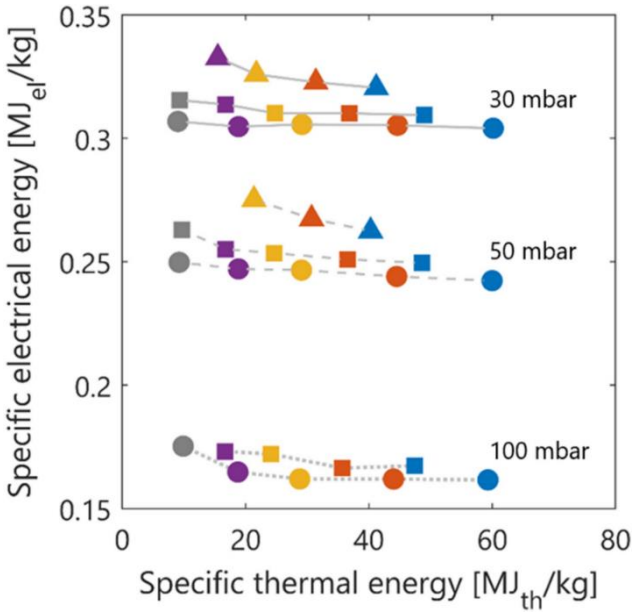

Fig. 56 Electrical vs. thermal energy consumption for CO_2 production rate isolines of 1.9 (circles), 2.2 (squares), and 2.45 × 10^{-5} kg h^{-1} (triangles) and evacuation pressures of p_L: 30 (solid), 50 (dashed), and 100 mbar (dotted). The color scheme corresponds to the flow rate of steam, increasing from left to right: F_s: 0 (gray), 5 (purple), 10 (yellow), 17.5 (orange), and 25 cm^3 s^{-1} (blue) (Reproduced from ref. 177 with permission from Springer Nature, copyright 2020).

The energy consumption of CO_2 capture was assessed using a thermodynamic tool. It was found that the minimum work mainly depended on the shape of the isotherm of the solid adsorbents.[198] The isotherm

shape varies according to the type of adsorbent and gas composition. Young *et al.*[136] used three water-CO_2 co-adsorption models to describe the adsorption isotherms of one amine-modified polymer. Elfving *et al.*[406] also proposed a kinetic model for CO_2 adsorption on amine-supported resin. Both Schellevis *et al.*[506] and Young *et al.*[136] used Guggenheim–Anderson–deBoer as the isotherm model of water, and the Toth isotherm model to describe CO_2 adsorption. However, this model must account for three effects: i) the amine sites would be blocked by water, resulting in a decrease in amine efficiency; ii) the increased stoichiometry; and iii) the heats of adsorption change in the presence of water. The modified Toth model is proposed to account for the above effects, and it has been proven that the DAC can be predicted by WADST and a mechanistic model. Thus, accurate mathematical descriptions of all gas components are required to describe the equilibrium and dynamics. The energy requirements can be determined after solving the differential equations.

7.3. Processes and systems

The design of energy-efficient and cost-effective adsorption-based DAC processes is pivotal for commercialization. Optimizing such processes faces challenges because they should satisfy various constraints such as purity, recovery, productivity, and energy consumption, and data uncertainty sometimes causes significant deviation.[168] Generally, TSA and TCSA, which are commonly used in adsorbent development,[108,127,507] are only applicable in specific cases such as greenhouses and indoor CO_2 control because the purge gas dilutes the desorbed CO_2. For instance, operating the TSA cycle at 70–80 °C produced a gas mixture containing 2% CO_2 for algae cultivation.[174,508] On the other hand, TSA with a CO_2 purge was technologically feasible to concentrate high purity CO_2 from air.[420] Potential drawbacks of CO_2 purge are slow desorption kinetics under high CO_2 partial pressures and amine degradation with the formation of

irreversible urea groups.[273] Vacuum swing adsorption (VSA) or vacuum pressure swing adsorption (VPSA) are not practical for DAC because of unacceptable vacuum requirement below 0.4 mbar during regeneration. To date, TVSA is the most widely applied DAC process, and it is also thermodynamically favorable, requiring only mild vacuum to concentrate high-purity CO_2.[173]

The combination of heating and vacuum allows high working capacities and reduces the amount of adsorbent needed. Comparative techno-economic analyses indicate TVSA-based DAC process offers better performance related to exergy demand (1.4–3.7 GJ t_{CO2}^{-1}) and CO_2 productivity (3.8–10.6 kg m^{-3} h^{-1}) than that of alkali and amine scrubbing (**Fig. 57**).[181] While all the technologies can potentially achieve an operating cost below 200 \$ t_{CO2}^{-1}, the TVSA-based DAC process achieves this more easily under wide conditions. Note that the minimum work for separating CO_2 at 400 ppm is only 0.45 GJ t_{CO2}^{-1}.[172] Cutting down the energy consumption of the TVSA process further relies on better understanding of multicomponent adsorption, and design of novel air contactors with high heat and mass transfer,[171] and integrating heat recovery through heat exchangers or heat pumps.[167]

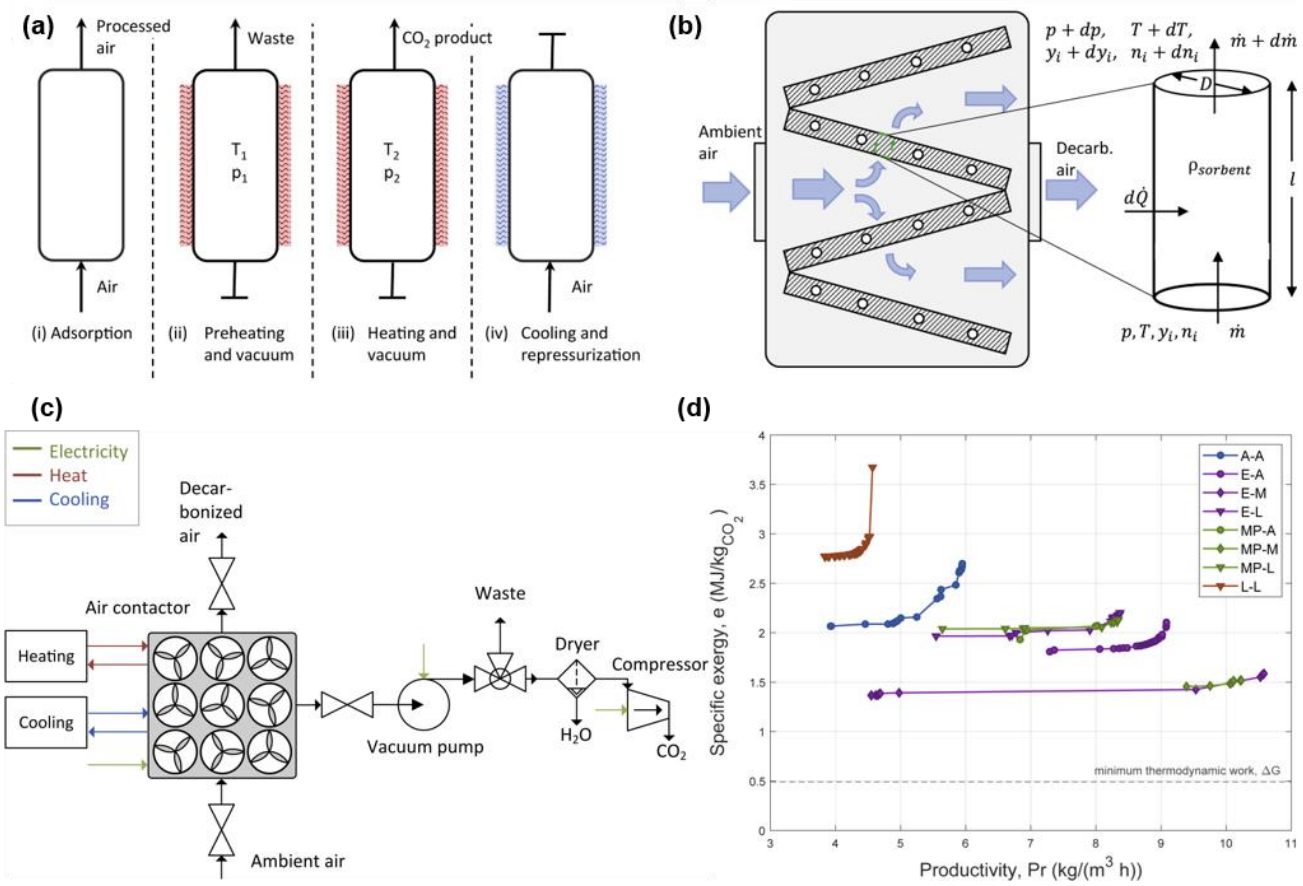

Fig. 57 Design of (a) the TVSA process with four cycles, (b) air contactor, and (c) adsorption-based CO_2 capture system. (d) Relationship between CO_2 productivity and separation exergy using adsorbents with different CO_2 and H_2O isotherms (Reproduced from ref. 181 with permission from Elsevier, copyright 2021).

Climeworks, whose technology originated from ETH Zurich, is a typical DAC company using the TVSA process. In this process, the saturated adsorbent coated on an air filter-like contactor is regenerated at 80–130 °C under reduced pressures of 20–400 mbar.[356,405] NFC adsorbents with aminopropyl grafting is primarily used, achieving a capacity of 1.39 mmol g^{-1} at 400 ppm CO_2 and 40% relative humidity. In a realistic TVSA cycle, the maximum CO_2 working capacity can reach 0.65 mmol g^{-1} at 10 °C and 80% relative humidity.[509] Climeworks built a pilot plant in Dresden based on the TVSA process to capture 80% of CO_2 from the air flowing into the system and convert it into synthetic diesel. Later, a commercial DAC unit was built for a greenhouse in Hinwil that is capable of capturing 900 tons of CO_2 per year. Another DAC demonstration unit (CarbFix2) was installed in Iceland. This project used double flashing to generate

hot water (120 °C) for heating. High-purity CO_2 obtained by desorption is compressed, mixed with water, and injected into a 700 m-deep basalt reservoir for mineralization.[70] Recently, Climeworks launched a scaled-up DAC plant, Orca, to capture 4000 tons of CO_2 per year. Climeworks currently has 15 DAC facilities; their near-term goal is to reduce the operating cost of the DAC to less than 92 \$ t_{CO2}^{-1}.[510]

Oy Hydrocell Ltd. designed a containerized modular DAC device composed of 8 beds (1 m × 0.2 m each) for VTT Technical Research Centre under the SOLETAIR project, with CO_2 productivity of 0.0038 TPD (**Fig. 58**).[511] The system contains two core technologies: a brush-type heat exchanger and a renewable CO_2 scrubber. Glycol/water mixture was used to achieve regeneration at 60–80 °C, broadening the heat source of DAC. A previous study identified the feasibility of applying a TVSA process for such a system with a low regeneration temperature.[173] Because humidity further increases the equilibrium working capacity up to 80%, a kinetic model was proposed to describe the CO_2/H_2O adsorption of the adsorbent, an amine-functionalized polystyrene resin.[406] Even so, a ten-day capture campaign showed 76% of the specific energy requirement due to the thermal energy requirement. An experimental comparison indicates using air purge under 100 °C has benefits over the TVSA process.[192] Their DAC prototype has successfully been applied in a Power-to-X plant[231] and a biological-inorganic system.[209] Recently, Schellevis *et al*.[506] developed a similar TVSA process based on thin 'flat bed' reactors (2.4 cm thickness and 40 cm in diameter). Interestingly, the authors argued that a high desorption temperature benefits both the energy duty and productivity, which was mainly ascribed to the reduction in the required desorption time.

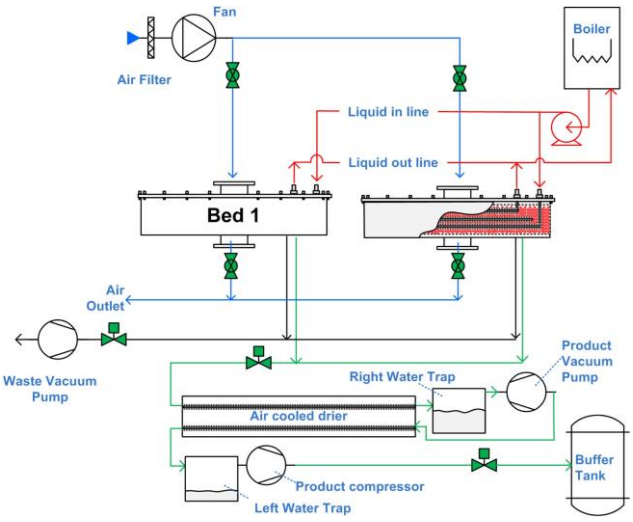

Fig. 58 Main components of the containerized modular DAC device designed by the VTT Technical Research Centre (Reproduced from ref. 511 with permission from Elsevier, copyright 2019). Blue line: air flow, black line: waste gas flow, red line: heating liquid flow, and green line: product flow.

Wilson and Tezel constructed a four-step TVSA cycle by applying seven commercial faujasite-structured zeolites that concentrated CO_2 from 400 ppm to 95% at a CO_2 capture ratio of 81%.[169] The adsorption bed filled with physical adsorbents reached a fast adsorption rate and a low pressure drop. In another study, a novel process configuration consisting of several adsorption beds filled with zeolite-type adsorbents and driven by low-grade heat and optional vacuum was proposed, which was able to concentrate CO_2 extracted from air to high pressures for pipeline transportation.[512] However, owing to the hydrophilicity of zeolite, it needs to introduce additional pre-drying beds. Monash University recently teamed up with Commonwealth Scientific and Industrial Research Organization to develop a mobile DAC prototype (Airthena) using an electric-supplied three-stage TVSA with air handling capacity of 50 $Nm^3\ h^{-1}$.[170] The core component of the device is a spiral substrate coated with MOF/polymer nanocomposites, which exhibits good adsorption properties and hydrophobicity and can be regenerated at 80 °C. When CO_2 purity is 70–80%, the operating energy consumption of Airthena reaches 5.76 $GJ_{th}\ t_{CO2}^{-1}$ in 2680 cycles, equivalent to the capture cost of 35–350 $\$\ t_{CO2}^{-1}$.

Because the desorption of TVSA is much slower than that of TCSA, a high temperature and low pressure

must be adopted.[194] The co-adsorption of H_2O in the adsorption step of TVSA also leads to additional energy consumption for regeneration. Steam-assisted temperature swing adsorption (S-TSA) is another highly efficient DAC cycle that concentrates CO_2 via steam purging instead of vacuum. Steam purge not only provides heat for regenerating the adsorbent material through direct contact but also induces an additional desorption driving force by the displacement effect. The steam in the desorbed gas can be easily separated by condensation. For amine-based materials, steam purging increases adsorption capacity and prevents CO_2-induced degradation. Global Thermostat is an S-TSA-based DAC company whose technology comes from the Georgia Institute of Technology. The company uses amine-based honeycomb ceramic adsorbents that are regenerated using the steam purge to produce 98% pure CO_2. Global Thermostat built its first commercial DAC for soda production in Alabama in 2018, with a capture capacity of 10.96 TPD and an operating cost of 150 \$ t_{CO2}^{-1}. Of all the commercial companies, Global Thermostat reports the current lowest DAC operating energy demand (0.54–0.94 GJ_e t_{CO2}^{-1} + 4.21–5.08 GJ_{th} t_{CO2}^{-1}).[205] Sinha *et al.*[178,179] recently conducted a comprehensive energy and cost assessment of a five-step S-TSA cycle for DAC. The device used monolithic contactors coated with two amine-functionalized MOF adsorbents with a layer thickness of 60 μm. The simulation showed that the minimum energy requirement of the S-TSA process was less than that generated by fuel combustion that releases CO_2. Energy consumption could be further reduced by increasing the adsorbent loading and decreasing the wall thickness of the contactors. Assuming that the lifetime of the adsorbent is 1–3 years, the estimated cost of the DAC with S-TSA is 60–190 \$ t_{CO2}^{-1}.

As the main energy source in an S-TSA cycle, steam can be significantly reduced if it is generated from low-grade renewable energy or industrial waste heat. Gebald *et al.*[513] proposed the concept of S-TVSA. By using the hybrid desorption step coupling vacuum, heating, and steam purge, solar energy or waste heat at

temperatures below 100 °C can be used to generate purge steam for S-TVSA. Wijesiri *et al.*[137,175] conducted experimental studies on the desorption process under the conditions of 0.12–0.56 bar and 70–100 °C (**Fig. 59**). They verified that the average desorption rate of S-TVSA reached 3.75 mmol g^{-1} h^{-1} at 0.12 bar and 100 °C, much higher than that of TVSA (0.23 mmol g^{-1} h^{-1}). A later modeling study confirmed that steam purge in TVSA cycles decreases the energy consumption of the DAC and allows high CO_2 production.[177] When steam purge was considered, high evacuation pressures were favorable for reducing the specific electrical energy. Recently, Zhu *et al.*[180] designed a three-step S-TVSA model based on a packed column for use in a DAC that comprehensively considered the effects of various operating parameters. They suggested that the adsorption of H_2O during steam purging significantly reduced the heating time required to reach the target desorption temperature. The optimal case with a variational steam purge step operating at 90 °C and 0.3 bar achieved a CO_2 productivity of 4.45 mol kg^{-1} day^{-1} and an energy requirement of 0.295 MJ mol^{-1}, in which steam accounted for 80.6% of the total energy consumption.

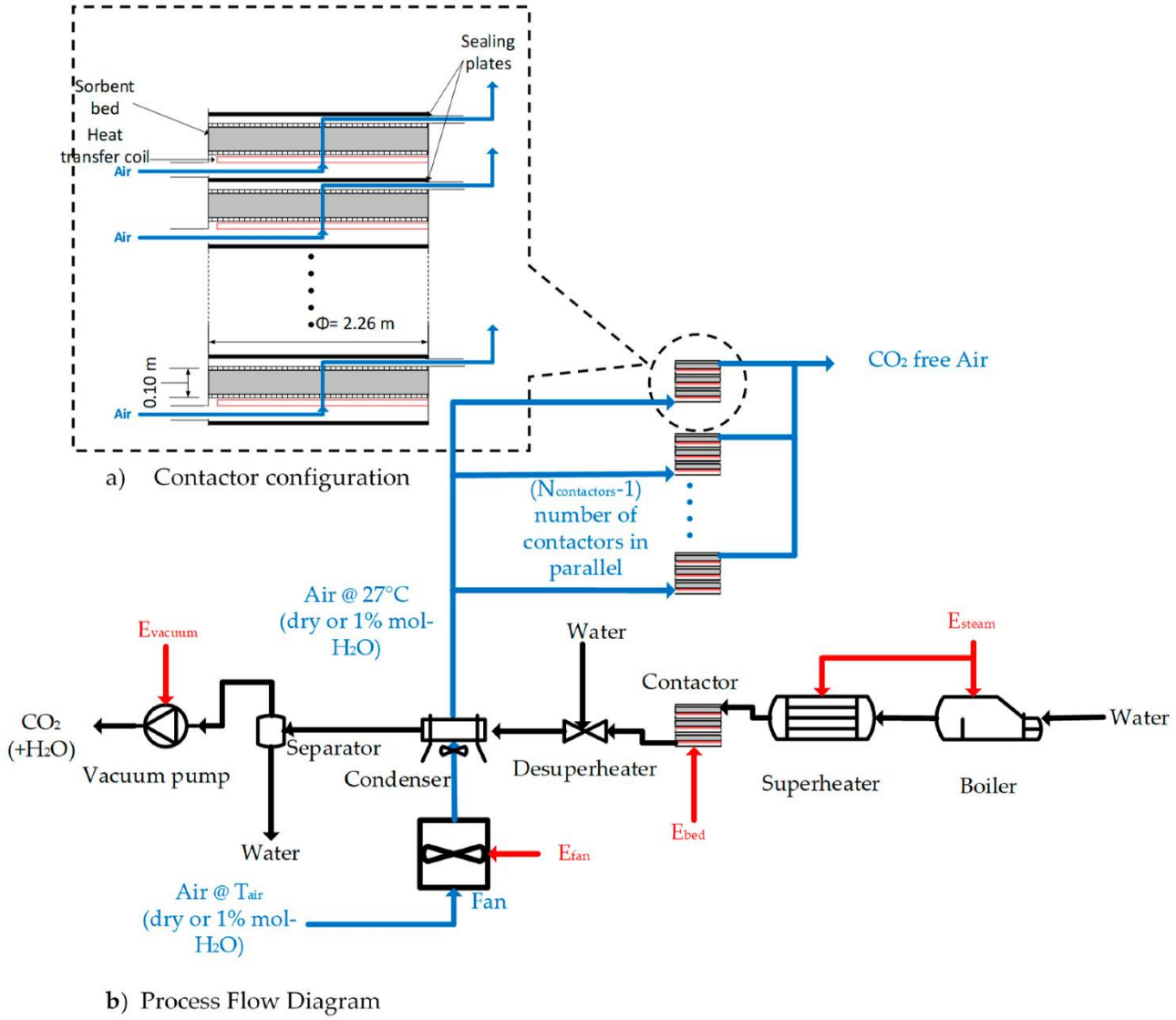

Fig. 59 Process flow of a S-TVSA-based DAC system (Reproduced from ref. 175 with permission from MDPI, copyright 2019).

Techno-economic assessments provided different opinions regarding the operating cost pricing of DAC. A pilot-scale DAC using aqueous KOH sorbent was estimated to cost 94–232 \$ t_{CO2}^{-1},[51] that drop below 60 \$ t_{CO2}^{-1} by 2040.[205] Adsorption-based DAC benefits from lower regeneration temperatures, and leads to minimum costs of 29–91 \$ t_{CO2}^{-1}.[81] On the other hand, some researchers hold more negative viewpoints that DAC technologies are far from being economically competitive to fight climate change, that is, costing 600–1000 \$ t_{CO2}^{-1}.[175,184] This difference is possibly due to the lack of publicly accessible data for the DAC prototype, causing insufficient process assumptions and specific system design.[176] The adsorbent cycle life

and stability are also critical to determining the operating cost but are often neglected in process design.[54] Integrating low-cost industrial waste heat[514] or low-carbon energy sources such as solar, geothermal, biomass, wind, and nuclear[515,516] for regeneration is an effective approach to significantly cut down the operating cost and increase the physical potential capacity of DAC. International cooperation further reduces the capture cost by about 50%.[517]

In fact, while most economic assessments consider DAC infrastructure as a large-scale individual facility, modularized DAC can be designed to achieve mass production by increasing the number rather than the size. In this way, the cost of DAC should decrease rapidly according to the rule of learning-by-doing.[518,519] It is expected that growth of three orders of magnitude in the cumulative installed capacity of DAC brings the cost down to 100 \$ t_{CO2}^{-1}. Another advantage of a modularized DAC is that it provides an independent installation location that can share a low cost for synthetic carbon-based fuels or storage in a sustainable energy system.[182,183]

7.4. Applications

Because DAC technology allows for CO_2 capture anywhere, it is suitable for a variety of applications.[84,520,521] In the following section, recent applications of DAC facilities for indoor CO_2 removal, greenhouse CO_2 fertilization and microbial cultivation, EOR, geological storage, and conversion to chemicals and fuels are discussed.

7.4.1. Indoor CO_2 removal. Indoor CO_2 removal research is motivated by concerns for human health, as well as the need to meet regulations for the indoor CO_2 concentration limit.[522] The CO_2 levels in residential and public places can reach 400–2000 ppm or even higher in densely populated rooms. In international space stations, 3000–7000 ppm could be reached.[6] Residents may experience nasal congestion, nausea,

headaches, drowsiness, and dizziness as a result of high CO_2 levels. DAC is being studied as a promising technology for use in indoor air quality management.

The pioneer study used amine-modified polymeric beads was supported by NASA for CO_2 capture in space shuttles.[523] Since then, amine-functionalized adsorbents such as PEI-modified silica monolith,[191] PEI-impregnated resin,[111] and MOFs[186] have attracted considerable attention for the removal of indoor CO_2. Out of safety considerations for air purifiers, the regeneration temperature is typically limited to a maximum of 70 °C.[111,186] Humid indoor environments, quantified as increased relative humidity in the range of 0–50%, enhance CO_2 adsorption capcities.[189,191] In contrast to industrial plants, moment-changing indoor humidity due to adsorption is also a matter of concern, and the coupling of DAC with an air handling unit was found to reduce the energy load of dehumidifying the air in buildings.[207] Innovative ideas, such as incorporating adsorbents into latex for paints,[9] coupled heating, ventilation, air conditioning, and DAC systems[524] offer the potential for energy-efficient ventilation and hygienically harmless provision strategies. **Table 6** summarizes the investigated operating conditions, CO_2 adsorption capacities, and desorption temperatures for indoor CO_2 removal.

Table 6 Technical specifications of indoor-air capture.

materials	Sorbent type	CO_2 (ppm)	Adsorption capacity (mmol g^{-1})	Desorption temperature (°C)	Desorption time (min)	Ref.
$PEI_{10,000}$-silica	monolith	5000	1.33/2.28 (dry/90% RH)	90	18/20	191
TEPA70	Powder	800	1.3/1.6 (15/50% RH)	25	180	189
		3000	1.33 (15% RH)			
	Paint	800	1.0/1.1 (15/50% RH)	25	180	
		3000	1.33 15% RH			
PEI50	Powder	800	0.9/1.0 (15/50% RH)	25	180	
		3000	1.1 (15% RH)			
	Paint	800	0.5/0.65 (15/50% RH)	25	180	
		3000	0.8 (15% RH)			
PEI-MR10	Resin	1000	2.06/2.27/2.72/2.92 (0/10/30/50% RH)	70	60	111
		500	2.2 (50% RH)			
		1500	2.98 (50% RH)			

2000	3.1 (50% RH)	

Considering that CO_2 adsorbents are still the subject of current research and are mostly available at small scales, their potential application in the building environment may offer easy market entry for commercial DAC installations in residential houses. Currently, indoor DAC only serves as a CO_2 transporter from buildings to the atmosphere. According to an estimation in Germany, ventilation systems transport 32 million tons of CO_2 per year.[524] Further studies are required to investigate the use of this amount of CO_2 as a carbon source.

7.4.2. CO_2 fertilization. CO_2 enrichment technologies used in cultivation not only boost yields but also help mitigate global warming. CO_2 fertilization can be accomplished using flue gas, which has disadvantages of such as high temperatures, contamination of SO_x/NO_x, toxic byproducts, and excessive CO_2 levels. To achieve the cultivation CO_2 concentrations of 1000–2000 ppm for terrestrial plants and 1%–6% for algae, DAC is deployable at reasonable costs.[212] Due to the moderate requirement of CO_2 concentration, desorption by steam or air is realizable, and desorption kinetics at mild temperatures 45–50 °C have been investigated.[174,208] The low regeneration temperature can be provided by waste heat or solar heating. A consensus has yet to be reached regarding the economic cost, safety, and environmental impact of DAC adsorbents. The decline in the fertilization effect of increasing CO_2 content, possibly resulting from the limitations of foliar nutrient concentrations, such as nitrogen and phosphorus, or water availability, should be taken care of in biological carbon fixation.[525]

Microalgae are increasingly being recognized as important CO_2 sequestration agents. Photosynthesis converts inorganic carbon into biochemical compounds, which can then be upgraded into products such as biofuels, biomedicine, and cosmetics through biorefinery.[213,526] Most microalgae thrive in the pH range of 7.0–8.4. The majority of carbon fixation by microalgae occurs through bicarbonate ions rather than the diffusive uptake of CO_2 in ambient air or dissolved in water.[526,527] Injecting concentrated CO_2 directly into

the culture medium lowers the pH and damages enzymes, causing growth inhibition and cell death. Furthermore, the CO_2 transportation cost from industrial sources was deemed to limit the microalgae production sites.[213] Therefore, DAC is an attractive option to provide a bicarbonate pool for microalgae production.[527]

DAC has also been used as a carbon source for the production of microbial food. The pilot scale Neo-Carbon Food in Finland employs a hybrid biological-inorganic process in which autotrophic hydrogen-oxidizing bacteria converts H_2 and O_2 (from water electrolysis) and CO_2 (from DAC) to protein.[209] Except for supplying H_2, O_2, and CO_2, microbial growth supported by more diverse chemicals, specifically methanol and formate produced from H_2 and CO_2, have also been discussed (**Fig. 60**).[210] Quantitative assessments show that microbial food production outperforms agricultural cultivation in terms of caloric and protein yield per land area, providing a compelling alternative to sustainable nutrition supplies.

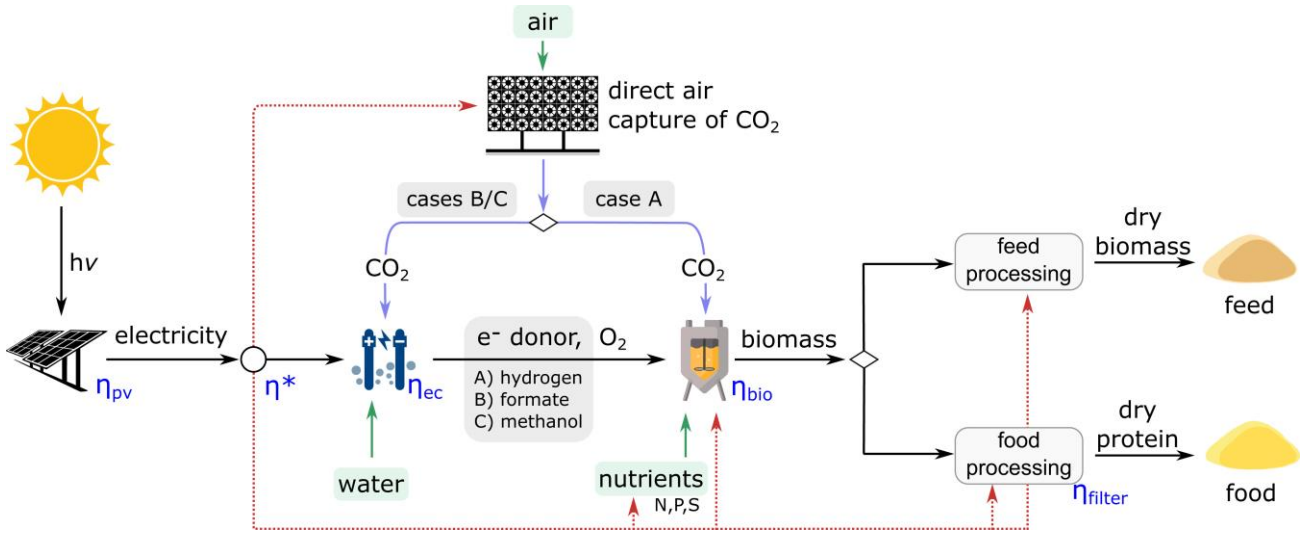

Fig. 60 Schematic representation of solar energy converted to biomass. When hydrogen (Case A) serves as an electron donor, CO_2 is supplied to the bioreactor along with the H_2 and O_2 produced in the electrochemical cell. When formate (case B) and methanol (case C) serve as electron donors, CO_2 is supplied to the electrochemical unit, and the only input gas supplied to the bioreactor is O_2 (Reproduced from ref. 210 with permission from National Academy of Sciences, copyright 2021).

7.4.3. Geological storage. CO_2 geological storage has substantial potential to handle large amounts of CO_2.[528] A recent assessment of 794 oil reservoirs and sedimentary basins for aquifer storage in 87 countries

revealed a potential storage capacity of 2,082 Gt with CO_2-enhanced oil recovery (CO_2-EOR) of 168 Gt (8%) and aquifer storage of 1914 Gt (92%).[529] CO_2, primarily from natural reservoirs, has been used for tertiary oil recovery in the SACROC field in the Permian Basin, Texas, since 1972.[530] In CO_2-EOR, CO_2 is injected into subsurface reservoirs to displace oil, and a large fraction is permanently trapped in different forms such as structural trapping, residual trapping, dissolution trapping, mineralization, and microbial methanogenesis.[530,531] In the traditional oil industry, this trap is considered as CO_2 retention, and the primary goal is to produce more oil with less CO_2. As CCUS is increasingly recognized for its climate portfolio, CO_2-EOR becomes economically and environmentally profitable by enhancing oil recovery and achieving CO_2 storage. Nonetheless, the source must be changed to anthropogenic CO_2 for negative emissions.[530,532] CO_2-enhanced gas recovery (CO_2-EGR) has been implemented for CO_2 sequestration and natural gas recovery, and is estimated to have a higher storage capacity of 390–750 Gt compared to 139–320 Gt of CO_2-EOR, while being more complex than CO_2-EOR.[533,534] At the moment, CO_2-EGR is mainly available at the pilot scale, and challenges such as CO_2/CH_4 separation cost due to miscibility, CO_2 injectivity, selection criteria for suitable depleted gas reservoirs for CO_2-EGR, and CO_2 leakage must be investigated.[535]

Transportation costs must be considered when using CO_2 from point-source carbon capture. In contrast, combining geological CO_2 storage with DAC technology can reduce transportation costs and ensure social acceptability, as CO_2 can be produced and stored in remote locations, such as deserts and offshore platforms. In 2019, Carbon Engineering and Oxy Low Carbon Ventures announced the design of a DAC facility to capture 500,000 tons of CO_2 per year for the EOR in the Permian Basin oil field. It was suggested that DAC-CO_2-EOR can provide an initial policy jumpstart to drive the DAC in the long run, but the trade-off between maximizing CO_2 storage and minimizing oil costs, among other issues, requires the deployment

of pressured policies.[530] While studies on DAC-CO_2-EGR are relatively rare, understanding the CO_2 and CH_4 adsorption mechanisms on the rock surface in CO_2-EGR may provide insights into the design of DAC adsorbents.

The identification of secure geological reservoirs is critical in minimizing the risks of unintended CO_2 release due to future leakage or seismic events, such as risk to human life due to rapid escape, risk to ecosystems such as water acidification, techno-economic risks such as public resistance and impediment to commercial deployment, waste of capital and energy resources of carbon capture, and malfunction of the carbon network.[244] Different methods have been developed for identifying secure storage sites based on geological data, such as depth, pressure, temperature, CO_2 density, reservoir thickness, and seal thickness. Machine learning tools, such as rough-set-based machine learning[244] and mixed-integer linear programing,[243] have been applied in conjunction with expert knowledge to classify storage sites. Special consideration has been given to false-positive decisions, which resulted in insecure sites being identified as secure, as well as false negative decisions. These algorithms aim for zero false positives and minimal false negative probabilities for decision-makers.

Furthermore, passive carbonation in mine tailing storage facilities or deposits is significant for offsetting greenhouse gas emissions or sequestration of CO_2 from DAC. Treatment strategies are being investigated to accelerate mineralization and base metal recovery.[239–242]

7.4.4. Conversion to fuels and chemicals. One of the most promising CO_2 destinations is the synthesis of carbon-based chemicals or fuels, which can improve the carbon and energy efficiencies of existing technologies and stimulate the development of new sustainable industrial processes. The use of CO_2, water, and renewable electricity as direct feedstocks for synthesis appears to be an appealing means of transitioning away from a reliance on fossil fuels.[222]

7.4.4.1. Nano-, micro- to mesoscopic scale studies. Green hydrogen produced by water splitting via electrolysis, thermolysis, photo-electrolysis, or biological processes is an important feedstock for the synthesis of hydrocarbons.[69,536] Recent research has been conducted in the integrated system of water splitting and DAC to produce CO_2, H_2, O_2, and electricity from solar energy.[71] To address the large air flowrates in DAC, a solar updraft tower was applied, and solar heated high temperature steam at 1000 °C was used to dry Na_2CO_3 solutions during sodium extraction. Heat recuperation and the direct use of renewable energy are critical for integrated DAC and synthesis systems. Schäppi *et al.*[537] designed a 5-kW pilot scale fuel production system entirely powered by solar energy. CO_2 and H_2O were both extracted directly from ambient air and converted to syngas before being further processed into liquid fuels, as shown in **Fig. 61**. Substantial improvements are required to upscale the thermochemical production of solar fuels.

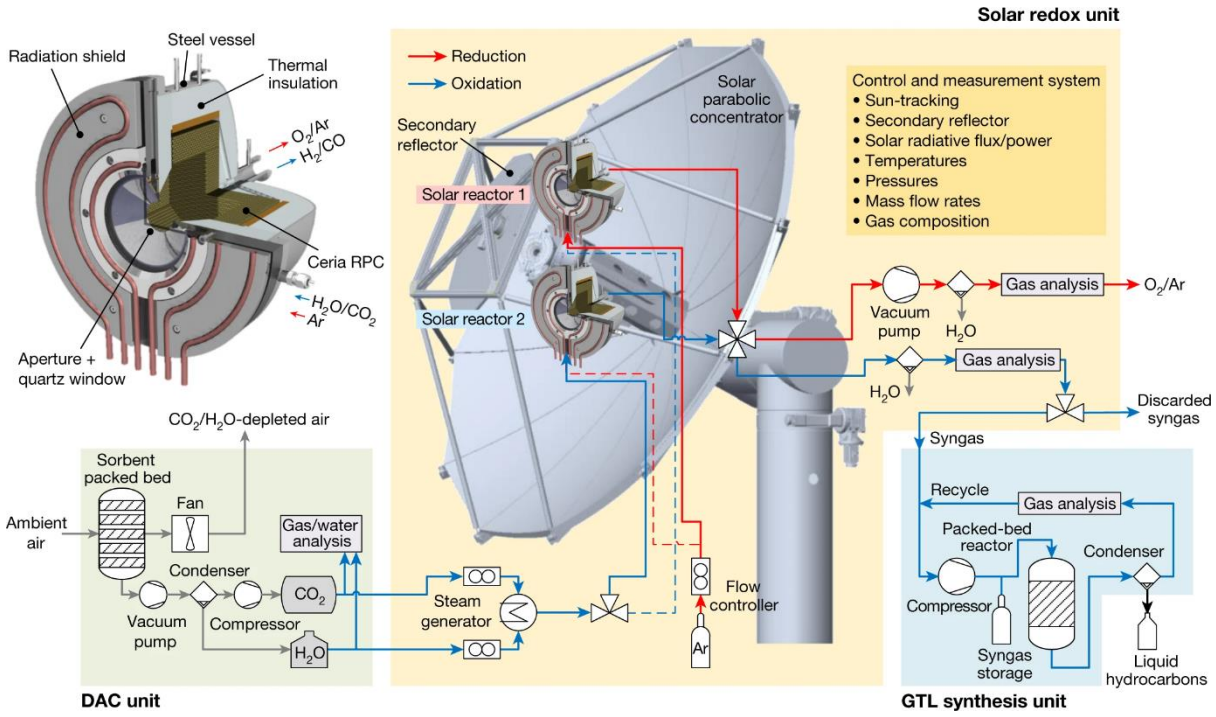

Fig. 61 5-kW pilot scale solar reactor design (Reproduced from ref. 537 with permission from Springer Nature, copyright 2022).

Methane can be transported and stored using existing infrastructure and used in current power and heat devices. Methanation, which is often considered a combination of Sabatier and CO methanation reactions,

has attracted much attention. A DAC/methanation process was designed in which the solid sorbent K_2CO_3/Al_2O_3[220,538,539] was used for DAC, and regeneration occurred in a hydrogen environment for further Sabatier conversion on the nickel catalyst NKM-2V.[220] More than 99% CO_2 conversion was achieved. Because of the deactivation of Ni-based catalysts at low temperatures caused by the reaction between Ni and CO, a Ru/Al_2O_3 catalyst was developed that can work at 325–400 °C, down from 425 °C for NKM-2V, with a promising conversion ratio of 98%.[540,541] Drechsler and Agar proposed an integrated DAC, electrolysis, and methanation process that focuses on synergies through process coupling.[66,68]

In addition to using highly concentrated CO_2, there are technologies that convert dilute CO_2 directly into hydrocarbons through DAC and *in situ* catalysis. Kosaka *et al.*[73] reported a Ni-based dual-functional catalyst, $Ni/Na\text{-}\gamma\text{-}Al_2O_3$, which was active in both CO_2 capture and methanation. Two steps of the reaction occurred in a fixed-bed reactor. Firstly, a dilute CO_2 gas was fed into the reactor, followed by purging to remove the unreacted CO_2. Finally, H_2 was fed into the reactor to reduce the CO_2. Thus, it can avoid the conventional CO_2 regeneration which requires large amounts of heat. Intermittent gas supply restricts productivity per unit time. It was shown that elevated pressure promoted both capture and conversion. For both high-concentration CO_2 (5–13%) and atmospheric concentrations (100–400 ppm), more than 90% CO_2 conversion and CH_4 selectivity were achieved. At atmospheric CO_2 concentrations, CH_4 production up to 160 μmol g^{-1}-catalyst has been reported. Catalyst degradation was reported to be insignificant when O_2 was present in the CO_2 capture process.

$Ce_{0.8}Zr_{0.2}O_2$ powder was found to be a multi-functional material for CO_2 adsorption and subsequent conversion to dimethyl carbonate under gaseous methanol stream feeding, despite the product being at the ppm level.[235] This study was meaningful because the conversion occurred at atmospheric pressure and a mild temperature range of 70–110 °C.

Methanol (MeOH) is one of the most important feedstocks in the chemical industry.[542,543] It can also be used to directly produce renewable fuels or power fuel cells. CO_2 can be converted to CO first and then to MeOH; alternatively, it can be directly reduced to MeOH. Smith *et al.*[222] investigated a solar-powered integrated system of DAC, electrolysis, and MeOH synthesis. The five processes considered included photovoltaic solar energy to electricity, DAC based on potassium hydroxide solvent, bipolar membrane electrodialysis for regeneration, electrolysis of water and CO_2 to produce CO and H_2, and methanol synthesis using Cu/ZnO-based catalysts (**Fig. 62**). This study emphasized the role of a CO_2 electrolyzer in the PtX process and aimed to provide relevant studies to contribute to energy transition.

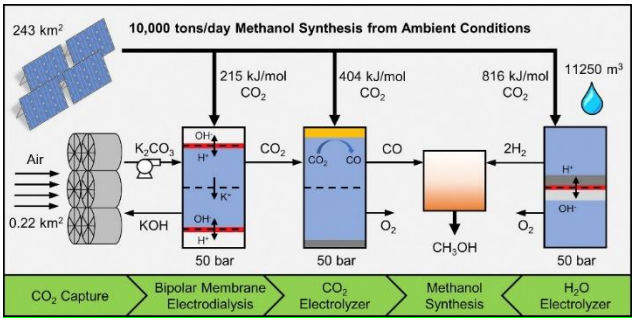

Fig. 62 Integrated DAC, electrolysis, and methanol synthesis system using a CO_2 electrolyzer (Reproduced from ref. 222 with permission from Elsevier, copyright 2019).

Bos *et al.*[544] designed a liquid out/gas in concept reactor (LOGIC) for the direct conversion of CO_2 to MeOH based on a commercial Cu/ZnO/Al_2O_3 catalyst. This design was later used to assess the cost and efficiency of wind power in the MeOH system.[69] Sen *et al.*[221,545,546] developed a one-pot DAC-MeOH system using alkali hydroxide in ethylene glycol for CO_2 capture from air and subsequent *in situ* conversion to methanol through Ru-PNP catalysts. In an integrated single-tank system, such a process proceeds at mild temperatures (100–140 °C) and yields 60% MeOH conversion rate. Unfortunately, dehydrogenation of ethylene glycol and the formation of carboxylates were observed. A later work[546] investigated the glycol solvent-assisted conversion of CO_2 and H_2 to MeOH using a Cu/ZnO/Al_2O_3 catalyst. The use of non-noble metal-based catalysts is advantageous for commercial applications. Similar eletroreduction of CO_2 is shown

in **Fig. 63**.[72]

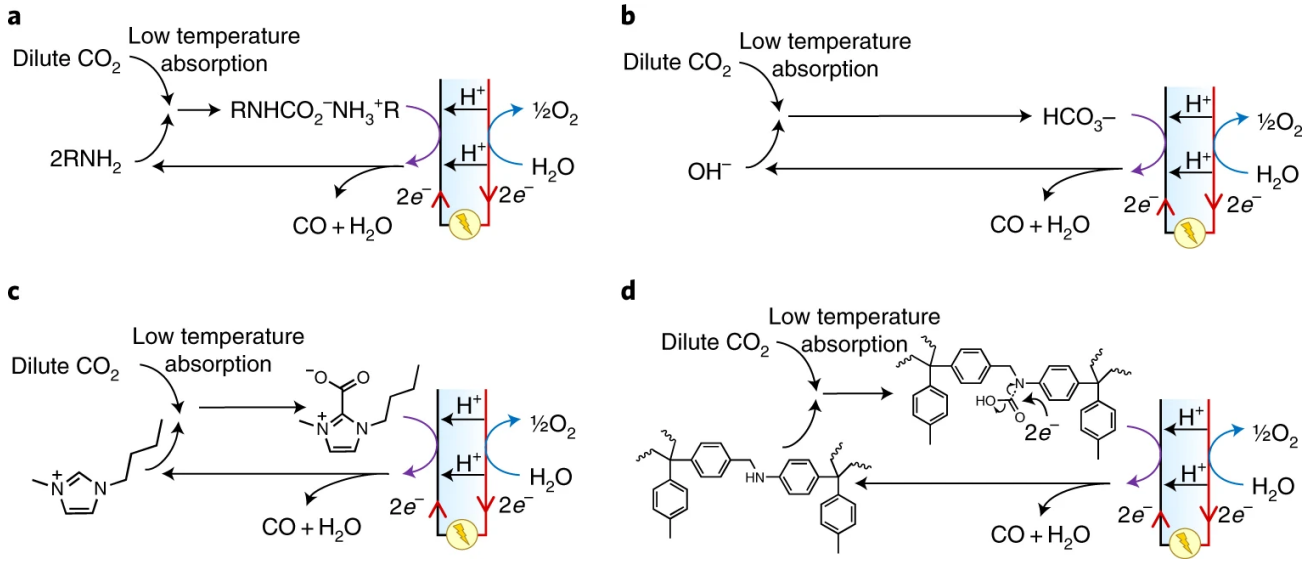

Fig. 63 Coupled CO_2 capture and *in situ* electroreduction (Reproduced from ref. 72 with permission from Springer Nature, copyright 2021).

For the aviation and heavy-duty transportation sectors, the use of synthetic liquid fuels is considered an effective way to achieve carbon neutrality. According to a recent analysis,[230] the share of CO_2 from DAC for the production of Power-to-Liquid demonstrated a maximum quota of up to 50% by 2050 for Germany. Fischer-Tropsch synthesis is commonly used to produce drop-in fuels.[228,230,232,233] A renewable energy driven pilot plant (SOLETAIR) has been experimentally demonstrated in 2017 in Finland.[231] The pilot plant consisted of a solar PV power plant, an amine-functioned DAC unit, a PEM water electrolyzer for hydrogen production, a RWGS, and a cobalt-based catalytic F-T synthesis unit, and produced 6.2 kg day^{-1} of combined F-T oil and wax.

The production of other chemicals, such as carbon nanotubes,[234] urea, and its derivatives,[547,548] and carboxylic acids[549] from atmospheric air is also technically feasible, but further scaling-up verification is currently lacking.

7.4.4.2. Integrated system. An integrated PtX system requires the integration of mass and/or energy between different processes in the pursuit of high degrees of synergy. For instance, under an appropriate electrolysis

cell voltage, the heat requirement of the DAC-electrolysis-methanation system can be compensated for by the exothermic Sabatier reaction and vapor condensation heat release.[66,68] Water recycling from co-adsorption in DAC, evaporation in electrolysis, and generation in the methanation process allows not only minor water loss but also energy integration. The theoretical energy and mass recirculation in SOLETAIR provides a promising energy efficiency of 47% and a carbon efficiency of 94%.[231] Careful consideration should be paid to the operation pressure, temperature, electrolysis cell voltage, slip streams of air in the DAC, and hydrogen loss.

7.4.4.3. National scale analysis. Synthetic chemicals and fuels from DAC have been demonstrated to be critical for achieving a national scale transition to 100% renewable energy. Bridging technologies allow for stronger coupling of all these sectors. For instance, DAC connects the power, heat, transportation, and industry sectors. An analysis of the Philippines' path to 2050 reveals that synthetic fuel, using DAC-CO_2 as the feedstock, facilitates sustainability in the transportation sector, particularly in marine and aviation transport.[227] In another modelling for the power, heat, transport, and industry sectors in Kazakhstan,[247] DAC requires heat from the heat generation system. The excess heat from synthetic fuel production can cover a portion of the low-temperature heat demand for district heating systems. F-T synthesis using DAC-CO_2 and H_2 from water electrolysis as feedstock supplies byproducts, such as naphtha, to chemical industry. All these technologies are based on electricity from the power sector. Additional flexibility is mainly provided to the energy system by electrolyzers. Integration of sectors with more flexible demands, lower final product storage costs, or the ability to alleviate the mismatch between overall energy supply and demand, reduces the levelized cost of energy and accelerates the defossilization of the power sector. In a study on global green ammonia production,[67] it was mentioned that the waste heat from the Haber-Bosch unit and electrolysis process can be used in DAC systems. Moreover, using waste heat from fusion power plants to

power a low-temperature DAC was found to reduce the effective fusion levelized cost of electricity by approximately 35%.[246]

7.4.4.4. Techno-economic analysis. In a comparison between DAC-CCS and DAC-CCU to MeOH,[223] it was concluded that DAC-CCS was better than DAC-CCU using indexes of CO_2 mitigation potential and cost. However, when carbon taxes, electricity prices, and learning rates are considered, CCU was demonstrated to be more competitive than the business-as-usual scenario under certain conditions. Some studies may have overestimated the CCU cost and its reliance on electricity because heat requirements were assumed to be met by electricity without any heat integration.[229] Some have focused on the effects of different sources of CO_2 and H_2. Do *et al.*[550] provided an analysis focusing on eight final products and four conversion technologies and concluded that H_2 price was the dominant factor in the unit production cost. However, the variations in costs of CO_2 capture from different pathways were not considered in this work, which could have a significant impact.[222] Tavasoli *et al.*[236] considered various CO_2 feedstocks from petrochemical, biogas, landfill gas, flue gas, and DAC for the photocatalytic dry reforming process as shown in **Fig. 64**; in most cases, the required catalyst activity enables the feedstock to compete with petrochemical alternatives. The highest production cost comes from using biogas as the feedstock option, which differs from other studies.[37] While in other studies, DAC in combination with H_2 from electrolysis produced more costly methane compared to others such as point sources and biogas.[219]

Fig. 64 Potential feedstock sources and downstream products that can be converted into or made from synthesis gas (or syngas) produced via solar dry reforming.[236]

Techno-economic analyses also directly show the extent of cost reduction using different approaches, efficiencies, and production costs of different energy carriers. For the production of liquefied synthetic methane based on DAC and electrolysis, various approaches including DAC system redesign, energy integration, and scale-up were demonstrated to reduce the DAC cost from 557 \$ t^{-1} to 114 \$ t^{-1}.[215] Comparing methane and H_2, although the power-to-hydrogen pathway was more efficient than the power-to-methane pathway, it was more expensive due to the hydrogen storage costs. In general, DAC and electrolyzer costs account for a large portion of the overall production costs and determine the overall energy efficiencies.[69,215,218,224,228]

Emphasis was also given to the cost of using different renewable energies and the inflexibility of processes, such as DAC, water desalination plants, and fuel synthesis. Berger *et al.*[217] studied methane production in North Africa using a combination of solar and wind energy as well as its delivery to northwestern European markets. Sensitivity analysis showed that the full electricity supply from solar PV was more expensive than that in the combination case. Wind power is sometimes considered to have greater carbon reduction than solar energy because of the carbon-intensive manufacturing of solar panels.[233] Curtailment was observed due to the inflexible processes despite the consideration of various storage nodes; thus, relaxing the inflexibility was presumed to have a pronounced impact on the plant design.[217,228] A more complicated study considered different chemical production routines, such as FA-routine and direct-routine for OME_1 production. Thus, the most energy-efficient and environmentally beneficial combination could be identified.[37,224]

By analyzing efficiencies, costs, and physical sizes, techno-economic analysis can also be used to identify gaps between current technologies and scaled plants. For industrial-scale solar-driven methanol production,[222] the physical sizes required for each sub-process were compared with the largest

existing/planned plants, and significant gaps for DAC and CO_2 electrolysis of three and six orders of magnitude, respectively, were determined. A similar analysis is necessary for adsorption-based DAC technologies to understand the ability to scale-up to sizes required to have a global impact, as well as the gaps in operating conditions and scales between research and industrial applications.

8. Perspectives and conclusions

In this paper, the state-of-the-art progress in the development of DAC technology in the fields of material synthesis, adsorption mechanism, system design, and application was presented and discussed. Adsorption-based DAC has experienced rapid development during the last decade, especially through the extensive exploration of amine-functionalized porous silicas, zeolites, MOFs, carbons, resins, and LDHs as air capture materials. At the same time, a better understanding of the correspondence of the structure, functionalization, and properties of supports is required. To improve the technical feasibility of DAC, it is necessary to develop an efficient gas-solid contactor that combines adsorbent research and separation processes. Additionally, systematic and in-depth techno-economic analyses of the large-scale application of DAC *via* adsorption are still lacking.

The key metrics for evaluating the effectiveness of DAC adsorbents include the CO_2 selectivity of the adsorbent in the presence of other gas compounds, CO_2 working capacity of the adsorbent during adsorption-desorption cycling, adsorption and desorption kinetics, energy required for the cycle or regenerative adsorption, chemical stability, mechanical stress robustness of the adsorbent during long-term cycling, as well as economic and environmental viability of the adsorbent in the cradle-to-grave full life cycle assessment. The final evaluation of adsorbents requires the analysis of the material structure (*e.g.*, particles, fibers, and monoliths) in a full-scale process, possible cycle configurations (*e.g.*, temperature,

pressure, and concentration changes), and adsorption unit configurations (*e.g.*, fixed-bed, fluidized-bed, and rotating-bed). New materials, devices, and architectures are likely to be developed collaboratively to meet the current and future carbon-capture needs.

Recent work indicates the importance of a better understanding of the synergistic enhancement between amines and supports. Polyamine-impregnated ordered mesoporous silica is still the most promising DAC adsorbent, with a good balance between capture performance and cost. The concept of "mixed-polyamines", which has been successfully adopted in amine solvent systems, may be attractive to further enhance the amine efficiencies.[551] While amine loading is considered to be the main factor determining the CO_2 adsorption capacity of DAC adsorbents, the texture characteristics and surface microstructure of the support also significantly affect the overall CO_2-capture efficiency. Amine-functionalized LDHs and LDH-derived mixed oxides are a new family of DAC adsorbents, which either have unexpectedly high adsorption capacities[107,317] or ultrafast kinetics[116] under ultradilute conditions. LDHs can form ideal CO_2 diffusion channels with the help of slit-like mesopores from exfoliated nanosheets and additional pore creation during calcination. Even in the absence of additives, amines can be strongly attached and well-dispersed over defect-rich LDHs. Furthermore, the morphology and chemical properties of LDHs can be adjusted by changing the types and ratios of divalent and trivalent metal cations, as well as interlayer anions; thus, providing infinite possibilities for the assembly of DAC adsorbents. More importantly, LDHs can be massively produced and shaped at a low cost, typically in the range of 2–8 \$ kg^{-1}.

Prototypical polyamines degrade oxidatively at elevated temperatures. For instance, temperatures above 70 °C cause the oxidative degradation of Lewatit VP OC 1065, a commercialized DAC adsorbent. Therefore, preventing oxidative degradation is an important topic that should be widely explored. To date, TEPA-loaded adsorbents that anchored PEI have exhibited very high CO_2 adsorption capacities under

various operating temperatures,[112] but they become less stable at elevated temperatures. It would be highly attractive if the thermal and oxidative stability of supported TEPA or other novel amines could be enhanced through surface modification and additives. Balancing the CO_2 adsorption capacity, manufacturing costs, and oxidative resistance is an additional challenge.

In addition to O_2, the effect of water vapor in the air on CO_2 adsorption is critical. The co-adsorption and desorption of H_2O and CO_2, followed by solar-driven catalytic conversion, has proved to be technically feasible for producing drop-in fuels from air,[537] and the improvement of efficiencies relies on an in-depth understanding of the co-adsorption behavior on DAC adsorbents. The establishment of mechanistic co-adsorption isotherm models for Lewatit VP OC 1065 is a meaningful attempt. Further work can be conducted on the high-throughput screening of the co-adsorption properties of H_2O and CO_2 on new amine-functionalized DAC adsorbents. The development of hydrophobic DAC adsorbents may also be useful in specific applications to avoid amine leaching, increased regeneration energy, and structural degradation due to H_2O co-adsorption. Although several ultramicroporous physisorbents have been confirmed to exhibit trace CO_2-capture capacities with low water affinities,[552–554] the development of hydrophobic amine-containing adsorbents for DAC is still less explored.

The exact chemisorbing CO_2 species on the surface of the aminopolymer under ultradilute conditions is still under debate because of the overlap of the IR bands and signal loss in conventional experiments. Combining advanced *in situ* spectroscopy and theoretical approaches can provide a molecular-level understanding of the CO_2 adsorption mechanism on DAC adsorbents. Notably, the existence of hydrated bicarbonate through CO_2 chemisorption has been confirmed previously.[141] Further mechanistic studies on DAC adsorbents are required to investigate the role of hydrogen bonding as a CO_2 binder, the effect of

densities and types of surface amines, the inconsistency of amine efficiency with the theoretical value, the enhancement upon exposure to H_2O, and the detailed pathway leading to the adsorption of CO_2 on amines. Several novel DAC adsorbents have been reviewed. Amine-tethered MOFs are a series of adsorbents with great potential for DAC, despite most recent research focusing on their application at higher CO_2 concentrations. While diamine-tethered Mg_2(dobpdc) maintain a record CO_2 adsorption capacity of 3 mmol/g at 0.4 mbar due to the synergistic insertion adsorption mechanism,[422] MOF-based materials are too expensive to be synthesized on a large scale. Finding inexpensive alternative supports, with abundant coordinatively unsaturated metals, is appealing for the large-scale synthesis of such adsorbents. LDH-derived materials containing high-density coordinatively unsaturated sites may be a potential choice. For instance, ultrathin and ultrafine ZnAl-LDH with abundant unsaturated Zn has been successfully used to achieve efficient photocatalytic CO_2 reduction.[555]

Special attention should also be paid to the design of gas-solid gas contactors with extremely low pressure drops and enhanced heat and mass transfer. Surprisingly, while rotating wheel-based contactors meet the abovementioned requirements, they have not yet been used for DAC. In addition, numerous experiments are required to verify the feasibility of structured-adsorbent enlargement. Studies on the DAC performance of structured adsorbents are limited; thus, a good understanding of adsorbent-shaping optimization is required. Novel shaping techniques, such as fiber spinning and 3D printing, are powerful tools for the early-stage structure design, and coating and extrusion are more likely applied for scale-up fabrication.[556] As 80% of the energy consumption of DAC comes from the regeneration stage, using renewable energy or industrial waste heat-driven steam purge, under negative pressures and reduced regeneration temperatures, can effectively reduce the DAC operating costs.[180]

Distributed DAC systems have the potential to achieve considerable social and environmental impacts. By boosting plants, DAC fertilization for the production of food, feed, or other biochemical compounds can help tackle global hunger. A portable DAC system for controlling air quality can benefit every home. For a synergistic DAC coupled with CO_2 conversion, a novel power system capable of delivering chemicals, work, and heat could be a new option in the transportation sector. A viable starting point could be DAC combined with dry reforming or electrochemical conversion for both carbon reduction and energy storage. Chemical energy can be converted into work and power *via* syngas combustion or fuel cells. Commercialized equipment and a comprehensive techno-economic analysis are still urgently required. For a holistic analysis, machine learning applied to DAC-related complex systems featuring multiple variables or options is also worth studying, as it is expected to provide the most viable or cost-effective technical path.

The current knowledge on climate reveals that combining low-carbon energy or renewable energy with a DAC system is crucial for reducing the effects of CO_2 on the global climate. At present, wind and photovoltaic power are proposed to drive the regeneration of the DAC system. Continuous research should be conducted to investigate the thermodynamic match between DAC and renewable sources. Additionally, actual demonstration systems are required. Other types of low-carbon energy, for example, low-grade waste heat, and geothermal energy, can also be considered. However, the CO_2 emissions caused by energy utilization should be carefully considered; otherwise, the advantages of DAC can be easily negated.

DAC can be recognized as a separate air handling system; in other words, it removes CO_2 from ambient air even though the concentration is ultra-diluted, similar to how the widely adopted air conditioning/purification system removes water vapor/contaminants from the atmosphere. As many adsorbents are also effective in adsorbing water vapor and contaminants, future research should focus on

developing adsorption systems that can remove both CO_2 and water vapor. This can be realized by exploiting suitable adsorbents that can simultaneously remove CO_2 and water vapor and regenerate them at a similar energy consumption. An air conditioning system is necessary even in the carbon-neutralization period if its energy for regeneration can also be utilized to drive CO_2 reduction; that is, no auxiliary material and energy are consumed by the DAC. As mentioned earlier, the present LCA results confirmed that the adverse environmental effects of DAC mainly originate from material and energy sources; thus, such a system is worth investigating.

Conflicts of interest

There are no conflicts to declare.

Acknowledgements

This work was supported by the National Natural Science Foundation of China (52006135), the Shanghai Agriculture Science and Technology Program (2022-02-08-00-12-F01176), the International Science and Technology Cooperation Project (20160712800), and the Science and Technology Commission of Shanghai Municipality (21DZ1206200). W. Xie is grateful for the financial support from the Deutsche Forschungsgemeinschaft (DFG, German Research Foundation) under Project Number 229243862. J. Li would like to thank the financial support from the National Natural Science Foundation of China (72140008).

Reference

1. D. Welsby, J. Price, S. Pye and P. Ekins, *Nature*, 2021, **597**, 230-234.
2. S. Uden, P. Dargusch and C. Greig, *Joule*, 2021, **5**, 1956-1970.
3. B. S. Koelbl, M. A. van den Broek, A. P. C. Faaij and D. P. van Vuuren, *Climatic Change*, 2014, **123**, 461-476.
4. J. Rogelj, G. Luderer, R. C. Pietzcker, E. Kriegler, M. Schaeffer, V. Krey and K. Riahi, *Nat. Clim. Change*, 2015, **5**, 519-527.
5. K. Zickfeld, D. Azevedo, S. Mathesius and H. D. Matthews, *Nat. Clim. Change*, 2021, **11**, 613-617.
6. J. O. Asibor, P. T. Clough, S. A. Nabavi and V. Manovic, *J. Environ. Manage.*, 2021, **294**, 113039.
7. M. Bui, C. S. Adjiman, A. Bardow, E. J. Anthony, A. Boston, S. Brown, P. S. Fennell, S. Fuss, A. Galindo, L. A. Hackett, J. P. Hallett, H. J. Herzog, G. Jackson, J. Kemper, S. Krevor, G. C. Maitland, M. Matuszewski, I. S. Metcalfe, C. Petit, G. Puxty, J. Reimer, D. M. Reiner, E. S. Rubin, S. A. Scott, N. Shah, B. Smit, J. P. M. Trusler, P. Webley, J. Wilcox and N. Mac Dowell, *Energ. Environ. Sci.*, 2018, **11**, 1062-1176.
8. F. Stenzel, P. Greve, W. Lucht, S. Tramberend, Y. Wada and D. Gerten, *Nat. Commun.*, 2021, **12**, 1512.
9. L. T. Keyßer and M. Lenzen, *Nat. Commun.*, 2021, **12**, 2676.
10. D. P. Keller, A. Lenton, V. Scott, N. E. Vaughan, N. Bauer, D. Ji, C. D. Jones, B. Kravitz, H. Muri and K. Zickfeld, *Geosci. Model Dev.*, 2018, **11**, 1133-1160.
11. J. Fuhrman, H. McJeon, P. Patel, S. C. Doney, W. M. Shobe and A. F. Clarens, *Nat. Clim. Change*, 2020, **10**, 920-927.
12. S. Pradhan, W. M. Shobe, J. Fuhrman, H. McJeon, M. Binsted, S. C. Doney and A. F. Clarens, *Frontiers in Climate*, 2021, **3**, 660787.
13. C. Chen and M. Tavoni, *Climatic Change*, 2013, **118**, 59-72.
14. S. Fuss, W. H. Reuter, J. Szolgayová and M. Obersteiner, *Climatic Change*, 2013, **118**, 73-87.
15. A. Marcucci, S. Kypreos and E. Panos, *Climatic Change*, 2017, **144**, 181-193.
16. J. Strefler, N. Bauer, E. Kriegler, A. Popp, A. Giannousakis and O. Edenhofer, *Environ. Res. Lett.*, 2018, **13**, 044015.
17. G. Realmonte, L. Drouet, A. Gambhir, J. Glynn, A. Hawkes, A. C. Köberle and M. Tavoni, *Nat. Commun.*, 2019, **10**, 3277.
18. S. D. Supekar, T.-H. Lim and S. J. Skerlos, *Environ. Res. Lett.*, 2019, **14**, 084013.
19. J. E. T. Bistline and G. J. Blanford, *Nat. Commun.*, 2021, **12**, 3732.
20. I. Butnar, O. Broad, B. Solano Rodriguez and P. E. Dodds, *GCB Bioenergy*, 2020, **12**, 198-212.
21. S. Chatterjee and K.-W. Huang, *Nat. Commun.*, 2020, **11**, 3287.
22. E. Cox, E. Spence and N. Pidgeon, *Nat. Clim. Change*, 2020, **10**, 744-749.
23. G. Realmonte, L. Drouet, A. Gambhir, J. Glynn, A. Hawkes, A. C. Köberle and M. Tavoni, *Nat. Commun.*, 2020, **11**, 3286.
24. R. Hanna, A. Abdulla, Y. Xu and D. G. Victor, *Nat. Commun.*, 2021, **12**, 368.
25. S. Jenkins, E. Mitchell-Larson, M. C. Ives, S. Haszeldine and M. Allen, *Joule*, 2021, **5**, 2777-2796.
26. J. Strefler, E. Kriegler, N. Bauer, G. Luderer, R. C. Pietzcker, A. Giannousakis and O. Edenhofer, *Nat. Commun.*, 2021, **12**, 2264.
27. *Net Zero by 2050 - A Roadmap for the Global Energy Sector*, International Energy Agency (IEA), 2021. https://www.iea.org/events/net-zero-by-2050-a-roadmap-for-the-global-energy-system
28. J. Fuhrman, A. Clarens, K. Calvin, S. C. Doney, J. A. Edmonds, P. O'Rourke, P. Patel, S. Pradhan, W. Shobe and H. McJeon, *Environ. Res. Lett.*, 2021, **16**, 114012.
29. *Annual Report* of *Carbon Capture, Utilization, and Storage in China*, Chinese Academy of Environmental Planning, 2021. http://www.caep.org.cn/sy/dqhj/gh/202107/t20210725_851241.shtml
30. E. Kato and A. Kurosawa, *Sustain. Sci.*, 2021, **16**, 463-475.
31. C. Pozo, Á. Galán-Martín, D. M. Reiner, N. Mac Dowell and G. Guillén-Gosálbez, *Nat. Clim. Change*, 2020, **10**, 640-

646.
32. K. Riahi, C. Bertram, D. Huppmann, J. Rogelj, V. Bosetti, A.-M. Cabardos, A. Deppermann, L. Drouet, S. Frank, O. Fricko, S. Fujimori, M. Harmsen, T. Hasegawa, V. Krey, G. Luderer, L. Paroussos, R. Schaeffer, M. Weitzel, B. van der Zwaan, Z. Vrontisi, F. D. Longa, J. Després, F. Fosse, K. Fragkiadakis, M. Gusti, F. Humpenöder, K. Keramidas, P. Kishimoto, E. Kriegler, M. Meinshausen, L. P. Nogueira, K. Oshiro, A. Popp, P. R. R. Rochedo, G. Ünlü, B. van Ruijven, J. Takakura, M. Tavoni, D. van Vuuren and B. Zakeri, *Nat. Clim. Change*, 2021, **11**, 1063-1069.
33. F. Babonneau, A. Badran, M. Benlahrech, A. Haurie, M. Schenckery and M. Vielle, *Climatic Change*, 2021, **165**, 64.
34. S. Deutz and A. Bardow, *Nat. Energy*, 2021, **6**, 203-213.
35. S. J. Davis, N. S. Lewis, M. Shaner, S. Aggarwal, D. Arent, I. L. Azevedo, S. M. Benson, T. Bradley, J. Brouwer, Y.-M. Chiang, C. T. M. Clack, A. Cohen, S. Doig, J. Edmonds, P. Fennell, C. B. Field, B. Hannegan, B.-M. Hodge, M. I. Hoffert, E. Ingersoll, P. Jaramillo, K. S. Lackner, K. J. Mach, M. Mastrandrea, J. Ogden, P. F. Peterson, D. L. Sanchez, D. Sperling, J. Stagner, J. E. Trancik, C.-J. Yang and K. Caldeira, *Science*, 2018, **360**, eaas9793.
36. C. van der Giesen, C. J. Meinrenken, R. Kleijn, B. Sprecher, K. S. Lackner and G. J. Kramer, *Environ. Sci. Technol.*, 2017, **51**, 1024-1034.
37. S. Deutz, D. Bongartz, B. Heuser, A. Kätelhön, L. Schulze Langenhorst, A. Omari, M. Walters, J. Klankermayer, W. Leitner, A. Mitsos, S. Pischinger and A. Bardow, *Energ. Environ. Sci.*, 2018, **11**, 331-343.
38. F. Creutzig, C. Breyer, J. Hilaire, J. Minx, G. P. Peters and R. Socolow, *Energ. Environ. Sci.*, 2019, **12**, 1805-1817.
39. M. Z. Jacobson, *Energ. Environ. Sci.*, 2019, **12**, 3567-3574.
40. G. Mori, S. Coccolo, R. Castello and J.-L. Scartezzini, *Journal of Physics: Conference Series*, 2019, **1343**, 012118.
41. N. Thonemann and M. Pizzol, *Energ. Environ. Sci.*, 2019, **12**, 2253-2263.
42. P. Arora, R. Chance, H. Hendrix, M. J. Realff, V. M. Thomas and Y. Yuan, *J. CO2 Util.*, 2020, **40**, 101213.
43. C. M. Liu, N. K. Sandhu, S. T. McCoy and J. A. Bergerson, *Sustain. Energ. Fuels*, 2020, **4**, 3129-3142.
44. A. Schreiber, A. Peschel, B. Hentschel and P. Zapp, *Front. Energy Res.*, 2020, **8**, 533850.
45. J. Sillman, V. Uusitalo, V. Ruuskanen, L. Ojala, H. Kahiluoto, R. Soukka and J. Ahola, *Int. J. Life Cycle Ass.*, 2020, **25**, 2190-2203.
46. J. B. Wevers, L. Shen and M. van der Spek, *Front. Energy Res.*, 2020, **8**, 104.
47. K. Madhu, S. Pauliuk, S. Dhathri and F. Creutzig, *Nat. Energy*, 2021, **6**, 1035-1044.
48. D. F. Rodríguez-Vallejo, A. Valente, G. Guillén-Gosálbez and B. Chachuat, *Sustain. Energ. Fuels*, 2021, **5**, 2504-2516.
49. U. Singh and L. M. Colosi, *Appl. Energ.*, 2021, **285**, 116394.
50. T. Terlouw, C. Bauer, L. Rosa and M. Mazzotti, *Energ. Environ. Sci.*, 2021, **14**, 1701-1721.
51. D. W. Keith, G. Holmes, D. St. Angelo and K. Heidel, *Joule*, 2018, **2**, 1573-1594.
52. S. U. Rege, R. T. Yang and M. A. Buzanowski, *Chem. Eng. Sci.*, 2000, **55**, 4827-4838.
53. L. A. DallBauman and J. E. Finn, in *Stud. Surf. Sci. Catal.*, ed. A. Dąbrowski, Elsevier, 1999, vol. 120, pp. 455-471.
54. B. R. Sutherland, *Joule*, 2019, **3**, 1571-1573.
55. P. Smith, S. J. Davis, F. Creutzig, S. Fuss, J. Minx, B. Gabrielle, E. Kato, R. B. Jackson, A. Cowie, E. Kriegler, D. P. van Vuuren, J. Rogelj, P. Ciais, J. Milne, J. G. Canadell, D. McCollum, G. Peters, R. Andrew, V. Krey, G. Shrestha, P. Friedlingstein, T. Gasser, A. Grübler, W. K. Heidug, M. Jonas, C. D. Jones, F. Kraxner, E. Littleton, J. Lowe, J. R. Moreira, N. Nakicenovic, M. Obersteiner, A. Patwardhan, M. Rogner, E. Rubin, A. Sharifi, A. Torvanger, Y. Yamagata, J. Edmonds and C. Yongsung, *Nat. Clim. Change*, 2016, **6**, 42-50.
56. J. Bednar, M. Obersteiner, A. Baklanov, M. Thomson, F. Wagner, O. Geden, M. Allen and J. W. Hall, *Nature*, 2021, **596**, 377-383.
57. V. Nikulshina, M. E. Gálvez and A. Steinfeld, *Chem. Eng. J.*, 2007, **129**, 75-83.
58. J. K. Stolaroff, D. W. Keith and G. V. Lowry, *Environ. Sci. Technol.*, 2008, **42**, 2728-2735.
59. C. A. Seipp, N. J. Williams, M. K. Kidder and R. Custelcean, *Angew. Chem. Int. Edit.*, 2017, **56**, 1042-1045.
60. F. M. Brethomé, N. J. Williams, C. A. Seipp, M. K. Kidder and R. Custelcean, *Nat. Energy*, 2018, **3**, 553-559.

61. R. Custelcean, *Chem*, 2021, **7**, 2848-2852.
62. R. Custelcean, K. A. Garrabrant, P. Agullo and N. J. Williams, *Cell Reports Physical Science*, 2021, **2**, 100385.
63. J. Wilcox, R. Haghpanah, E. C. Rupp, J. He and K. Lee, *Annu. Rev. Chem. Biomol.*, 2014, **5**, 479-505.
64. M. Erans, E. S. Sanz-Pérez, D. P. Hanak, Z. Clulow, D. M. Reiner and G. A. Mutch, *Energ. Environ. Sci.*, 2022, DOI: 10.1039/d1ee03523a.
65. A. Gambhir and M. Tavoni, *One Earth*, 2019, **1**, 405-409.
66. C. Drechsler and D. W. Agar, *Appl. Energ.*, 2020, **273**, 115076.
67. M. Fasihi, R. Weiss, J. Savolainen and C. Breyer, *Appl. Energ.*, 2021, **294**, 116170.
68. C. Drechsler and D. W. Agar, *Int. J. Greenh. Gas Con.*, 2021, **105**, 103230.
69. M. J. Bos, S. R. A. Kersten and D. W. F. Brilman, *Appl. Energ.*, 2020, **264**, 114672.
70. V. Gutknecht, S. Ó. Snæbjörnsdóttir, B. Sigfússon, E. S. Aradóttir and L. Charles, *Energy Procedia*, 2018, **146**, 129-134.
71. C. Brady, M. E. Davis and B. Xu, *P. Natl. Acad. Sci. USA*, 2019, **116**, 25001-25007.
72. I. Sullivan, A. Goryachev, I. A. Digdaya, X. Li, H. A. Atwater, D. A. Vermaas and C. Xiang, *Nat. Catal.*, 2021, **4**, 952-958.
73. F. Kosaka, Y. Liu, S.-Y. Chen, T. Mochizuki, H. Takagi, A. Urakawa and K. Kuramoto, *ACS Sustain. Chem. Eng.*, 2021, **9**, 3452-3463.
74. S. Lawson, K. Baamran, K. Newport, T. Alghamadi, G. Jacobs, F. Rezaei and A. A. Rownaghi, *Appl. Catal. B-Environ.*, 2022, **303**, 120907.
75. N. Grant, A. Hawkes, S. Mittal and A. Gambhir, *Joule*, 2021, **5**, 2593-2605.
76. V. Campbell-Arvai, P. S. Hart, K. T. Raimi and K. S. Wolske, *Climatic Change*, 2017, **143**, 321-336.
77. J. Hansen, M. Sato, P. Kharecha, K. von Schuckmann, D. J. Beerling, J. Cao, S. Marcott, V. Masson-Delmotte, M. J. Prather, E. J. Rohling, J. Shakun, P. Smith, A. Lacis, G. Russell and R. Ruedy, *Earth Syst. Dynam.*, 2017, **8**, 577-616.
78. K. S. Wolske, K. T. Raimi, V. Campbell-Arvai and P. S. Hart, *Climatic Change*, 2019, **152**, 345-361.
79. P. Viebahn, A. Scholz and O. Zelt, *Energies*, 2019, **12**, 3443.
80. H. A. Daggash, C. F. Heuberger and N. Mac Dowell, *Int. J. Greenh. Gas Con.*, 2019, **81**, 181-198.
81. H. Azarabadi and K. S. Lackner, *Appl. Energ.*, 2019, **250**, 959-975.
82. M. Honegger and D. Reiner, *Clim. Policy*, 2018, **18**, 306-321.
83. A. Aghahosseini, D. Bogdanov and C. Breyer, *Energy Strateg. Rev.*, 2020, **28**, 100466.
84. J. Meckling and E. Biber, *Nat. Commun.*, 2021, **12**, 2051.
85. *Main work programme of Horizon Europe for the period 2021-2022*, European Commission, 2021. https://ec.europa.eu/commission/presscorner/detail/en/IP_21_2993
86. *Net Zero Strategy: Build Back Greener*, HM Government, 2021. https://www.gov.uk/government/publications/net-zero-strategy
87. E. National Academies of Sciences and Medicine, *Negative Emissions Technologies and Reliable Sequestration: A Research Agenda*, The National Academies Press, Washington, DC, 2019.
88. *The Long-Term Strategy of the United States - Pathways to Net-Zero Greenhouse Gas Emissions by 2050*, the United States Department of State and the United States Executive Office of the President, 2021. https://unfccc.int/documents/308100
89. *An energy sector roadmap to carbon neutrality in China*, International Energy Agency (IEA), 2021. https://www.iea.org/reports/an-energy-sector-roadmap-to-carbon-neutrality-in-china
90. *Shanghai Science and Technology Innovation Action Plan Project*, Science and Technology Commission of Shanghai Municipality, 2021. http://stcsm.sh.gov.cn/zwgk/kyjhxm/xmsb/20210623/996a33eb6f7e4a8ba0aedb4f3381bea1.html
91. E. S. Sanz-Pérez, C. R. Murdock, S. A. Didas and C. W. Jones, *Chem. Rev.*, 2016, **116**, 11840-11876.
92. J. C. Minx, W. F. Lamb, M. W. Callaghan, S. Fuss, J. Hilaire, F. Creutzig, T. Amann, T. Beringer, W. de Oliveira Garcia,

J. Hartmann, T. Khanna, D. Lenzi, G. Luderer, G. F. Nemet, J. Rogelj, P. Smith, J. L. Vicente Vicente, J. Wilcox and M. del Mar Zamora Dominguez, *Environ. Res. Lett.*, 2018, **13**, 063001.
93. S. A. Didas, S. Choi, W. Chaikittisilp and C. W. Jones, *Accounts Chem. Res.*, 2015, **48**, 2680-2687.
94. G. F. Nemet, M. W. Callaghan, F. Creutzig, S. Fuss, J. Hartmann, J. Hilaire, W. F. Lamb, J. C. Minx, S. Rogers and P. Smith, *Environ. Res. Lett.*, 2018, **13**, 063003.
95. X. Shi, H. Xiao, H. Azarabadi, J. Song, X. Wu, X. Chen and K. S. Lackner, *Angew. Chem. Int. Edit.*, 2020, **59**, 6984-7006.
96. R. L. Siegelman, E. J. Kim and J. R. Long, *Nat. Mater.*, 2021, **20**, 1060-1072.
97. M. Ozkan, A.-A. Akhavi, W. C. Coley, R. Shang and Y. Ma, *Chem*, 2022, **8**, 141-173.
98. A. Cherevotan, J. Raj and S. C. Peter, *J. Mater. Chem. A*, 2021, **9**, 27271-27303.
99. S. Lawson, X. Li, H. Thakkar, A. A. Rownaghi and F. Rezaei, *Chem. Rev.*, 2021, **121**, 6246-6291.
100. J. M. Kolle, M. Fayaz and A. Sayari, *Chem. Rev.*, 2021, **121**, 7280-7345.
101. M. Jahandar Lashaki, S. Khiavi and A. Sayari, *Chem. Soc. Rev.*, 2019, **48**, 3320-3405.
102. O. Gutiérrez-Sánchez, B. Bohlen, N. Daems, M. Bulut, D. Pant and T. Breugelmans, *ChemElectroChem*, 2022, **9**, e202101540.
103. F. Mantei, R. E. Ali, C. Baensch, S. Voelker, P. Haltenort, J. Burger, R.-U. Dietrich, N. v. d. Assen, A. Schaadt, J. Sauer and O. Salem, *Sustain. Energ. Fuels*, 2022, **6**, 528-549.
104. R. Sharifian, R. M. Wagterveld, I. A. Digdaya, C. Xiang and D. A. Vermaas, *Energ. Environ. Sci.*, 2021, **14**, 781-814.
105. J. Sillman, L. Nygren, H. Kahiluoto, V. Ruuskanen, A. Tamminen, C. Bajamundi, M. Nappa, M. Wuokko, T. Lindh, P. Vainikka, J.-P. Pitkänen and J. Ahola, *Glob. Food Secur.-Agr.*, 2019, **22**, 25-32.
106. G. Rim, T. G. Feric, T. Moore and A.-H. A. Park, *Adv. Funct. Mater.*, 2021, **31**, 2010047.
107. X. Zhu, T. Ge, F. Yang, M. Lyu, C. Chen, D. O'Hare and R. Wang, *J. Mater. Chem. A*, 2020, **8**, 16421-16428.
108. H. T. Kwon, M. A. Sakwa-Novak, S. H. Pang, A. R. Sujan, E. W. Ping and C. W. Jones, *Chem. Mater.*, 2019, **31**, 5229-5237.
109. X. Xu, M. B. Myers, F. G. Versteeg, B. Pejcic, C. Heath and C. D. Wood, *Chem. Commun. (Cambridge, U. K.)*, 2020, **56**, 7151-7154.
110. E. S. Sanz-Pérez, A. Arencibia, G. Calleja and R. Sanz, *Micropor. Mesopor. Mat.*, 2018, **260**, 235-244.
111. W. Wang, F. Liu, Q. zhang, G. Yu and S. Deng, *Chem. Eng. J.*, 2020, **399**, 125734.
112. Y. Miao, Z. He, X. Zhu, D. Izikowitz and J. Li, *Chem. Eng. J.*, 2021, **426**, 131875.
113. D. R. Kumar, C. Rosu, A. R. Sujan, M. A. Sakwa-Novak, E. W. Ping and C. W. Jones, *ACS Sustain. Chem. Eng.*, 2020, **8**, 10971-10982.
114. M. L. Sarazen, M. A. Sakwa-Novak, E. W. Ping and C. W. Jones, *ACS Sustain. Chem. Eng.*, 2019, **7**, 7338-7345.
115. A. R. Sujan, D. R. Kumar, M. Sakwa-Novak, E. W. Ping, B. Hu, S. J. Park and C. W. Jones, *ACS Appl. Polym. Mater.*, 2019, **1**, 3137-3147.
116. X. Zhu, M. Lyu, T. Ge, J. Wu, C. Chen, F. Yang, D. O'Hare and R. Wang, *Cell Reports Physical Science*, 2021, **2**, 100484.
117. H. Li, K. Wang, Z. Hu, Y.-P. Chen, W. Verdegaal, D. Zhao and H.-C. Zhou, *J. Mater. Chem. A*, 2019, **7**, 7867-7874.
118. E. S. Sanz-Pérez, A. Fernández, A. Arencibia, G. Calleja and R. Sanz, *Chem. Eng. J.*, 2019, **373**, 1286-1294.
119. M. Jahandar Lashaki and A. Sayari, *Chem. Eng. J.*, 2018, **334**, 1260-1269.
120. S. Loganathan and A. K. Ghoshal, *Chem. Eng. J.*, 2017, **308**, 827-839.
121. Y. Wang and R. T. Yang, *ACS Sustain. Chem. Eng.*, 2020, **8**, 8295-8304.
122. M. E. Potter, K. M. Cho, J. J. Lee and C. W. Jones, *ChemSusChem*, 2017, **10**, 2192-2201.
123. J. J. Lee, C.-J. Yoo, C.-H. Chen, S. E. Hayes, C. Sievers and C. W. Jones, *Langmuir*, 2018, **34**, 12279-12292.
124. J.-T. Anyanwu, Y. Wang and R. T. Yang, *Ind. Eng. Chem. Res.*, 2021, **60**, 6277-6286.
125. J.-T. Anyanwu, Y. Wang and R. T. Yang, *Ind. Eng. Chem. Res.*, 2020, **59**, 7072-7079.

126. S. H. Pang, L.-C. Lee, M. A. Sakwa-Novak, R. P. Lively and C. W. Jones, *J. Am. Chem. Soc.*, 2017, **139**, 3627-3630.
127. A. Goeppert, H. Zhang, R. Sen, H. Dang and G. K. S. Prakash, *ChemSusChem*, 2019, **12**, 1712-1723.
128. S. H. Pang, R. P. Lively and C. W. Jones, *ChemSusChem*, 2018, **11**, 2628-2637.
129. C. Rosu, S. H. Pang, A. R. Sujan, M. A. Sakwa-Novak, E. W. Ping and C. W. Jones, *ACS Appl. Mater. Inter.*, 2020, **12**, 38085-38097.
130. C.-J. Yoo, S. J. Park and C. W. Jones, *Ind. Eng. Chem. Res.*, 2019, **59**, 7061-7071.
131. I. Nezam, J. Xie, K. W. Golub, J. Carneiro, K. Olsen, E. W. Ping, C. W. Jones and M. A. Sakwa-Novak, *ACS Sustain. Chem. Eng.*, 2021, **9**, 8477-8486.
132. C. Drechsler and D. W. Agar, *Energy*, 2020, **192**, 116587.
133. M. J. Bos, S. Pietersen and D. W. F. Brilman, *Chemical Engineering Science: X*, 2019, **2**, 100020.
134. Y. C. Ng, L. Yang and Z. R. Jovanovic, *Ind. Eng. Chem. Res.*, 2018, **57**, 13987-13998.
135. R. P. Wijesiri, G. P. Knowles, H. Yeasmin, A. F. A. Hoadley and A. L. Chaffee, *Ind. Eng. Chem. Res.*, 2019, **58**, 3293-3303.
136. J. Young, E. García-Díez, S. Garcia and M. van der Spek, *Energ. Environ. Sci.*, 2021, **14**, 5377-5394.
137. R. P. Wijesiri, G. P. Knowles, H. Yeasmin, A. F. A. Hoadley and A. L. Chaffee, *Ind. Eng. Chem. Res.*, 2019, **58**, 15606-15618.
138. R. Afonso, M. Sardo, L. Mafra and J. R. B. Gomes, *Environ. Sci. Technol.*, 2019, **53**, 2758-2767.
139. Y. Zhai and S. S. C. Chuang, *Energy Technol.-GER*, 2017, **5**, 510-519.
140. M. Sardo, R. Afonso, J. Juźków, M. Pacheco, M. Bordonhos, M. L. Pinto, J. R. B. Gomes and L. Mafra, *J. Mater. Chem. A*, 2021, **9**, 5542-5555.
141. C.-H. Chen, D. Shimon, J. J. Lee, F. Mentink-Vigier, I. Hung, C. Sievers, C. W. Jones and S. E. Hayes, *J. Am. Chem. Soc.*, 2018, **140**, 8648-8651.
142. W. Buijs, *Ind. Eng. Chem. Res.*, 2019, **58**, 14705-14708.
143. W. Buijs, *Ind. Eng. Chem. Res.*, 2019, **58**, 17760-17767.
144. E. J. Kim, R. L. Siegelman, H. Z. H. Jiang, A. C. Forse, J.-H. Lee, J. D. Martell, P. J. Milner, J. M. Falkowski, J. B. Neaton, J. A. Reimer, S. C. Weston and J. R. Long, *Science*, 2020, **369**, 392-396.
145. A. C. Forse, P. J. Milner, J.-H. Lee, H. N. Redfearn, J. Oktawiec, R. L. Siegelman, J. D. Martell, B. Dinakar, L. B. Porter-Zasada, M. I. Gonzalez, J. B. Neaton, J. R. Long and J. A. Reimer, *J. Am. Chem. Soc.*, 2018, **140**, 18016-18031.
146. R. L. Siegelman, T. M. McDonald, M. I. Gonzalez, J. D. Martell, P. J. Milner, J. A. Mason, A. H. Berger, A. S. Bhown and J. R. Long, *J. Am. Chem. Soc.*, 2017, **139**, 10526-10538.
147. J. D. Martell, L. B. Porter-Zasada, A. C. Forse, R. L. Siegelman, M. I. Gonzalez, J. Oktawiec, T. Runčevski, J. Xu, M. Srebro-Hooper, P. J. Milner, K. A. Colwell, J. Autschbach, J. A. Reimer and J. R. Long, *J. Am. Chem. Soc.*, 2017, **139**, 16000-16012.
148. R. L. Siegelman, P. J. Milner, A. C. Forse, J.-H. Lee, K. A. Colwell, J. B. Neaton, J. A. Reimer, S. C. Weston and J. R. Long, *J. Am. Chem. Soc.*, 2019, **141**, 13171-13186.
149. P. J. Milner, R. L. Siegelman, A. C. Forse, M. I. Gonzalez, T. Runčevski, J. D. Martell, J. A. Reimer and J. R. Long, *J. Am. Chem. Soc.*, 2017, **139**, 13541-13553.
150. V. Y. Mao, P. J. Milner, J.-H. Lee, A. C. Forse, E. J. Kim, R. L. Siegelman, C. M. McGuirk, L. B. Porter-Zasada, J. B. Neaton, J. A. Reimer and J. R. Long, *Angew. Chem. Int. Edit.*, 2020, **59**, 19468-19477.
151. J.-H. Lee, R. L. Siegelman, L. Maserati, T. Rangel, B. A. Helms, J. R. Long and J. B. Neaton, *Chem. Sci.*, 2018, **9**, 5197-5206.
152. P. J. Milner, J. D. Martell, R. L. Siegelman, D. Gygi, S. C. Weston and J. R. Long, *Chem. Sci.*, 2018, **9**, 160-174.
153. M. Kang, J. E. Kim, D. W. Kang, H. Y. Lee, D. Moon and C. S. Hong, *J. Mater. Chem. A*, 2019, **7**, 8177-8183.
154. X. Shi, H. Xiao, K. Kanamori, A. Yonezu, K. S. Lackner and X. Chen, *Joule*, 2020, **4**, 1823-1837.
155. C. Hou, D. R. Kumar, Y. Jin, Y. Wu, J. J. Lee, C. W. Jones and T. Wang, *Chem. Eng. J.*, 2021, **413**, 127532.

156. T. Wang, C. Hou, K. Ge, K. S. Lackner, X. Shi, J. Liu, M. Fang and Z. Luo, *J. Phys. Chem. Lett.*, 2017, **8**, 3986-3990.
157. T. Wang, X. Wang, C. Hou and J. Liu, *Sci. Rep.-UK*, 2020, **10**, 21429.
158. X. Wang, J. Song, Y. Chen, H. Xiao, X. Shi, Y. Liu, L. Zhu, Y.-L. He and X. Chen, *Ind. Eng. Chem. Res.*, 2020, **59**, 16507-16515.
159. Y. Han, L. Zhu, Y. Yao, X. Shi, Y. Zhang, H. Xiao and X. Chen, *Phys. Chem. Chem. Phys.*, 2021, **23**, 14811-14817.
160. H. Xiao, X. Shi, Y. Zhang, X. Liao, F. Hao, K. S. Lackner and X. Chen, *Phys. Chem. Chem. Phys.*, 2017, **19**, 27435-27441.
161. J. Song, L. Zhu, X. Shi, Y. Liu, H. Xiao and X. Chen, *Energ. Fuel.*, 2019, **33**, 6562-6567.
162. C. Hou, Y. Wu, T. Wang, X. Wang and X. Gao, *Energ. Fuel.*, 2019, **33**, 1745-1752.
163. T. Wang, K. Ge, Y. Wu, K. Chen, M. Fang and Z. Luo, *Energ. Fuel.*, 2017, **31**, 11127-11133.
164. A. M. Rather, P. Srikrishnarka, A. Baidya, A. Shome, T. Pradeep and U. Manna, *ACS Appl. Energ. Mater.*, 2020, **3**, 10541-10549.
165. M. Guo, S. Liang, J. Liu, J. Jin and J. Mi, *ACS Sustain. Chem. Eng.*, 2020, **8**, 3853-3864.
166. A. Baidya, A. Yatheendran, T. Ahuja, C. Sudhakar, S. K. Das, R. H. A. Ras and T. Pradeep, *Adv. Mater. Interfaces*, 2019, **6**, 1901013.
167. L. Jiang, R. Q. Wang, A. Gonzalez-Diaz, A. Smallbone, R. O. Lamidi and A. P. Roskilly, *Appl. Therm. Eng.*, 2020, **169**, 114973.
168. G. Hüllen, J. Zhai, S. H. Kim, A. Sinha, M. J. Realff and F. Boukouvala, *Comput. Chem. Eng.*, 2020, **136**, 106519.
169. S. M. W. Wilson and F. H. Tezel, *Ind. Eng. Chem. Res.*, 2020, **59**, 8783-8794.
170. M. M. Sadiq, M. P. Batten, X. Mulet, C. Freeman, K. Konstas, J. I. Mardel, J. Tanner, D. Ng, X. Wang, S. Howard, M. R. Hill and A. W. Thornton, *Adv. Sustain. Syst.*, 2020, **4**, 2000101.
171. J. Gao, Y. Hoshino and G. Inoue, *Chem. Eng. J.*, 2020, **383**, 123123.
172. R. Zhao, L. Liu, L. Zhao, S. Deng, S. Li, Y. Zhang and H. Li, *Energ. Convers. Manage.*, 2019, **183**, 418-426.
173. J. Elfving, C. Bajamundi, J. Kauppinen and T. Sainio, *J. CO2 Util.*, 2017, **22**, 270-277.
174. R. Rodríguez-Mosqueda, J. Rutgers, E. A. Bramer and G. Brem, *J. CO2 Util.*, 2019, **29**, 65-73.
175. R. P. Wijesiri, G. P. Knowles, H. Yeasmin, A. F. A. Hoadley and A. L. Chaffee, *Processes*, 2019, **7**, 503.
176. A. Sinha and M. J. Realff, *AIChE J.*, 2019, **65**, e16607.
177. V. Stampi-Bombelli, M. van der Spek and M. Mazzotti, *Adsorption*, 2020, **26**, 1183-1197.
178. A. Sinha, L. A. Darunte, C. W. Jones, M. J. Realff and Y. Kawajiri, *Ind. Eng. Chem. Res.*, 2017, **56**, 750-764.
179. A. Sinha, L. A. Darunte, C. W. Jones, M. J. Realff and Y. Kawajiri, *Ind. Eng. Chem. Res.*, 2020, **59**, 503-505.
180. X. Zhu, T. Ge, F. Yang and R. Wang, *Renew. Sust. Energ. Rev.*, 2021, **137**, 110651.
181. F. Sabatino, A. Grimm, F. Gallucci, M. van Sint Annaland, G. J. Kramer and M. Gazzani, *Joule*, 2021, **5**, 2047-2076.
182. M. D. Eisaman, *Joule*, 2020, **4**, 516-520.
183. C. Breyer, M. Fasihi, C. Bajamundi and F. Creutzig, *Joule*, 2019, **3**, 2053-2057.
184. D. Krekel, R. C. Samsun, R. Peters and D. Stolten, *Appl. Energ.*, 2018, **218**, 361-381.
185. A. R. Sujan, S. H. Pang, G. Zhu, C. W. Jones and R. P. Lively, *ACS Sustain. Chem. Eng.*, 2019, **7**, 5264-5273.
186. J. Park, J. R. Park, J. H. Choe, S. Kim, M. Kang, D. W. Kang, J. Y. Kim, Y. W. Jeong and C. S. Hong, *ACS Appl. Mater. Inter.*, 2020, **12**, 50534-50540.
187. L. A. Darunte, Y. Terada, C. R. Murdock, K. S. Walton, D. S. Sholl and C. W. Jones, *ACS Appl. Mater. Inter.*, 2017, **9**, 17042-17050.
188. H. Thakkar, S. Eastman, A. Al-Mamoori, A. Hajari, A. A. Rownaghi and F. Rezaei, *ACS Appl. Mater. Inter.*, 2017, **9**, 7489-7498.
189. A. Krishnamurthy, B. Salunkhe, A. Zore, A. Rownaghi, T. Schuman and F. Rezaei, *ACS Appl. Mater. Inter.*, 2019, **11**, 16594-16604.
190. M. Armstrong, X. Shi, B. Shan, K. Lackner and B. Mu, *AIChE J.*, 2019, **65**, 214-220.

191. Y. Zhao, J. Zhou, L. Fan, L. Chen, L. Li, Z. P. Xu and G. Qian, *Ind. Eng. Chem. Res.*, 2019, **58**, 19465-19474.
192. J. Elfving, J. Kauppinen, M. Jegoroff, V. Ruuskanen, L. Järvinen and T. Sainio, *Chem. Eng. J.*, 2021, **404**, 126337.
193. L. A. Darunte, T. Sen, C. Bhawanani, K. S. Walton, D. S. Sholl, M. J. Realff and C. W. Jones, *Ind. Eng. Chem. Res.*, 2019, **58**, 366-377.
194. M. J. Bos, V. Kroeze, S. Sutanto and D. W. F. Brilman, *Ind. Eng. Chem. Res.*, 2018, **57**, 11141-11153.
195. T. von Hippel, *Climatic Change*, 2018, **148**, 491-501.
196. H. A. Petersen and O. R. Luca, *Phys. Chem. Chem. Phys.*, 2021, **23**, 12533-12536.
197. C. Drechsler and D. W. Agar, *Chem. Ing. Tech.*, 2020, **92**, 282-287.
198. H. S. Caram, R. Gupta, H. Thomann, F. Ni, S. C. Weston and M. Afeworki, *Int. J. Greenh. Gas Con.*, 2020, **97**, 102986.
199. Q. Yu and W. Brilman, *Applied Sciences*, 2020, **10**, 1080.
200. C. Drechsler and D. W. Agar, *Comput. Chem. Eng.*, 2019, **126**, 520-534.
201. L. Joppa, A. Luers, E. Willmott, S. J. Friedmann, S. P. Hamburg and R. Broze, *Nature*, 2021, **597**, 629-632.
202. C. J. J. Haertel, M. McNutt, M. Ozkan, E. S. P. Aradóttir, K. T. Valsaraj, P. R. Sanberg, S. Talati and J. Wilcox, *Chem*, 2021, **7**, 2831-2834.
203. J. Tollefson, *Nature*, 2018, **558**, 173-174.
204. M. Sakwa-Novak, *Global Thermostat: direct air capture update*, in 2020 Integrated Project Review Meeting - Carbon Capture, 2020. https://netl.doe.gov/2020CC-proceedings
205. M. Fasihi, O. Efimova and C. Breyer, *J. Clean. Prod.*, 2019, **224**, 957-980.
206. H. Bryan and F. Ben Salamah, *Building-Integrated Carbon Capturing 2.0: Moving a Concept from R&D to a Prototype*, in Proceedings of the 34th International Conference on Passive and Low Energy Architecture, 2018, pp. 110-115.
207. M. K. Kim, L. Baldini, H. Leibundgut and J. A. Wurzbacher, *Appl. Energ.*, 2020, **259**, 112869.
208. C.-l. Hou, Y.-s. Wu, Y.-z. Jiao, J. Huang, T. Wang, M.-x. Fang and H. Zhou, *J. Zhejiang Univ.-Sc. A*, 2017, **18**, 819-830.
209. V. Ruuskanen, G. Givirovskiy, J. Elfving, P. Kokkonen, A. Karvinen, L. Järvinen, J. Sillman, M. Vainikka and J. Ahola, *J. Clean. Prod.*, 2021, **278**, 123423.
210. D. Leger, S. Matassa, E. Noor, A. Shepon, R. Milo and A. Bar-Even, *P. Natl. Acad. Sci. USA*, 2021, **118**, e2015025118.
211. W. J. Sagues, S. Park, H. Jameel and D. L. Sanchez, *Sustain. Energ. Fuels*, 2019, **3**, 3135-3146.
212. J. Wilcox, P. C. Psarras and S. Liguori, *Environ. Res. Lett.*, 2017, **12**, 065001.
213. C. H. Greene, M. E. Huntley, I. Archibald, L. N. Gerber, D. L. Sills, J. Granados, C. M. Beal and M. J. Walsh, *Earth's Future*, 2017, **5**, 278-284.
214. L. Weimann, A. Grimm, J. Nienhuis, P. Gabrielli, G. J. Kramer and M. Gazzania, in *Computer Aided Chemical Engineering*, eds. S. Pierucci, F. Manenti, G. L. Bozzano and D. Manca, Elsevier, 2020, vol. 48, pp. 1471-1476.
215. A. Kiani, M. Lejeune, C. Li, J. Patel and P. Feron, *J. Nat. Gas Sci. Eng.*, 2021, **94**, 104079.
216. C. Jeong-Potter and R. Farrauto, *Appl. Catal. B-Environ.*, 2021, **282**, 119416.
217. M. Berger, D. Radu, G. Detienne, T. Deschuyteneer, A. Richel and D. Ernst, *Front. Energy Res.*, 2021, **9**, 671279.
218. J. G. Yao, M. Bui and N. M. Dowell, *Sustain. Energ. Fuels*, 2019, **3**, 3147-3162.
219. R. Peters, M. Baltruweit, T. Grube, R. C. Samsun and D. Stolten, *J. CO2 Util.*, 2019, **34**, 616-634.
220. J. V. Veselovskaya, P. D. Parunin and A. G. Okunev, *Catal. Today*, 2017, **298**, 117-123.
221. R. Sen, A. Goeppert, S. Kar and G. K. S. Prakash, *J. Am. Chem. Soc.*, 2020, **142**, 4544-4549.
222. W. A. Smith, T. Burdyny, D. A. Vermaas and H. Geerlings, *Joule*, 2019, **3**, 1822-1834.
223. H. A. Daggash, C. F. Patzschke, C. F. Heuberger, L. Zhu, K. Hellgardt, P. S. Fennell, A. N. Bhave, A. Bardow and N. Mac Dowell, *Sustain. Energ. Fuels*, 2018, **2**, 1153-1169.
224. M. Held, Y. Tönges, D. Pélerin, M. Härtl, G. Wachtmeister and J. Burger, *Energ. Environ. Sci.*, 2019, **12**, 1019-1034.
225. W. Luc, B. H. Ko, S. Kattel, S. Li, D. Su, J. G. Chen and F. Jiao, *J. Am. Chem. Soc.*, 2019, **141**, 9902-9909.
226. A. P. H. Goede, *EPJ Web Conf.*, 2018, **189**, 00010.
227. A. Gulagi, M. Alcanzare, D. Bogdanov, E. Esparcia, J. Ocon and C. Breyer, *Renew. Sust. Energ. Rev.*, 2021, **144**, 110934.

228. E. D. Sherwin, *Environ. Sci. Technol.*, 2021, **55**, 7583-7594.
229. V. Becattini, P. Gabrielli and M. Mazzotti, *Ind. Eng. Chem. Res.*, 2021, **60**, 6848-6862.
230. S. Drünert, U. Neuling, T. Zitscher and M. Kaltschmitt, *Appl. Energ.*, 2020, **277**, 115578.
231. F. V. Vázquez, J. Koponen, V. Ruuskanen, C. Bajamundi, A. Kosonen, P. Simell, J. Ahola, C. Frilund, J. Elfving, M. Reinikainen, N. Heikkinen, J. Kauppinen and P. Piermartini, *J. CO2 Util.*, 2018, **28**, 235-246.
232. M. Marchese, G. Buffo, M. Santarelli and A. Lanzini, *J. CO2 Util.*, 2021, **46**, 101487.
233. A. García, J. Monsalve-Serrano, D. Villalta, R. Lago Sari, V. Gordillo Zavaleta and P. Gaillard, *Appl. Energ.*, 2019, **253**, 113622.
234. X. Wang, X. Liu, G. Licht and S. Licht, *Sci. Rep.-UK*, 2020, **10**, 15146.
235. A. Wotzka, R. Dühren, T. Suhrbier, M. Polyakov and S. Wohlrab, *ACS Sustain. Chem. Eng.*, 2020, **8**, 5013-5017.
236. A. V. Tavasoli, M. Preston and G. Ozin, *Energ. Environ. Sci.*, 2021, **14**, 3098-3109.
237. A. Maggi, M. Wenzel and K. Sundmacher, *Front. Energy Res.*, 2020, **8**, 161.
238. K. Leben, R. Motlep, A. Konist, T. Pihu and K. Kirsimae, *Oil Shale*, 2021, **38**, 65-88.
239. K. Rausis, A. Ćwik and I. Casanova, *Int. J. Greenh. Gas Con.*, 2020, **100**, 103114.
240. I. M. Power, G. M. Dipple, P. M. D. Bradshaw and A. L. Harrison, *Int. J. Greenh. Gas Con.*, 2020, **94**, 102895.
241. C. D. Hills, N. Tripathi and P. J. Carey, *Front. Energy Res.*, 2020, **8**, 142.
242. J. L. Hamilton, S. A. Wilson, B. Morgan, A. L. Harrison, C. C. Turvey, D. J. Paterson, G. M. Dipple and G. Southam, *Econ. Geol.*, 2020, **115**, 303-323.
243. R. R. Tan, K. B. Aviso, J. I. B. Janairo and M. A. B. Promentilla, *J. Clean. Prod.*, 2020, **272**, 122181.
244. K. B. Aviso, J. I. B. Janairo, M. A. B. Promentilla and R. R. Tan, *Clean. Technol. Envir.*, 2019, **21**, 1655-1664.
245. G. Gonzalo, P. Raul, T. Rodolfo and E.-E. Eleonora, *Ct&F-Ciencia Tecnologia Y Futuro*, 2020, **10**, 39-47.
246. M. C. Handley, D. Slesinski and S. C. Hsu, *J. Fusion Energ.*, 2021, **40**, 18.
247. D. Bogdanov, A. Gulagi, M. Fasihi and C. Breyer, *Appl. Energ.*, 2021, **283**, 116273.
248. L. Yang and Z. Li, *IOP Conference Series: Earth and Environmental Science*, 2020, **508**, 012022.
249. A. M. Varghese and G. N. Karanikolos, *Int. J. Greenh. Gas Con.*, 2020, **96**, 103005.
250. M. Yang, C. Ma, M. Xu, S. Wang and L. Xu, *Curr. Pollut. Rep.*, 2019, **5**, 272-293.
251. S. J. Park, J. J. Lee, C. B. Hoyt, D. R. Kumar and C. W. Jones, *Adsorption*, 2020, **26**, 89-101.
252. S. Bali, T. T. Chen, W. Chaikittisilp and C. W. Jones, *Energ. Fuel.*, 2013, **27**, 1547-1554.
253. H. Zerze, A. Tipirneni and A. J. McHugh, *Sep. Sci. Technol.*, 2017, **52**, 2513-2522.
254. W. Chaikittisilp, R. Khunsupat, T. T. Chen and C. W. Jones, *Ind. Eng. Chem. Res.*, 2011, **50**, 14203-14210.
255. A. Koutsianos, L. B. Hamdy, C.-J. Yoo, J. J. Lee, M. Taddei, J. M. Urban-Klaehn, J. Dryzek, C. W. Jones, A. R. Barron and E. Andreoli, *J. Mater. Chem. A*, 2021, **9**, 10827-10837.
256. H. Thakkar, A. Issa, A. A. Rownaghi and F. Rezaei, *Chem. Eng. Technol.*, 2017, **40**, 1999-2007.
257. L. Qi, Y. Han, G. Bai, Q. Liu, Z. Fei, X. Chen, Z. Zhang, J. Tang, M. Cui and X. Qiao, *J. Environ. Chem. Eng.*, 2021, **9**, 106709.
258. L. A. Darunte, A. D. Oetomo, K. S. Walton, D. S. Sholl and C. W. Jones, *ACS Sustain. Chem. Eng.*, 2016, **4**, 5761-5768.
259. A. Heydari-Gorji, Y. Belmabkhout and A. Sayari, *Langmuir*, 2011, **27**, 12411-12416.
260. K. Li, J. Jiang, F. Yan, S. Tian and X. Chen, *Appl. Energ.*, 2014, **136**, 750-755.
261. M. W. Hahn, J. Jelic, E. Berger, K. Reuter, A. Jentys and J. A. Lercher, *J. Phys. Chem. B*, 2016, **120**, 1988-1995.
262. J. Heo, M. Choi, D. Choi, H. Jeong, H. Y. Kim, H. Jeon, S. W. Kang and J. Hong, *J. Membrane Sci.*, 2020, **601**, 117905.
263. J. J. Lee, C.-H. Chen, D. Shimon, S. E. Hayes, C. Sievers and C. W. Jones, *J. Phys. Chem. C*, 2017, **121**, 23480-23487.
264. X. Xu, C. Song, J. M. Andresen, B. G. Miller and A. W. Scaroni, *Energ. Fuel.*, 2002, **16**, 1463-1469.
265. A. Holewinski, M. A. Sakwa-Novak and C. W. Jones, *J. Am. Chem. Soc.*, 2015, **137**, 11749-11759.
266. G. Rother, U. Tumuluri, K. Huang, W. T. Heller, S. Dai, J.-M. Carrillo and B. G. Sumpter, *Langmuir*, 2021, **37**, 4622-4631.

267. S. Choi, J. H. Drese and C. W. Jones, *ChemSusChem*, 2009, **2**, 796-854.
268. C. F. Cogswell, H. Jiang, J. Ramberger, D. Accetta, R. J. Willey and S. Choi, *Langmuir*, 2015, **31**, 4534-4541.
269. C. F. Cogswell, Z. Xie, A. Wolek, Y. Wang, A. Stavola, M. Finkenaur, E. Gilmore, M. Lanzillotti and S. Choi, *J. Mater. Chem. A*, 2017, **5**, 8526-8536.
270. J. Fonseca and S. Choi, *Inorg. Chem.*, 2020, **59**, 3983-3992.
271. N. A. Brunelli, S. A. Didas, K. Venkatasubbaiah and C. W. Jones, *J. Am. Chem. Soc.*, 2012, **134**, 13950-13953.
272. S. A. Didas, A. R. Kulkarni, D. S. Sholl and C. W. Jones, *ChemSusChem*, 2012, **5**, 2058-2064.
273. A. Sayari and Y. Belmabkhout, *J. Am. Chem. Soc.*, 2010, **132**, 6312-6314.
274. C.-J. Yoo, S. J. Park and C. W. Jones, *Ind. Eng. Chem. Res.*, 2020, **59**, 7061-7071.
275. N. R. Stuckert and R. T. Yang, *Environ. Sci. Technol.*, 2011, **45**, 10257-10264.
276. A. Wagner, B. Steen, G. Johansson, E. Zanghellini, P. Jacobsson and P. Johansson, *International Journal of Spectroscopy*, 2013, **2013**, 690186.
277. C. Gebald, J. A. Wurzbacher, A. Borgschulte, T. Zimmermann and A. Steinfeld, *Environ. Sci. Technol.*, 2014, **48**, 2497-2504.
278. L. He, M. Fan, B. Dutcher, S. Cui, X.-d. Shen, Y. Kong, A. G. Russell and P. McCurdy, *Chem. Eng. J.*, 2012, **189-190**, 13-23.
279. S. Bali, J. Leisen, G. S. Foo, C. Sievers and C. W. Jones, *ChemSusChem*, 2014, **7**, 3145-3156.
280. S. A. Didas, M. A. Sakwa-Novak, G. S. Foo, C. Sievers and C. W. Jones, *J. Phys. Chem. Lett.*, 2014, **5**, 4194-4200.
281. Y. Kong, X. Shen, S. Cui and M. Fan, *Green Chem.*, 2015, **17**, 3436-3445.
282. Y. Kong, G. Jiang, Y. Wu, S. Cui and X. Shen, *Chem. Eng. J.*, 2016, **306**, 362-368.
283. X. Jiang, Y. Kong, Z. Zhao and X. Shen, *RSC Adv.*, 2020, **10**, 25911-25917.
284. L. F. Feitosa, B. B. Pozes, A. S. Silva, L. F. Castro, L. S. C. Júnior, C. B. Quitete and M. A. Fraga, *J. Environ. Chem. Eng.*, 2021, **9**, 104951.
285. X. Jiang, Y. Kong, H. Zou, Z. Zhao, Y. Zhong and X. Shen, *J. Porous Mat.*, 2021, **28**, 93-97.
286. B. Wadi, A. Golmakani, V. Manovic and S. A. Nabavi, *Ind. Eng. Chem. Res.*, 2021, **60**, 13309-13317.
287. M. A. Alkhabbaz, P. Bollini, G. S. Foo, C. Sievers and C. W. Jones, *J. Am. Chem. Soc.*, 2014, **136**, 13170-13173.
288. A. Sayari, A. Heydari-Gorji and Y. Yang, *J. Am. Chem. Soc.*, 2012, **134**, 13834-13842.
289. J. A. Wurzbacher, C. Gebald and A. Steinfeld, *Energ. Environ. Sci.*, 2011, **4**, 3584-3592.
290. C. Gebald, J. A. Wurzbacher, P. Tingaut, T. Zimmermann and A. Steinfeld, *Environ. Sci. Technol.*, 2011, **45**, 9101-9108.
291. Y. Sánchez-Vicente, L. Stevens, C. Pando and A. Cabañas, *Energies*, 2020, **13**, 5804.
292. Y. Belmabkhout, R. Serna-Guerrero and A. Sayari, *Ind. Eng. Chem. Res.*, 2010, **49**, 359-365.
293. Y. Belmabkhout, R. Serna-Guerrero and A. Sayari, *Chem. Eng. Sci.*, 2010, **65**, 3695-3698.
294. J.-T. Anyanwu, Y. Wang and R. T. Yang, *Chem. Eng. J.*, 2022, **427**, 131561.
295. W. Lu, J. P. Sculley, D. Yuan, R. Krishna and H.-C. Zhou, *J. Phys. Chem. C*, 2013, **117**, 4057-4061.
296. P. J. E. Harlick and A. Sayari, *Ind. Eng. Chem. Res.*, 2006, **45**, 3248-3255.
297. J.-T. Anyanwu, Y. Wang and R. T. Yang, *Chem. Eng. Sci.*, 2021, **241**, 116717.
298. R. Kishor and A. K. Ghoshal, *Chem. Eng. J.*, 2015, **262**, 882-890.
299. J. J. Lee, C. Sievers and C. W. Jones, *Ind. Eng. Chem. Res.*, 2019, **58**, 22551-22560.
300. Y. Sánchez-Vicente, C. Pando, M. Cortijo and A. Cabañas, *Micropor. Mesopor. Mat.*, 2014, **193**, 145-153.
301. Y. Sánchez-Vicente, L. A. Stevens, C. Pando, M. J. Torralvo, C. E. Snape, T. C. Drage and A. Cabañas, *Chem. Eng. J.*, 2015, **264**, 886-898.
302. Y. Sánchez-Vicente, O. Alonso-Pastor, C. Pando and A. Cabañas, *J. Chem. Thermodyn.*, 2016, **103**, 152-156.
303. Y. Kuwahara, D.-Y. Kang, J. R. Copeland, P. Bollini, C. Sievers, T. Kamegawa, H. Yamashita and C. W. Jones, *Chem.-Eur. J.*, 2012, **18**, 16649-16664.
304. M. A. Sakwa-Novak, A. Holewinski, C. B. Hoyt, C.-J. Yoo, S.-H. Chai, S. Dai and C. W. Jones, *Langmuir*, 2015, **31**,

9356-9365.
305. L. Liu, J. Chen, L. Tao, H. Li and Q. Yang, *ChemNanoMat*, 2020, **6**, 1096-1103.
306. P. G. Parzuchowski, M. Stefańska, A. Świderska, M. Roguszewska and M. Zybert, *J. CO2 Util.*, 2018, **27**, 145-160.
307. J. Wang, H. Huang, M. Wang, L. Yao, W. Qiao, D. Long and L. Ling, *Ind. Eng. Chem. Res.*, 2015, **54**, 5319-5327.
308. L. Keller, B. Ohs, J. Lenhart, L. Abduly, P. Blanke and M. Wessling, *Carbon*, 2018, **126**, 338-345.
309. W. Chaikittisilp, H.-J. Kim and C. W. Jones, *Energ. Fuel.*, 2011, **25**, 5528-5537.
310. M. A. Sakwa-Novak and C. W. Jones, *ACS Appl. Mater. Inter.*, 2014, **6**, 9245-9255.
311. M. A. Sakwa-Novak, C.-J. Yoo, S. Tan, F. Rashidi and C. W. Jones, *ChemSusChem*, 2016, **9**, 1859-1868.
312. H. Cai, F. Bao, J. Gao, T. Chen, S. Wang and R. Ma, *Environ. Technol.*, 2015, **36**, 1273-1280.
313. J. Wang, M. Wang, W. Li, W. Qiao, D. Long and L. Ling, *AIChE J.*, 2015, **61**, 972-980.
314. Z. Chen, S. Deng, H. Wei, B. Wang, J. Huang and G. Yu, *ACS Appl. Mater. Inter.*, 2013, **5**, 6937-6945.
315. W. Si, S. Ye, D. Zhang, B. Yang, Y. Hou, Z. Li, X. Zhang, J. Zhu and L. Lei, *Can. J. Chem. Eng.*, 2019, **97**, 697-701.
316. G. Rim, F. Kong, M. Song, C. Rosu, P. Priyadarshini, R. P. Lively and C. W. Jones, *JACS Au*, 2022, **2**, 380-393.
317. M. Zhao, J. Xiao, W. Gao and Q. Wang, *J. Energy Chem.*, 2022, **68**, 401-410.
318. G. Zhang, P. Zhao, Y. Xu, Z. Yang, H. Cheng and Y. Zhang, *ACS Appl. Mater. Inter.*, 2018, **10**, 34340-34354.
319. N. Rao, M. Wang, Z. Shang, Y. Hou, G. Fan and J. Li, *Energ. Fuel.*, 2018, **32**, 670-677.
320. C. Zhou, K. He, W. Lv, Y. Chen, S. Tang, C. Liu, H. Yue and B. Liang, *Energ. Fuel.*, 2019, **33**, 1774-1784.
321. Y. Liu and X. Yu, *Appl. Energ.*, 2018, **211**, 1080-1088.
322. R. Kishor and A. K. Ghoshal, *Ind. Eng. Chem. Res.*, 2017, **56**, 6078-6087.
323. Y. Han, G. Bai, J. Yang, J. Huang, Z. Fei, Q. Liu, Z. Zhang, X. Chen, J. Tang, M. Cui and X. Qiao, *J. Solid State Chem.*, 2020, **290**, 121531.
324. M. E. Potter, S. H. Pang and C. W. Jones, *Langmuir*, 2017, **33**, 117-124.
325. M. V. Zakharova, N. Masoumifard, Y. Hu, J. Han, F. Kleitz and F.-G. Fontaine, *ACS Appl. Mater. Inter.*, 2018, **10**, 13199-13210.
326. F.-Q. Liu, L. Wang, Z.-G. Huang, C.-Q. Li, W. Li, R.-X. Li and W.-H. Li, *ACS Appl. Mater. Inter.*, 2014, **6**, 4371-4381.
327. W.-J. Son, J.-S. Choi and W.-S. Ahn, *Micropor. Mesopor. Mat.*, 2008, **113**, 31-40.
328. G. P. Knowles, Z. Liang and A. L. Chaffee, *Micropor. Mesopor. Mat.*, 2017, **238**, 14-18.
329. X. Yan, L. Zhang, Y. Zhang, K. Qiao, Z. Yan and S. Komarneni, *Chem. Eng. J.*, 2011, **168**, 918-924.
330. W. Li, P. Bollini, S. A. Didas, S. Choi, J. H. Drese and C. W. Jones, *ACS Appl. Mater. Inter.*, 2010, **2**, 3363-3372.
331. M. Chintapalli, S. Meckler, G. Iftime, R. Pandey, M. Louie and E. S. M. Beh, *Tunable, rapid uptake, aminopolymer aerogel sorbent for direct air capture of CO_2.* US Patent Application 17/211,588, 2021.
332. N. Linneen, R. Pfeffer and Y. S. Lin, *Micropor. Mesopor. Mat.*, 2013, **176**, 123-131.
333. R. Begag, H. Krutka, W. Dong, D. Mihalcik, W. Rhine, G. Gould, J. Baldic and P. Nahass, *Greenh. Gases*, 2013, **3**, 30-39.
334. K. Wörmeyer and I. Smirnova, *Micropor. Mesopor. Mat.*, 2014, **184**, 61-69.
335. K. Wörmeyer and I. Smirnova, *Chem. Eng. J.*, 2013, **225**, 350-357.
336. K. Wörmeyer, M. Alnaief and I. Smirnova, *Adsorption*, 2012, **18**, 163-171.
337. Y. Kong, X. Shen, S. Cui and M. Fan, *RSC Adv.*, 2014, **4**, 64193-64199.
338. Y. Kong, G. Jiang, M. Fan, X. Shen, S. Cui and A. G. Russell, *Chem. Commun. (Cambridge, U. K.)*, 2014, **50**, 12158-12161.
339. U. Kamran and S.-J. Park, *J. Clean. Prod.*, 2021, **290**, 125776.
340. A. Mohd, W. A. W. Ab Karim Ghani, N. Z. Resitanim and L. Sanyang, *J. Disper. Sci. Technol.*, 2013, **34**, 974-984.
341. H. W. Kua, C. Pedapati, R. V. Lee and S. Kawi, *J. Clean. Prod.*, 2019, **210**, 860-871.
342. K. Tomas and F. Karel, *AIP Conf. Proc.*, 2017, **1889**, 020023.
343. M. E. Potter, J. J. Lee, L. A. Darunte and C. W. Jones, *J. Mater. Sci.*, 2019, **54**, 7563-7575.

344. M. A. Sakwa-Novak, S. Tan and C. W. Jones, *ACS Appl. Mater. Inter.*, 2015, **7**, 24748-24759.
345. W. H. Chan, M. N. Mazlee, Z. A. Ahmad, M. A. M. Ishak and J. B. Shamsul, *J. Mater. Cycles Waste*, 2017, **19**, 1-14.
346. C. G. Piscopo and S. Loebbecke, *ChemPlusChem*, 2020, **85**, 538-547.
347. J. Liu, Y. Wei and Y. Zhao, *ACS Sustain. Chem. Eng.*, 2019, **7**, 82-93.
348. C. Chen, M. Yang, Q. Wang, J.-C. Buffet and D. O'Hare, *J. Mater. Chem. A*, 2014, **2**, 15102-15110.
349. J. Yu, Q. Wang, D. O'Hare and L. Sun, *Chem. Soc. Rev.*, 2017, **46**, 5950-5974.
350. Q. Wang and D. O'Hare, *Chem. Commun. (Cambridge, U. K.)*, 2013, **49**, 6301-6303.
351. H. Y. Huang, R. T. Yang, D. Chinn and C. L. Munson, *Ind. Eng. Chem. Res.*, 2003, **42**, 2427-2433.
352. G. P. Knowles, J. V. Graham, S. W. Delaney and A. L. Chaffee, *Fuel Process. Technol.*, 2005, **86**, 1435-1448.
353. G. P. Knowles, S. W. Delaney and A. L. Chaffee, *Ind. Eng. Chem. Res.*, 2006, **45**, 2626-2633.
354. L. Wang and R. T. Yang, *J. Phys. Chem. C*, 2011, **115**, 21264-21272.
355. M.-H. Yuan, L. Wang and R. T. Yang, *Langmuir*, 2014, **30**, 8124-8130.
356. C. Gebald, J. A. Wurzbacher, P. Tingaut and A. Steinfeld, *Environ. Sci. Technol.*, 2013, **47**, 10063-10070.
357. Y. Zhao, Y. Zhao, G. I. N. Waterhouse, L. Zheng, X. Cao, F. Teng, L.-Z. Wu, C.-H. Tung, D. O'Hare and T. Zhang, *Adv. Mater.*, 2017, **29**, 1703828.
358. A.-Y. Park, H. Kwon, A. J. Woo and S.-J. Kim, *Adv. Mater.*, 2005, **17**, 106-109.
359. C. Chen, J.-C. Buffet and D. O'Hare, *Dalton T.*, 2020, **49**, 8498-8503.
360. P. J. E. Harlick and A. Sayari, *Ind. Eng. Chem. Res.*, 2007, **46**, 446-458.
361. Y. Kong, X. Shen, M. Fan, M. Yang and S. Cui, *Chem. Eng. J.*, 2016, **283**, 1059-1068.
362. Y. Kong, X. Shen, S. Cui and M. Fan, *Appl. Energ.*, 2015, **147**, 308-317.
363. D. Cheng, Y. Liu, H. Wang, X. Weng and Z. Wu, *J. Environ. Sci.*, 2015, **38**, 1-7.
364. J. Ma, Q. Liu, D. Chen, Y. Zhou and S. Wen, *J. Mater. Sci.*, 2014, **49**, 7585-7596.
365. Y. Labreche, Y. Fan, F. Rezaei, R. P. Lively, C. W. Jones and W. J. Koros, *ACS Appl. Mater. Inter.*, 2014, **6**, 19336-19346.
366. J. Liu, D. Cheng, Y. Liu and Z. Wu, *Energ. Fuel.*, 2013, **27**, 5416-5422.
367. Y. Du, Z. Du, W. Zou, H. Li, J. Mi and C. Zhang, *J. Colloid Interf. Sci.*, 2013, **409**, 123-128.
368. W. Yan, J. Tang, Z. Bian, J. Hu and H. Liu, *Ind. Eng. Chem. Res.*, 2012, **51**, 3653-3662.
369. Y. Fan, F. Rezaei and X. Yang, *Energy Technol.-GER*, 2019, **7**, 253-262.
370. M. Wang, L. Yao, J. Wang, Z. Zhang, W. Qiao, D. Long and L. Ling, *Appl. Energ.*, 2016, **168**, 282-290.
371. L. Zhang, X. Wang, M. Fujii, L. Yang and C. Song, *J. Energy Chem.*, 2017, **26**, 1030-1038.
372. L. Wang, M. Al-Aufi, C. N. Pacheco, L. Xie and R. M. Rioux, *ACS Sustain. Chem. Eng.*, 2019, **7**, 14785-14795.
373. R. Sanz, G. Calleja, A. Arencibia and E. S. Sanz-Pérez, *Energ. Fuel.*, 2013, **27**, 7637-7644.
374. R. Sanz, G. Calleja, A. Arencibia and E. S. Sanz-Pérez, *J. Mater. Chem. A*, 2013, **1**, 1956-1962.
375. Q. T. Vu, H. Yamada and K. Yogo, *Ind. Eng. Chem. Res.*, 2019, **58**, 15598-15605.
376. F. Liu, K. Huang and L. Jiang, *AIChE J.*, 2018, **64**, 3671-3680.
377. X. Wang and C. Song, *Energ. Fuel.*, 2014, **28**, 7742-7745.
378. J. Wang, D. Long, H. Zhou, Q. Chen, X. Liu and L. Ling, *Energ. Environ. Sci.*, 2012, **5**, 5742-5749.
379. J. Tanthana and S. S. C. Chuang, *ChemSusChem*, 2010, **3**, 957-964.
380. C. S. Srikanth and S. S. C. Chuang, *ChemSusChem*, 2012, **5**, 1435-1442.
381. P. Bollini, S. Choi, J. H. Drese and C. W. Jones, *Energ. Fuel.*, 2011, **25**, 2416-2425.
382. M. E. Potter, K. M. Cho, J. J. Lee and C. W. Jones, *Energ. Fuel.*, 2019, **33**, 1372-1382.
383. A. Heydari-Gorji, Y. Belmabkhout and A. Sayari, *Micropor. Mesopor. Mat.*, 2011, **145**, 146-149.
384. A. Heydari-Gorji and A. Sayari, *Ind. Eng. Chem. Res.*, 2012, **51**, 6887-6894.
385. S. A. Didas, R. Zhu, N. A. Brunelli, D. S. Sholl and C. W. Jones, *J. Phys. Chem. C*, 2014, **118**, 12302-12311.
386. C. S. Srikanth and S. S. C. Chuang, *J. Phys. Chem. C*, 2013, **117**, 9196-9205.

387. W. Choi, K. Min, C. Kim, Y. S. Ko, J. W. Jeon, H. Seo, Y.-K. Park and M. Choi, *Nat. Commun.*, 2016, **7**, 12640.
388. A. Ahmadalinezhad, R. Tailor and A. Sayari, *Chem.-Eur. J.*, 2013, **19**, 10543-10550.
389. A. Ahmadalinezhad and A. Sayari, *Phys. Chem. Chem. Phys.*, 2014, **16**, 1529-1535.
390. Y. Meng, J. Jiang, A. Aihemaiti, T. Ju, Y. Gao, J. Liu and S. Han, *ACS Appl. Mater. Inter.*, 2019, **11**, 33781-33791.
391. G. Calleja, R. Sanz, A. Arencibia and E. S. Sanz-Pérez, *Top. Catal.*, 2011, **54**, 135-145.
392. A. P. Hallenbeck and J. R. Kitchin, *Ind. Eng. Chem. Res.*, 2013, **52**, 10788-10794.
393. Q. Yu, J. d. l. P. Delgado, R. Veneman and D. W. F. Brilman, *Ind. Eng. Chem. Res.*, 2017, **56**, 3259-3269.
394. W. Si, B. Yang, Q. Yu, L. Lei and J. Zhu, *ACS Omega*, 2019, **4**, 11237-11244.
395. Q. T. Vu, H. Yamada and K. Yogo, *Energ. Fuel.*, 2019, **33**, 3370-3379.
396. Y. Zhai and S. S. C. Chuang, *Ind. Eng. Chem. Res.*, 2017, **56**, 13766-13775.
397. K. Min, W. Choi, C. Kim and M. Choi, *Nat. Commun.*, 2018, **9**, 726.
398. W. Choi, J. Park and M. Choi, *Ind. Eng. Chem. Res.*, 2021, **60**, 6147-6152.
399. R. Veneman, N. Frigka, W. Zhao, Z. Li, S. Kersten and W. Brilman, *Int. J. Greenh. Gas Con.*, 2015, **41**, 268-275.
400. I. M. Smal, Q. Yu, R. Veneman, B. Fränzel-Luiten and D. W. F. Brilman, *Energy Procedia*, 2014, **63**, 6834-6841.
401. D. G. Madden, H. S. Scott, A. Kumar, K.-J. Chen, R. Sanii, A. Bajpai, M. Lusi, T. Curtin, J. J. Perry and M. J. Zaworotko, *Philos. T. R. SOC. A*, 2017, **375**, 20160025.
402. B. Ray, S. R. Churipard and S. C. Peter, *J. Mater. Chem. A*, 2021, **9**, 26498-26527.
403. W. Buijs and S. de Flart, *Ind. Eng. Chem. Res.*, 2017, **56**, 12297-12304.
404. J. Young, E. García-Díez, S. Garcia, C. Ireland, B. Smit and M. van der Spek, *Available at SSRN 3814942*, 2021. http://dx.doi.org/10.2139/ssrn.3814942
405. J. A. Wurzbacher, C. Gebald, S. Brunner and A. Steinfeld, *Chem. Eng. J.*, 2016, **283**, 1329-1338.
406. J. Elfving and T. Sainio, *Chem. Eng. Sci.*, 2021, **246**, 116885.
407. R. B. Said, J. M. Kolle, K. Essalah, B. Tangour and A. Sayari, *ACS Omega*, 2020, **5**, 26125-26133.
408. A. Danon, P. C. Stair and E. Weitz, *J. Phys. Chem. C*, 2011, **115**, 11540-11549.
409. Z. Bacsik, N. Ahlsten, A. Ziadi, G. Zhao, A. E. Garcia-Bennett, B. Martín-Matute and N. Hedin, *Langmuir*, 2011, **27**, 11118-11128.
410. Z. Bacsik and N. Hedin, *Vib. Spectrosc.*, 2016, **87**, 215-221.
411. A. Sayari, Y. Belmabkhout and E. Da'na, *Langmuir*, 2012, **28**, 4241-4247.
412. L. Mafra, T. Čendak, S. Schneider, P. V. Wiper, J. Pires, J. R. B. Gomes and M. L. Pinto, *J. Am. Chem. Soc.*, 2017, **139**, 389-408.
413. C.-T. Hung, C.-F. Yang, J.-S. Lin, S.-J. Huang, Y.-C. Chang and S.-B. Liu, *Micropor. Mesopor. Mat.*, 2017, **238**, 2-13.
414. D. Shimon, C.-H. Chen, J. J. Lee, S. A. Didas, C. Sievers, C. W. Jones and S. E. Hayes, *Environ. Sci. Technol.*, 2018, **52**, 1488-1495.
415. F. Mani, M. Peruzzini and P. Stoppioni, *Green Chem.*, 2006, **8**, 995-1000.
416. X. Li, E. Hagaman, C. Tsouris and J. W. Lee, *Energ. Fuel.*, 2003, **17**, 69-74.
417. G. S. Foo, J. J. Lee, C.-H. Chen, S. E. Hayes, C. Sievers and C. W. Jones, *ChemSusChem*, 2017, **10**, 266-276.
418. W. Buijs, *Ind. Eng. Chem. Res.*, 2021, **60**, 11309-11316.
419. J. A. Mason, T. M. McDonald, T.-H. Bae, J. E. Bachman, K. Sumida, J. J. Dutton, S. S. Kaye and J. R. Long, *J. Am. Chem. Soc.*, 2015, **137**, 4787-4803.
420. T. M. McDonald, W. R. Lee, J. A. Mason, B. M. Wiers, C. S. Hong and J. R. Long, *J. Am. Chem. Soc.*, 2012, **134**, 7056-7065.
421. W. R. Lee, S. Y. Hwang, D. W. Ryu, K. S. Lim, S. S. Han, D. Moon, J. Choi and C. S. Hong, *Energ. Environ. Sci.*, 2014, **7**, 744-751.
422. T. M. McDonald, J. A. Mason, X. Kong, E. D. Bloch, D. Gygi, A. Dani, V. Crocellà, F. Giordanino, S. O. Odoh, W. S. Drisdell, B. Vlaisavljevich, A. L. Dzubak, R. Poloni, S. K. Schnell, N. Planas, K. Lee, T. Pascal, L. F. Wan, D.

Prendergast, J. B. Neaton, B. Smit, J. B. Kortright, L. Gagliardi, S. Bordiga, J. A. Reimer and J. R. Long, *Nature*, 2015, **519**, 303.

423. W. R. Lee, H. Jo, L.-M. Yang, H. Lee, D. W. Ryu, K. S. Lim, J. H. Song, D. Y. Min, S. S. Han, J. G. Seo, Y. K. Park, D. Moon and C. S. Hong, *Chem. Sci.*, 2015, **6**, 3697-3705.
424. P.-Q. Liao, X.-W. Chen, S.-Y. Liu, X.-Y. Li, Y.-T. Xu, M. Tang, Z. Rui, H. Ji, J.-P. Zhang and X.-M. Chen, *Chem. Sci.*, 2016, **7**, 6528-6533.
425. S. Choi, T. Watanabe, T.-H. Bae, D. S. Sholl and C. W. Jones, *J. Phys. Chem. Lett.*, 2012, **3**, 1136-1141.
426. R. Hughes, G. Kotamreddy, A. Ostace, D. Bhattacharyya, R. L. Siegelman, S. T. Parker, S. A. Didas, J. R. Long, B. Omell and M. Matuszewski, *Energ. Fuel.*, 2021, **35**, 6040-6055.
427. H. Jo, W. R. Lee, N. W. Kim, H. Jung, K. S. Lim, J. E. Kim, D. W. Kang, H. Lee, V. Hiremath, J. G. Seo, H. Jin, D. Moon, S. S. Han and C. S. Hong, *ChemSusChem*, 2017, **10**, 541-550.
428. W. R. Lee, J. E. Kim, S. J. Lee, M. Kang, D. W. Kang, H. Y. Lee, V. Hiremath, J. G. Seo, H. Jin, D. Moon, M. Cho, Y. Jung and C. S. Hong, *ChemSusChem*, 2018, **11**, 1694-1707.
429. B. Dinakar, A. C. Forse, H. Z. H. Jiang, Z. Zhu, J.-H. Lee, E. J. Kim, S. T. Parker, C. J. Pollak, R. L. Siegelman, P. J. Milner, J. A. Reimer and J. R. Long, *J. Am. Chem. Soc.*, 2021, **143**, 15258-15270.
430. Ü. Kökçam-Demir, A. Goldman, L. Esrafili, M. Gharib, A. Morsali, O. Weingart and C. Janiak, *Chem. Soc. Rev.*, 2020, **49**, 2751-2798.
431. Y. K. Hwang, D.-Y. Hong, J.-S. Chang, S. H. Jhung, Y.-K. Seo, J. Kim, A. Vimont, M. Daturi, C. Serre and G. Férey, *Angew. Chem. Int. Edit.*, 2008, **47**, 4144-4148.
432. J. Park, Y. S. Chae, D. W. Kang, M. Kang, J. H. Choe, S. Kim, J. Y. Kim, Y. W. Jeong and C. S. Hong, *ACS Appl. Mater. Inter.*, 2021, **13**, 25421-25427.
433. H. Zhang, L.-M. Yang and E. Ganz, *ACS Appl. Mater. Inter.*, 2020, **12**, 18533-18540.
434. H. Zhang, L.-M. Yang and E. Ganz, *Langmuir*, 2020, **36**, 14104-14112.
435. J. D. Martell, P. J. Milner, R. L. Siegelman and J. R. Long, *Chem. Sci.*, 2020, **11**, 6457-6471.
436. R. W. Flaig, T. M. Osborn Popp, A. M. Fracaroli, E. A. Kapustin, M. J. Kalmutzki, R. M. Altamimi, F. Fathieh, J. A. Reimer and O. M. Yaghi, *J. Am. Chem. Soc.*, 2017, **139**, 12125-12128.
437. K. S. Lackner, *Eur. Phys. J.-Spec. Top.*, 2009, **176**, 93-106.
438. T. Wang, K. S. Lackner and A. Wright, *Environ. Sci. Technol.*, 2011, **45**, 6670-6675.
439. T. Wang, K. S. Lackner and A. B. Wright, *Phys. Chem. Chem. Phys.*, 2013, **15**, 504-514.
440. M. Mahmoudkhani and D. W. Keith, *Int. J. Greenh. Gas Con.*, 2009, **3**, 376-384.
441. H. He, M. Zhong, D. Konkolewicz, K. Yacatto, T. Rappold, G. Sugar, N. E. David and K. Matyjaszewski, *J. Mater. Chem. A*, 2013, **1**, 6810-6821.
442. H. He, M. Zhong, D. Konkolewicz, K. Yacatto, T. Rappold, G. Sugar, N. E. David, J. Gelb, N. Kotwal, A. Merkle and K. Matyjaszewski, *Adv. Funct. Mater.*, 2013, **23**, 4720-4728.
443. H. He, W. Li, M. Zhong, D. Konkolewicz, D. Wu, K. Yaccato, T. Rappold, G. Sugar, N. E. David and K. Matyjaszewski, *Energ. Environ. Sci.*, 2013, **6**, 488-493.
444. J. Song, J. Liu, W. Zhao, Y. Chen, H. Xiao, X. Shi, Y. Liu and X. Chen, *Ind. Eng. Chem. Res.*, 2018, **57**, 4941-4948.
445. T. Wang, K. Ge, K. Chen, C. Hou and M. Fang, *Phys. Chem. Chem. Phys.*, 2016, **18**, 13084-13091.
446. X. Shi, H. Xiao, K. S. Lackner and X. Chen, *Angew. Chem. Int. Edit.*, 2016, **55**, 4026-4029.
447. T. Wang, J. Liu, H. Huang, M. Fang and Z. Luo, *Chem. Eng. J.*, 2016, **284**, 679-686.
448. X. Y. Shi, Q. B. Li, T. Wang and K. S. Lackner, *PLoS One*, 2017, **12**, e0179828.
449. T. Wang, J. Liu, K. S. Lackner, X. Shi, M. Fang and Z. Luo, *Greenh. Gases*, 2016, **6**, 138-149.
450. X. Shi, H. Xiao, X. Chen and K. S. Lackner, *Chem.-Eur. J.*, 2016, **22**, 18326-18330.
451. L. Wei, W. Wei, N. Xue, F. Cheng and H. Yang, *ACS Appl. Mater. Inter.*, 2021, **13**, 5814-5822.
452. F. Inagaki, C. Matsumoto, T. Iwata and C. Mukai, *J. Am. Chem. Soc.*, 2017, **139**, 4639-4642.

453. L. B. Hamdy, R. J. Wakeham, M. Taddei, A. R. Barron and E. Andreoli, *Chem. Mater.*, 2019, **31**, 4673-4684.
454. P. D. Mobley, A. V. Rayer, J. Tanthana, T. R. Gohndrone, M. Soukri, L. J. I. Coleman and M. Lail, *Ind. Eng. Chem. Res.*, 2017, **56**, 11958-11966.
455. B. Wadi, A. Mahomed, Y. Bai, A. Osatiashtiani, V. Manovic and S. A. Nabavi, *Powder Technol.*, 2021, **393**, 257-264.
456. L. Ma, C. Qin, S. Pi and H. Cui, *Chem. Eng. J.*, 2020, **379**, 122385.
457. E. Luzzi, P. Aprea, M. Salzano de Luna, D. Caputo and G. Filippone, *ACS Appl. Mater. Inter.*, 2021, **13**, 20728-20734.
458. L. Nie, J. Jin, J. Chen and J. Mi, *Energy*, 2018, **161**, 60-69.
459. D. Nikjoo and F. Akhtar, *J. CO2 Util.*, 2017, **21**, 473-479.
460. J. H. Choe, J. R. Park, Y. S. Chae, D. W. Kim, D. S. Choi, H. Kim, M. Kang, H. Seo, Y.-K. Park and C. S. Hong, *Communications Materials*, 2021, **2**, 3.
461. M. Guo, H. Wu, L. Lv, H. Meng, J. Yun, J. Jin and J. Mi, *ACS Appl. Mater. Inter.*, 2021, **13**, 21775-21785.
462. Y. Seok Chae, S. Park, D. Won Kang, D. Won Kim, M. Kang, D. San Choi, J. Hyeak Choe and C. Seop Hong, *Chem. Eng. J.*, 2022, **433**, 133856.
463. R. Rodríguez-Mosqueda, E. A. Bramer, T. Roestenberg and G. Brem, *Ind. Eng. Chem. Res.*, 2018, **57**, 3628-3638.
464. A. Shiue, T. H. Hsu, S. M. Chang and G. Leggett, *Int. J. Environ. Sci. Te.*, 2021, DOI: 10.1007/s13762-021-03442-8.
465. K. B. Yoon, *Accounts Chem. Res.*, 2007, **40**, 29-40.
466. R. Gaikwad, S. Gaikwad, Y. Kim and S. Han, *Micropor. Mesopor. Mat.*, 2021, **323**, 111233.
467. S. Lawson, Q. Al-Naddaf, A. Krishnamurthy, M. S. Amour, C. Griffin, A. A. Rownaghi, J. C. Knox and F. Rezaei, *ACS Appl. Mater. Inter.*, 2018, **10**, 19076-19086.
468. F. Rezaei, S. Lawson, H. Hosseini, H. Thakkar, A. Hajari, S. Monjezi and A. A. Rownaghi, *Chem. Eng. J.*, 2017, **313**, 1346-1353.
469. M. Wilson, S. N. Barrientos-Palomo, P. C. Stevens, N. L. Mitchell, G. Oswald, C. M. Nagaraja and J. P. S. Badyal, *ACS Appl. Mater. Inter.*, 2018, **10**, 4057-4065.
470. H.-G. Zhen, H. Mao, I. U. Haq, S.-H. Li, A. Ahmad and Z.-P. Zhao, *Sep. Purif. Technol.*, 2020, **233**, 116042.
471. H.-G. Zhen, Z.-P. Zhao, H. Mao, T. Li, J.-H. Li and T.-S. Hou, *IOP Conference Series: Earth and Environmental Science*, 2019, **330**, 032107.
472. Q. Al-Naddaf, S. Lawson, A. A. Rownaghi and F. Rezaei, *AIChE J.*, 2020, **66**, e16297.
473. M. J. Regufe, A. F. P. Ferreira, J. M. Loureiro, Y. Shi, A. Rodrigues and A. M. Ribeiro, *Adsorption*, 2018, **24**, 249-265.
474. A. Masala, J. G. Vitillo, G. Mondino, G. Martra, R. Blom, C. A. Grande and S. Bordiga, *Ind. Eng. Chem. Res.*, 2017, **56**, 8485-8498.
475. W. Y. Hong, S. P. Perera and A. D. Burrows, *Micropor. Mesopor. Mat.*, 2020, **308**, 110525.
476. M. Alnaief and I. Smirnova, *J. Supercrit. Fluid.*, 2011, **55**, 1118-1123.
477. J. Singh, H. Bhunia and S. Basu, *Chem. Eng. J.*, 2019, **374**, 1-9.
478. R. P. Lively, R. R. Chance, B. T. Kelley, H. W. Deckman, J. H. Drese, C. W. Jones and W. J. Koros, *Ind. Eng. Chem. Res.*, 2009, **48**, 7314-7324.
479. P. J. Brennan, H. Thakkar, X. Li, A. A. Rownaghi, W. J. Koros and F. Rezaei, *Energy Technol.-GER*, 2017, **5**, 327-337.
480. G. Chen, W. J. Koros and C. W. Jones, *ACS Appl. Mater. Inter.*, 2016, **8**, 9700-9709.
481. Y. Labreche, Y. Fan, R. P. Lively, C. W. Jones and W. J. Koros, *J. Appl. Polym. Sci.*, 2015, **132**.
482. Y. Fan, J. Kalyanaraman, Y. Labreche, F. Rezaei, R. P. Lively, M. J. Realff, W. J. Koros, C. W. Jones and Y. Kawajiri, *Ind. Eng. Chem. Res.*, 2015, **54**, 1783-1795.
483. F. Rezaei, S. Subramanian, J. Kalyanaraman, R. P. Lively, Y. Kawajiri and M. J. Realff, *Chem. Eng. Sci.*, 2014, **113**, 62-76.
484. F. S. Li, Y. Labreche, R. P. Lively, J. S. Lee, C. W. Jones and W. J. Koros, *Polymer*, 2014, **55**, 1341-1346.
485. G. Chen, R. P. Lively, C. W. Jones and W. J. Koros, *Ind. Eng. Chem. Res.*, 2014, **53**, 7113-7120.
486. F. Rezaei, R. P. Lively, Y. Labreche, G. Chen, Y. Fan, W. J. Koros and C. W. Jones, *ACS Appl. Mater. Inter.*, 2013, **5**,

3921-3931.
487. F. S. Li, W. Qiu, R. P. Lively, J. S. Lee, A. A. Rownaghi and W. J. Koros, *ChemSusChem*, 2013, **6**, 1216-1223.
488. Y. Labreche, R. P. Lively, F. Rezaei, G. Chen, C. W. Jones and W. J. Koros, *Chem. Eng. J.*, 2013, **221**, 166-175.
489. D. Bhandari, K. O. Olanrewaju, N. Bessho, V. Breedveld and W. J. Koros, *Sep. Purif. Technol.*, 2013, **104**, 68-80.
490. R. P. Lively, R. R. Chance, J. A. Mysona, V. P. Babu, H. W. Deckman, D. P. Leta, H. Thomann and W. J. Koros, *Int. J. Greenh. Gas Con.*, 2012, **10**, 285-294.
491. R. P. Lively, N. Bessho, D. A. Bhandari, Y. Kawajiri and W. J. Koros, *Int. J. Hydrogen Energ.*, 2012, **37**, 15227-15240.
492. R. P. Lively, D. P. Leta, B. A. DeRites, R. R. Chance and W. J. Koros, *Chem. Eng. J.*, 2011, **171**, 801-810.
493. R. P. Lively, R. R. Chance and W. J. Koros, *Ind. Eng. Chem. Res.*, 2010, **49**, 7550-7562.
494. Y. H. Lee, Y. Kwon, C. Kim, Y.-E. Hwang, M. Choi, Y. Park, A. Jamal and D.-Y. Koh, *JACS Au*, 2021, **1**, 1198-1207.
495. R. Ostermann, J. Cravillon, C. Weidmann, M. Wiebcke and B. M. Smarsly, *Chem. Commun. (Cambridge, U. K.)*, 2011, **47**, 442-444.
496. M. Armstrong, C. Balzer, B. Shan and B. Mu, *Langmuir*, 2017, **33**, 9066-9072.
497. M. R. Armstrong, B. Shan, S. V. Maringanti, W. Zheng and B. Mu, *Ind. Eng. Chem. Res.*, 2016, **55**, 9944-9951.
498. M. R. Armstrong, K. Y. Y. Arredondo, C.-Y. Liu, J. E. Stevens, A. Mayhob, B. Shan, S. Senthilnathan, C. J. Balzer and B. Mu, *Ind. Eng. Chem. Res.*, 2015, **54**, 12386-12392.
499. Y.-n. Wu, F. Li, H. Liu, W. Zhu, M. Teng, Y. Jiang, W. Li, D. Xu, D. He, P. Hannam and G. Li, *J. Mater. Chem.*, 2012, **22**, 16971-16978.
500. S. Lawson, C. Griffin, K. Rapp, A. A. Rownaghi and F. Rezaei, *Energ. Fuel.*, 2019, **33**, 2399-2407.
501. H. Thakkar, S. Eastman, Q. Al-Naddaf, A. A. Rownaghi and F. Rezaei, *ACS Appl. Mater. Inter.*, 2017, **9**, 35908-35916.
502. H. Thakkar, S. Eastman, A. Hajari, A. A. Rownaghi, J. C. Knox and F. Rezaei, *ACS Appl. Mater. Inter.*, 2016, **8**, 27753-27761.
503. C. Dhoke, A. Zaabout, S. Cloete and S. Amini, *Ind. Eng. Chem. Res.*, 2021, **60**, 3779-3798.
504. Q. Yu and D. W. F. Brilman, *Energy Procedia*, 2017, **114**, 6102-6114.
505. S. J. A. DeWitt, A. Sinha, J. Kalyanaraman, F. Zhang, M. J. Realff and R. P. Lively, *Annu. Rev. Chem. Biomol.*, 2018, **9**, 129-152.
506. H. M. Schellevis, T. N. van Schagen and D. W. F. Brilman, *Int. J. Greenh. Gas Con.*, 2021, **110**, 103431.
507. A. Sayari, Q. Liu and P. Mishra, *ChemSusChem*, 2016, **9**, 2796-2803.
508. W. Brilman, L. Garcia Alba and R. Veneman, *Biomass Bioenerg.*, 2013, **53**, 39-47.
509. J. A. Wurzbacher, C. Gebald, N. Piatkowski and A. Steinfeld, *Environ. Sci. Technol.*, 2012, **46**, 9191-9198.
510. C. Beauttler, *Climeworks: direct air capture update*, in 2020 Integrated Project Review Meeting - Carbon Capture, 2020. https://netl.doe.gov/2020CC-proceedings
511. C. J. E. Bajamundi, J. Koponen, V. Ruuskanen, J. Elfving, A. Kosonen, J. Kauppinen and J. Ahola, *J. CO2 Util.*, 2019, **30**, 232-239.
512. G. Santori, C. Charalambous, M.-C. Ferrari and S. Brandani, *Energy*, 2018, **162**, 1158-1168.
513. C. Gebald, N. Repond and J. A. Wurzbacher, *Steam assisted vacuum desorption process for carbon dioxide capture*. US Patent 10279306, 2019.
514. N. McQueen, P. Psarras, H. Pilorgé, S. Liguori, J. He, M. Yuan, C. M. Woodall, K. Kian, L. Pierpoint, J. Jurewicz, J. M. Lucas, R. Jacobson, N. Deich and J. Wilcox, *Environ. Sci. Technol.*, 2020, **54**, 7542-7551.
515. S. Fahr, J. Powell, A. Favero, A. J. Giarrusso, R. P. Lively and M. J. Realff, *Greenh. Gases*, 2022, **12**, 170-188.
516. J. Wohland, D. Witthaut and C.-F. Schleussner, *Earth's Future*, 2018, **6**, 1380-1384.
517. C. Breyer, M. Fasihi and A. Aghahosseini, *Mitig. Adapt. Strat. Gl.*, 2020, **25**, 43-65.
518. H. Azarabadi and K. S. Lackner, *Environ. Sci. Technol.*, 2020, **54**, 5102-5111.
519. K. S. Lackner and H. Azarabadi, *Ind. Eng. Chem. Res.*, 2021, **60**, 8196-8208.
520. I. Ghiat and T. Al-Ansari, *J. CO2 Util.*, 2021, **45**, 101432.

521. C. Hepburn, E. Adlen, J. Beddington, E. A. Carter, S. Fuss, N. Mac Dowell, J. C. Minx, P. Smith and C. K. Williams, *Nature*, 2019, **575**, 87-97.
522. S. A. Abdul-Wahab, S. Chin Fah En, A. Elkamel, L. Ahmadi and K. Yetilmezsoy, *Atmos. Polluti. Res.*, 2015, **6**, 751-767.
523. S. Satyapal, T. Filburn, J. Trela and J. Strange, *Energ. Fuel.*, 2001, **15**, 250-255.
524. L. Baus and S. Nehr, *Build. Environ.*, 2022, **208**, 108629.
525. S. Wang, Y. Zhang, W. Ju, J. M. Chen, P. Ciais, A. Cescatti, J. Sardans, I. A. Janssens, M. Wu, J. A. Berry, E. Campbell, M. Fernández-Martínez, R. Alkama, S. Sitch, P. Friedlingstein, W. K. Smith, W. Yuan, W. He, D. Lombardozzi, M. Kautz, D. Zhu, S. Lienert, E. Kato, B. Poulter, T. G. M. Sanders, I. Krüger, R. Wang, N. Zeng, H. Tian, N. Vuichard, A. K. Jain, A. Wiltshire, V. Haverd, D. S. Goll and J. Peñuelas, *Science*, 2020, **370**, 1295-1300.
526. E. Daneshvar, R. J. Wicker, P.-L. Show and A. Bhatnagar, *Chem. Eng. J.*, 2022, **427**, 130884.
527. C. Zhu, X. Zhai, Y. Xi, J. Wang, F. Kong, Y. Zhao and Z. Chi, *J. CO2 Util.*, 2020, **37**, 320-327.
528. D. Y. C. Leung, G. Caramanna and M. M. Maroto-Valer, *Renew. Sust. Energ. Rev.*, 2014, **39**, 426-443.
529. Y.-M. Wei, J.-N. Kang, L.-C. Liu, Q. Li, P.-T. Wang, J.-J. Hou, Q.-M. Liang, H. Liao, S.-F. Huang and B. Yu, *Nat. Clim. Change*, 2021, **11**, 112-118.
530. V. Núñez-López and E. Moskal, *Frontiers in Climate*, 2019, **1**, 5.
531. R. L. Tyne, P. H. Barry, M. Lawson, D. J. Byrne, O. Warr, H. Xie, D. J. Hillegonds, M. Formolo, Z. M. Summers, B. Skinner, J. M. Eiler and C. J. Ballentine, *Nature*, 2021, **600**, 670-674.
532. N. A. Azzolina, W. D. Peck, J. A. Hamling, C. D. Gorecki, S. C. Ayash, T. E. Doll, D. V. Nakles and L. S. Melzer, *Int. J. Greenh. Gas Con.*, 2016, **51**, 369-379.
533. T. Wang, S. Tian, G. Li, M. Sheng, W. Ren, Q. Liu and S. Zhang, *J. Phys. Chem. C*, 2018, **122**, 17009-17018.
534. C. M. Oldenburg, K. Pruess and S. M. Benson, *Energ. Fuel.*, 2001, **15**, 293-298.
535. A. Hamza, I. A. Hussein, M. J. Al-Marri, M. Mahmoud, R. Shawabkeh and S. Aparicio, *J. Petrol. Sci. Eng.*, 2021, **196**, 107685.
536. P. Nikolaidis and A. Poullikkas, *Renew. Sust. Energ. Rev.*, 2017, **67**, 597-611.
537. R. Schäppi, D. Rutz, F. Dähler, A. Muroyama, P. Haueter, J. Lilliestam, A. Patt, P. Furler and A. Steinfeld, *Nature*, 2022, **601**, 63-68.
538. V. S. Derevschikov, J. V. Veselovskaya, T. Y. Kardash, D. A. Trubitsyn and A. G. Okunev, *Fuel*, 2014, **127**, 212-218.
539. J. V. Veselovskaya, V. S. Derevschikov, T. Y. Kardash and A. G. Okunev, *Renewable Bioresources*, 2015, **3**, 1.
540. J. V. Veselovskaya, P. D. Parunin, O. V. Netskina and A. G. Okunev, *Top. Catal.*, 2018, **61**, 1528-1536.
541. J. V. Veselovskaya, P. D. Parunin, O. V. Netskina, L. S. Kibis, A. I. Lysikov and A. G. Okunev, *Energy*, 2018, **159**, 766-773.
542. S. Navarro-Jaén, M. Virginie, J. Bonin, M. Robert, R. Wojcieszak and A. Y. Khodakov, *Nat. Rev. Chem.*, 2021, **5**, 564-579.
543. A. Kätelhön, R. Meys, S. Deutz, S. Suh and A. Bardow, *P. Natl. Acad. Sci. USA*, 2019, **116**, 11187-11194.
544. M. J. Bos, Y. Slotboom, S. R. A. Kersten and D. W. F. Brilman, *Ind. Eng. Chem. Res.*, 2019, **58**, 13987-13999.
545. R. Sen, A. Goeppert and G. K. S. Prakash, *Aldrichim. Acta*, 2020, **53**, 39-56.
546. R. Sen, C. J. Koch, V. Galvan, N. Entesari, A. Goeppert and G. K. S. Prakash, *J. CO2 Util.*, 2021, **54**, 101762.
547. H. Koizumi, K. Takeuchi, K. Matsumoto, N. Fukaya, K. Sato, M. Uchida, S. Matsumoto, S. Hamura and J.-C. Choi, *Commun. Chem.*, 2021, **4**, 66.
548. H. Ishaq, O. Siddiqui, G. Chehade and I. Dincer, *Int. J. Hydrogen Energ.*, 2021, **46**, 4749-4760.
549. B. B. Asare Bediako, Q. Qian, Y. Wang, J. Zhang, Z. Wang, S. Li, H. Liu, T. Wu, M. Ge and B. Han, *Chem Catalysis*, 2022, **2**, 114-124.
550. T. N. Do, C. You and J. Kim, *Energ. Environ. Sci.*, 2022, **15**, 169-184.
551. Z. He, Y. Wang, Y. Miao, H. Wang, X. Zhu and J. Li, *J. Environ. Chem. Eng.*, 2022, **10**, 107239.

552. Y. Belmabkhout, P. M. Bhatt, K. Adil, R. S. Pillai, A. Cadiau, A. Shkurenko, G. Maurin, G. Liu, W. J. Koros and M. Eddaoudi, *Nat. Energy*, 2018, **3**, 1059-1066.
553. S. Mukherjee, N. Sikdar, D. O'Nolan, D. M. Franz, V. Gascón, A. Kumar, N. Kumar, H. S. Scott, D. G. Madden, P. E. Kruger, B. Space and M. J. Zaworotko, *Sci. Adv.*, 2019, **5**, eaax9171.
554. T. Wang, E. Lin, Y.-L. Peng, Y. Chen, P. Cheng and Z. Zhang, *Coordin. Chem. Rev.*, 2020, **423**, 213485.
555. Y. Zhao, G. Chen, T. Bian, C. Zhou, G. I. N. Waterhouse, L.-Z. Wu, C.-H. Tung, L. J. Smith, D. O'Hare and T. Zhang, *Adv. Mater.*, 2015, **27**, 7824-7831.
556. J. Wu, X. Zhu, F. Yang, T. Ge and R. Wang, *Chem. Eng. J.*, 2021, **425**, 131409.